

REPORT DOCUMENTATION PAGE

0259

The public reporting burden for this collection of information is estimated to average 1 hour per response, including the gathering and maintaining the data needed, and completing and reviewing the collection of information. Send comments regarding this burden estimate or any other aspect of this collection of information, including suggestions for reducing the burden, to Department of Defense, Washington Headquarters Services, Directorate for Information Operations and Reports (0704-0188), 1215 Jefferson Davis Highway, Suite 1204, Arlington, VA 22202-4302. Respondents should be aware that notwithstanding any other provision of law, no person shall be subject to any penalty for failing to comply with a collection of information if it does not display a currently valid OMB control number.

PLEASE DO NOT RETURN YOUR FORM TO THE ABOVE ADDRESS.

1. REPORT DATE (DD-MM-YYYY) 05/20/03		2. REPORT TYPE Final Report		3. DATES COVERED (From - To) 03/15/98 - 03/14/03	
4. TITLE AND SUBTITLE Dynamics and Control of Fluid-Structure Interaction				5a. CONTRACT NUMBER F 49620-98-1-0383	
				5b. GRANT NUMBER	
				5c. PROGRAM ELEMENT NUMBER	
6. AUTHOR(S) Clark, Robert L.				5d. PROJECT NUMBER	
				5e. TASK NUMBER	
				5f. WORK UNIT NUMBER	
7. PERFORMING ORGANIZATION NAME(S) AND ADDRESS(ES) Duke University PO Box 90077 Durham, NC 27708-0077				8. PERFORMING ORGANIZATION REPORT NUMBER	
9. SPONSORING/MONITORING AGENCY NAME(S) AND ADDRESS(ES) USAF, AFRL AF Office of Scientific Research 4015 Wilson Blvd, Room 713 Arlington, VA 22203-1954				10. SPONSOR/MONITOR'S ACRONYM(S) AFOSR	
				11. SPONSOR/MONITOR'S REPORT NUMBER(S)	
12. DISTRIBUTION/AVAILABILITY STATEMENT None DISTRIBUTION STATEMENT A Approved for Public Release Distribution Unlimited					
13. SUPPLEMENTARY NOTES N/A					
14. ABSTRACT The primary objective of the research program was to advance a fundamental method of developing dynamic models of fluid-structure interaction which capture the essential physics required to design and evaluate the application of adaptive structures for the control of aeroelastic, structural acoustic, and coupled aeroelastic, structural acoustic systems. Analytical, numerical, and experimental procedures were conducted as part of the research effort. A total of eight journal papers were published and an additional three journal papers are currently under review as a result of this funding.					
15. SUBJECT TERMS Dynamic models of fluid-structure interaction Hybrid active/passive control systems					
16. SECURITY CLASSIFICATION OF:			17. LIMITATION OF ABSTRACT U U	18. NUMBER OF PAGES 4	19a. NAME OF RESPONSIBLE PERSON Robert L. Clark
a. REPORT	b. ABSTRACT	c. THIS PAGE			19b. TELEPHONE NUMBER (Include area code) (919) 660-5359

20030909 098

Final Report

Dynamics and Control of Fluid-Structure Interaction

AFOSR Grant Number F49620-98-1-0383

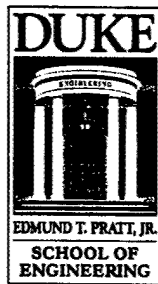
Robert L. Clark, PI

Duke University

Department of Mechanical Engineering and Materials Science

Box 90300

Durham, NC 27708-0300



Objective

The primary objective of the proposed research program was to advance a fundamental method of developing dynamic models of fluid-structure interaction which capture the essential physics required to design and evaluate the application of adaptive structures for the control of aeroelastic, structural acoustic, and coupled aeroelastic, structural acoustic systems. Analytical, numerical, and experimental procedures were conducted as part of the research effort.

Summary of Effort and Accomplishments

Significant progress was made towards the advancement and development of control strategies for the mitigation of damage due to acoustic loading in rocket fairings at launch. A successful demonstration of a hybrid active/passive control system and the creation of broadly applicable hybrid acoustic and vibration control design techniques were both substantial outcomes of the funded research. The research demonstrates innovative control solutions that coordinate the best efforts of active and passive techniques with minimal impact on payload weight and volume.

Another focus of the research emphasized adaptive control strategies since many Air Force related applications involve the implementation of controllers on systems that are time-varying or experience significant change in environmental operating conditions. Such examples include the acoustics of rocket fairing interiors at launch and aeroelastic systems. A recursive generalized predictive control approach was developed that provides a mechanism for on-line system identification and closed-loop feedback control simultaneously. The controller has been tested on a number of different test-beds including a rocket payload fairing and an optical system for the suppression of jitter, an important control problem for implementation of the airborne laser.

Efforts devoted to development of design methodologies for actively controlled aeroelastic structures have focused on flutter control, although the approach is also applicable to maneuverability. A reduced-order model of a delta wing was used to produce an efficient computational approach to design optimization of sensors and actuators. A number of methods were developed that yielded dramatic improvements over previously employed methods. Experimental implementation was used to validate the findings. Significant control was achieved with the experimental test rig, extending the flutter boundary by nearly 10% without control spillover. Work to further refine the approach toward improved results is underway.

Detailed Research Summary/Accomplishments

This report contains all of the journal publications which resulted from the funded effort. A total of 8 journal papers were published and an additional 3 journal papers are currently under review. All of the journal articles are listed in the section devoted to publications. Journal articles 1, 2, 4, and 8 are focused on the control of low-frequency sound in rocket fairings. Journal article 3 addresses the adaptive feedback control strategy, and journal articles 5, 6, 7, 9, 10, and 11 are devoted to design methodologies focused on the control of aeroelastic systems. The consolidation of these articles forms an archival report for the research effort conducted.

Personnel Supported

1. Robert L. Clark, (PI)
2. Jonathan D. Kemp (Graduate Student)

3. Suk-Min Moon (Graduate Student)
4. Robert E. Richard (Graduate Student)

Publications

Journals

1. J. D. Kemp and R. L. Clark, 2003. "Optimal Collocated and Multi-Variable Hybrid Active/Passive Vibration Control Design," submitted to *Journal of Intelligent Materials and Materials Systems*.
2. J. D. Kemp and R. L. Clark, 2002. "Optimal hybrid active/passive vibration control design," submitted to *Journal of Sound and Vibration*.
3. Suk-Min Moon, Robert L. Clark and Daniel G. Cole, 2002. "The Recursive Generalized Predictive Feedback Control: Theory and Experiments", submitted to the *Journal of Sound and Vibration*.
4. Kemp, J. D. and R. L. Clark, 2003. "Noise Reduction in a Launch Vehicle Fairing Using Actively Controlled Loudspeakers," *Journal of the Acoustical Society of America*, **113**(4), 1986-1994.
5. Rule, J. A., R. E. Richard, and R. L., Clark, 2001. "Design of an Aeroelastic Delta Wing Model for Active Flutter Control," *AIAA Journal of Guidance, Control, and Dynamics*, **24**(5), 918-924.
6. Clark, R. L., 2001. "Adaptive Structures: Compensators by Design," *Noise Control Engineering Journal*, **49**(1), 15-20.
7. Richard, R. E., Rule, J. A., and R. L. Clark, 2001. "Genetic Spatial Optimization of Active Elements on an Aeroelastic Delta Wing," *ASME Journal of Vibration and Acoustics*, **123**, 466-471.
8. Lane, S. A., J. D. Kemp, S. Griffin, and R. L. Clark, 2001. "Feasibility Analysis for Active Acoustic Control of a Rocket Fairing using Spatially Weighted Transducer Arrays," *AIAA Journal of Spacecraft and Rockets*, **38**(1).
9. Smith, G. Clark and Clark, Robert L., 2000. "Frequency-Shaping with Spatial Compensators," *Journal of Intelligent Material Systems and Structures* **11**, 811-820.
10. Clark, R. L., and Cox, D. E., 1999. "Experimental Demonstration of a Band-Limited Actuator / Sensor Selection Strategy for Structural Acoustic Control," *Journal of the Acoustical Society of America*, **106**(6), 3407-3414.
11. Clark, R. L., and Cox, D. E., 1999. "Band-Limited Actuator and Sensor Selection for Disturbance Rejection: Application to Structural Acoustic Control," *AIAA Journal of Guidance, Control, and Dynamics*, **22**(5), 740-743.

Student Paper Awards

1. Kemp, J. D., and R. L. Clark, "Noise Reduction in a Rocket Fairing Using Actively Tuned Loudspeakers," Presented at the 140th Meeting of the Acoustical Society of America, 108(5), New Port Beach, CA, November 2000. (First Place Award, Best Student Paper Competition, Structural Acoustics and Vibrations Technical Committee of the Acoustical Society of America, winter 2000.)

Invited Papers

1. Clark, R. L., J. A. Rule, and R. E. Richard, 2000. "Application of Reduced-Order Models to the Design of Adaptive Aeroelastic Structures," Presented at the 139th Meeting of the Acoustical Society of America, 107(5), Atlanta, GA, May 31, 2824.
2. Clark, R. L., 1999. "Adaptive Structures: Compensators by Design," *Proceedings of Active 99*, Fort Lauderdale, FL, December 2-4, (**Keynote Address**).

Conference Papers

1. M. A. McEver, S-M. Moon, D. G. Cole and R. L. Clark, 2003. "Adaptive Control for Interior Noise Control in Rocket Fairings." In Proceedings of 2003 AIAA/ASME/AHS Adaptive Structures Forum, Norfolk, VA AIAA Paper 2003-1811, April.
2. R. E. Richard and R. L. Clark, 2002. "Computationally Efficient Piezoelectric Modeling for System Optimization," Proceedings of the 9th Annual SPIE Smart Structures and Materials Symposium, San Diego, CA.
3. Kemp, Jonathan D., and R. L. Clark, 2002. "Optimal Hybrid Active/Passive Vibration Control Design," Smart Structures and Materials 2002: Modeling, Signal Processing, and Control, *Proc. SPIE*, 4693, 2002.
4. Moon, Suk-Min and Clark, Robert L., 2002. "Recursive methods for optical jitter suppression using acoustic actuators," SPIE Smart Structures and Materials 2002: SPIE 9th Annual International Symposium on Smart Structures and Materials, San Diego CA. 2002 . (In Press)
5. Moon, Suk-Min and Clark, Robert L., 2001. "Advanced methods for optical jitter suppression using acoustic actuators," Smart Structures and Materials 2001: Damping and Isolation, *Proc. SPIE Vol. 4331*, pp. 72-81, 2001
6. Lane, S. A., Kemp, J. D., Clark, R. L., Griffin, S. F., 2000. "Acoustic Control of a Rocket Fairing Using Spatially Weighted Transducer Arrays." In Proceedings of 2000 AIAA/ASME/AHS Adaptive Structures Forum, Atlanta, GA AIAA Paper 2000-1423, April.
7. Griffin, S. F., Gussy, J., Lane, S. A., Kemp, J. D., Clark, R. L., 2000. "Innovative Passive Mechanisms For Control of Sound in a Launch Vehicle Fairing." In Proceedings of 2000 AIAA/ASME/AHS Adaptive Structures Forum, Atlanta, GA AIAA Paper 2000-1436, April.
8. Rule, J. A., Richard, R. E., and Clark, R. L., 1999. "Design of an Aeroelastic Delta Wing Model for Active Flutter Control," *Proceedings of Active 99*, Fort Lauderdale, FL, December 2-4.

Honors and Awards

2002 – PI named Fellow of the American Society of Mechanical Engineers

2000 – Graduate Student, J. D. Kemp honored with First Place Award, Best Student Paper Competition, Structural Acoustics and Vibrations Technical Committee of the Acoustical Society of America

1998 – PI honored with the R. Bruce Lindsey Award, Acoustical Society of America, in recognition of outstanding contributions to the science of acoustics.

OPTIMAL COLLOCATED AND MULTI-VARIABLE HYBRID ACTIVE/PASSIVE VIBRATION CONTROL DESIGN *

Jonathan D. Kemp [†]

Acentech, Inc.

Cambridge, Massachusetts, USA.

Robert L. Clark

Duke University

Durham, North Carolina, USA

ABSTRACT

Hybrid control measures are optimized for collocated and multi-variable attenuation of vibratory energy in a typical aircraft panel. Design techniques first optimize collocated hybrid controllers combining active and passive technology on the same footprint. These techniques are then extended to multi-variable hybrid controllers containing at least two pairs of actuators and sensors in addition to passive damping. An optimization routine based on an energy-balancing cost metric selects active and passive control elements to minimize both the broad-band vibratory energy of the structure and the weight, volume, and energy use of the control system. Further, optimization of inherent energy exchanges within the hybrid controller allows more aggressive active control. Optimization also reveals idealized placements, sizes, and orientations of active and passive control elements. Active piezoceramic patches partner with passive constrained layer damping treatment to extend and demonstrate the potential of optimal hybrid vibration control.

Keywords: Vibration, Hybrid, Multi-variable, Control, Optimization

*Portions of this work are to be presented at the Eighth International Conference on Recent Advances in Structural Dynamics, Institute for Sound and Vibration Research, Southampton, UK, July 2003

[†]Corresponding Author: Acentech Inc., 33 Moulton St., Cambridge, MA 02138, USA
(617)499-8091 (office), (617)499-8074 (fax), jkemp@acentech.com

INTRODUCTION

Preliminary study of single-variable optimal hybrid active/passive control (Kemp and Clark, 2002) has prompted this expansion of hybrid design techniques to encompass the applications of collocated, and multi-variable, hybrid vibration control in panel structures.

Many have investigated active vibration control with patch actuators (Baumann et al., 1992; Fuller et al., 1992; Maestrello, 1996; Clark and Cox, 1997; Viperman and Clark, 1999; Smith and Clark, 1999) and active/passive constrained layer devices (Austin and Inman, 1998; Baz and Ro, 1994; Velez and Rao, 1995; Poh et al., 1996), but few have attempted hybrid control (Lam et al., 1997), and the optimal interaction between hybrid technology and structures has only received recent attention (Griffin et al., 2000; Kemp and Clark, 2002). Optimization of multi-variable control structures has been introduced (Clark and Cox, 2000b), but numerical limitations of that approach required a different solution for effective optimization, as discussed below. This work seeks the advancement of hybrid control through optimal combination and coordination of active and passive control measures in collocated and multi-variable arrangements.

Active piezoceramic (PZT) patches and passive constrained layer damping (CLD) devices partner in a coordinated optimal design for vibration control. An energy-based design metric allows a genetic algorithm to locate and match optimal groups of active and passive control patches for maximum control with a minimum footprint. Solutions presented here direct the control designer by allowing evaluation of:

1. Trade-offs between active and passive performance, through inclusion of passive effects in the hybrid design scheme, allowing more efficient design of all hybrid elements.
2. Coordination between active and passive control, promoting more aggressive active control design, particularly within collocated hybrid controllers.
3. Optimality of multi-variable controllers through simultaneous evaluation of all available control paths, a numerical challenge for schemes based upon previous research.
4. Comparative predicted closed-loop hybrid control results for multi-variable and collocated control schemes without burden of control law design and testing.

COLLOCATED HYBRID CONTROL DESIGN

Following construction of coupled analytical models of the structure and an array of attached control devices, the models are processed to allow performance evaluation of a given group of active and passive patch candidates. These patch candidates form sets from which optimal groups of passive and active patches are selected for targeted attenuation of key frequency ranges. A genetic algorithm provides the candidate selection through evaluation of an energy based design metric. The metric evaluates the performance of each candidate in critical design areas: control effectiveness in and out of the targeted bandwidth and coordinated hybrid control performance. As the models and genetic algorithm have been previously described in detail (Kemp and Clark, 2002), this paper will focus on the development and application of the design metric for collocated and, later, for multi-variable hybrid control of vibration in a panel structure. The physical properties of the panel and attached control materials are listed in Table 1. All locations in (x, y) form are measured from the arbitrary lower left corner of the panel.

Design Metric

Lim (Lim and Gawronski, 1996; Lim, 1997) first addressed the ability to use approximations of squared Hankel Singular Values (HSVs), γ^2 , of a coupled structure model to estimate the coupling of a particular sensor and actuator arrangement to a targeted mode of the structure. Expansion of Lim's work by others (Clark and Cox, 2000a; Rule et al., 2001) sought to decrease coupling at modes out of the control bandwidth to reduce control spillover due to unmodeled dynamics. Here, spillover is defined as increased response at non-targeted modes induced by the reaction of the controller to unmodeled dynamics out of the control bandwidth. In this case, the energy in one group of modes is minimized while the energy in another group of modes is maximized. A parallel metric evaluates passive patch placement, as the CLD is treated as a collocated patch pair targeting a range of high-frequency vibration.

For a hybrid design, the resulting damping effects of a given CLD placement must be considered throughout the bandwidth. Thus, Lim's equation for approximating HSVs is augmented with passive damping, and the total hybrid scoring metric for a particular

controller candidate (active and passive patches) is written as:

$$J_{\text{hybrid}} = \frac{1}{\beta_{\kappa}} \sum_{i=\kappa} \gamma_{i_{\text{hybrid}}}^4 \left(1 - \frac{1}{\beta_{\mu}} \sum_{i=\mu} \gamma_{i_{\text{hybrid}}}^4 \right) + \frac{1}{\beta_{\xi}} \sum_{i=\xi} \gamma_{i_{\text{hybrid}}}^4 \quad (1)$$

Calculation of $\gamma_{i_{\text{hybrid}}}^4$ requires knowledge of both the passive control material and the placement on the panel, and is carried out as described by Kemp and Clark (Kemp and Clark, 2002). The candidate score evaluates the potential hybrid control performance and allows a selection scheme to identify the best hybrid control candidate in a given population.

Collocated Hybrid Application.

Preliminary extension of this hybrid metric allows investigation of collocated hybrid controllers. Previous work in Active Constrained Layer Damping (Baz and Ro, 1994; Veley and Rao, 1995; Poh et al., 1996) sought the efficient construction of a tunable passive control device in which the constraining layer of a viscoelastic patch damper is replaced with an active piezoceramic material. The limitations encountered in two dimensional applications revealed a product which could not significantly outperform its passive counterpart enough to warrant the use of active control. Additionally, the control system retains all of the complexity of active control without the benefits of active vibratory attenuation. To re-evaluate the problem and the possibilities of combining active and passive technologies, adjustments in the optimization routine allow placement and design of a single hybrid control patch.

Primary efforts here reconstruct the hybrid patch by reversing the order of the ACLD sandwich. In the traditional application, a piezoelectric transducer forms the constraining layer for the viscoelastic film. If the order is reversed, such that the PZT is bonded directly to the surface of the panel, covered with the viscoelastic film, and then topped with a constraining layer of aluminum, then the hybrid effects should be apparent. ACLD would be a misnomer for this application, but the benefits of collocated, single patch hybrid control remain. An alternative formulation, if the environmental or structural requirements of the panel would allow it, is the application of the passive CLD in the same position on the opposite side of the panel from the active patch. Though this application would be undesirable on the skin of any airborne transport, various industrial applications could easily benefit from this technique: motor and transformer housings, manufacturing equipment

enclosures, and double-walled cowlings. In either case, the optimization routine is handed the same problem: find the best single patch placement targeting all of the modes in the targeted bandwidth.

The passive effects of the damping treatment are included in the optimization scheme, as developed previously (Kemp and Clark, 2002). The effective damping is calculated under the assumption that the active patch (the structural attachment surface for the viscoelastic material) is bonded to the surface of the panel and demonstrates negligible damping across its thickness. Therefore, the top surface of the piezoceramic should demonstrate similar vibration response to the surface of the panel to which it is attached. The response of the modelled panel with an attached optimal collocated active and passive patch is shown in Figure 1. The placement description of this hybrid structure can be found in Table 1. Here, the response from PZT actuator to PZT sensor with and without applied passive damping is shown to demonstrate the coupling effects included in the optimization scheme. Note that, although the response at the 180 Hz mode is significant, the addition of passive damping reduces the response to an acceptable level for implementation of an active controller targeting the first three modes (47-121 Hz). The response of the previously optimized multiple-location hybrid controller (Kemp and Clark, 2002) is also included to graphically demonstrate the trade-offs in damping and controllability that must be evaluated when choosing the collocated control strategy. The multiple-location hybrid controller is capable of greater damping, resulting in steeper control path roll off at passively targeted frequencies.

The passive effects visible in the performance path (disturbance to velocity sensor at point of optimal coupling to all modelled modes), and the response of the resulting active closed-loop system are displayed in Figure 2. Note that high and low frequency attenuation is apparent. However, the magnitude of that attenuation is less than that predicted for a multiple-location hybrid controller targeting the same frequencies, particularly between 200 and 700 Hz. The predicted passive RMS reduction in the 1 kHz bandwidth with the collocated controller is 6.0 dB while the multiple-location design provided 7.3 dB of reduction. For the 500 Hz bandwidth, the reductions are predicted as 4.2 dB and 5.8 db, respectively. These observations demonstrate the trade-off between maximum passive attenuation and minimum controller footprint.

The controllability and effective damping at the location with good coupling to all modes should be less than that demonstrated by the multiple location controller. As an experiment, the collocated controller designed above was adjusted to use the same control energy as the previously optimized multiple-location controller, assuming the same control goals. If two-norm of the control path,

$$\left\| \frac{u}{w} \right\|_2, \quad (2)$$

is equivalent in each case, then a fair comparison of the predicted control success is possible. Sensor noise floors and control effort penalties were adjusted in both cases until the two-norm above reached an arbitrary value of 80 in each case. This value seemed a fair performance limit in the collocated case, as the loop gain reached unity at a non-targeted mode. With this control energy, the predicted RMS active control reduction in the 500 Hz bandwidth is 2.26 dB for the collocated controller and 3.20 dB for the multiple-location controller. Again, the trade-off between minimum controller size and maximum control is quantified.

A further cost of the single patch placement is the forfeiture of high-frequency deselection to promote active control. A hybrid patch found through deselection of higher-order modes would certainly exhibit less than desirable damping at these frequencies. The trade-off between the loss of controllability due to high-frequency spillover and the gain of damping at those frequencies would depend greatly on the specific application, but the additional damping seems to carry the day in this case. Just as shown with the previous hybrid controllers, the damping added to the system by the CLD outweighs predicted control spillover across the bandwidth. However, it must be noted that the weaker active decoupling due to the single hybrid placement provided a significant performance limitation. While the maximum stable control path norm (Equation 2) of the multiple-location controller is approximately 120, the maximum stable norm in the collocated case is less than 90. Though actual control performance depends on far more factors, the stability limits here further quantify the advantages and disadvantages of the collocated design.

MULTI-VARIABLE HYBRID DESIGN

Expansion of Lim's HSV approach to multi-input, multi-output (MIMO) systems requires further approximation of system dynamics, but will result in a similarly useful approximation of closed-loop system performance. For obvious reasons, the HSVs of a MIMO system, even with balanced Grammians, can no longer be exclusively represented by the square of a particular term in the input or output matrices divided by the modal damping. In fact, the HSVs cannot accurately be represented as a linear combination of those terms: the approximation must account for added paths through the control plant.

Multi-Variable Design Metric

Individual path-based scores can be determined for a given set of multiple sensors and actuators, and these scores can be combined to give a total score for the MIMO system candidate (Clark and Cox, 2000b). For example, given a system with n inputs and outputs, there are n^2 possible control paths: Actuator No. 1 to Sensor No. 1, Actuator No. 1 to Sensor No. 2, etc. Each of these paths could be considered in a SISO realization of the system, yielding n^2 HSV's corresponding to the respective paths. The linear combination of these paths yields an approximation of total system performance. The benefits of the Lim method are preserved: relative closed-loop performance can be predicted without calculation of either the closed-loop response or even the MIMO realization of the system.

Advancements herein apply this multiple path technique for more successful placement optimization and solution to a hybrid control problem with significantly fewer limits on input/output size. Clark and Cox (Clark and Cox, 2000b) evaluated a given set of arbitrary candidates in order to select the best two-input, two-output (TITO) control patch locations, from that candidate set, for control of a vibrating panel. They noted that the number of control path evaluations grows with the square of the number of inputs or outputs (20 sensors and 20 actuators have 400 possible control paths), and that this growth provides a severe limitation on the number of possible patch candidates considered.

In this work, application of the scoring metric noted in Equation 1 and the genetic algorithm allows evaluation of an unlimited number of patch candidates in any input and output orientation. The summation of the coupling scores for all direct paths and all cross paths yields a reasonable estimate of closed-loop system performance. The genetic algorithm offers a workable solution methodology because of the nature of the candidate

population. Given a set of one hundred control patches and the design goal of a two-input, two output controller, an apparent solution would be to find the best four patches in the population based upon their summed coupling scores. However, this solution would require the calculation of all cross paths in the population: a factorial of one hundred system realizations! A more feasible solution is to generate a population of one hundred candidates, each of which contains four patches. The four coupling scores of individual control paths within the candidate can be calculated and summed as discussed above, yielding a total score for the candidate. The strength of the optimization routine is now apparent, as the algorithm, through generations of mating and mutating, will converge upon the four best patches for the given control problem without the need to calculate the enormous system realization. Again, the simplicity of the scoring metric allows this two by two problem to be expanded to any number of inputs and outputs.

In a TITO system, the number of operations required to evaluate 20 sensors and actuators under the previous scheme can now evaluate 200 sensor and actuator placements. Additionally, iterations of the optimization routine will evaluate orders of magnitude more patch candidates in all shapes, sizes, and orientations. A total score for a given candidate group (two sensors and two actuators in the TITO case) of patches can be compared to similarly determined scores for other candidate groups, allowing the algorithm to converge upon the ideal group of n actuators.

The accuracy of this metric with respect to the HSVs of the actual MIMO system is good, but unpredictable. The relative magnitudes of the variables in the input and output matrices determines the strength of the off-diagonal terms in the controllability and observability Grammians from which the HSVs can be determined. In the original Lim method, a SISO realization with light damping allows the assumption of diagonal dominance in these matrices and therefore the approximation of the singular values of the matrix as the terms on the diagonal. Here, however, the Grammian matrices may be fully populated without any dominant trends. The contribution of the path-based approach to the MIMO optimization problem lies not in the approximation of the actual HSVs but rather in the approximation of closed-loop system performance without the computationally expensive realization of each individual system. Thus, the computational cost of a multi-variable optimization routine has been reduced to a level comparable to that of SISO systems.

Optimal MIMO Control

To demonstrate the effectiveness of the MIMO optimization, a control problem was formulated to target several modes of an aluminum panel with multiple active control patches. Though more iterations of the algorithm are required for convergence, the total number of iterations increases linearly with the number of patches in the candidate: a two by two system requires approximately twice as many iterations as the single patch pair case, a three by three requires three times the iterations, etc. These computation times are confirmed through multiple calculations of the algorithm.

In each of the following multivariable predictions, active patch size was limited to two inches by three inches to retain the total area of active material modelled in the SISO case (Kemp and Clark, 2002). Thus, model accuracy remains constant; mass and stiffness effects of the control material are minimal.

The results of the optimization and control prediction for the two input, two output system targeting the first six modes (47-254 Hz) are shown in Figure 3. The placement description of this hybrid structure can be found in Table 2.

This plot represents the frequency response of the system from disturbance to a velocity output placed at a location with optimized coupling to all modelled modes. Again, the disturbance is modelled through application of uniform, broadband noise to each modal state. This relatively conservative controller shows good attenuation at the first three modes, some attenuation at the next three modes, and some spillover due to unmodeled dynamics at higher frequencies. The total RMS reduction in the 1000 Hz bandwidth is 3.73 dB.

The response of a more aggressive multivariable controller is displayed in Figure 4. The predicted attenuation of the first six modes is significant for this aggressive, yet mathematically stable, controller. The H_2 norms of the disturbance to control input transfer function (w to u) increase from 5.53 and 9.56 for the two paths of the conservative controller to 105 and 186 for the two paths in the aggressive controller. The benefit of aggressive control is apparent in the 6.02 dB RMS response decrease in the 1000 Hz bandwidth. The price of aggression remains the spillover due to unmodeled dynamics evident at higher frequencies.

The benefit of the optimization routine lies in the ability to find an optimal solution for multiple patches, not as a summation of the best answers for SISO cases, but as an

approximate Multiple-Input, Multiple-Output controller. This achievement is best showcased through comparison of the frequency response of the maximum singular values for two systems, one utilizing the two best SISO placements, and the other utilizing the best MIMO placement. In both cases, the optimization routine selected patches which couple best to the first six modes of the panel (47 – 254 Hz). The results of this investigation are shown in Figure 5. The solid line represents the response of the combined best SISO candidates, while the dashed line shows the response of the MIMO design. Note that the MIMO design outperforms the SISO designs at the first three targeted modes (2 – 3 dB more response), and at all of the non-targeted modes (10 – 20 dB more roll off). While the two SISO designs demonstrate more coupling at modes 4, 5, and 6, the lack of roll off at higher frequencies would negate this benefit. Modes 4 and 6 would be uncontrollable due to the sensor noise floor requirement of the non-targeted modes, and mode 5 is less controllable than in the MIMO case. Essentially, the targeting of six modes is too complicated for any single sensor/actuator pair placement, but the MIMO design metric incorporates enough complexity to evaluate the coordination of multiple patch pairs.

Optimal Hybrid MIMO Control

The control spillover due to unmodeled dynamics and obvious performance limits in the most successful multivariable control case begs for the addition of passive control to enable a true broadband solution. Addition of a third control “path” in the form of a passive patch again modelled as a collocated pair of patches targeting a range of higher frequency vibration (> 200 Hz) allows optimization of a multivariable hybrid control system. Open-loop system responses, from actuator to sensor, of the optimal MIMO configuration and the optimal hybrid MIMO configuration are aligned in Figures 6 and 7 to demonstrate the advantages inherent in the hybrid design. Note that the addition of the passive material allows the optimization scheme to select active patches which couple stronger to the targeted first six modes, as the decoupling to higher modes is of less importance and more easily obtained. Note that the high frequency modes (350-700 Hz) that were decoupled in the MIMO case have returned in the hybrid optimization, as only three modes from 254 Hz to 316 Hz were deselected to reduce spillover. The addition of passive damping guarantees this advantage by attenuating the response of the passively-targeted modes. Further observation yields the true benefit of hybrid control: the magnitude margin between the smallest actively targeted

mode and the largest non-actively-targeted mode has been increased significantly, allowing a significant increase in available active control authority.

The results of the hybrid control prediction for the optimal result are shown in Figure 8. The placement description of this hybrid structure can be found in Table 3. The frequency response of the disturbance to performance path is plotted here. Optimally placed passive damping successfully attenuates vibration energy, particularly at higher frequencies. The hybrid controller outperforms the previous active controller, even at the targeted frequencies, and not just because of added damping: the modes remain dominant even after predicted damping application. Among the hybrid advantages, the deselection vector for optimization of the active patch placements has been reduced from nineteen modes to five, improving both convergence and the coupling of the resulting patches to the targeted first six modes. The increased control authority allows more control effort without instability. Additionally, even if an aggressive controller generates spillover due to unmodeled dynamics at higher frequencies, the total reduction at those modes remains significant. In other words, spillover energy added to a passively damped mode does not drive the response back to the original uncontrolled level.

CONCLUSIONS

Two forms of optimal, hybrid, vibration control have been designed and studied for coordinately targeted broadband control of the vibration in an aluminum panel. The active materials have been placed to optimize control authority at targeted modes while minimizing coupling to non-targeted modes, thereby increasing attenuation and decreasing spillover from unmodeled dynamics. Passive material use has been reduced over 90 percent while maintaining performance in the targeted frequency ranges.

Collocated control measures facilitate vibration attenuation with a minimum footprint; actively targeted low-frequency attenuation combines with successful high-frequency damping. The new design also retains the previous advantages of a space-saving, single patch design that could be applied for wide-band attenuation of almost any vibrating surface. Optimal, hybrid, MIMO systems offer significant, broad-band vibration control, even in complex structures. The new MIMO design technique can optimize sensor and actuator coupling and passive material performance for multiple patches targeting groups of modes across broad frequency ranges.

ACKNOWLEDGEMENTS

The authors would like to gratefully acknowledge the partial support for this research provided under the AFOSR Presidential Early Career Award for Scientists and Engineers, grant number F49620-98-1-0383, monitored by Major Brian Sanders and Dr. Dan Segalman.

REFERENCES

- Austin, E. M. and Inman, D. J. (1998). Modeling of sandwich structures. In *Passive Damping and Isolation Proceedings, 5th International Symposium on Smart Structures and Materials*, volume SPIE 3327. Ed. L. P. Davis.
- Baumann, W. T., Saunders, W. R., and Robertshaw, H. H. (1992). Active structural acoustic control of broadband disturbances. *Journal of the Acoustical Society of America*, 92(4):1998-2005.
- Baz, A. M. and Ro, J. J. (1994). The concept and performance of active constrained layer damping treatments. *Journal of Sound and Vibration*, pages 18-21.
- Clark, R. L. and Cox, D. E. (1997). Multi-variable structural acoustic control with static compensation. *Journal of the Acoustical Society of America*, 102(5):2747-2756.
- Clark, R. L. and Cox, D. E. (2000a). Band-limited actuator and sensor selection for disturbance rejection. *Journal of Guidance, Control and Dynamics*, 23(5):903-906.
- Clark, R. L. and Cox, D. E. (2000b). Multi-input, multi-output, band-limited transducer selection for disturbance rejection. *AIAA Journal of Guidance, Control, and Dynamics*, 23(5):903-906.
- Fuller, C. R., Rogers, C. A., and Robertshaw, H. H. (1992). Control of sound radiation with active/adaptive structures. *Journal of Sound and Vibration*, 157(1):19-39.
- Griffin, S. F., Gussy, J., Lane, S. A., Kemp, J. D., and Clark, R. L. (2000). Innovative passive mechanisms for control of sound in a launch vehicle fairing. In *Proceedings of the 41st Structures, Structural Dynamics, and Materials Conference, Atlanta, GA*.

- Kemp, J. D. and Clark, R. L. (2002). Optimal hybrid active/passive vibration control design. *submitted for publication in Journal of Sound and Vibration*.
- Lam, M. J., Inman, D. J., and Saunders, W. R. (1997). Vibration control through passive constrained layer damping and active control. *Journal of Intelligent Materials Systems and Structures*, 8:663–677.
- Lim, K. B. (1997). Disturbance rejection approach to actuator and sensor placement. *AIAA Journal of Guidance, Control and Dynamics*, 20(1):202–204.
- Lim, K. B. and Gawronski, W. (1996). Hankel singular values of flexible structures in discrete time. *AIAA Journal of Guidance, Control and Dynamics*, 19(6):1370–1377.
- Maestrello, L. (1996). Control of panel response to turbulent boundary-layer and acoustic excitation. *AIAA Journal*, 34(4):259–264.
- Poh, S., Baz, A. M., and Balachandran, B. (1996). Experimental adaptive control of sound radiation from a panel into an acoustic cavity using active constrained layer damping. *Journal of Smart Materials and Structures*, 5:649–659.
- Rule, J. A., Richard, R. E., and Clark, R. L. (2001). Design of an aeroelastic wing model for active flutter control. *AIAA Journal of Guidance, Control, and Dynamics*, 24(5):918–924.
- Smith, G. C. and Clark, R. L. (1999). Adaptive structure design through optimal spatial compensation. In *Proceedings of Active-99*, Fort Lauderdale, FL. Noise Control Foundation, Poughkeepsie, NY.
- Veley, D. E. and Rao, S. S. (1995). Optimal design of structures with active constrained layer damping. *Proceedings of Smart Structures and Materials 1995, SPIE*, 2445(2):98–109.
- Vipperman, J. S. and Clark, R. L. (1999). Multivariable feedback active structural acoustic control with adaptive piezoelectric sensor/actuators. *Journal of the Acoustical Society of America*, 105(1):219–225.

List of Tables

1	Material and geometric properties of panel and attached control devices. . .	15
2	Placement, size, and orientation of MIMO control systems	16
3	Placement, size, and orientation of MIMO Hybrid (MH) control systems . .	17

Table 1: Material and geometric properties of panel and attached control devices.

Property	Value	Property	Value
Panel Length	0.457 m	E_s	$69.3 \times 10^9 \text{ N/m}^2$
Panel Width	0.406 m	ν_s	0.33
Panel Thickness	1.52 mm	ρ_s	2680 kg/m^3
PZT Thickness	0.38 mm	E_p	$5.0 \times 10^{10} \text{ N/m}^2$
ν_p	0.3	ρ_p	7650 kg/m^2
PZT dielectric	-180×10^{-12}		
Viscoelastic Thickness	0.12 mm	E_{ve}	$14 \times 10^6 \text{ N/m}^2$
ρ_{ve}	1000 kg/m^2		
CL Thickness	0.76 mm	E_{cl}	$69.3 \times 10^9 \text{ N/m}^2$
ν_{cl}	0.33	ρ_{cl}	2680 kg/m^3
Collocated Patch Length	75 mm	Collocated Patch Width	126 mm
Collocated Patch Location	(38,90)mm	Collocated Patch Rotation	3°

Table 2: Placement, size, and orientation of MIMO control systems

Property	Value	Property	Value
MIMO Actuator 1 Length	96 mm	MIMO Actuator 1 Width	62 mm
MIMO Actuator 1 Location	(120,99)mm	MIMO Actuator 1 Rotation	135°
MIMO Actuator 2 Length	97 mm	MIMO Actuator 2 Width	68 mm
MIMO Actuator 2 Location	(326,103)mm	MIMO Actuator 2 Rotation	107°
MIMO Sensor 1 Length	97 mm	MIMO Sensor 1 Width	48 mm
MIMO Sensor 1 Location	(112,282)mm	MIMO Sensor 1 Rotation	91°
MIMO Sensor 2 Length	99 mm	MIMO Sensor 2 Width	73 mm
MIMO Sensor 2 Location	(355,285)mm	MIMO Sensor 2 Rotation	84°

Table 3: Placement, size, and orientation of MIMO Hybrid (MH) control systems

Property	Value	Property	Value
MH Actuator 1 Length	88 mm	MH Actuator 1 Width	76 mm
MH Actuator 1 Location	(222,64)mm	MH Actuator 1 Rotation	176°
MH Actuator 2 Length	99 mm	MH Actuator 2 Width	67 mm
MH Actuator 2 Location	(221,133)mm	MH Actuator 2 Rotation	3°
MH Sensor 1 Length	93 mm	MH Sensor 1 Width	75 mm
MH Sensor 1 Location	(160,92)mm	MH Sensor 1 Rotation	84°
MH Sensor 2 Length	94 mm	MH Sensor 2 Width	73 mm
MH Sensor 2 Location	(110,243)mm	MH Sensor 2 Rotation	3°
MH CLD Length	147 mm	MH CLD Width	99 mm
MH CLD Location	(187,214)mm	MH CLD Rotation	124°

List of Figures

1	Comparison, control path response (G_{yu}) of modelled panel structure without (- - -) and with passive control (—) collocated with a single active control patch, and control path response through optimal multiple-location hybrid controller (-.-.-) (Kemp and Clark, 2002).	19
2	Comparison of panel response (G_{zw}) without hybrid control (- - -), with passive control (—) and with improved ACLD hybrid control (-.-.-). . . .	20
3	Comparison, modelled panel structure without and with active multivariable control targeting the first six modes (47-254 Hz)	21
4	Comparison, modelled panel structure without and with aggressive active multivariable control targeting the first six modes (47-254 Hz)	22
5	Frequency responses of the maximum singular values of MIMO systems resulting from the SISO metric and from the MIMO design metric, each targeting six modes	23
6	Open-loop modelled response from actuator to sensor (G_{yu}) for active MIMO system targeting the first six modes (47-248 Hz).	24
7	Comparison of modelled response from actuator to sensor (G_{yu}) with (—) and without (- - -) optimal passive material placement; first six modes (47-248 Hz) are targeted actively, while all higher modes are targeted with the passive patch.	24
8	Comparison, modelled panel structure without hybrid control (- - -), with passive control (—), and with hybrid control (-.-.-) actively targeting the first six modes (47-248 Hz); response measured from disturbance to performance (G_{zw}).	25

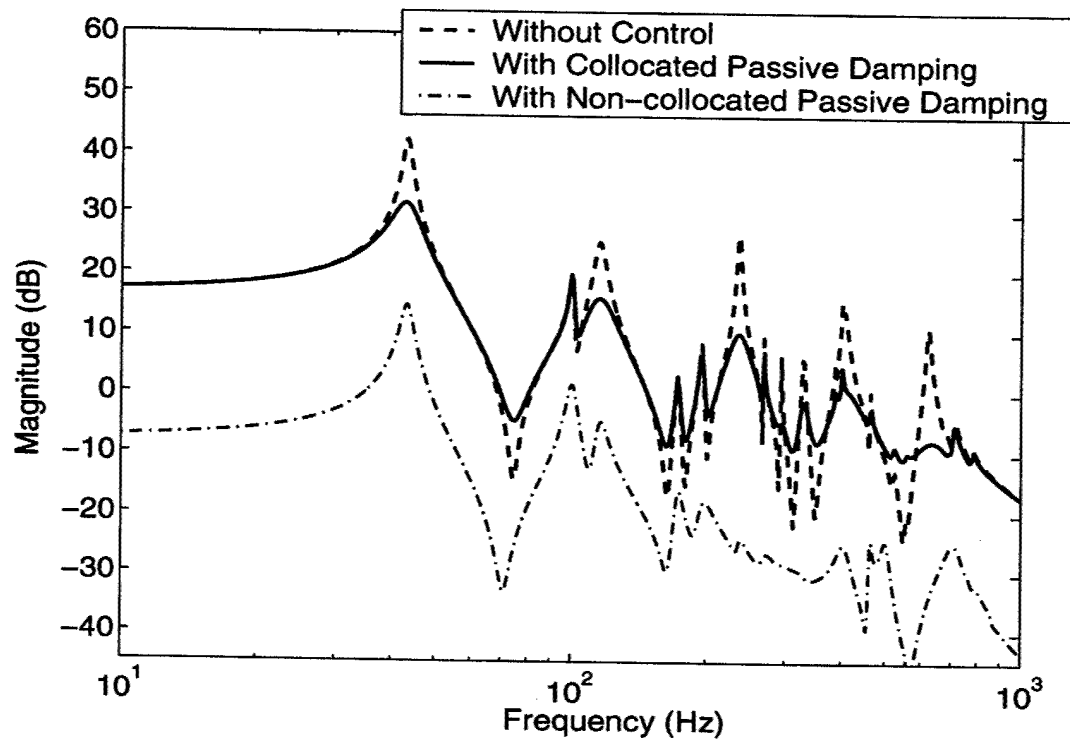


Figure 1: Comparison, control path response (G_{yu}) of modelled panel structure without (---) and with passive control (—) collocated with a single active control patch, and control path response through optimal multiple-location hybrid controller (-.-.) (Kemp and Clark, 2002).

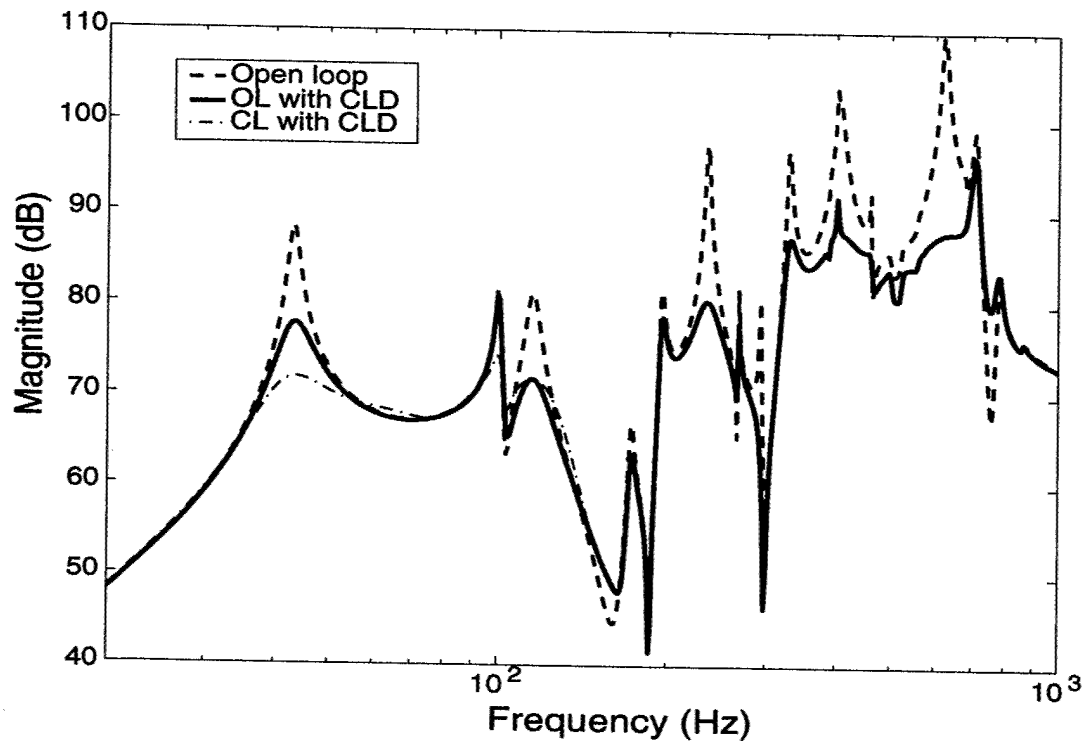


Figure 2: Comparison of panel response (G_{zw}) without hybrid control (- - -), with passive control (—) and with improved ACLD hybrid control (-·-·-).

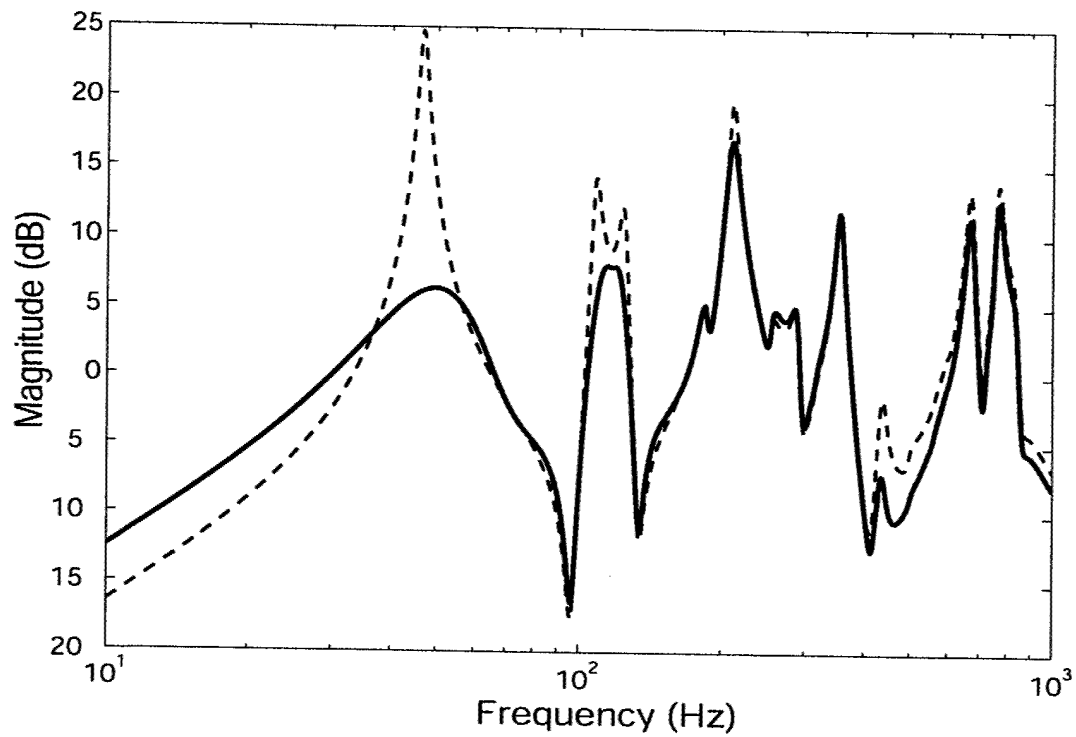


Figure 3: Comparison, modelled panel structure without (- - -) and with (—) active multivariable control targeting the first six modes (47-254 Hz); response measured from disturbance to performance (G_{zw}).

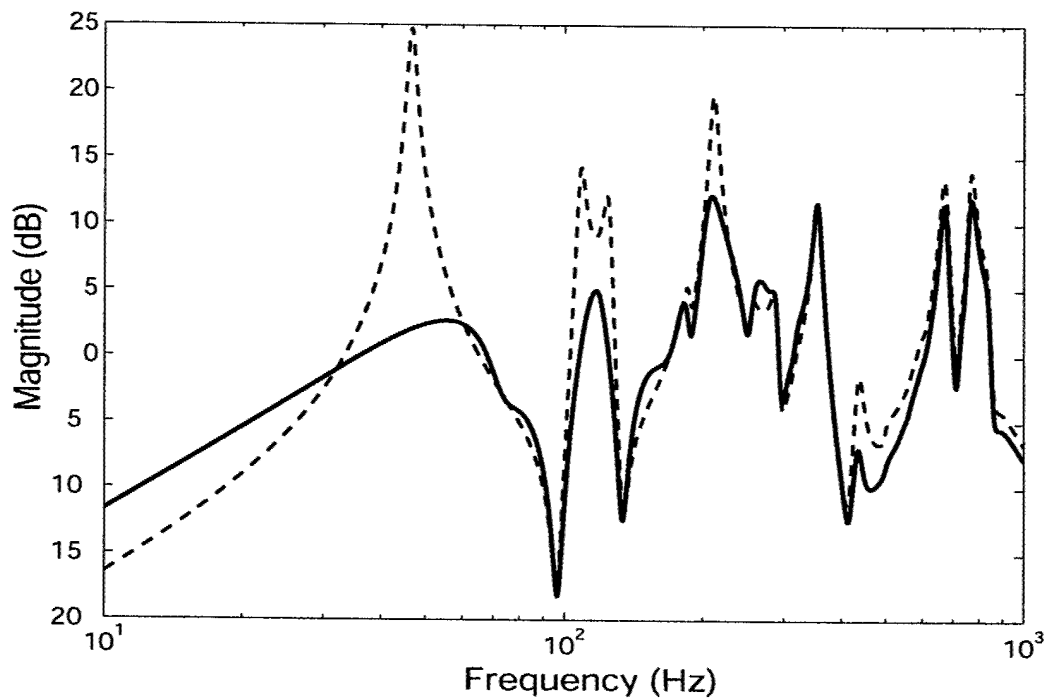


Figure 4: Comparison, modelled panel structure without (---) and with (—) aggressive active multivariable control targeting the first six modes (47-254 Hz); response measured from disturbance to performance (G_{zw}).

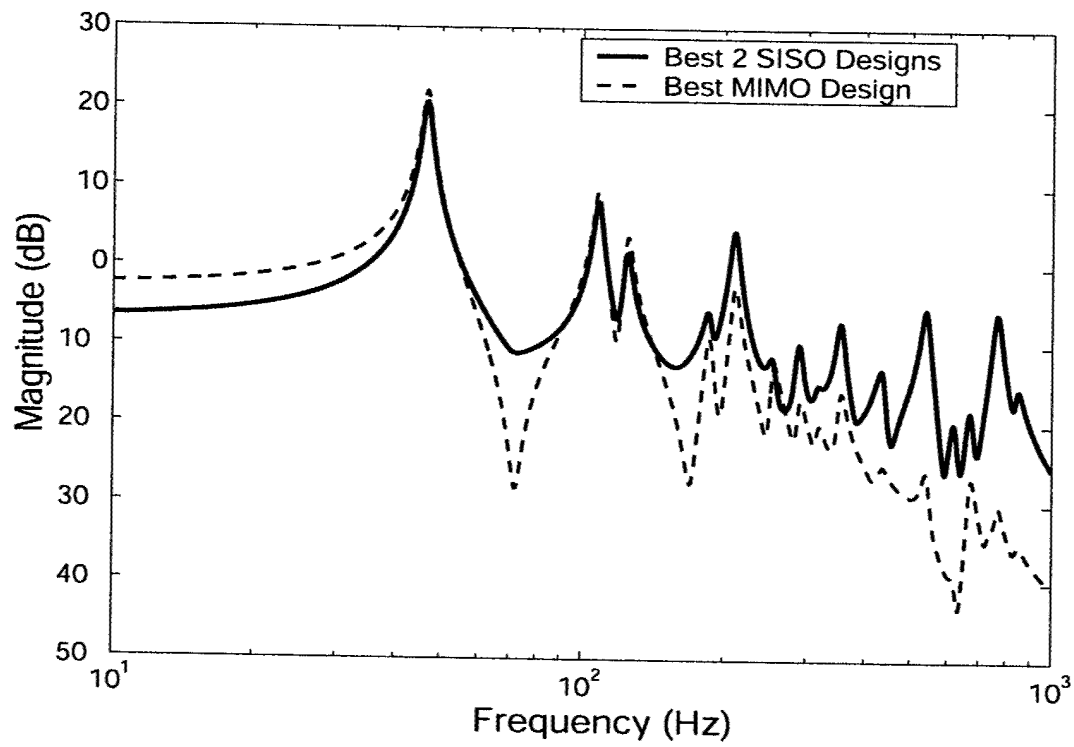


Figure 5: Frequency responses of the maximum singular values of MIMO systems resulting from the SISO metric (—) and from the MIMO design metric (- - -), each targeting six modes (47-254 Hz).

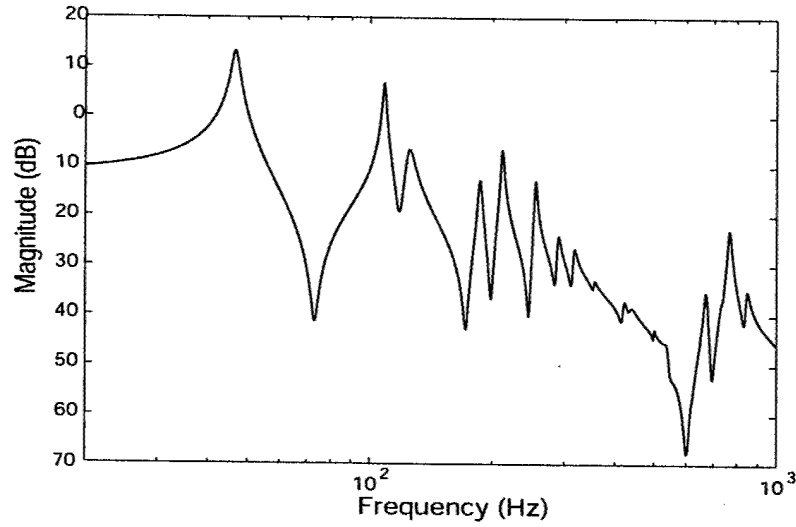


Figure 6: Open-loop modelled response from actuator to sensor (G_{yu}) for active MIMO system targeting the first six modes (47-248 Hz).

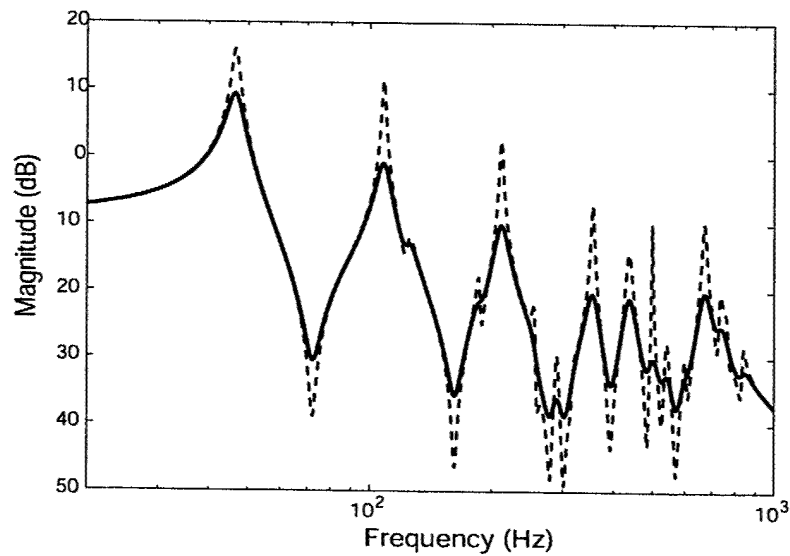


Figure 7: Comparison of modelled response from actuator to sensor (G_{yu}) with (—) and without (---) optimal passive material placement; first six modes (47-248 Hz) are targeted actively, while all higher modes are targeted with the passive patch.

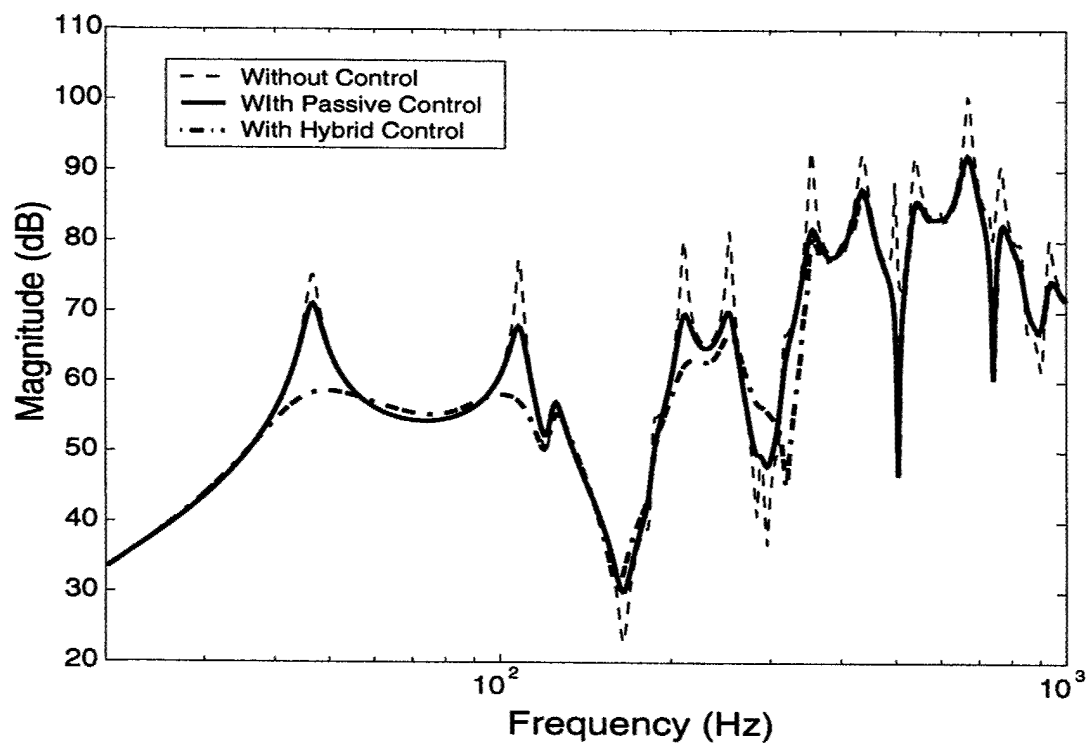


Figure 8: Comparison, modelled panel structure without hybrid control (- - -), with passive control (—), and with hybrid control (-·-·-) actively targeting the first six modes (47-248 Hz); response measured from disturbance to performance (G_{zw}).

Optimal Hybrid Active/Passive Vibration Control Design

Jonathan D. Kemp and Robert L. Clark

Duke University, Durham, North Carolina

Hybrid active/passive control systems present unique, energy-efficient solutions to noise and vibration problems. In many applications, active systems offer the only feasible control of low-frequency, high intensity vibrations, while passive materials offer superior attenuation at higher frequencies. These two systems can be optimally coordinated for broad-band control. An energy balancing metric forms the basis of an optimization routine designed to minimize both the broad-band vibratory energy of the structure and the weight, volume, and energy use of the control system. The metric further coordinates inherent energy exchanges within the elements of the hybrid controller: effective passive damping allows more aggressive active control. The optimization routine also investigates placement, size, and orientation of the active and passive control system elements. Initial experimentation on two-dimensional panels confirms the advancements provided by the optimization scheme. Here, active piezoceramic patches partner with passive constrained layer damping treatment to present the achievement of a coordinated control system no longer confined to a particular frequency range.

© 2002 Academic Press

KEY WORDS: Vibration, Hybrid Control, Passive, Active, Optimization

1. INTRODUCTION

Previous successes in active structural acoustic control and optimal control design prompt investigation of optimal hybrid active/passive control schemes. This work combines available active and passive vibration control technology for efficiency and effectiveness across a broad frequency range. A design technique is presented to develop and implement hybrid control for vibration attenuation in a typical aircraft panel.

Though many have investigated active vibration control with patch actuators [1–6] and active/passive constrained layer devices [7–10], few have attempted hybrid control [11], and the optimal interaction between hybrid technology and structures has received little attention. This work seeks the advancement of hybrid control through optimal combination and coordination of active and passive control measures.

Toward this end, active piezoceramic (PZT) patches and passive constrained layer damping (CLD) devices partner in a coordinated optimal design for vibration control. An energy-based design metric allows a genetic algorithm to locate and match optimal groups of active and passive control patches for maximum control with a

© 2002 Academic Press

minimum footprint. Following the constructs of this modelled solution, experimental results demonstrate the effectiveness of the hybrid control design technique.

2. DESIGN TECHNIQUE

This hybrid control design begins with construction of coupled analytical models of the structure and an array of attached control devices. These models are then processed to allow performance evaluation of a given active or passive patch candidate. These patch candidates form sets from which optimal groups of passive and active patches are selected for targeted attenuation of key frequency ranges. A genetic algorithm provides the candidate selection through evaluation of an energy based design metric. The metric evaluates the performance of each candidate in critical design areas: control effectiveness in and out of the targeted bandwidth and coordinated hybrid control performance.

2.1. STRUCTURAL MODELLING

For analytical construction, an energy-based model of a simply-supported aluminum plate coupled to models of active (PZT) and passive (CLD) control materials are adapted from work by Hagood, et al. [12], Clark, et. al. [13], and Friswell, et al [14]. From Hamilton's principle for electromechanical systems, substitution of material and system properties, definition of assumed mode shapes for the simply supported panel, and application of the variational approach of the Rayleigh-Ritz method results in the following simplified equations of motion for the coupled structural model [12–14]:

$$[\mathbf{M}_s + \mathbf{M}_p + \mathbf{M}_{ve} + \mathbf{M}_{cl}] \{\ddot{\mathbf{w}}\} + [\mathbf{D}_{ve}] \{\dot{\mathbf{w}}\} + [\mathbf{K}_s + \mathbf{K}_p + \mathbf{K}_{ve} + \mathbf{K}_{cl}] \{\mathbf{w}\} = [\Theta] \{\mathbf{v}\} + \mathbf{B}_f \{\mathbf{f}\}. \quad (1)$$

where \mathbf{w} is a vector of generalized structural coordinates, and \mathbf{B}_f is a matrix of modal influence functions. The mass and stiffness matrices for the structure \mathbf{M}_s , \mathbf{K}_s and piezoceramic material \mathbf{M}_p , \mathbf{K}_p are defined as in Clark [13]. The mass, stiffness, and damping matrices for the viscoelastic material \mathbf{M}_{ve} , \mathbf{K}_{ve} , \mathbf{D}_{ve} are derived with the Golla, Hughes, and McTavish (GHM) method as defined by Golla [15], McTavish and Hughes [16], and Friswell, Inman, and Lam [14]. The mass and stiffness matrices of the constraining layer \mathbf{M}_{cl} , \mathbf{K}_{cl} are defined similarly to those of the panel, though free-free boundary conditions are assumed. The sensor equation for the attached piezoelectric transducers is:

$$[\Theta]^T \{\mathbf{w}\} + [\mathbf{C}_p] \{\mathbf{v}\} = \{\mathbf{r}\}, \quad (2)$$

where \mathbf{r} is the vector of sensed electrode charges and Θ is the electromechanical coupling matrix [13]. The capacitance matrix is \mathbf{C}_p while \mathbf{v} is a vector of electrical coordinates. In all design cases the disturbance is modelled as a constant-gain broadband stochastic input applied equally at each modal state. The dynamic models can now be cast in state-space form for numerical implementation.

2.2. ACTIVE AND PASSIVE PLACEMENT METRICS

Following model construction, the hybrid design procedure continues with model adaptation for inclusion in an optimization routine. A schematic outline of the resulting design procedure is provided in Figure 1, and is described as follows.

Efficient evaluation of multiple sets of control patch candidates is possible through approximations of individual patch candidate coupling without the burden of full system calculation for each candidate. Because the panel and the types of control materials remain unchanged, the traits of individual candidates are described as the location, orientation, and size of the attached active and passive patches.

Description of these traits and evaluation of patch coupling are accomplished through an element scheme developed by Rule, Richard, and Clark [17], which covers the surface of the panel with elemental pieces of the control materials. The coupling coefficients (terms in the structural \mathbf{B} and \mathbf{C} matrices) for these individual elements can be calculated outside of the optimization loop, called individually based upon the location of the corresponding patch candidate, and linearly summed to formulate the overall coupling coefficients for that candidate in a coupled system model. Selection of the element size for proper resolution in the targeted frequency bandwidth provides solutions that approximate the continuous solution. Adaptation of this active patch technique for passive control materials is straightforward, as passive patch dynamics can be assumed constant across an element with the same frequency resolution as in the active case.

Next, a metric for the evaluation of a given set of patch candidates is developed. Lim [18, 19] first addressed the ability to use approximations of squared Hankel Singular Values (HSVs), γ^2 , of a coupled structure model to estimate the coupling of a particular sensor and actuator arrangement to a targeted mode of the structure:

$$\gamma_i^2 = \frac{\phi_i^2}{4\zeta_i\omega_{n_i}}, \quad (3)$$

where ϕ is modal participation factor derived from the \mathbf{B} or \mathbf{C} matrices of a balanced system, and ζ and ω_n are the damping ratio and natural frequency of the mode. If open-loop properties are improved such that closed-loop properties directly benefit, then placement optimization can be accomplished without calculation of closed-loop performance, vastly improving efficiency of the optimization scheme. Expansion of Lim's work by others [20, 17] sought to decrease coupling at modes out of the control bandwidth to reduce control spillover due to unmodelled dynamics. Here, spillover is defined as increased response at non-targeted modes induced by the reaction of the controller to unmodelled dynamics out of the control bandwidth. In this case, the energy in one group of modes μ is minimized while the energy in the group of modes κ is maximized:

$$J_{\text{active}} = \frac{1}{\beta_\kappa} \sum_{i=\kappa} \gamma_i^4 \left(1 - \frac{1}{\beta_\mu} \sum_{i=\mu} \gamma_i^4 \right) \quad (4)$$

The sums of the squared estimated HSVs are normalized by an estimate (β_κ, β_μ) of the sum of maximum squared HSVs over all possible sensors and actuators for scaling and evaluation.

A parallel metric evaluates passive patch placement. The CLD is treated as a collocated patch pair targeting a range of high-frequency vibration. The element scheme treats the patch as sum of small damper elements which couple to the panel motion through surface strain, exactly as the active patches do. For optimal passive placement, however, the metric only maximizes the energy in the passively targeted modes ξ :

$$J_{\text{passive}} = \frac{1}{\beta_{\xi}} \sum_{i=\xi} \gamma_i^4. \quad (5)$$

Again, the metric is normalized by the sum of maximum HSVs, β_{ξ} . Applied damping at other non-targeted modes would improve the total control solution, so coupling at those modes is not penalized in the passive case.

2.3. HYBRID DESIGN METRIC

The hybrid design metric seeks the combination of active and passive elements which most successfully attenuates all modes in a chosen broad frequency range. Active control is hindered at higher frequencies by modal density while long wavelengths hinder effective passive control at low frequencies. Ideally, passive patches focus on modes which are not easily controlled actively, while the active patches target the low frequency modes that are not easily controlled with passive patches. For a hybrid design, the resulting damping effects of a given CLD placement must be considered throughout the bandwidth. Thus, Lim's equation for approximating HSVs is augmented with passive damping ζ_{CLD} :

$$\gamma_{i\text{hybrid}}^2 = \frac{\phi_i^2}{4(\zeta_i + \zeta_{\text{CLD}_i})\omega_{n_i}}. \quad (6)$$

Estimation of ζ_{CLD} requires knowledge of both the material and the placement on the panel. Design of an optimal hybrid controller therefore requires a two-step process. First, the active and passive metric evaluation (Equations 4 and 5) determines the efficiency with which candidate patches target their respective modes for control. Then, the passive patch placement provides an estimate of total open-loop damping across the bandwidth, yielding an evaluation of total hybrid control performance.

For the most accurate and efficient prediction of passive damping levels, a model of the modal damping ratios of the system is constructed from published material data and scaled appropriately. The viscoelastic material used in the constrained layer damping exhibits impressive damping characteristics, but performance changes with temperature, frequency, and thickness. To maximize performance in the temperature (20° – 25° C) and frequency (30 Hz to 900 Hz) range of interest, a product called 112P05, manufactured by 3M, was chosen. This viscoelastic film has a thickness of 0.127 mm (0.005 in.) and is designed for performance at room temperature over a wide range of frequencies. Utilizing material nomographs published by the manufacturer [21], an estimated curve fit of the performance data yielded an equation for the normalized damping factor, ζ_{norm} , as a function of frequency ω in the bandwidth of interest:

$$\zeta_{\text{norm}}(\omega) = e^{\frac{-\omega-318}{378}} + 0.6. \quad (7)$$

The success of this curve fit is shown graphically in Figure 2. This normalized damping factor can now be multiplied by the maximum damping factor, 0.09, for a single CLD covering the entire panel using this viscoelastic material and a constraining layer with half the effective modulus of the panel[21].

Finally, the damping factor is scaled by the fraction of maximum coupling exhibited by a given element within the CLD. To calculate the fraction of coupling, the modal strain of a given CLD element at a given mode is compared to the modal strain of an element at a point of peak strain for that mode. The overall damping factor for each element within a given CLD patch can be calculated, and those damping factors can be incorporated in the denominator of the scoring metric for each patch given in Equation 6.

Now the full hybrid design metric is assimilated to form the total score for a given hybrid candidate consisting of one PZT sensor patch, one PZT actuator patch, and one CLD patch.

$$J_{\text{hybrid}} = \frac{1}{\beta_{\kappa}} \sum_{i=\kappa} \gamma_{i_{\text{hybrid}}}^4 \left(1 - \frac{1}{\beta_{\mu}} \sum_{i=\mu} \gamma_{i_{\text{hybrid}}}^4 \right) + \frac{1}{\beta_{\xi}} \sum_{i=\xi} \gamma_{i_{\text{hybrid}}}^4 \quad (8)$$

The candidate score evaluates the potential hybrid control performance and allows a selection scheme to identify the best hybrid control candidate in a given population.

2.4. OPTIMAL SELECTION

The hybrid control design technique concludes with selection of a hybrid controller containing an optimal combination of active and passive elements. Optimal control material placement and coordination requires the structural models in Equation 1, the design metric in Equation 8, and an optimization method for placement determination. For fast convergence to an optimal answer, a genetic algorithm is chosen as the foundation of the optimization routine. Due to the complexity of the coupled system models, the number of iterations required for convergence is the most significant contribution to the time required for a given optimization run, and genetic algorithms typically minimize these iterations. Details of the algorithm are available in references by Goldberg [22] and Deb [23], as the application of the algorithm is the focus of this work.

The optimization candidates are coupled structural systems consisting of two PZT patches and one CLD patch bonded to a typical aircraft panel. Each candidate is described by the element scheme as the sum of the coupling terms for each element included within the boundaries of the three candidate patches. These candidate descriptions are scaled and transcribed into binary vectors for algorithm implementation. The energy-based metric used to judge the success of a given candidate is given in Equation 8. Each iteration of the routine evaluates the scores of one hundred hybrid candidates and mates the better candidates to generate the next population. For convergence, each successive generation is compared to the best candidate from the previous generation. Convergence is determined by the number of generations evaluated without improving upon the best candidate.

3. DESIGN APPLICATION

Hybrid control of vibration on a simply-supported panel is accomplished through application of the design procedure in the previous section. Coupled structural models and the hybrid design metric combine in an optimization routine to select active and passive patch locations for control of response in the 0-1000 Hz bandwidth.

3.1. EXPERIMENTAL HYBRID PLACEMENT

Typical implementations of CLDs require 75–100 percent coverage of the panel surface for vibration control [21]. For this study, passive patch size was limited to ten percent of the panel area as a demonstration of damping ability with a smaller patch. Active patches were selected to target the first three modes of the panel at 47, 101, and 116 Hz, as passive damping with small CLDs is less successful at these modes. The higher modes (189-973 Hz) were targeted for control with the passive patch. The geometry of the optimal selection for these constraints is shown in Figure 3(A-C). The predicted system response from a common modal disturbance to strain output at locations of PZT and CLD patches is shown in Figure 3(D). Note that a spatial filtering effect has decreased coupling of the active patches to modes above 116 Hz, while the passive patch couples well at these modes. Figure 3(E) demonstrates the convergence of the routine. The best candidate score changed little over the last 150 generations, and the selected candidate remained the best candidate for the last 50 generations. Therefore, the selected hybrid candidate, after being chosen as the best of more than 20,700 candidates (207 iterations of 100 candidates each), was compared to five thousand more genetically created candidates before being chosen as a trial solution.

3.2. OPTIMAL PASSIVE PLACEMENT APPLICATION

To demonstrate predicted damping effects, the optimization routine was set to target the first three modes of the system at 45, 105, and 121 HZ actively and the next five modes at 182, 205, 248, 281, and 346 Hz passively, with and without considering the predicted damping in the candidate score. Figures 4(A) and 4(B) plot the frequency responses of two systems with the different optimized patch placements. Both system responses have been calculated including the damping model developed above, but only one system was optimized with it. As the magnitude of the response reflects coupling, the system optimized with knowledge of the damping effects shows slightly more coupling and considerably more effective damping, particularly at frequencies above 300 Hz. Effectively, the addition of modelled damping allows the algorithm to concentrate on damping of the non-actively targeted modes, as performance of the damping material at low frequencies is limited by the size of the applied patch.

Increased control authority is a further benefit of including the damping estimate. Note that the magnitude difference between the smallest actively targeted mode (121 Hz) and the highest non-actively-targeted mode increases significantly when damping is included. The sensor noise floor for active control design can be set much lower without high-frequency instability, increasing active control authority.

3.3. EXPERIMENTAL SETUP

The material and geometric constants utilized in this development are detailed in Table 1. Here, the subscripts s , p , ve , and cl correspond to the panel structure, PZT, viscoelastic, and constraining layer, respectively. The patch locations correspond to those shown in Figure 3(A-C).

The panel was clamped in a support structure on a vibration isolation table to minimize the effects of unintended vibration disturbances. Simply supported boundary conditions were simulated by milling a groove at the edge of the panel as suggested by Hoppinan and Greenspon [24]. In this case, the milling removed 85 percent of the panel thickness, creating a flexible hinge at the boundary. The clamped corners have also been removed to improve boundary flexibility.

Further construction and connection of the remaining hardware allows both response calculation and control design. Initial measurements are recorded as the frequency response function between a band-limited stochastic acoustic disturbance and an accelerometer placed arbitrarily on the surface of the panel at the normalized position (0.8056, 0.7968). The accelerometer location was chosen, with the help of the design models, to reflect strong coupling at all modes in the bandwidth while remaining distant from the hybrid control materials. The acoustic disturbance is created by amplifying a generated stochastic signal and broadcasting with an eighteen-inch loudspeaker. The acoustic disturbance functions as an effective broadband disturbance without the addition of unwanted dynamics typical of shakers, piezoceramic actuators, and other physically attached disturbance sources.

Following attachment of the control devices, the open-loop plant is connected to a Digital Signal Processor for system identification and control law design. The disturbance to performance (w to z) path describes the transfer function from the acoustic disturbance to the arbitrarily placed accelerometer described above. The control sensor signal is sent through a bandpass filter designed to allow response between 10 Hz and 1600 Hz. Both corner frequencies are well outside the control bandwidth. A filter also removed the feed-through dynamics in the performance path. All other signals remain unfiltered throughout the experiment.

3.4. HYBRID CONTROL IMPLEMENTATION

Applying the design technique, a single, optimally placed, passive patch demonstrates significant damping at the targeted modes from 189-973 Hz. Figure 5 displays the frequency response of the system measured from the acoustic disturbance to the accelerometer. The damping performance at the targeted modes represents nearly 75% of the mean-square magnitude reduction available in the 75-100% coverage case as modelled with the assumption of a damping ratio of 0.09 [21]. However, active materials are also required for successful attenuation of the lower frequency modes, even in the full-coverage application.

Piezoceramic patches are then attached to the panel for active attenuation at the three lowest modal frequencies, according to the conscripts of the hybrid design. The optimization goal of strong coupling to the modes of interest and decoupling to higher modes (spatial filtering) is best showcased through comparison of the frequency responses of the disturbance to performance path and the actuator to

sensor path. These responses are shown in Figure 6. Note that the patches highlight the targeted low-frequency modes (47-116 Hz) and exhibit relative decoupling at the next five deselected modes (181-317 Hz). The decoupling shown here should alleviate many spillover problems due to unmeasured dynamics, allowing the design of more aggressive control laws and the realization of more substantial attenuation. The even more apparent decoupling to high frequency modes (600-1000 Hz) should further reduce spillover due to unmodelled dynamics in this bandwidth.

Two primary advantages of hybrid control are apparent here. First, the addition of passive damping has magnified the effects of targeted coupling to the low frequency modes for active control by attenuating the response at passively-targeted, higher-frequency modes. This effect increases the magnitude difference between the smallest actively targeted mode and the largest non-targeted mode, allowing the controller to be more aggressive at the targeted modes. Second, passive damping reduces the need for high-frequency roll-off in the active sensor-actuator transfer function: any spillover that may occur should still be damped enough to demonstrate overall reduction with the hybrid controller. Alleviation of the roll-off requirement has freed the optimization routine to select patches that couple better to the actively targeted modes because the concern for the coupling at higher frequencies is diminished.

For active control implementation, system identification with the Eigensystem Realization Algorithm yields a discrete open loop plant. After transformation to the continuous domain, the augmented plant is realized using Simulink, and an H_2 control law is synthesized in MATLAB. Model reduction is accomplished through system balancing and truncation. Following a Tustin transformation to the discrete domain, the control law is implemented with the DSP. Iterative tuning of the control effort penalty and sensor noise floor allow development of a stable controller with notable performance.

Assimilation and computation of various dynamic control laws routinely yielded controllers with fewer than twenty states achieving notable control on the vibration of the panel. Figure 7 displays the open-loop and closed-loop disturbance to performance response of a seventeen state controller designed to attenuate vibration response at the first three modes of the panel (47, 101, 118 Hz). The panel was excited acoustically with band-limited white noise, and the performance response was measured by an accelerometer. Note the significant attenuation of the first three targeted modes. Some spillover from unmodelled dynamics is apparent at frequencies below the first mode, and at the 255 Hz mode. Reference to Figure 6 reveals the actuator to sensor response demonstrated more coupling at 255 Hz than at any other non-targeted frequency: the magnitude of this mode represents the lower bound for the sensor noise floor in control law design. Additionally, this status implies that the first apparent high-frequency spillover should appear at this frequency, as shown in Figure 7. However, comparison of this closed-loop response to the response of the panel without any control shows that even this spillover is negligible in the hybrid control sense. The total hybrid reduction at this mode remains significant.

To demonstrate model accuracy and predicted design effectiveness, Figure 8 compares experimental and modelled hybrid control results through the same in-

put/output path. These plots demonstrate the incredible effectiveness of broadband optimal hybrid control and the validity of the model used in design development.

Thus, experimentation has confirmed a primary advantage of hybrid control: active controllers can be designed more aggressively. The optimal placement of passive patches will decrease both the occurrence probability and the effects of undesirable spillover. In fact, the controller designed above would not have been stable or effective in a purely active implementation, as the sensor noise response, and resulting spillover from unmodelled dynamics, would have been too large at non-targeted frequencies. Sensor noise feedback, particularly at high frequencies, will also be damped by the passive material, thereby limiting the effects of spillover due to unmodelled dynamics. The magnitude of non-targeted modes at higher frequencies is decreased 8–10 dB by the passive material, allowing a lower sensor noise floor and more aggressive control. Further, the passive damping allows 8–10 dB of spillover at non-targeted modes before the total hybrid controller demonstrates undesired additional response at those modes.

The flexibility of the active controller and the strong performance of the damping material have combined for significant attenuation across the entire targeted bandwidth. Calculation of RMS reductions in the 500 Hz bandwidth revealed a passive broadband reduction of 6.11 dB and a total hybrid reduction of 8.11 dB in the 500 Hz bandwidth, implying an active broadband reduction of 2.0 dB. In the 200 Hz bandwidth, these reductions are 5.09 dB, 10.17 dB, and 5.08 dB respectively. Obviously, the attenuation is shared more evenly between the active and passive elements as the percentage of actively targeted modes in a given bandwidth increases.

4. CONCLUSIONS

Passive and active control devices have been designed for coordinately targeted broadband control of the vibration in an aluminum panel. The size of the passive damping material has been reduced from typical full coverage application to less than nine percent coverage, while maintaining 75 percent of damping capability, based upon predicted damping ratios for typical CLD applications. The active materials have been placed to optimize control authority at targeted modes while minimizing coupling to non-targeted modes, thereby increasing attenuation and decreasing spillover from unmodelled dynamics. The combination of active and passive materials has promoted development of significant hybrid advantages inherent in the design. The end result of successful hybrid control is the global reduction of vibration response across a wide frequency range.

REFERENCES

1. W. T. Baumann, W. R. Saunders, and H. H. Robertshaw, "Active structural acoustic control of broadband disturbances," *Journal of the Acoustical Society of America* **92**(4), pp. 1998–2005, 1992.
2. C. R. Fuller, C. A. Rogers, and H. H. Robertshaw, "Control of sound radiation with active/adaptive structures," *Journal of Sound and Vibration* **157**(1), pp. 19–39, 1992.
3. L. Maestrello, "Control of panel response to turbulent boundary-layer and acoustic excitation," *AIAA Journal* **34**(4), pp. 259–264, 1996.

4. R. L. Clark and D. E. Cox, "Multi-variable structural acoustic control with static compensation," *Journal of the Acoustical Society of America* **102**(5), pp. 2747-2756, 1997.
5. J. S. Vipperman and R. L. Clark, "Multivariable feedback active structural acoustic control with adaptive piezoelectric sensor/actuators," *Journal of the Acoustical Society of America* **105**(1), pp. 219-225, 1999.
6. G. C. Smith and R. L. Clark, "Adaptive structure design through optimal spatial compensation," in *Proceedings of Active-99*, Noise Control Foundation, Poughkeepsie, NY, (Fort Lauderdale, FL), December 2-4 1999.
7. E. M. Austin and D. J. Inman, "Modeling of sandwich structures," in *Passive Damping and Isolation Proceedings, 5th International Symposium on Smart Structures and Materials*, SPIE **3327**, March 1998. Ed. L. P. Davis.
8. A. M. Baz and J. J. Ro, "The concept and performance of active constrained layer damping treatments," *Journal of Sound and Vibration*, pp. 18-21, March 1994.
9. D. E. Veley and S. S. Rao, "Optimal design of structures with active constrained layer damping," *Proceedings of Smart Structures and Materials 1995*, SPIE **2445**(2), pp. 98-109, 1995.
10. S. Poh, A. M. Baz, and B. Balachandran, "Experimental adaptive control of sound radiation from a panel into an acoustic cavity using active constrained layer damping," *Journal of Smart Materials and Structures* **5**, pp. 649-659, 1996.
11. M. J. Lam, D. J. Inman, and W. R. Saunders, "Vibration control through passive constrained layer damping and active control," *Journal of Intelligent Materials Systems and Structures* **8**, pp. 663-677, August 1997.
12. N. W. Hagood, W. H. Chung, and A. von Flotow, "Modeling of piezoelectric actuator dynamics for active structural control," *Journal of Intelligent Material Systems and Structures* **1**, pp. 327-354, July 1990.
13. R. L. Clark, G. P. Gibbs, and W. R. Saunders, *Adaptive Structures, Dynamics and Control*, John Wiley and Sons, New York, 1998.
14. M. I. Friswell, D. J. Inman, and M. J. Lam, "On the realization of GHM models in viscoelasticity," *Journal of Intelligent Material Systems and Structures* **8**, pp. 986-993, November 1997.
15. D. F. Golla and P. C. Hughes, "Dynamics of viscoelastic structures - a time domain, finite element formulation," *Journal of Applied Mechanics* **52**, pp. 897-906, 1985.
16. D. J. McTavish and P. C. Hughes, "Modeling of linear viscoelastic space structures," *ASME Journal of Vibration and Acoustics* **115**, pp. 103-113, 1993.
17. J. A. Rule, R. E. Richard, and R. L. Clark, "Design of an aeroelastic wing model for active flutter control," *AIAA Journal of Guidance, Control, and Dynamics* **24**(5), pp. 918-924, 2001.
18. K. B. Lim and W. Gawronski, "Hankel singular values of flexible structures in discrete time," *AIAA Journal of Guidance, Control and Dynamics* **19**(6), pp. 1370-1377, 1996.
19. K. B. Lim, "Disturbance rejection approach to actuator and sensor placement," *AIAA Journal of Guidance, Control and Dynamics* **20**(1), pp. 202-204, 1997.
20. R. L. Clark and D. E. Cox, "Band-limited actuator and sensor selection for disturbance rejection," *Journal of Guidance, Control and Dynamics* **23**(5), pp. 903-906, 2000.
21. "Viscoelastic material properties," tech. rep., 3M, Inc., St. Paul, MN, February 1999. Technical Data.
22. D. E. Goldberg, *Genetic Algorithms in Search, Optimization, and Machine Learning*, Addison Wesley, Menlo Park, NJ, 1989.
23. K. Deb, *Multiobjective Optimization Using Evolutionary Algorithms*, John Wiley & Sons, New York, 2001.
24. W. Hoppman and J. Greenspon, "An experimental device for obtaining elastic rotational constraints on the boundary of a plate," in *Proceedings of the 2nd National Congress on Applied Mechanics*, pp. 187-191, 1954.

TABLE 1

Material and geometric properties of panel and attached control devices.

Property	Value	Property	Value
Panel Length	0.457 m	E_s	$69.3 \times 10^9 \text{ N/m}^2$
Panel Width	0.406 m	ν_s	0.33
Panel Thickness	1.52 mm	ρ_s	2680 kg/m^3
PZT Actuator Length	99 mm	PZT Sensor Length	84 mm
PZT Actuator Width	72 mm	PZT Sen. Width	74 mm
PZT Act. Location	(65,118)mm	PZT Sen. Location	(163,134)mm
PZT Actuator Rotation	77°	PZT Sensor Rotation	65°
PZT Thickness	0.38 mm	E_p	$5.0 \times 10^{10} \text{ N/m}^2$
ν_p	0.3	ρ_p	7650 kg/m^3
PZT dielectric	-180×10^{-12}		
Viscoelastic Thickness	0.12 mm	E_{ve}	$14 \times 10^6 \text{ N/m}^2$
ρ_{ve}	1000 kg/m^3		
CL Thickness	0.76 mm	E_{cl}	$69.3 \times 10^9 \text{ N/m}^2$
ν_{cl}	0.33	ρ_{cl}	2680 kg/m^3
CLD Length	149 mm	CLD Width	99 mm
CLD Location	(109,327)mm	CLD Rotation	152°

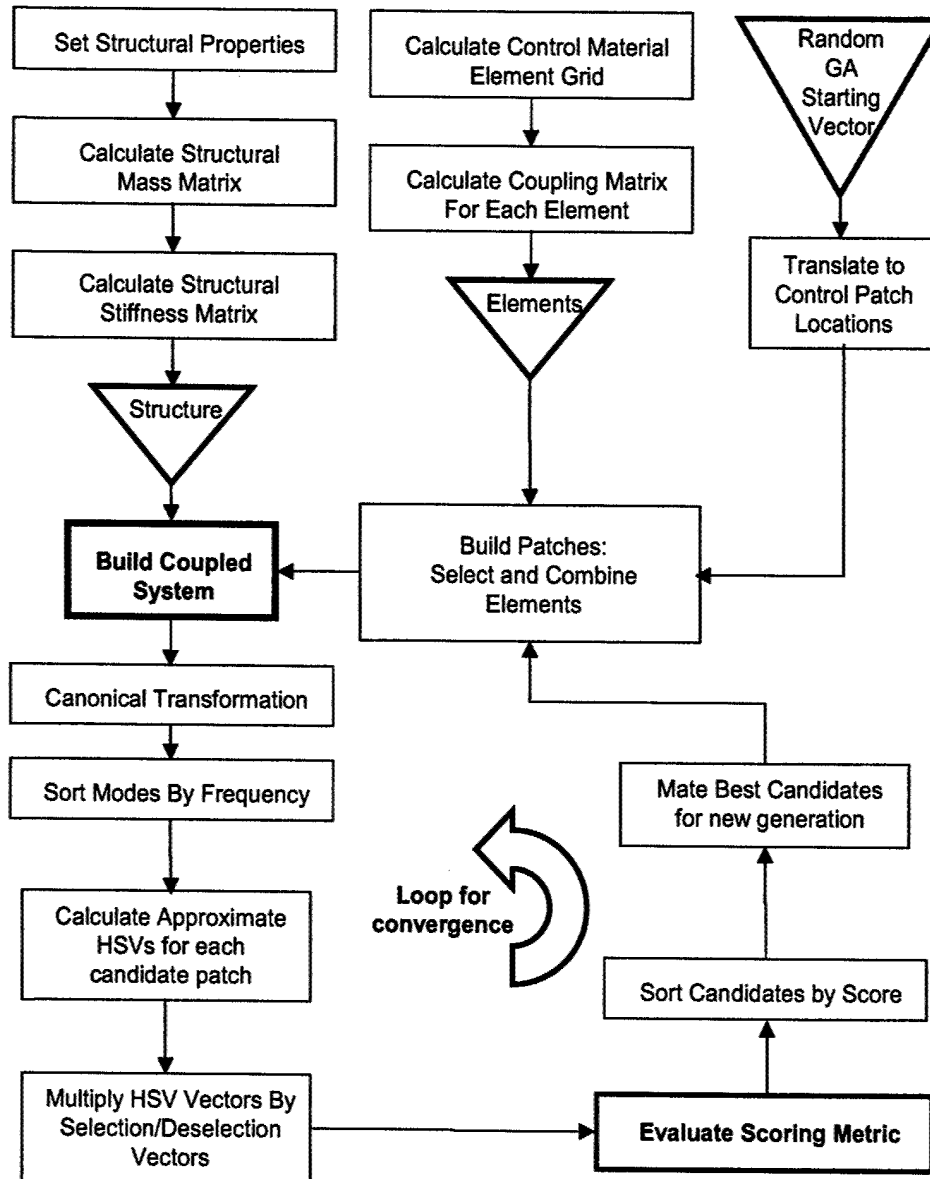


Figure 1. Schematic of model adaptation and implementation of design technique with genetic algorithm

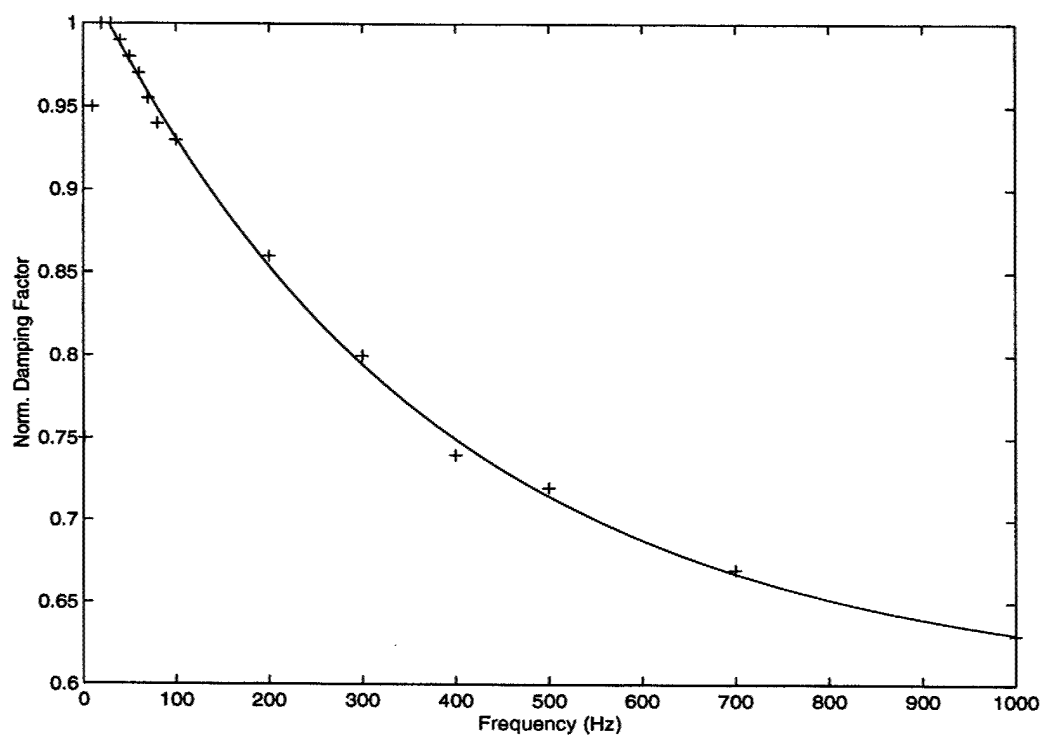


Figure 2. Curve fit (—) of normalized damping factor data (+ + +) for viscoelastic 112P05 from 3M nomograph [21].

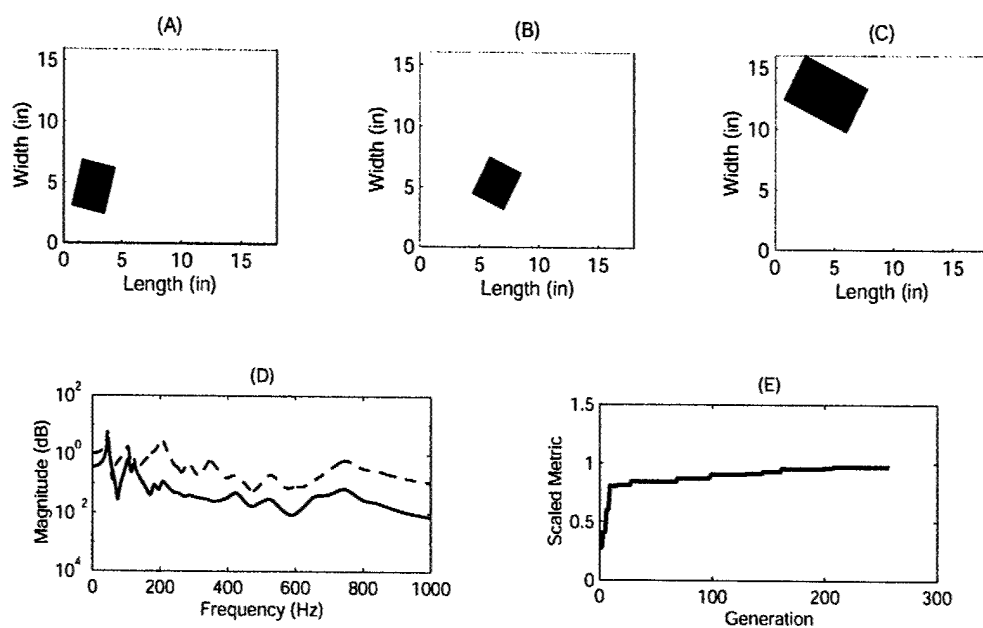


Figure 3. Schematic of optimal placement results as implemented experimentally: locations of (A) PZT Actuator, (B) PZT Sensor, and (C) CLD; (D) predicted system response, through the respective control paths G_{yu} , to a modal disturbance measured at locations of active (—) and passive(---) patches; (E) convergence plot for scaled optimization metric scores.

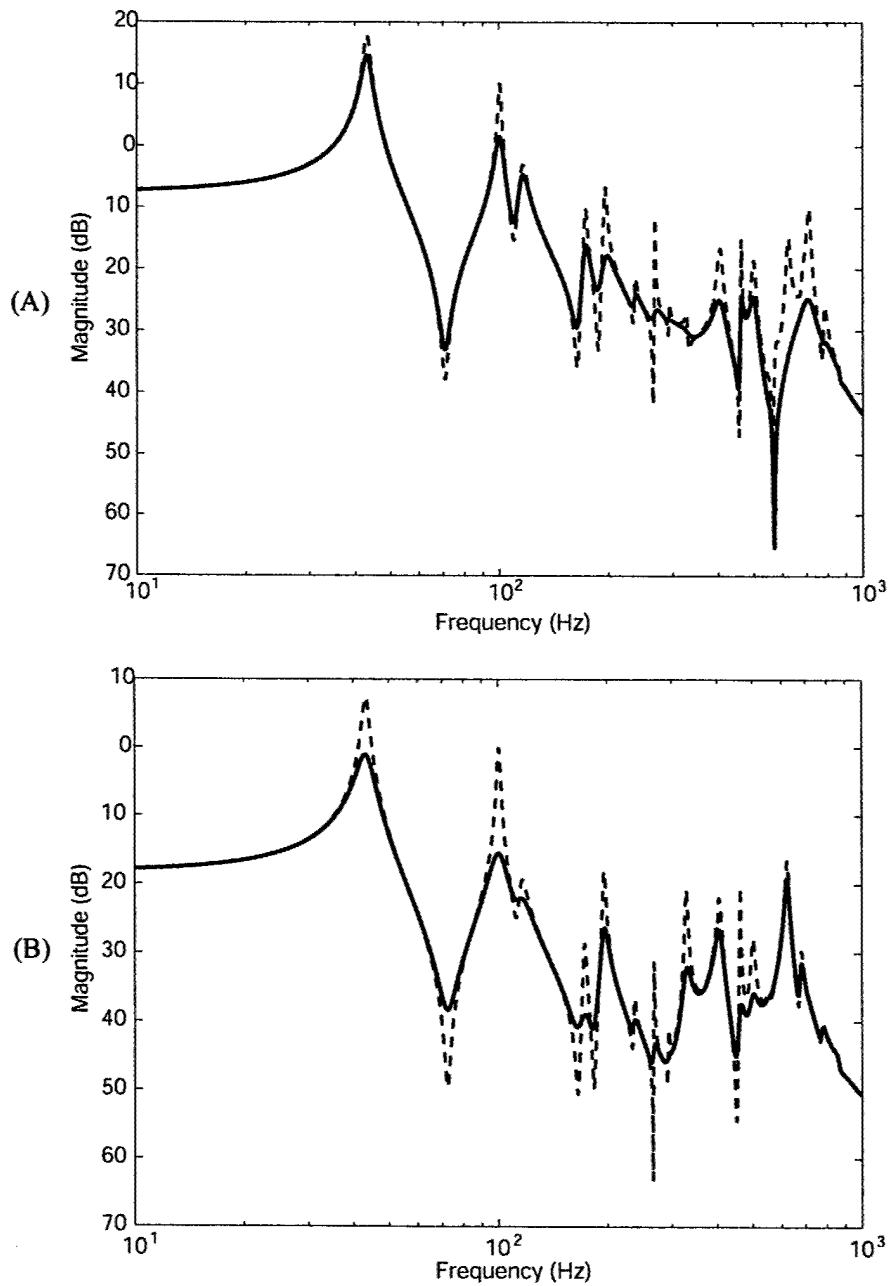


Figure 4. Comparison of system response, with (—) and without (---) optimal passive material placement, measured from sensor to actuator (G_{yu}); (A) estimated damping considered in the scoring routine, (B) estimated damping NOT considered in scoring routine.

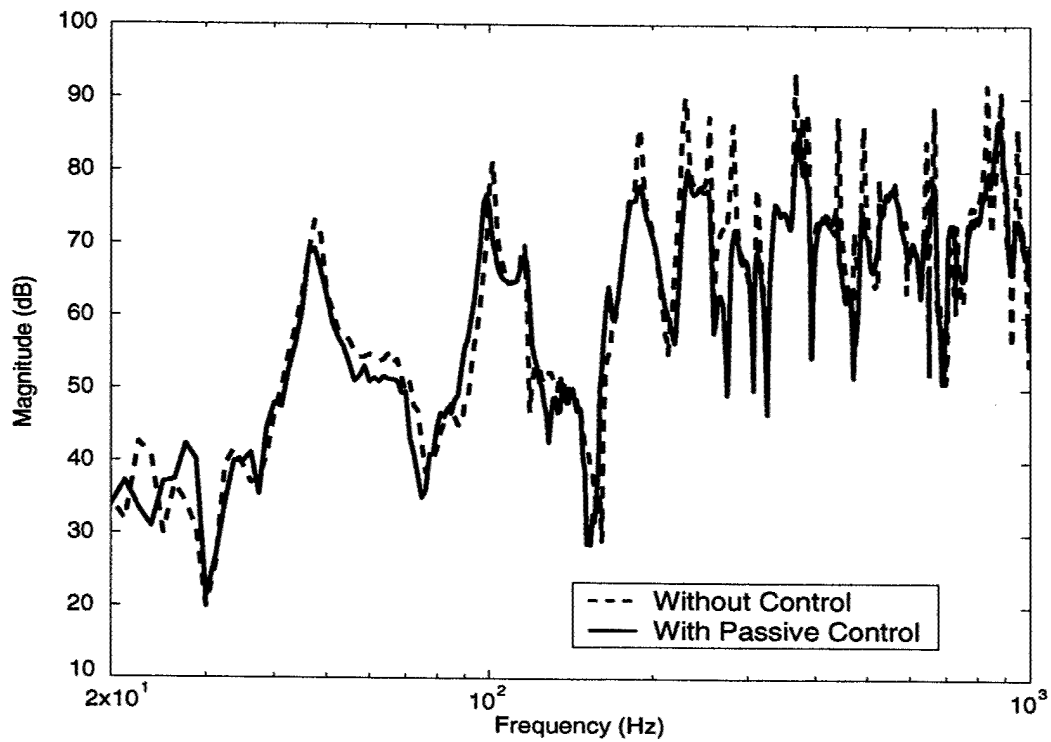


Figure 5. Comparison, experimental response measured from disturbance to performance (G_{zw}) without (—) and with (---) applied optimal constrained layer patch

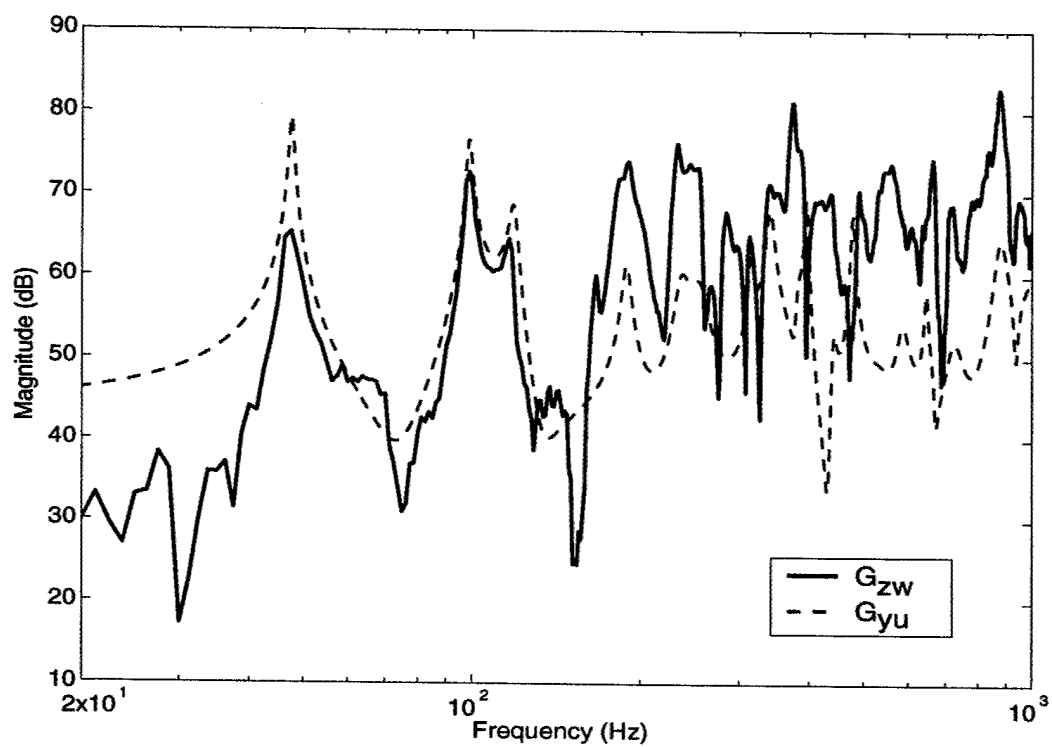


Figure 6. Comparison, experimental frequency response measured from disturbance to performance (G_{zw}) (—) and actuator to sensor (G_{yu}) (- -).

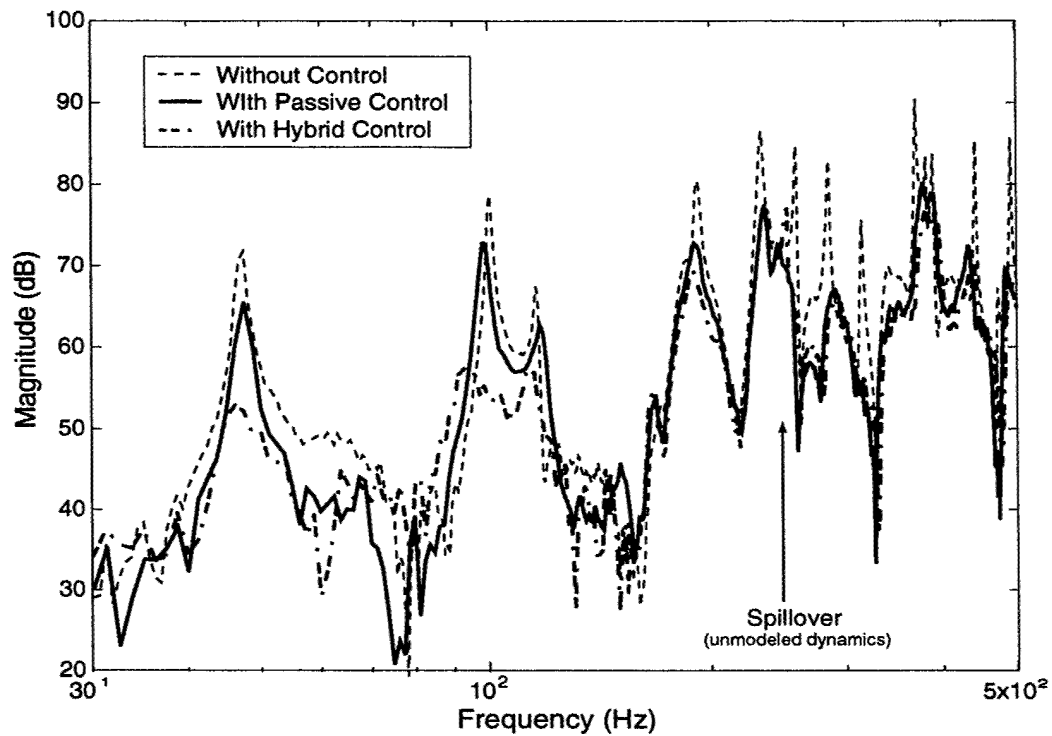


Figure 7. Comparison, response measured from disturbance to performance (G_{zw}) without control (---), with passive control (—), and with hybrid control (-.-.): active patches targeting the first three modes (47, 101, 118 Hz).

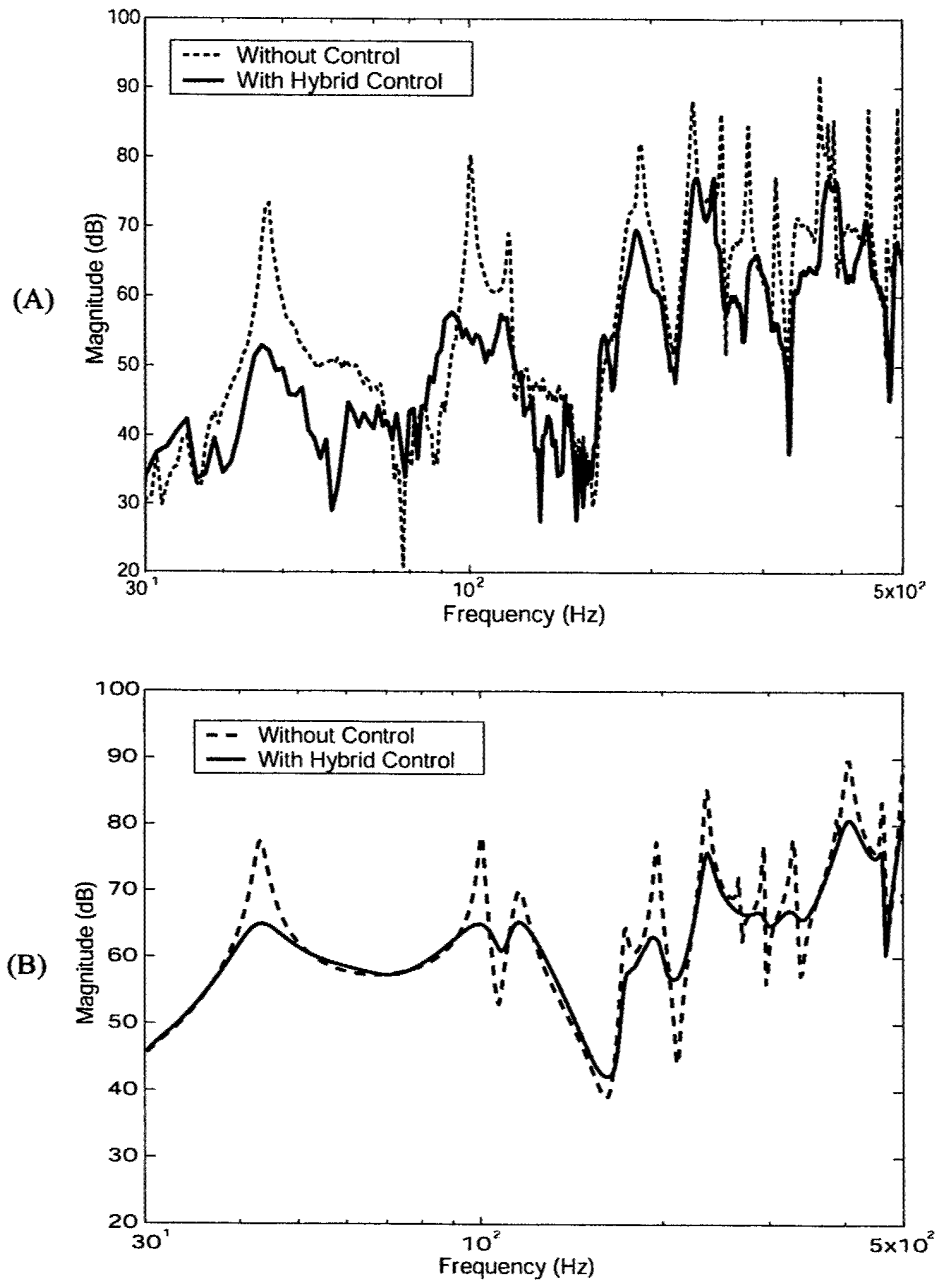


Figure 8. Comparison, open and closed-loop response measured from disturbance to performance (G_{zw}) with (—) and without (---) hybrid control; (A) experimental results on aluminum panel, (B) modelled results on aluminum panel.

THE RECURSIVE GENERALIZED PREDICTIVE FEEDBACK CONTROL: THEORY AND EXPERIMENTS

Suk-Min Moon and Robert L. Clark and Daniel G. Cole

*Department of Mechanical Engineering and Materials Science
Duke University
Durham, NC 27708, USA*

The recursive generalized predictive feedback control algorithm, combining the process of system identification and the process of the controller design, is presented. In the generalized predictive control design process, there are three parameters to be chosen: the prediction horizon, the control horizon, and the input weighting factor. Two new parameters are defined for the practical choice of the prediction horizon and the control horizon. A time varying algorithm for the input weighting factor and a dual-sampling-rate algorithm between system identification and control design are presented. The recursive generalized predictive feedback control algorithm is applied to three different systems: a cantilevered beam, a sound enclosure, and an optical jitter suppression testbed.

© 2002 Academic Press

1. INTRODUCTION

The predictive control concept can be thought of as an extension of the one-step-ahead predictors [1, 2]. Predictive control is based upon the following steps: output prediction, control calculation, and feedback implementation [3]. The general concept of output prediction is presented in [4]. Early predictive control methods are based on the simple impulse [5], or step [6] response models of the plant. Later methods removed the shortcomings of the earlier design model [1]. Of these, generalized predictive control by Clarke and his coworkers has been shown to be particularly effective [1, 2, 7].

© 2002 Academic Press

The predictive control methods, including generalized predictive control (GPC) [1, 2, 7], can be related to the linear quadratic (LQ) optimal control design method [8]. The GPC solution approaches the LQ regulator by extending the control and prediction horizons to very large values, but there are also significant differences. The weighting matrices are used as tuning parameters in the LQ approach but the prediction and control horizons are used in the GPC approach. In the LQ approach, the Riccati equation is to be solved. In the GPC approach, the solution is obtained using the pseudo inverse of a matrix that results from posing the problem as least squares minimization.

Generalized predictive control can be derived from a state-space model [9, 10] or a transfer function model [11, 12]. In the state-space formulation, the issue of state estimation arises. Previous works in formulating GPC in the state-space framework have mostly concentrated on showing the equivalence of transfer function and state-space approaches [13]. In [10], the design of the state estimator is treated in the least squares framework similar to that of the control formulation, i.e. by minimizing a receding finite horizon cost function related to the estimation error. Such an approach is extended to designing state estimators in a multirate sampling and control environment [9, 10]. The generalized predictive control derived using a transfer function model or input-output model can be found in [14, 15, 3].

Generalized Predictive Control (GPC) starts with the ARX model with the absence of the direct transmission term and builds a multi-step ahead output predictor. The predictive control law is then computed using the Toeplitz matrix formed from the step response time history of the system in conjunction with a cost function with weighted input and output [15]. There are three

design parameters involved including the control weight, the prediction horizon and the control horizon. Properties of those parameters are discussed in [7, 16]. Since a proper combination of these parameters is required in order to guarantee stability of the predictive control law, different variants of the method have been proposed which yield stabilizing control [17, 12, 18, 19].

One of the recent works for the extension of the generalized predictive control is the continuous generalized predictive control (CGPC) [16]. Since CGPC guarantees closed-loop stability only in some special limiting case [16, 20], a number of papers remedied this problem in the case of discrete-time systems and a continuous-time extension [20, 21]. These are referred to as stable continuous generalized predictive control (SCGPC) [22, 23].

A similar technique to generalized predictive control (GPC) is deadbeat predictive control (DPC) [11]. The DPC algorithm is similar to GPC in that it is a receding horizon controller, but differs from GPC in that it does not try to drive the error to zero immediately [24].

Recently, direct adaptive GPC controllers for single-input and single-output systems have been proposed [25, 26, 3, 27]. In [25], a direct version of an adaptive GPC controller is suggested for deterministic systems by using a correct Markov parameter assumption. In [26], direct adaptive GPC algorithms both for deterministic systems and stochastic systems are proposed under the assumption of correct Markov parameters but only using an estimator. In [3], continuous generalized predictive control algorithm is applied to the system adaptively.

Generalized predictive control has been applied to practical control problems [28–30]. Control of muscle-relaxation in a biomedical application is described

in [31]. The continuous generalized predictive control design is applied to a cascaded water tank in [3]. Generalized predictive control (GPC) and dead-beat predictive control are applied to vibration suppression of an aluminum plate in [24].

In this research, the recursive generalized predictive feedback control algorithm, which combines the process of system identification and the process of the generalized predictive feedback control design, is developed. The proposed algorithm extends the recursive system identification algorithm and the generalized predictive control design algorithm for multi-input and multi-output system. The algorithm is also designed for real time control and applied to actual testbed. The experimental results from this research will demonstrate the feasibility of the control algorithm.

2. RECURSIVE SYSTEM IDENTIFICATION

Using the linear combinations of past output and input measurements as states, a system can be identified in ARX representation,

$$y(t) = -\alpha_1 y(t-1) - \dots - \alpha_p y(t-p) + \beta_1 u(t-1) + \dots + \beta_p u(t-p) + e(t) \quad (1)$$

where $y(t)$ is the measured output and $u(t)$ is the input to the system. For m outputs and n inputs system, the output, $y(t)$, is m by 1 vector and the input, $u(t)$, is n by 1 vector. Each α_i ($i = 1, 2, \dots, p$) is a m by m matrix and each β_i ($i = 1, 2, \dots, p$) is a m by n matrix.

The system identification process involves identifying the coefficients, α_i and β_i , to minimize the prediction error, $e(t)$. The prediction error, $e(t)$, can be written as

$$e(t) = y(t) - \hat{y}(t|t-1) \quad (2)$$

where the one-step-ahead prediction, $\hat{y}(t|t-1)$, is the conditional expectation of $y(t)$ which is given as

$$\hat{y}(t|t-1) = \theta(t-1)\varphi^T(t) \quad (3)$$

where $\theta(t-1)$ is a system parameter matrix,

$$\theta(t-1) = \begin{bmatrix} \alpha_1 & \cdots & \alpha_p & \beta_1 & \cdots & \beta_p \end{bmatrix}, \quad (4)$$

and $\varphi(t)$ is a data vector,

$$\varphi(t) = \begin{bmatrix} -y^T(t-1) & \cdots & -y^T(t-p) & u^T(t-1) & \cdots & u^T(t-p) \end{bmatrix}. \quad (5)$$

A system parameter matrix, $\theta(t-1)$, is an m by $(m+n)p$ matrix, and a data vector, $\varphi^T(t)$, is a $(m+n)p$ by 1 vector.

With input and output measured at time $t = k$, where $k = 1, 2, \dots, N$, the total number of $N - p - 1$ equations of the form

$$y(k) = \theta(k-1)\varphi^T(k) + e(k) \quad (6)$$

can be written in vector equation form,

$$\mathbf{y} = \theta\Psi + \mathbf{e} \quad (7)$$

where

$$\mathbf{y} = \begin{bmatrix} y(p+1) & y(p+2) & \cdots & y(N) \end{bmatrix}, \quad (8)$$

$$\Psi = \begin{bmatrix} -y(p) & -y(p+1) & \cdots & -y(N-1) \\ -y(p-1) & -y(p) & \cdots & -y(N-2) \\ \vdots & \vdots & \vdots & \vdots \\ -y(1) & -y(2) & \cdots & -y(N-p) \\ u(p) & u(p+1) & \cdots & u(N-1) \\ u(p-1) & u(p) & \cdots & u(N-2) \\ \vdots & \vdots & \vdots & \vdots \\ u(1) & u(2) & \cdots & u(N-p) \end{bmatrix}, \quad (9)$$

and

$$\mathbf{e} = \begin{bmatrix} e(p+1) & e(p+2) & \cdots & e(N) \end{bmatrix}. \quad (10)$$

Assuming $N \geq 2p$, and defining the loss function, $V = \mathbf{e}^T \cdot \mathbf{e}$, the minimization of the loss function,

$$\left. \frac{dV}{d\theta} \right|_{\theta=\hat{\theta}} = 0, \quad (11)$$

results in

$$\hat{\theta} = \mathbf{y} \Psi^T \mathbf{P} \quad (12)$$

where $\mathbf{P} = [\Psi \Psi^T]^{-1}$.

This is the nonrecursive system parameter estimation using the least squares method. This estimation method is valid only after measuring and storing all input and output measurements. Using the preceding nonrecursive estimation equations, the recursive parameter estimation algorithm using least squares method can be obtained. The recursive algorithm can be expressed such that the estimation of the new system parameters can be updated from the one-step previous system parameters using the one-step-ahead prediction of the

new measurement with a correcting vector and the new measurement of the signals.

Suppose that the nonrecursive estimation matrix, Ψ , given in Equation (9), and the output history vector, \mathbf{y} , given in Equation (8), using time index, t , can be written as

$$\Psi(t) = [\Psi(t-1) \quad \varphi^T(t)] \quad \mathbf{y}(t) = [\mathbf{y}(t-1) \quad y(t)] \quad (13)$$

where $\Psi(t-1)$ is the estimation matrix constructed using input and output data up to time $t-1$. $\varphi^T(t)$ is the vector of output and input data at time t , which is the last column of the estimation matrix at time t , $\Psi(t)$. The output history vector at time t , $\mathbf{y}(t)$, is divided into the output history vector up to time $t-1$, and the new output value at time t , $y(t)$.

The system parameter matrix at time $t-1$, obtained using output and input data up to time $t-1$, can be written as

$$\hat{\theta}(t-1) = \mathbf{y}(t-1)\Psi^T(t-1)\mathbf{P}(t-1), \quad (14)$$

where $\mathbf{P}(t-1) = [\Psi(t-1)\Psi^T(t-1)]^{-1}$.

The system parameter vector, $\hat{\theta}(t)$, at time t can be written as

$$\hat{\theta}(t) = \hat{\theta}(t-1) + \{y(t) - \hat{\theta}(t-1)\varphi^T(t)\}\varphi(t) [\Psi^T(t)\Psi(t)]^{-1}, \quad (15)$$

which means the new system parameters, $\hat{\theta}(t)$, can be obtained from the one-step previous system parameters, $\hat{\theta}(t-1)$, the new output measurement, $y(t)$, the output and input history vector, $\varphi(t)$, and the estimation matrix, $[\Psi(t)\Psi^T(t)]^{-1}$.

To avoid calculating $\mathbf{P}(t) = [\Psi(t)\Psi^T(t)]^{-1}$ at each step, the Matrix Inversion Lemma is applied,

$$[A + BCD]^{-1} = A^{-1} - A^{-1}B [DA^{-1}B + C^{-1}]^{-1} DA^{-1}. \quad (16)$$

Taking $A = \Psi(t-1)\Psi^T(t-1)$, $B = \varphi^T(t)$, $C = 1$, and $D = \varphi(t)$ gives

$$\mathbf{P}(t) = \mathbf{P}(t-1) [\mathbf{I} - \varphi^T(t)L(t)] \quad (17)$$

where the correcting factor, $L(t)$, is

$$L(t) = \frac{\varphi(t)\mathbf{P}(t-1)}{1 + \varphi(t)\mathbf{P}(t-1)\varphi^T(t)}. \quad (18)$$

Moreover,

$$\begin{aligned} \varphi(t)\mathbf{P}(t) &= \varphi(t)\mathbf{P}(t-1) - \frac{\varphi(t)\mathbf{P}(t-1)\varphi^T(t)\varphi(t)\mathbf{P}(t-1)}{1 + \varphi(t)\mathbf{P}(t-1)\varphi^T(t)} \\ &= \frac{\varphi(t)\mathbf{P}(t-1)}{1 + \varphi(t)\mathbf{P}(t-1)\varphi^T(t)}. \end{aligned} \quad (19)$$

It is noted that the denominator of $L(t)$, $1 + \varphi(t)\mathbf{P}(t-1)\varphi^T(t)$, becomes a scalar. So, the updating algorithm for correcting factors, $L(t)$, has scalar division rather than matrix inversion.

As a result, the recursive least squares (RLS) method can be summarized as

$$\hat{\theta}(t) = \hat{\theta}(t-1) + \{y(t) - \hat{\theta}(t-1)\varphi^T(t)\}L(t) \quad (20)$$

where $\hat{\theta}(t)$ is the new estimation of system parameters, $\hat{\theta}(t-1)$ is the old estimation of system parameters, $y(t)$ is the new output measurement, $\hat{\theta}(t-1)\varphi^T(t)$ is the one-step-ahead prediction of the new measurement, and $L(t)$ is the correcting factor given in Equation (18).

The initial conditions for the recursive system identification algorithm can be set as

$$\begin{aligned} \hat{\theta}(0) &= \text{zeros}(m, (m+n)p) \\ \mathbf{P}(0) &= \alpha \text{eye}((m+n)p) \end{aligned} \quad (21)$$

where $\text{zeros}(m, (m+n)p)$ is a m by $(m+n)p$ zero matrix, and $\text{eye}((m+n)p)$ is a $(m+n)p$ identity matrix. Recall that m is the number of system outputs and n is the number of system inputs. The gain, α , is any positive number. For the time invariant system, a small value of the gain will allow the system parameters to be updated gradually, without significant changes. In this work, the the gain, α , is set to be 10^1 in the recursive system identification process.

3. THE GENERALIZED PREDICTIVE CONTROL

In this chapter, generalized predictive feedback control algorithm is developed for multi-input and multi-output system, and the stability test algorithm of the controller is presented.

3.1. GENERALIZED PREDICTIVE FEEDBACK CONTROL

The generalized predictive feedback controller is designed for a system written in ARX form such as

$$\alpha_0 y(t) + \alpha_1 y(t-1) + \dots + \alpha_p y(t-p) = \beta_0 u(t) + \beta_1 u(t-1) + \dots + \beta_p u(t-p) \quad (22)$$

where α_i ($i = 0, \dots, p$) and β_i ($i = 0, \dots, p$) are ARX parameters. Each output ARX parameter, $\alpha_0 = \text{eye}(m)$ and α_i , is an m by m matrix, where $\text{eye}(m)$ is an m by m identity matrix. Each input ARX parameter, $\beta_0 = \text{zeros}(m, n)$ and β_i , is an m by n matrix, where $\text{zeros}(m, n)$ is an m by n matrix with zero entries. For m outputs and n inputs system, the output, $y(t)$, is m by 1 vector and the input, $u(t)$, is n by 1 vector. For a single-input and single-output system, $\alpha_0 = 1$ and $\beta_0 = 0$.

The ARX system equation, given in Equation (22), can be written in matrix form,

$$\mathbf{A}\mathbf{y}_p = \mathbf{B}\mathbf{u}_p, \quad (23)$$

where output ARX parameter matrix, \mathbf{A} , is an m by $m(p+1)$ matrix, and input ARX parameter matrix, \mathbf{B} , is an m by $n(p+1)$ matrix, which are written as

$$\begin{aligned} \mathbf{A} &= [\text{eye}(m) \quad \alpha_1 \quad \cdots \quad \alpha_p] \\ \mathbf{B} &= [\text{zeros}(m, n) \quad \beta_1 \quad \cdots \quad \beta_p]. \end{aligned} \quad (24)$$

The output vector, \mathbf{y}_p , and the input vector, \mathbf{u}_p , in Equation (23), are

$$\mathbf{y}_p = \begin{bmatrix} y(t) \\ y(t-1) \\ \vdots \\ y(t-p) \end{bmatrix} \quad \mathbf{u}_p = \begin{bmatrix} u(t) \\ u(t-1) \\ \vdots \\ u(t-p) \end{bmatrix} \quad (25)$$

Constructing the q step predictor at time k and partitioning into past and future parts, the following matrix equation is obtained:

$$[\mathbf{F} \mid \mathbf{G}] \begin{bmatrix} \mathbf{y}_P(k) \\ \mathbf{y}_F(k) \end{bmatrix} = [\mathbf{H} \mid \mathbf{J}] \begin{bmatrix} \mathbf{u}_P(k) \\ \mathbf{u}_F(k) \end{bmatrix}, \quad (26)$$

where matrices \mathbf{F} and \mathbf{G} are written as

$$[\mathbf{F} \mid \mathbf{G}] = \left[\begin{array}{ccc|cccccc} \alpha_p & \cdots & \alpha_1 & \alpha_0 & 0 & 0 & \cdots & 0 & 0 \\ 0 & \ddots & \ddots & \ddots & \ddots & \ddots & \vdots & \vdots & \vdots \\ \vdots & 0 & \alpha_p & \vdots & \alpha_1 & \alpha_0 & 0 & \cdots & 0 \\ \vdots & \vdots & 0 & \alpha_p & \vdots & \alpha_1 & \alpha_0 & 0 & 0 \\ \vdots & \vdots & \vdots & \ddots & \ddots & \ddots & \ddots & \vdots & \vdots \\ 0 & \cdots & 0 & 0 & 0 & \alpha_p & \cdots & \alpha_1 & \alpha_0 \end{array} \right] \quad (27)$$

and matrices \mathbf{H} and \mathbf{J} are written as

$$[\mathbf{H} \mid \mathbf{J}] = \left[\begin{array}{ccc|cccccc} \beta_p & \cdots & \beta_1 & \beta_0 & 0 & 0 & \cdots & 0 & 0 \\ 0 & \ddots & \ddots & \ddots & \ddots & \ddots & \vdots & \vdots & \vdots \\ \vdots & 0 & \beta_p & \vdots & \beta_1 & \beta_0 & 0 & \cdots & 0 \\ \vdots & \vdots & 0 & \beta_p & \vdots & \beta_1 & \beta_0 & 0 & 0 \\ \vdots & \vdots & \vdots & \ddots & \ddots & \ddots & \ddots & \vdots & \vdots \\ 0 & \cdots & 0 & 0 & 0 & \beta_p & \cdots & \beta_1 & \beta_0 \end{array} \right]. \quad (28)$$

It is noted that the coefficient matrix of the past output, \mathbf{F} , is an $m(p+q)$ by mp block upper triangular matrix, the coefficient matrix of the future output, \mathbf{G} , is $m(p+q)$ by $m(p+q)$ block lower triangular matrix, the coefficient matrix of the past input, \mathbf{H} , is $m(p+q)$ by np block upper triangular matrix, and the coefficient matrix of the future input, \mathbf{J} , is $m(p+q)$ by $n(p+q)$ block lower triangular matrix. The matrix \mathbf{G} is a square matrix. It is also noted that system parameters in Equations (27) and (28) are reordered from Equation (24).

The mp by 1 output past history vector, $\mathbf{y}_P(k)$, and the $m(p+q)$ by 1 future output vector, $\mathbf{y}_F(k)$, can be written as

$$\mathbf{y}_P(k) = \begin{bmatrix} y(k-p) \\ \vdots \\ y(k-1) \end{bmatrix} \quad \mathbf{y}_F(k) = \begin{bmatrix} y(k) \\ \vdots \\ y(k+p+q-1) \end{bmatrix}. \quad (29)$$

The np by 1 input past history vector, $\mathbf{u}_P(k)$, and the $n(p+q)$ by 1 future input vector, $\mathbf{u}_F(k)$, can be written as

$$\mathbf{u}_P(k) = \begin{bmatrix} u(k-p) \\ \vdots \\ u(k-1) \end{bmatrix} \quad \mathbf{u}_F(k) = \begin{bmatrix} u(k) \\ \vdots \\ u(k+p+q-1) \end{bmatrix}. \quad (30)$$

It is easy to solve equation (26) for future outputs and normalize the coefficients by multiplying the inverse of the coefficient matrix of the future output,

$$\mathbf{y}_F(k) = \mathbf{G}^{-1}\mathbf{J}\mathbf{u}_F(k) + \mathbf{G}^{-1}\mathbf{H}\mathbf{u}_P(k) - \mathbf{G}^{-1}\mathbf{F}\mathbf{y}_P(k). \quad (31)$$

Writing the normalized coefficient matrices as,

$$\mathbf{T}_c = \mathbf{G}^{-1}\mathbf{J}, \quad \mathbf{B}_c = \mathbf{G}^{-1}\mathbf{H}, \quad \mathbf{A}_c = -\mathbf{G}^{-1}\mathbf{F}, \quad (32)$$

equation (31) can be rewritten as

$$\mathbf{y}_F(k) = \mathbf{T}_c\mathbf{u}_F(k) + \mathbf{B}_c\mathbf{u}_P(k) + \mathbf{A}_c\mathbf{y}_P(k). \quad (33)$$

Defining the prediction horizon to be $h_p = p+q-1$, the normalized coefficient matrix of the future input, \mathbf{T}_c , is an $m(h_p + 1)$ by $n(h_p + 1)$ matrix. The normalized coefficient matrix of the past input, \mathbf{B}_c , is an $m(h_p + 1)$ by np matrix, and the normalized coefficient matrix of the past output, \mathbf{A}_c , is an $m(h_p + 1)$ by mp matrix.

The cost function to be minimized in the generalized predictive control is defined as [15, 11]

$$\begin{aligned} J(k) &= \mathbf{y}_F^T(k)\mathbf{y}_F(k) + \mathbf{u}_F^T(k)\lambda\mathbf{u}_F(k) \\ &= \sum_{j=0}^{h_p} \{y(k+j)^T y(k+j)\} + \sum_{j=0}^{h_c} \{u(k+j)^T \lambda u(k+j)\} \end{aligned} \quad (34)$$

where λ is the input weighting factor or control penalty, h_p is the prediction horizon, and h_c is the control horizon, which is less than the prediction horizon, i.e. $h_c \leq h_p$.

The future input, \mathbf{u}_F , that satisfies the equation, $dJ(k)/d\mathbf{u}_F = 0$, is

$$\mathbf{u}_F(k) = -[\mathbf{T}_c^T\mathbf{T}_c + \lambda\mathbf{I}]^{-1}\mathbf{T}_c(\mathbf{B}_c\mathbf{u}_P(k) + \mathbf{A}_c\mathbf{y}_P(k)) \quad (35)$$

The control input at time k is defined by the first n rows of the future input, i.e.,

$$\mathbf{u}(k) = \text{the first } n \text{ rows of } \{-[\mathbf{T}_c^T\mathbf{T}_c + \lambda\mathbf{I}]^{-1}\mathbf{T}_c\}(\mathbf{B}_c\mathbf{u}_P(k) + \mathbf{A}_c\mathbf{y}_P(k)). \quad (36)$$

The input weighting factor or the control penalty, λ , is assumed to be a positive scalar. The closed-loop system will be unstable when $\lambda = 0$ because \mathbf{T}_c will be rank deficient ($\mathbf{T}_c = \mathbf{G}^{-1}\mathbf{J}$ and \mathbf{J} is rank deficient by $\beta_0 = 0$).

The control input given in Equation (36) is when the control horizon is equal to the prediction horizon. When the control horizon is less than the prediction horizon, the solution that minimizes the cost function, $J(k)$, given in Equation (34), can be achieved by reducing the size of the coefficient matrix \mathbf{J} in Equation (28) to be $\mathbf{J}(1 : m(h_p + 1), 1 : n(h_c + 1))$. The shorter control horizon means the control input is assumed to be zero for all values beyond the control horizon.

3.2. STABILITY TEST OF THE CONTROLLER

Since it is shown that in the absence of pole-zero cancellations in the transfer function, system eigenvalues and transfer function poles are identical, the stability of the controller can also be checked in the following manner.

From Equation (36), the controller can be written in the discrete transfer form,

$$y_c(k) = \beta_1^c y_c(k-1) + \beta_2^c y_c(k-2) + \cdots + \beta_p^c y_c(k-p) + \alpha_1^c u_c(k-1) + \alpha_2^c u_c(k-2) + \cdots + \alpha_p^c u_c(k-p) \quad (37)$$

where the input to the controller, $u_c(k)$, is the output of the system, $y(k)$, and the output of the controller, $y_c(k)$, is the input to the system, $u(k)$. The coefficients of $u_c(k-i)$, α_i^c ($i = 1, \dots, p$), and the coefficients of $y_c(k-i)$, β_i^c ($i = 1, \dots, p$), use superscript c to distinguish them from the coefficients used for the system ARX parameters, α_i and β_i . Each α_i^c has the size of n by m and each β_i^c has the size of n by n , where m is the number of system

outputs and n is the number of system inputs.

Writing the controller in the discrete transfer function form,

$$\frac{y_c(k)}{u_c(k)} = \frac{\alpha_1^c z^{-1} + \alpha_2^c z^{-2} + \dots + \alpha_p^c z^{-p}}{1 - \beta_1^c z^{-1} - \beta_2^c z^{-2} - \dots - \beta_p^c z^{-p}} \quad (38)$$

the stability condition of the controller is as follows,

$$\max(\text{abs}(\text{roots}([1 \quad -\beta_1^c \quad -\beta_2^c \quad \dots \quad -\beta_p^c]))) < 1 \quad (39)$$

where the operator $\max(\cdot)$ is the maximum value of the given vector, the operator $\text{abs}(\cdot)$ means the magnitude of the given vector elements, and the operator $\text{roots}(\cdot)$ is the roots of the given polynomial coefficient vector.

For a multiple input system, each β_i^c ($i = 1, \dots, p$) is n by n matrix, where n is the number of system input. In such a case, stability is checked for each element of β_i^c 's. When all the polynomials satisfy the stability condition, the multi-input, multi-output controller is stable.

4. CHOICE OF THE PREDICTION HORIZON AND THE CONTROL HORIZON

In this section, two new normalized parameters are defined to express the effect of a greater prediction horizon and a shorter control horizon.

4.1. PREDICTION HORIZON PARAMETER, L_{hp}

To express the effect of a greater prediction horizon, the generalized predictive controller is derived in the following manner. For a given set of the identified system parameters, each coefficient matrix in Equation (27) and (28), is partitioned by the last row and the last column:

$$\mathbf{F} = \begin{bmatrix} \mathbf{F}_1 \\ \mathbf{F}_2 \end{bmatrix} \quad \mathbf{G} = \begin{bmatrix} \mathbf{G}_1 & \mathbf{0} \\ \mathbf{A}_{hp} & \alpha_0 \end{bmatrix} \quad \mathbf{H} = \begin{bmatrix} \mathbf{H}_1 \\ \mathbf{H}_2 \end{bmatrix} \quad \mathbf{J} = \begin{bmatrix} \mathbf{J}_1 & \mathbf{0} \\ \mathbf{B}_{hp} & \beta_0 \end{bmatrix} \quad (40)$$

where the coefficient matrices, \mathbf{F} , \mathbf{G} , \mathbf{H} , and \mathbf{J} , are for the prediction horizon, h_p , and the control horizon, $h_c = h_p$. The coefficient matrices with subscript 1, \mathbf{F}_1 , \mathbf{G}_1 , \mathbf{H}_1 , and \mathbf{J}_1 , correspond to a one-step shorter prediction horizon and control horizon, $h_p - 1$. The matrix \mathbf{G}_1 is the coefficient matrix of the future output when the prediction horizon is $h_p - 1$. Hence, the size of the square matrix \mathbf{G}_1 is $m(h_p - 1)$ by $m(h_p - 1)$. The matrix \mathbf{J}_1 is the coefficient matrix of the future input when the prediction horizon is $h_p - 1$, and its size is $n(h_p - 1)$ by $m(h_p - 1)$. Vectors \mathbf{A}_{hp} and \mathbf{F}_2 are generated from identified system output parameters, α_i , and vectors \mathbf{B}_{hp} and \mathbf{H}_2 are generated from identified system input parameters, β_i . For a larger prediction horizon than the identified system order, the extra row in matrices \mathbf{F} and \mathbf{H} , \mathbf{F}_2 and \mathbf{H}_2 , are zero vectors.

Since matrix G_1 is invertable and α_0 is a nonzero value, the following Matrix Inversion Lemma can be used to obtain the inverse of G ,

$$\begin{bmatrix} \mathbf{A} & \mathbf{0} \\ \mathbf{B} & \mathbf{C} \end{bmatrix}^{-1} = \begin{bmatrix} \mathbf{A}^{-1} & \mathbf{0} \\ -\mathbf{C}^{-1}\mathbf{B}\mathbf{A}^{-1} & \mathbf{C}^{-1} \end{bmatrix} \quad (41)$$

With $\alpha_0 = 1$ and $\beta_0 = 0$, the normalized coefficient matrix, \mathbf{T}_c , for the future input vector is obtained as

$$\mathbf{T}_c = \mathbf{G}^{-1}\mathbf{J} = \begin{bmatrix} \mathbf{T}_{c1} & \mathbf{0} \\ \mathbf{A}_{hp}\mathbf{T}_{c1} + \mathbf{B}_{hp} & \mathbf{0} \end{bmatrix} \quad (42)$$

where $\mathbf{T}_{c1} = \mathbf{G}_1^{-1}\mathbf{J}_1$, which is the normalized coefficient matrices for the future input when the prediction horizon is one-step short, $h_p - 1$.

Similarly, the normalized coefficient matrices for the past input and the past output can be obtained as

$$\mathbf{B}_c = \mathbf{G}^{-1}\mathbf{H} = \begin{bmatrix} \mathbf{B}_{c1} \\ -\mathbf{A}_{hp}\mathbf{B}_{c1} + \mathbf{H}_2 \end{bmatrix} \quad (43)$$

$$\mathbf{A}_c = \mathbf{G}^{-1}\mathbf{F} = \begin{bmatrix} -\mathbf{A}_{c1} \\ \mathbf{A}_{hp}\mathbf{A}_{c1} + \mathbf{F}_2 \end{bmatrix} \quad (44)$$

where $\mathbf{A}_{c1} = -\mathbf{G}_1^{-1}\mathbf{F}_1$ and $\mathbf{B}_{c1} = \mathbf{G}_1^{-1}\mathbf{H}_1$, which are the normalized coefficient matrices for the past output and the past input when the prediction horizon and the control horizon are $h_p - 1$, respectively.

Since $\mathbf{T}_c^T \mathbf{T}_c + \lambda \mathbf{I}$ is a block diagonal matrix, its inverse can be obtained easily,

$$(\mathbf{T}_c^T \mathbf{T}_c + \lambda \mathbf{I})^{-1} = \begin{bmatrix} \{\bullet\}^{-1} & \mathbf{0} \\ \mathbf{0} & \lambda^{-1} \end{bmatrix} \quad (45)$$

and

$$(\mathbf{T}_c^T \mathbf{T}_c + \lambda \mathbf{I})^{-1} \mathbf{T}_c^T = \begin{bmatrix} \{\bullet\}^{-1} \mathbf{T}_{c1}^T & \{\bullet\}^{-1} (-\mathbf{A}_{hp} \mathbf{T}_{c1} + \mathbf{B}_{hp})^T \\ \mathbf{0} & 0 \end{bmatrix} \quad (46)$$

where

$$\{\bullet\} = \mathbf{T}_{c1}^T \mathbf{T}_{c1} + (-\mathbf{A}_{hp} \mathbf{T}_{c1} + \mathbf{B}_{hp})^T (-\mathbf{A}_{hp} \mathbf{T}_{c1} + \mathbf{B}_{hp}) + \lambda \mathbf{I}_1 \quad (47)$$

and the size of the identity matrix, \mathbf{I}_1 , is the same as the size of the matrix \mathbf{G}_1 .

The generalized predictive control gain of the past input data is the first n rows of the following matrix, where n is the number of the system input.

$$\begin{aligned} & \left(\mathbf{T}_c^T \mathbf{T}_c + \lambda \mathbf{I} \right)^{-1} \mathbf{T}_c^T \mathbf{B}_c = \\ & \begin{bmatrix} \{\bullet\}^{-1} \mathbf{T}_{c1}^T \mathbf{B}_{c1} + \{\bullet\}^{-1} (-\mathbf{A}_{hp} \mathbf{T}_{c1} + \mathbf{B}_{hp})^T (-\mathbf{A}_{hp} \mathbf{B}_{c1} + \mathbf{H}_2) \\ 0 \end{bmatrix} \end{aligned} \quad (48)$$

Similarly, the gain of the past output data is the first n rows of the following matrix.

$$\begin{aligned} & \left(\mathbf{T}_c^T \mathbf{T}_c + \lambda \mathbf{I} \right)^{-1} \mathbf{T}_c^T \mathbf{A}_c = \\ & \begin{bmatrix} -\{\bullet\}^{-1} \mathbf{T}_{c1}^T \mathbf{A}_{c1} + \{\bullet\}^{-1} (-\mathbf{A}_{hp} \mathbf{T}_{c1} + \mathbf{B}_{hp})^T (\mathbf{A}_{hp} \mathbf{A}_{c1} + \mathbf{F}_2) \\ 0 \end{bmatrix} \end{aligned} \quad (49)$$

The term of $\left(\mathbf{T}_{c1}^T \mathbf{T}_{c1} + \lambda \mathbf{I}\right)^{-1} \mathbf{T}_{c1}^T \mathbf{B}_{c1}$ in Equation (48) and the term of $\left(\mathbf{T}_{c1}^T \mathbf{T}_{c1} + \lambda \mathbf{I}\right)^{-1} \mathbf{T}_{c1}^T \mathbf{A}_{c1}$ in Equation (49) are the control gains of the past input and output data for one-step short prediction horizon. All other terms in Equations (48) and (49) represent the effect of the extra prediction horizon.

There could be several ways to define the effect of the extra prediction horizon, but it can be seen that the term of $-\mathbf{A}_{hp} \mathbf{T}_{c1} + \mathbf{B}_{hp}$ is appeared in every extra term. With the fact that longer prediction horizon improves the response, the following parameter can be defined to represent the effect of extra prediction horizon.

$$L = \frac{1}{\text{trace}\left(\left(-\mathbf{A}_{hp} \mathbf{T}_{c1} + \mathbf{B}_{hp}\right)^T \left(-\mathbf{A}_{hp} \mathbf{T}_{c1} + \mathbf{B}_{hp}\right)\right)} \quad (50)$$

In addition, the parameter, L , can be normalized by the parameter value, L , when the prediction horizon is set to be the identified system order, p . Writing the parameter value, L when the prediction horizon is set to be the identified system order, p , as L_p , the normalized parameter value, L_{hp} , can be written as

$$L_{hp} = \frac{L}{L_p} = \frac{\text{trace}\left(\left(-\mathbf{A}_{hp} \mathbf{T}_{c1} + \mathbf{B}_{hp}\right)^T \left(-\mathbf{A}_{hp} \mathbf{T}_{c1} + \mathbf{B}_{hp}\right)\right)\big|_{hp=p}}{\text{trace}\left(\left(-\mathbf{A}_{hp} \mathbf{T}_{c1} + \mathbf{B}_{hp}\right)^T \left(-\mathbf{A}_{hp} \mathbf{T}_{c1} + \mathbf{B}_{hp}\right)\right)} \quad (51)$$

The parameter L_{hp} has the following properties:

1. L_{hp} is a positive number.
2. When $L_{hp} \geq 1$, the prediction horizon is smaller than the identified system order. When $L_{hp} \leq 1$, the prediction horizon is larger than the identified system order. The prediction horizon parameter, L_{hp} , is equal to 1 when the prediction horizon is set to be the identified system order, p .

3. For infinite prediction horizon and control horizon, L_{hp} goes to zero.
4. A smaller value of L_{hp} corresponds to a larger prediction horizon.
5. The parameter is independent of the input weighting factor, λ .

Longer calculation time is required to design a controller with a smaller value of the prediction horizon parameter, L_{hp} , because the prediction horizon increases, which determines the size of the coefficient matrices.

When the normalized parameter is chosen such that $L_{hp} \leq 1$, the computational step to obtain the corresponding prediction horizon can be summarized as follows:

- 1) For $h_p = h_c = p$, where p is the identified system order, generate a matrix \mathbf{G}_1 and a vector \mathbf{A}_{hp} using identified system output parameters, α_i , ($i = 1, \dots, p$), and a matrix \mathbf{J}_1 and a vector \mathbf{B}_{hp} using identified system input parameters, β_i , ($i = 1, \dots, p$).
- 2) Calculate the parameter value of L , and set as L_p .
- 3) Set the new matrix \mathbf{J}_1 to be the matrix \mathbf{J} of the previous step, and the new matrix \mathbf{G}_1 to be the matrix \mathbf{G} of the previous step. The size of square matrices, \mathbf{G} and \mathbf{J} , increase as the prediction horizon increases. Since the prediction horizon is larger than the identified system order, the vectors of \mathbf{A}_{hp} and \mathbf{B}_{hp} can be obtained by adding zeros in the front.
- 4) Calculate the parameter value of L , given in Equation (50), and the prediction horizon parameter value, L_{hp} , given in Equation (51) with the parameter value obtained in step 2.
- 5) Repeat step 3 and 4 until the normalized parameter value, L_{hp} , is close to the chosen value.

4.2. CONTROL HORIZON PARAMETER, L_{hc}

Assuming the prediction horizon, \hat{h}_p , is obtained from the chosen value of L_{hp} , the shorter control horizon than prediction horizon can be defined. The effect of the shorter control horizon can be expressed by partitioning matrix \mathbf{J} in Equation (28) as follows:

$$\mathbf{J} = [\mathbf{J}_3 \quad \mathbf{J}_4] \quad (52)$$

where \mathbf{J} is the coefficient matrix when control horizon is $h_c = \hat{h}_p$. A matrix with subscript 3 corresponds the coefficient matrices when the control horizon is $\hat{h}_p - 1$. As mentioned before, the shorter control horizon affects only to the coefficient matrix \mathbf{J} . Hence, coefficient matrices \mathbf{F} , \mathbf{G} , and \mathbf{H} remain the same for the shorter control horizon. As control horizon decreases, the column of matrix \mathbf{J}_3 decreases but the row of matrix \mathbf{J}_3 remains the same.

The normalized coefficient matrix of the future output, \mathbf{T}_c , is obtained as

$$\mathbf{T}_c = \mathbf{G}^{-1}\mathbf{J} = [\mathbf{T}_{c3} \quad \mathbf{T}_{c4}] \quad (53)$$

where $\mathbf{T}_{c3} = \mathbf{G}^{-1}\mathbf{J}_3$, which is the normalized coefficient matrices for the future input when the control horizon is $\hat{h}_p - 1$, and $\mathbf{T}_{c4} = \mathbf{G}^{-1}\mathbf{J}_4$.

The matrix, $\mathbf{T}_c^T\mathbf{T}_c + \lambda\mathbf{I}$ can be written as,

$$\mathbf{T}_c^T\mathbf{T}_c + \lambda\mathbf{I} = \begin{bmatrix} \mathbf{T}_{c3}^T\mathbf{T}_{c3} + \lambda\mathbf{I}_3 & \mathbf{T}_{c3}^T\mathbf{T}_{c4} \\ \mathbf{T}_{c4}^T\mathbf{T}_{c3} & \mathbf{T}_{c4}^T\mathbf{T}_{c4} + \lambda\mathbf{I}_4 \end{bmatrix} \quad (54)$$

where matrices \mathbf{I}_3 and \mathbf{I}_4 are identity matrices.

From the properties of the normalized coefficient matrices, $\mathbf{T}_{c3} + \lambda\mathbf{I}_3$ is invertable. The matrix $\mathbf{T}_{c4} + \lambda\mathbf{I}_4$ is also invertable except when $h_c = \hat{h}_p$ (because $\beta_0 = 0$).

When $h_c < \hat{h}_p$, the following Matrix Inversion Lemma can be applied to obtain the inverse of the matrix, $\mathbf{T}_c^T \mathbf{T}_c + \lambda \mathbf{I}$, given in Equation (54),

$$\begin{bmatrix} \mathbf{A} & \mathbf{B}^T \\ \mathbf{B} & \mathbf{C} \end{bmatrix}^{-1} = \begin{bmatrix} \mathbf{K} & -\mathbf{K}\mathbf{B}^T\mathbf{C}^{-1} \\ -\mathbf{C}^{-1}\mathbf{B}\mathbf{K} & \mathbf{C}^{-1} + \mathbf{C}^{-1}\mathbf{B}\mathbf{K}\mathbf{B}^T\mathbf{C}^{-1} \end{bmatrix} \quad (55)$$

where $\mathbf{K} = (\mathbf{A} - \mathbf{B}^T\mathbf{C}^{-1}\mathbf{B})^{-1}$.

Using Matrix Inversion Lemma, given in Equation (55),

$$(\mathbf{T}_c^T \mathbf{T}_c + \lambda \mathbf{I})^{-1} = \begin{bmatrix} \mathbf{T}_{c11} & \mathbf{T}_{c12} \\ \mathbf{T}_{c21} & \mathbf{T}_{c22} \end{bmatrix} \quad (56)$$

where

$$\begin{aligned} \mathbf{T}_{c11} &= \mathbf{M} \\ \mathbf{T}_{c12} &= -\mathbf{M}\mathbf{T}_{c3}^T \mathbf{T}_{c4} (\mathbf{T}_{c4}^T \mathbf{T}_{c4} + \lambda \mathbf{I}_4)^{-1} \\ \mathbf{T}_{c21} &= -(\mathbf{T}_{c4}^T \mathbf{T}_{c4} + \lambda \mathbf{I}_4)^{-1} \mathbf{T}_{c4}^T \mathbf{T}_{c3} \mathbf{M} \\ \mathbf{T}_{c22} &= (\mathbf{T}_{c4}^T \mathbf{T}_{c4} + \lambda \mathbf{I}_4)^{-1} + \\ &\quad (\mathbf{T}_{c4}^T \mathbf{T}_{c4} + \lambda \mathbf{I}_4)^{-1} \mathbf{T}_{c4}^T \mathbf{T}_{c3} \mathbf{M} \mathbf{T}_{c3}^T \mathbf{T}_{c4} (\mathbf{T}_{c4}^T \mathbf{T}_{c4} + \lambda \mathbf{I}_4)^{-1} \end{aligned} \quad (57)$$

and

$$\mathbf{M} = \left((\mathbf{T}_{c3}^T \mathbf{T}_{c3} + \lambda \mathbf{I}_3) - \mathbf{T}_{c3}^T \mathbf{T}_{c4} (\mathbf{T}_{c4}^T \mathbf{T}_{c4} + \lambda \mathbf{I}_4)^{-1} \mathbf{T}_{c4}^T \mathbf{T}_{c3} \right)^{-1}. \quad (58)$$

The generalized predictive control gains of the past input data and the past output data are the first n rows of the following matrices, where n is the number of system input,

$$\left(\mathbf{T}_c^T \mathbf{T}_c + \lambda \mathbf{I} \right)^{-1} \mathbf{T}_c^T \mathbf{B}_{c3} = \begin{bmatrix} \{\mathbf{T}_{c11} \mathbf{T}_{c3}^T + \mathbf{T}_{c12} \mathbf{T}_{c4}^T\} \mathbf{B}_{c3} \\ \{\mathbf{T}_{c21} \mathbf{T}_{c3}^T + \mathbf{T}_{c22} \mathbf{T}_{c4}^T\} \mathbf{B}_{c3} \end{bmatrix} \quad (59)$$

and

$$\left(\mathbf{T}_c^T \mathbf{T}_c + \lambda \mathbf{I} \right)^{-1} \mathbf{T}_c^T \mathbf{A}_{c3} = \begin{bmatrix} \{\mathbf{T}_{c11} \mathbf{T}_{c3}^T + \mathbf{T}_{c12} \mathbf{T}_{c4}^T\} \mathbf{A}_{c3} \\ \{\mathbf{T}_{c21} \mathbf{T}_{c3}^T + \mathbf{T}_{c22} \mathbf{T}_{c4}^T\} \mathbf{A}_{c3} \end{bmatrix} \quad (60)$$

where $\mathbf{A}_{c3} = -\mathbf{G}^{-1}\mathbf{F}$ and $\mathbf{B}_{c3} = \mathbf{G}^{-1}\mathbf{H}$ are the normalized coefficient matrices for the past output and the past input, respectively.

In Equation (59), all terms except the term of $(\mathbf{T}_{c3}^T \mathbf{T}_{c3} + \lambda \mathbf{I}_3)^{-1} \mathbf{T}_{c3} \mathbf{B}_{c3}$ represents the effect of the extra control horizon. Similarly, in Equation (60), all terms except the term of $(\mathbf{T}_{c3}^T \mathbf{T}_{c3} + \lambda \mathbf{I}_3)^{-1} \mathbf{T}_{c3} \mathbf{A}_{c3}$ represent the effect of the extra control horizon. Among all extra terms, the term of $\mathbf{T}_{c4}(\mathbf{T}_{c4}^T \mathbf{T}_{c4} + \lambda \mathbf{I}_4)^{-1} \mathbf{T}_{c4}^T$ exists in every term. With the fact that the shorter control horizon improves system response, the following parameter can be defined to represent the effect of the shorter control horizon.

$$L_{hc} = \frac{1}{\text{trace}(\mathbf{S}^T \mathbf{S})} \quad (61)$$

where

$$\mathbf{S} = \mathbf{T}_{c4}(\mathbf{T}_{c4}^T \mathbf{T}_{c4} + \epsilon \mathbf{I}_4)^{-1} \mathbf{T}_{c4}^T \quad (62)$$

Note that λ is replaced by ϵ , which is a very small positive number. With a very small positive number, ϵ , the control horizon parameter, L_{hc} , becomes 1 when $h_c = \hat{h}_p - 1$. When $h_c = \hat{h}_p$, the matrix, \mathbf{T}_{c4} , becomes zero matrix because $\beta_0 = 0$, and the parameter, L_{hc} , becomes infinity.

Hence, the control horizon parameter, L_{hc} , has the following properties:

1. L_{hc} is a positive number.
2. When control horizon is equal to prediction horizon, $h_c = \hat{h}_p$, the parameter, L_{hc} , becomes infinity. When control horizon is less than the prediction horizon, $L_{hc} \leq 1$ ($L_{hc} = 1$ when $h_c = \hat{h}_p - 1$).
3. A smaller value of L_{hc} corresponds to a shorter control horizon.

The computational step to obtain the corresponding control horizon for a chosen L_{hc} can be summarized as follows:

- 1) For $h_p = h_c = \hat{h}_p$, where \hat{h}_p is the prediction horizon that corresponds to

the chosen value of L_{hp} , generate coefficient matrices \mathbf{G} and \mathbf{J} .

2) Partition \mathbf{J} as in equation (52). The column of matrix \mathbf{J}_4 increases as the control horizon decreases, but the row of \mathbf{J}_4 remains the same.

3) Calculate the parameter value of L_{hc} , using Equation (61).

4) Repeat step 2 and 3 until the normalized parameter value, L_{hc} , is close to the chosen value.

4.3. EXAMPLES

4.3.1. Example 1: Simple Mass-Spring-Damper System

In this section, the following two simple systems are considered:

$$\begin{aligned} \text{System 1: } y(t) - 1.611y(t-1) + 0.991y(t-2) = \\ 1.701 \times 10^{-8}u(t-1) + 1.693 \times 10^{-8}u(t-2) \end{aligned} \quad (63)$$

$$\begin{aligned} \text{System 2: } y(t) - 1.549y(t-1) + 0.915y(t-2) = \\ 2.348 \times 10^{-8}u(t-1) + 2.279 \times 10^{-8}u(t-2) \end{aligned} \quad (64)$$

Both systems have the sampling rate of 1 kHz. System 1, given in Equation (63), is the 2nd order identified model of a mass-spring-damper system, which mass is 10 kg, natural frequency is 100 Hz, and damping ratio is 0.0707. System 2, given in Equation (64), is the 2nd order identified model of the same system as system 1 but different damping ratio of 0.707. So, system 1 is the lightly damped system and system 2 is the heavily damped system.

Using the coefficients of each system, the prediction horizon parameters, L_{hp} , are calculated for the prediction horizon from $h_p = p = 2$ to $h_p = 100$, and plotted in Figure 1 (a). In Figure 1 (b), the control horizon parameters are plotted from $h_c = 2$ to $h_c = \hat{h}_c = 40$.

As seen in Figure 1, the prediction horizon parameter for the lightly-damped system (system 1) varies from 0.02 to 1.0, but the prediction horizon parameter for the heavily-damped system (system 2) varies from 0.12 to 1. This is because the lightly damped system is relatively easy to control compared to the heavily damped system.

4.3.2. Example 2: Identified Beam Model

To illustrate the prediction horizon parameters, L_{hp} , and the control horizon parameter, L_{hc} , the identified system of the cantilevered beam model is used. The nonrecursively identified system with the order of $p = 16$ and sampling rate of 250 Hz is expressed as

$$A(1)y(t) + \cdots + A(p+1)y(t-p) = B(1)u(t) + \cdots + B(p+1)u(t-p) \quad (65)$$

where the output coefficient vector, \mathbf{A} , and the input coefficient vector, \mathbf{B} , are identified system parameters, obtained as:

$$\mathbf{A} = [1, -0.0443, -0.0232, -0.0856, 0.1898, -0.0223, -0.1500, -0.0157, -0.2728, -0.1018, 0.1246, -0.0611, 0.1652, 0.0380, -0.2291, -0.0467, -0.1759]$$

$$\mathbf{B} = [0, -0.0052, -0.0157, 0.0263, -0.0076, 0.0070, 0.0210, -0.0390, 0.0032, 0.0021, -0.0154, 0.0266, -0.0004, -0.0035, 0.0067, -0.0135, 0.0015]$$

Calculating the prediction horizon parameter, $L_{hp} = 50\%$, and the control horizon parameter, $L_{hc} = 25\%$, the prediction horizon is obtained as $\hat{h}_p = 32$ and the control horizon is obtained as $h_c = 26$.

To show the changes of the prediction horizon parameter, L_{hp} , each value for the prediction horizon from $h_p = p$ to $h_p = 7p$ is calculated and plotted

in Figure 2. In Figure 2(a), $L_{hp} = 50\%$ is marked. As a reference, the generalized predictive controller is designed for each prediction horizon value with input weighting factor $\lambda = 0.1$, and the closed-loop system is obtained. The $H(t)_{cl}/H(t)_{ol}$, where $H(t)$ is 2-norm of the impulse response, is calculated and plotted in Figure 2(b). As seen in Figure 2(a) and 2(b), as the value of L_{hp} is decreased, the prediction horizon becomes longer and the $H(t)_{cl}/H(t)_{ol}$ becomes smaller.

Similarly, the control horizon parameter, L_{hc} , for each value for the control horizon from $h_c = 2$ to $h_c = \hat{h}_p$, is calculated and plotted in Figure 3(a). The closed-loop impulse response with input weighting factor $\lambda = 0.1$ is calculated and its $H(t)_{cl}/H(t)_{ol}$ is plotted in Figure 3(b).

As observed in Figure 2, as the prediction horizon increases, the system response is improving. But, as mentioned before, the larger prediction horizon requires longer computational time in the controller design. As seen in Figure 3, the shorter control horizon improves the system response. Hence, the generalized predictive controller will be more aggressive as the prediction horizon becomes longer and the control horizon becomes shorter.

5. RECURSIVE GENERALIZED PREDICTIVE CONTROL

The recursive generalized predictive feedback controller can be obtained by designing the generalized predictive feedback controller using the updated system parameters obtained by the recursive system identification algorithm. In the process of the recursive system identification, the system order must be chosen. The identified system order will be the order of the generalized predictive controller. In the process of the generalized predictive controller de-

sign, the following control parameters must be chosen properly: the prediction horizon, the control horizon, and the input weighting factor. The prediction horizon and the control horizon are the finite horizons of the system output and control input predictions. Choosing a prediction horizon and a control horizon, the smaller values of the prediction horizon parameter and the control horizon parameter will improve the system performance, but the following effects should be considered.

1. The smaller prediction horizon parameter, L_{hp} , requires longer sampling time for the control design process.
2. The smaller control horizon parameter, L_{hc} , requires a larger magnitude of the control input.

In the following sections, a dual-sampling-rate and a time varying input weighting factor are introduced to design higher order controllers and aggressive controllers. A stability test algorithm is added to avoid implementation of unstable controllers.

5.1. DUAL-SAMPLING-RATE ALGORITHM

When the recursive generalized predictive controller is applied to a real experimental setup, a dual-sampling-rate algorithm can be applied to design a higher-order controller. First, the recursive system identification can be applied with the same sampling rate as the data acquisition since it updates the system parameters using matrix summations and multiplications without any time consuming process such as matrix inversion. Second, assuming that the system parameters do not change significantly, which can be controlled by the initial conditions of the recursive system identification algorithm, a slower sampling rate than the data acquisition sampling rate can be used for

controller design, because matrix inversion must be performed twice during the control design, (see Equations (32) and (36)). The controller is fixed until a new controller is computed and updated. Third, the control input can be calculated with the measured and stored input and output data using the same sampling rate as that used for the data acquisition. Graphical implementation for dual-sampling-rate algorithm is shown in Figure 4.

5.2. TIME VARYING INPUT WEIGHTING FACTOR

A time varying input weighting factor algorithm is applied to solve the following problems. As detailed earlier, a zero value of the input weighting factor will result in an unstable controller. When a small positive constant value of the input weighting factor is chosen in the controller design, the controller also can create an instability since the matrix, \mathbf{T}_c in Equation (32), is close to singular. Second, even if the controller is stable, when applied to a real experimental setup, it may result in a large magnitude of initial control input, which may cause an overload in the experimental hardware. Third, a large constant value of the input weighting factor may reduce the magnitude of the initial control input, but limits performance.

To avoid those problems, a time varying input weighting factor is added to the controller design,

$$\lambda_{new} = \lambda_{old} \pm \tau \quad (66)$$

where λ_{new} is the updated input weighting factor from the previous input weighting factor, λ_{old} . The value of τ is added or subtracted, depending on the stability of the controller. The negative sign is applied for stable controllers and the positive sign is applied for unstable controllers. The different values,

τ , for stable controllers and unstable controllers can be assigned,

$$\lambda_{new} = \begin{cases} \lambda_{old} - \tau_1 & \text{for stable controller} \\ \lambda_{old} + \tau_2 & \text{for unstable controller} \end{cases} \quad (67)$$

where τ_1 is the decrement of the input weighting factor when controllers are stable and τ_2 is increment of the input weighting factor when controllers are unstable.

By assigning a large initial value of the input weighting factor, a large magnitude of the initial control input can be avoided. Once the controller is designed and applied to the system, the input weighting factor will be updated based on the stability of the controller. The value will be reduced for a stable controller and increased for an unstable controller until a stable controller is obtained. Graphical implementation for time varying input weighting factor algorithm is shown in Figure 4.

The value of τ in Equation (66) or τ_1 and τ_2 in Equation (67) can be scaled with respect to the input weighting factor. For example, when the input weighting factor is 0.01, the proper size of τ is 0.001, an order of magnitude less. When controllers are to be updated faster in case of instability, a larger value of τ_2 than τ_1 can be assigned.

To apply the time varying input weighting factor to the system, the following process should be added in the controller design. When the value of λ approaches a very small number, λ_{min} , the decrement should be zero because the input weighting factor is a positive real number. By adding this process, a zero or negative value of the input weighting factor can be avoided. Second, since the weighting factor is updated after the stability test, application of unstable controllers must be avoided. If unstable controller results upon checking for stability, the previous stable controller is implemented instead. By adding

this process in the controller design, only stable controllers are applied to the system.

6. EXPERIMENTAL RESULTS

The recursive generalized predictive feedback control algorithm is applied to three different testbeds: a cantilevered beam, a sound enclosure, and an optical jitter suppression testbed. The recursive generalized predictive feedback control algorithm was implemented using a National Instrument PCI-6024E data acquisition board. The interface between the computer and the board are performed using MATLAB, Simulink, and xPC target.

6.1. CANTILEVERED BEAM

The structural system to be regulated is shown in Figure 5. The control input and the disturbance input are applied to the structure through the piezoelectric device mounted on the beam. The sensor output is the signal from PCB Model 352C67 accelerometer. Ithaco 24dB/octave low pass filters, set at a frequency of 125 Hz, and Krohn-Hite Model 7600 wideband amplifiers, set at a gain of 14 dB, are used for the piezoelectric actuator. Ithaco 24dB/octave low pass filter, set at 125 Hz, and PCB model 480E09 signal conditioner is used for each accelerometer signal. The sampling rate is set as 250 Hz.

Keeping a single control input and a single disturbance input, two different output configurations are chosen. One configuration is a single sensor output and a single performance output. The other configuration is based upon two sensor outputs and a performance output. Figure 6 and 7 show the experimental results of the first output configuration: one sensor output and one performance output. Figure 6 shows the estimation of the frequency response

magnitude corresponding to the identified system from disturbance input to the sensor output. The dashed line is the open-loop estimation and the solid line is the closed-loop estimation. The mode at 32.6 Hz is reduced 21.8 dB and the mode at 90.0 Hz is reduced 19.7 dB. Figure 7 shows the estimation of the frequency response magnitude corresponding to the identified system from the disturbance input to the performance output. Using the recursive generalized predictive feedback controller, the mode at 32.6 Hz is reduced 22.1 dB and the mode at 90.0 Hz is reduced 19.4 dB. The order of the identified system and the controller is chosen to be 18 and the prediction horizon and the control horizon are chosen to be the same value of 18,. The output signals are acquired with a sampling rate of 250 Hz and the recursive generalized predictive controller is updated 2 times slower than the data acquisition, i.e., 125 Hz.

Figure 8, 9, and 10 show the experimental results of the second output configuration: two sensor outputs and one performance output. Figure 8 shows the estimation of the frequency response magnitude corresponding to the identified system from disturbance input to the first sensor output. The dashed line is the open-loop estimation and the solid line is the closed-loop estimation. The mode at 32.6 Hz is reduced 24.5 dB and the mode at 90.0 Hz is reduced 26.1 dB. Figure 9 shows the estimation of the frequency response magnitude corresponding to the identified system from disturbance input to the second sensor output. The mode at 32.6 Hz is reduced 21.5 dB and the mode at 90.0 Hz is reduced 22.6 dB. Figure 10 shows the estimation of the frequency response magnitude corresponding to the identified system from disturbance input to the performance output. Using the recursive generalized

predictive feedback controller, the mode at 32.6 Hz is reduced 21.20 dB and the mode at 90.0 Hz is reduced 23.3 dB. The order of the identified system and the controller is chosen to be 18 and the prediction horizon and the control horizon are chosen to be the same value of 18. The output signals are acquired with sampling rate of 250 Hz and the recursive generalized predictive feedback controller is updated 2 times slower than the data acquisition, i.e., 125 Hz.

6.2. SOUND ENCLOSURE

The plant to be regulated is shown in Figure 11. The sound enclosure is configured with two DYNAUDIO 15 W-75 acoustic loudspeakers and a Brüel & Kjær type 4190 microphone. One of the speakers is used for the control source and the other speaker is used for the primary disturbance. A microphone is used as the error sensor. Ithaco 24dB/octave low pass filters, set at a frequency of 250 Hz, are applied to the control input. A Brüel & Kjær type 2635 amplifier and another Ithaco 24dB/octave low pass filter, set at 250 Hz, are used for the error sensor. The sampling rate is set at 500 Hz.

For the closed-closed sound enclosure illustrated in Figure 11, recursive generalized predictive feedback control is applied. The open-loop and closed-loop frequency response estimation are computed, and the magnitude response of each system is presented in Figure 12. The dashed line is the open-loop response and the solid line is the closed-loop response. The mode at 54 Hz, 106 Hz, 155 Hz, and 205 Hz are reduced 9.0 dB, 5.8 dB, 6.3 dB and 13.2 dB, respectively. The integrated response of the sound enclosure is attenuated by approximately 2.1 dB at resonant frequencies between 50 Hz and 250 Hz, with no observed increase in response outside of this bandwidth. The order of the identified system and controller is chosen to be 16. The prediction horizon

is chosen to be 24 and the control horizon is chosen to be 12. The recursive generalized predictive feedback controller is updated 4 times slower than the data acquisition, i.e., 125 Hz.

While feedback controller for the closed-closed sound enclosure is running, the cover on the control speaker side is opened manually to yield the open-closed sound enclosure configuration. The open-loop and closed-loop frequency response estimation are computed, and the magnitude response of each system is presented in Figure 13. The dashed line is the open-loop response and the solid line is the closed-loop response. The mode at 78 Hz, 128 Hz, 177 Hz, and 227 Hz are reduced 4.7 dB, 7.4 dB, 7.5 dB and 5.9 dB, respectively. The integrated response of the sound enclosure is attenuated by approximately 2.2 dB at resonant frequencies between 50 Hz and 250 Hz, with no observed increase in response outside of the bandwidth.

6.3. OPTICAL JITTER SUPPRESSION TESTBED

The plant to be regulated is shown in Figure 14. The experiment is performed with the optical jitter suppression testbed built in an anechoic chamber at Duke University. Two optical benches are used to isolate metrology components from vibrating optical elements. A Helium-Neon laser and a position sensor are mounted on one optical bench and a turning flat mirror and a 3-axis fast steering mirror are on the other optical bench. External acoustic disturbances from speakers are used to generate vibration in the optical components. The fast steering mirror is the allowable control actuator and the optical position sensor is the allowable error sensor in the experiment.

Ithaco 24dB/octave filters, set at a frequency of 250 Hz, are used for anti-aliasing and 10 \times amplification of the position sensing detector (PSD)

signal. An additional Ithaco highpass filter, set at 10 Hz, is used to remove the DC offset in the PSD signal to prevent the static position of the laser from saturating the ± 10 V A/D channels on the DSP board. An amplifier is used to generate the disturbance signals. The sampling rate is set as 600 Hz.

Figures 15 and 16 shows the computed open-loop and closed-loop auto-spectrum of vertical position signal from position sensing detector (PSD). The dashed line is the open-loop response and the solid line is the closed-loop response. Figure 15 is when one disturbance source, which is placed behind the optical bench, is used, and Figure 16 is when all three disturbance sources are used. When one disturbance source is used, a reduction of 15.6 dB is obtained between 30 Hz and 300 Hz. When all three disturbance sources are used, a reduction of 11.9 dB is obtained between 30 Hz and 300 Hz. The order of the identified system and controller is chosen to be 16. The prediction horizon is chosen to be 32 and the control horizon is chosen to be 4. The recursive generalized predictive feedback controller is updated 4 times slower than the data acquisition, i.e., 150 Hz.

7. SUMMARY AND CONCLUSION

The recursive generalized predictive control algorithm, combining the process of the recursive system identification algorithm and the process of the generalized predictive control design, has been developed. In the generalized predictive control design, there are three parameters to be determined: the prediction horizon, the control horizon, and the input weighting factor. By defining the prediction horizon parameter, L_{hp} , and the control horizon pa-

parameter, L_{hc} , the corresponding values of the prediction horizon, h_p , and the control horizon, h_c , can be obtained. A time varying input weighting factor algorithm allows the recursive generalized predictive controller to be designed aggressively. By adding a dual-sampling-rate algorithm between data acquisition and control design, higher-order controllers can be designed and applied to the system.

Experiments were performed for three different testbeds: a cantilevered beam, a sound enclosure, and an optical jitter suppression testbed. For each experiment, the estimation of the frequency response magnitude corresponding to the open-loop identified system and the closed-loop identified system was shown and compared. For a cantilevered beam, recursive generalized predictive feedback control algorithm is applied. Two different output configurations were chosen. For the single-output case, the mode at 32.6 Hz is reduced 21.8 dB and the mode at 90.0 Hz is reduced 19.4 dB. For the multiple-output case, the mode at 32.6 Hz is reduced 24.5 dB and the mode at 90.0 dB is reduced 26.1 dB for the first output. For the second output, the mode at 32.6 Hz is reduced 21.5 dB and the mode at 90.0 dB is reduced 22.6 dB. For a closed-closed sound enclosure, the integrated response is attenuated by approximately 2.1 dB at resonant frequencies between 50 Hz and 250 Hz using recursive generalized predictive feedback control design algorithm. While the feedback controller for closed-closed sound enclosure is running, the cover on the control speaker side is opened manually to yield the open-closed sound enclosure configuration. For a open-closed sound enclosure, the integrated response is attenuated by approximately 2.2 dB at resonant frequencies between 50 Hz and 250 Hz. For an optical jitter suppression testbed, a reduction of

15.6 dB is obtained between 30 Hz and 300 Hz using recursive generalized predictive feedback control with one disturbance source, and a reduction of 11.9 dB is obtained between 30 Hz and 300 Hz with three disturbance sources.

The advantages of the proposed recursive generalized predictive control algorithm are: no prior system information is required since the process of the system identification is performed recursively from real time system input and output data, and the controller is updated adaptively in the presence of a changing operating environment.

REFERENCES

1. D. W. Clarke, C. Mohtad, and P. S. Tuffs. Generalized predictive control - part I. the basic algorithm. *Automatica*, 23(2):137-148, 1987.
2. D. W. Clarke, C. Mohtad, and P. S. Tuffs. Generalized predictive control - part II. extensions and interpretations. *Automatica*, 23(2):149-160, 1987.
3. H. Demirciloglu and E. Karasu. Generalized predictive control. *IEEE Control Systems Magazine*, 20(5):36-47, 2000.
4. G. Favier and D. Dubois. A review of k-step-ahead predictors. *Automatica*, 26(1):75-84, January 1990.
5. J. Richalet, A. Rault, J. L. Testud, and J. Papon. Model predictive heuristic control: Applications to industrial processes. *Automatica*, 14:413-428, 1978.
6. C. R. Cutler and B. L. Ramaker. Dynamic matrix control: a computer control algorithm. *In Proceedings of Joint Automatic Control Conference*, 1980.
7. D. W. Clarke and C. Mohtadi. Properties of generalized predictive control. *Automatica*, 25(6):859-875, 1989.
8. R. R. Bitmead, M. Gevers, and V. Wertz. *Adaptive Optimal Control, The Thinking Man's GPC*. Prentice Hall, Englewood Cliffs, NJ., 1990.
9. J. Sheng, T. Chen, and S. Shah. On stability robustness of dual-rate generalized predictive control systems. *Proceedings of the American Control Conference*, 5:3415-3420, June 2001.
10. K. V. Ling and K. W. Lim. A state space GPC with extensions to multirate control. *Automatica*, 32(7):1067-1071, July 1996.
11. J.-N. Juang and M. Phan. Deadbeat predictive controllers. Technical Report TM-112862, NASA, May 1997.

12. G. Nunes, S. Kincal, and O. D. Crisalle. Stability analysis of multivariable predictive control - a polynomial approach (I). *Proceedings of the American Control Conference*, 3:2424-2429, June 2001.
13. A. W. Ordys and D. W. Clarke. A state-space description for GPC controllers. *International Journal of System and Science*, 24(9):1727-1744, 1993.
14. M. Q. Phan and J.-N. Juang. Predictive controllers for feedback stabilization. *Journal of Guidance, Control, and Dynamics*, 21(5):747-753, September-October 1998.
15. J.-N. Junag and K. W. Eure. Predictive feedback and feedforward control for systems with unknown disturbance. Technical Report TM-208744, NASA, December 1998.
16. H. Demircioglu and P. J. Gawthrop. Continuous-time generalized predictive control (CGPC). *Automatica*, 27(1):55-74, 1991.
17. P. O. M. Scokaert. Infinite horizon generalized predictive control. *International Journal of Control*, 66(1):161-175, 1997.
18. B. Kouvaritakis, J. A. Rossiter, and G. J. Ju. Robust stable generalized predictive control. *International Journal of Control*, 67(3):411-434, 1997.
19. C. Kambhampati, J. D. Mason, and K. Warwick. A stable one-step-ahead predictive control of non-linear systems. *Automatica*, 36(4):485-495, April 2000.
20. B. Kouvaritakis, M. Cannon, and J. A. Rossiter. Recent developments in generalized predictive control for continuous-time systems. *International Journal of Control*, 72(2):164-173, 1999.
21. E. Mosca, J. M. Lemos, and J. Zhang. Stabilising I/O receding-horizon control. *Proceedings of 29th IEEE Conference on Decision and Control*, 1990.
22. J. R. Gossner, B. Kouvaritakis, and J. A. Rossiter. Stable and generalized predictive control with constraints and bounded disturbances. *Automatica*, 33(4):551-568, 1997.
23. J. R. Gossner, B. Kouvaritakis, and J. A. Rossiter. Cautious stable predictive ncontrol: a guaranteed stable predictive control algorithm with low input activity and good robustness. *International Journal of Control*, 67(5):675-697, 1997.
24. K. W. Eure and J.-N. Juang. Broadband noise control using predictive techniques. Technical Report TM-110320, NASA, January 1997.
25. R. Ortega and G. Sanchez. Globally convergent multistep receding horizon adaptive control. *International Journal of Control*, 46:1655-1664, 1989.
26. W. Wang and R. Henriksen. Directive adaptive generalized predictive control. *Proceedings of the American Control Conference*, pages 2402-2406, 1992.
27. W. Wang. A direct adaptive generalized predictive control algorithm for mimo systems. *International Journal of Control*, 60(6):1371-1381, December 1994.
28. J. M. Martin-Sanchez and S. L. Shah. Multivariable adaptive predictive control of a binary distillation column. *Automatica*, 20(5):607-620, 1984.

29. D. W. Clarke. Application of generalized predictive control to industrial processes. *IEEE Control System Magazine*, 8:49–55, 1988.
30. P. Bendotti and M. M'Saad. A skid-to-run missile autopilot design: The generalized predictive adaptive control approach. *International Journal of Adaptive Control Signal Processing*, 7(2):13–31, 1993.
31. M. Mahfouf, D. A. Linkens, A. J. Asbury, W. M. Gray, and J. E. Peacock. Generalized predictive control in the operating theatre. *Proceedings of the Inst. Elect. Eng.*, 139(4):404–420, 1992.

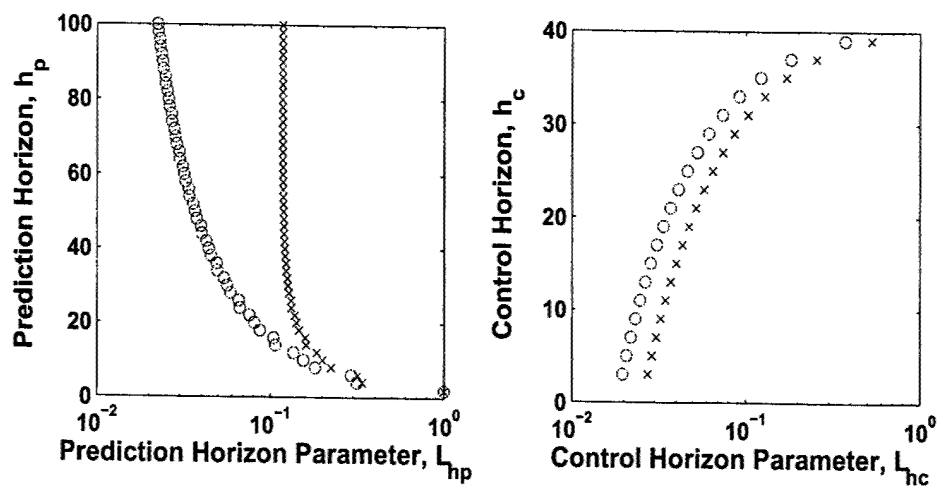


Figure 1. (a) The prediction horizon parameter, L_{hp} , (b) The control horizon parameter, L_{hc} ('o': System 1 – lightly damped system, 'x': System 2 – heavily damped system.)

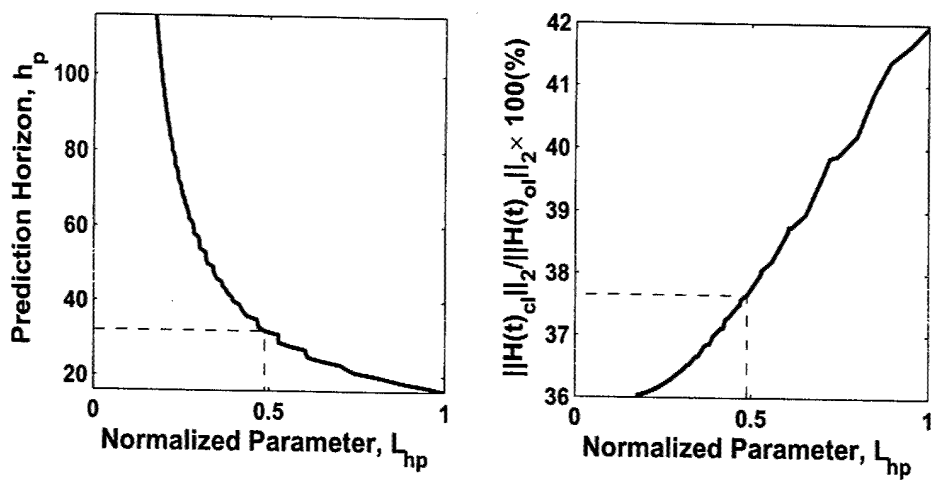


Figure 2. (a) The prediction horizon, h_p , as a function of the prediction horizon parameter, L_{hp} , (b) The H_2 -norm of the closed-loop impulse response normalized by the H_2 -norm of the open-loop impulse response as a function of the prediction horizon parameter, L_{hp} .

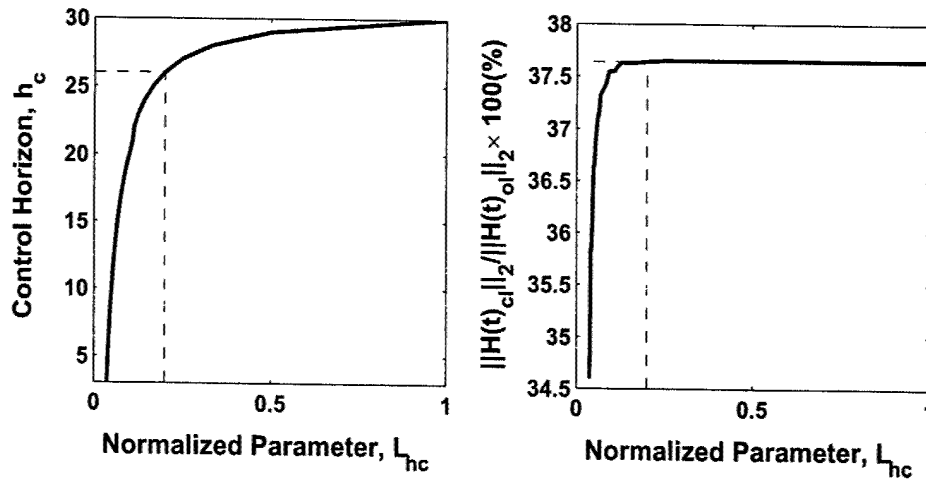


Figure 3. (a) The control horizon, h_c , as a function of the control horizon parameter, L_{hc} , (b) The H_2 -norm of the closed-loop impulse response normalized by the H_2 -norm of the open-loop impulse response as a function of the control horizon parameter, L_{hc} .

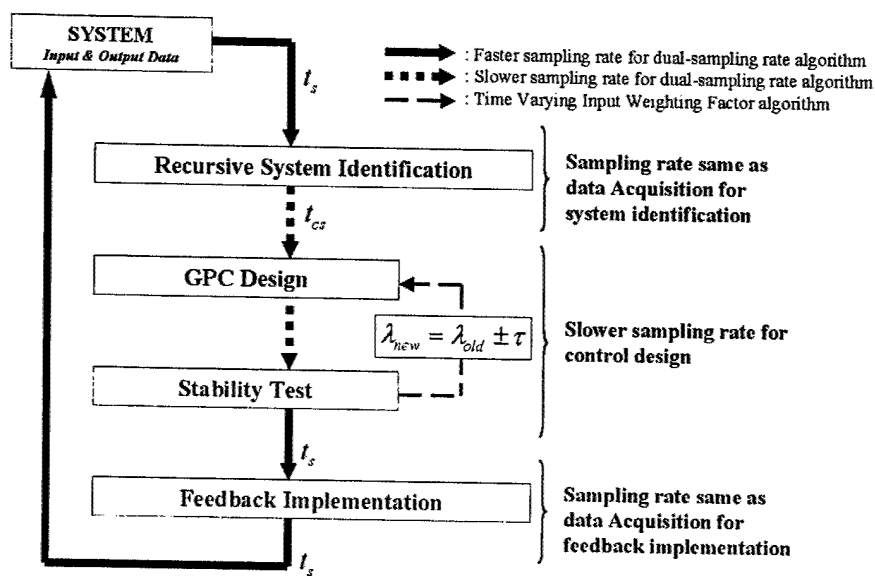


Figure 4. The generalized predictive control design process with dual-sampling-rate algorithm and time varying input weighting factor

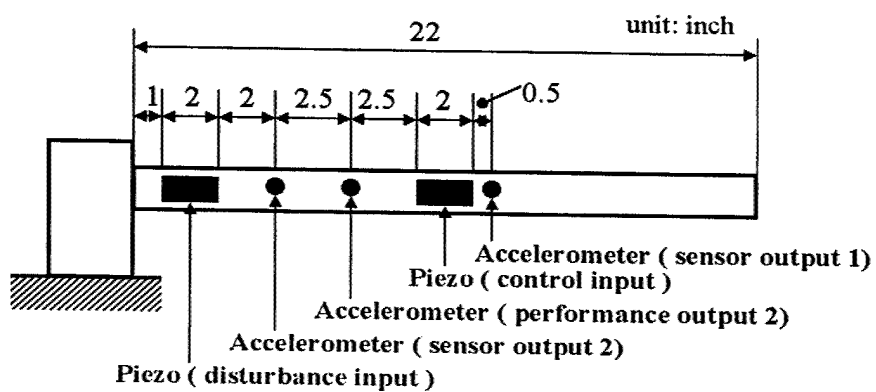


Figure 5. A cantilevered beam

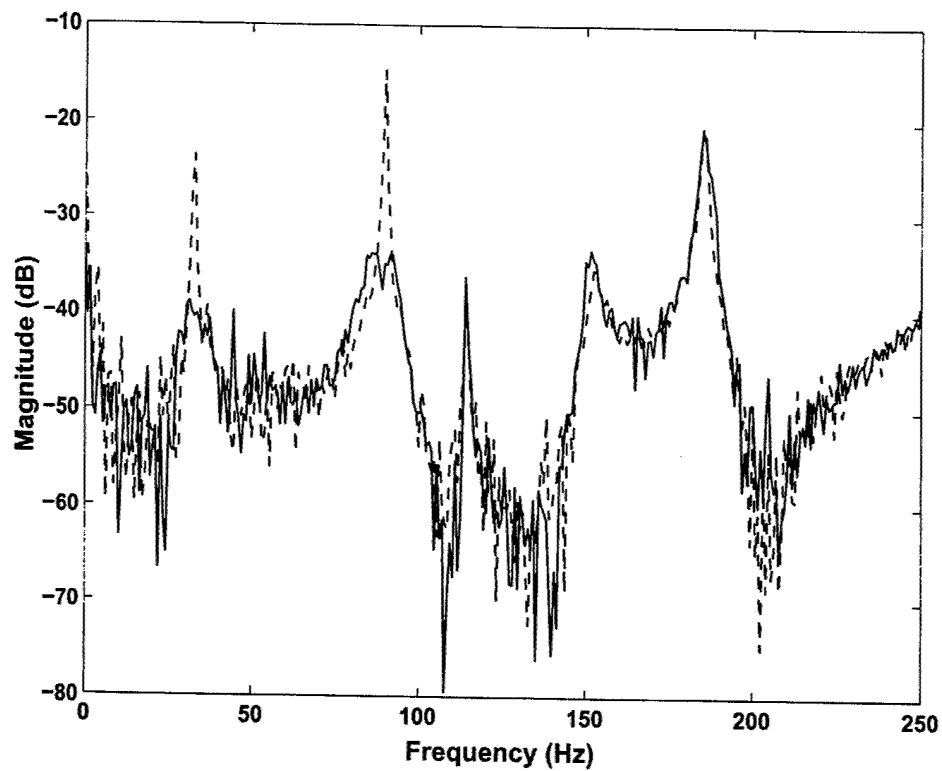


Figure 6. Comparison of computed open-loop (dashed line) and closed-loop (solid line) frequency response estimation between the disturbance input and the control sensor output of a cantilevered beam: magnitude of frequency response ($t_s = 250Hz$).

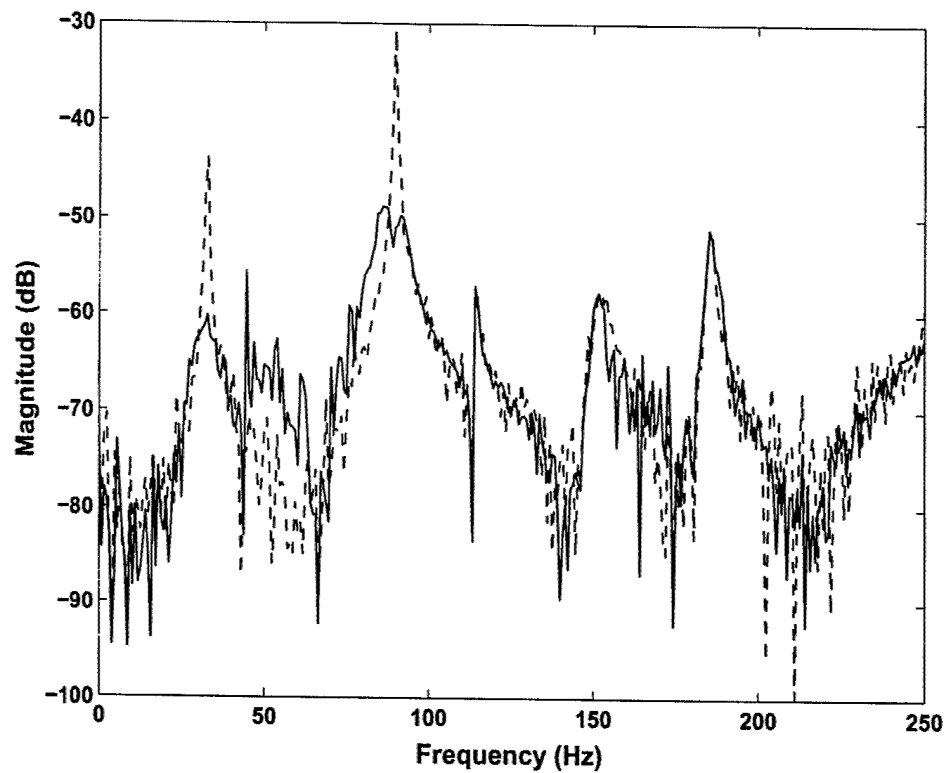


Figure 7. Comparison of computed open-loop (dashed line) and closed-loop (solid line) frequency response estimation between the disturbance input and the performance output of a cantilevered beam: magnitude of frequency response ($t_s = 250Hz$).

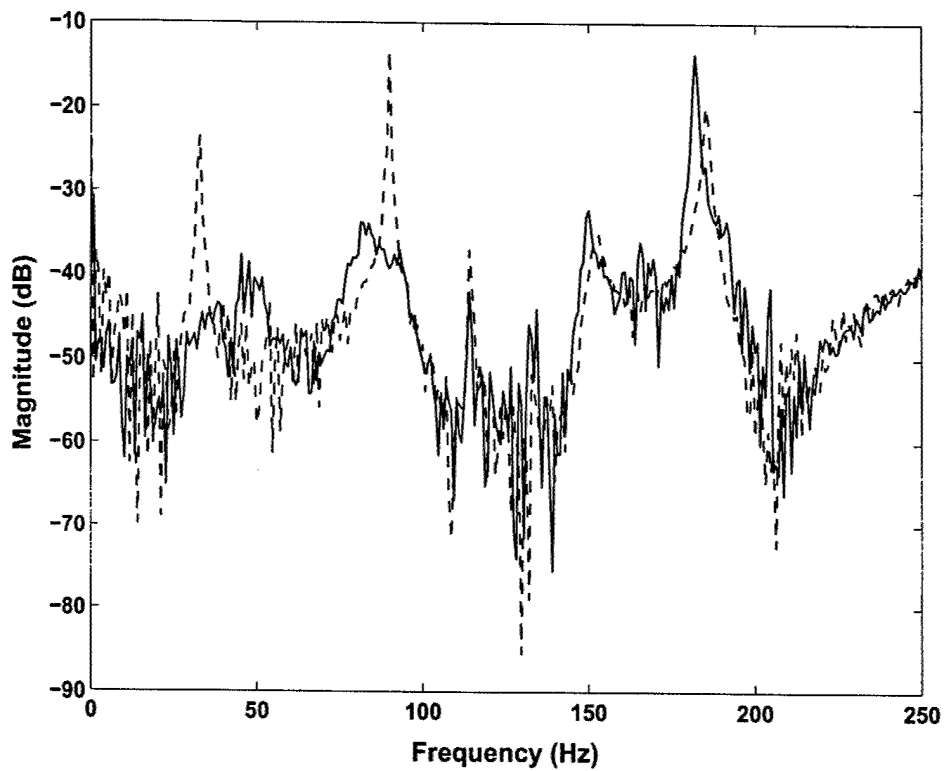


Figure 8. Comparison of computed open-loop (dashed line) and closed-loop (solid line) frequency response estimation between the disturbance input and the first sensor output of a cantilevered beam: magnitude of frequency response ($t_s = 250Hz$).

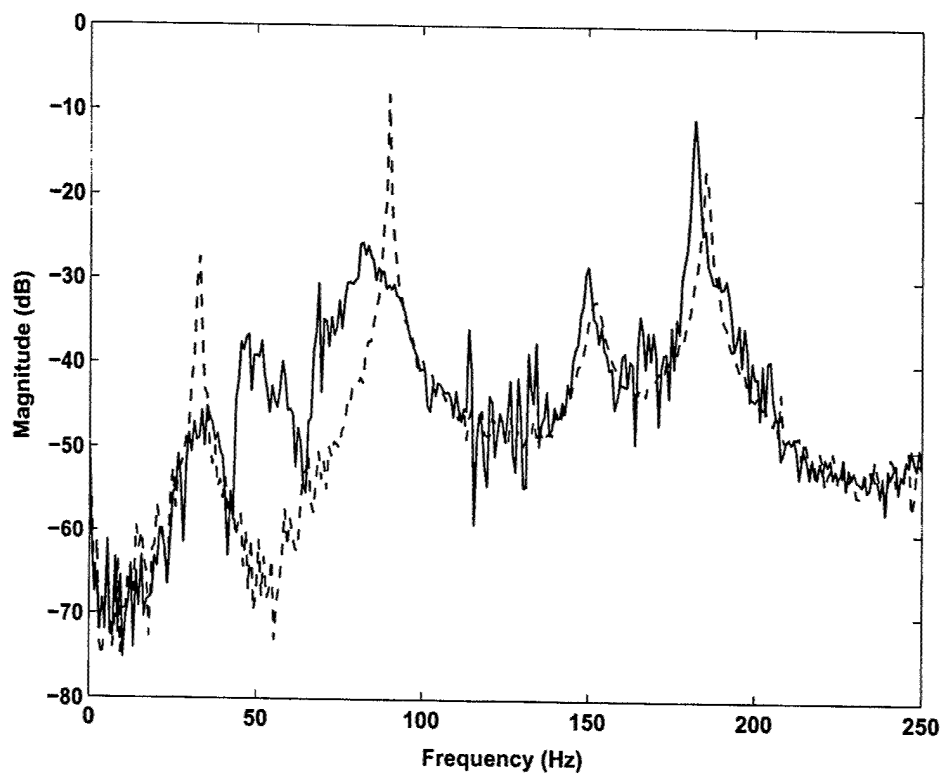


Figure 9. Comparison of computed open-loop (dashed line) and closed-loop (solid line) frequency response estimation between the disturbance input and the second sensor output of a cantilevered beam: magnitude of frequency response ($t_s = 250Hz$).

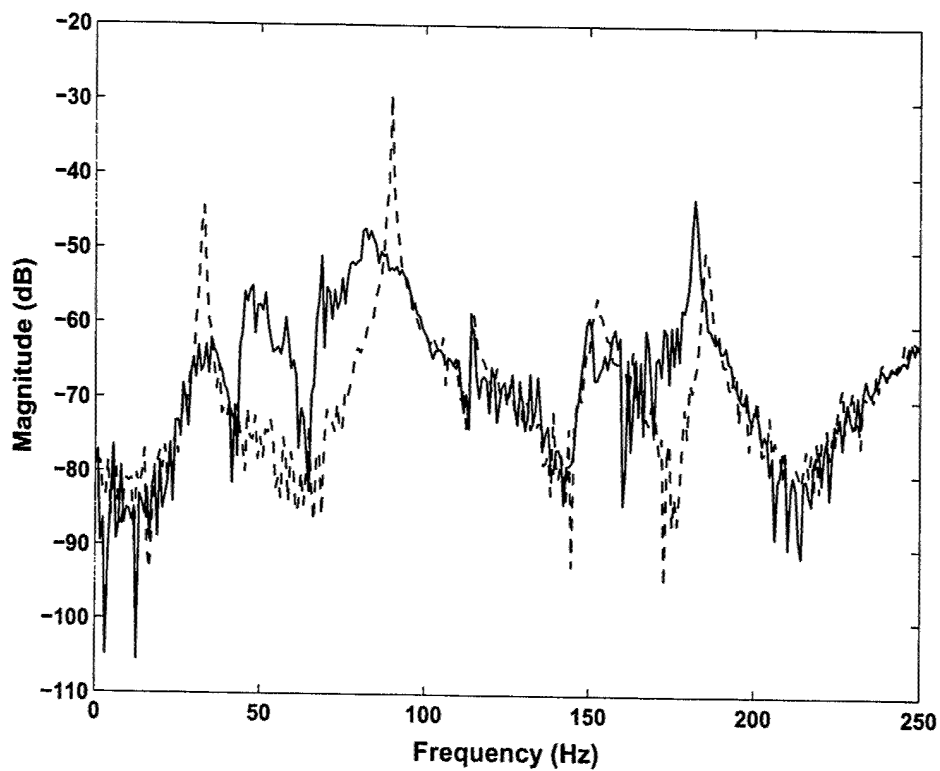


Figure 10. Comparison of computed open-loop (dashed line) and closed-loop (solid line) frequency response estimation between the disturbance input and the performance output of a cantilevered beam: magnitude of frequency response ($t_s = 250Hz$).

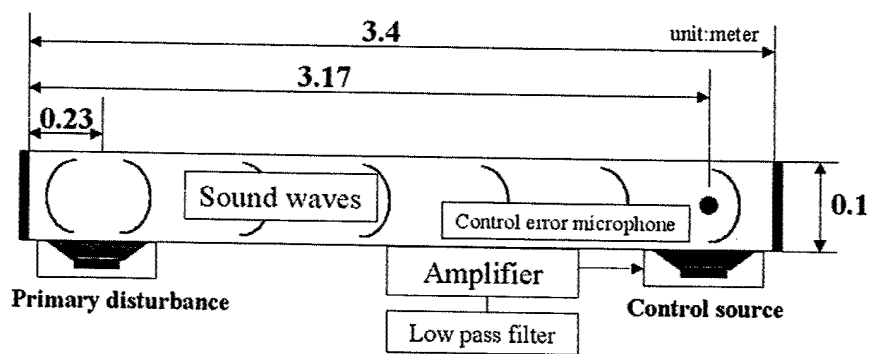


Figure 11. Schematic of diagram and picture of closed-closed sound enclosure configured with acoustic loudspeakers and microphone.

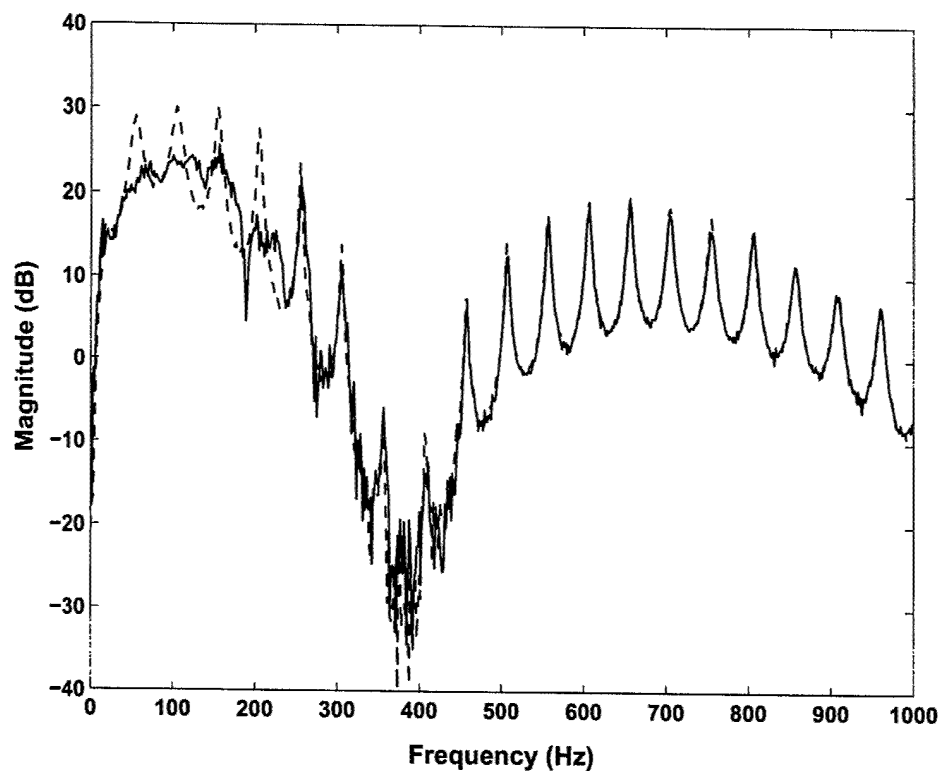


Figure 12. Comparison of computed open-loop (dashed line) and closed-loop (solid line) frequency response estimation between the disturbance loudspeaker and the control error microphone of the closed-closed sound enclosure: magnitude of frequency response ($t_s = 500Hz$).

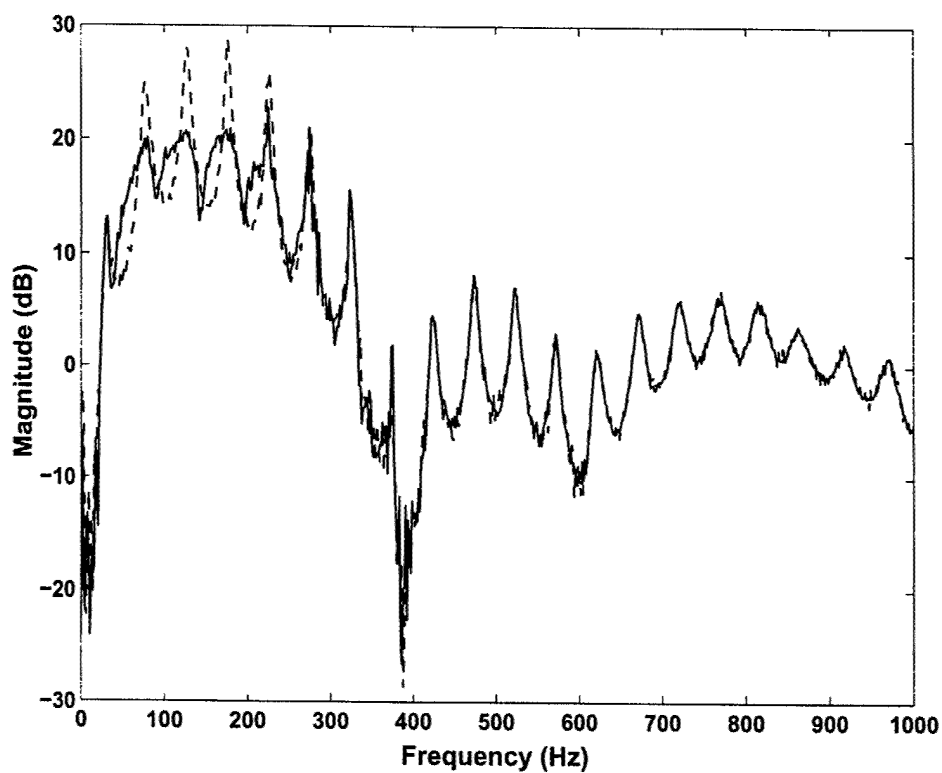


Figure 13. Comparison of computed open-loop (dashed line) and closed-loop (solid line) frequency response estimation between the disturbance loudspeaker and the control error microphone of the open-closed sound enclosure: magnitude of frequency response ($t_s = 500\text{Hz}$).

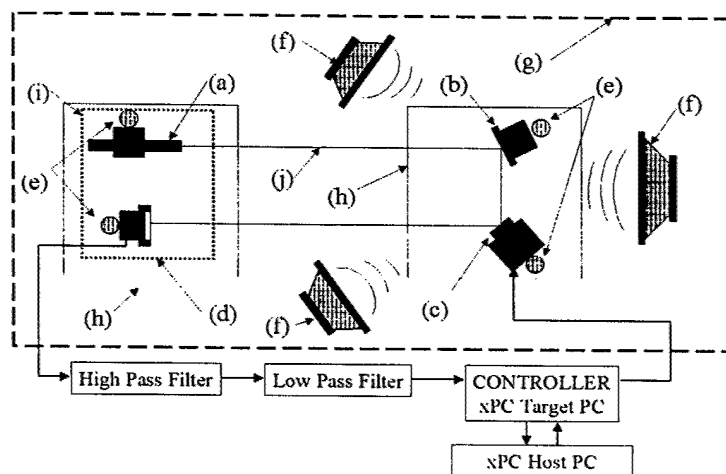


Figure 14. Experimental system setup of an optical jitter suppression testbed
(a) HeNe Laser, (b) Turning Flat Mirror, (c) Fast Steering Mirror, (d) Position Sensing Detector, (e) Mounting Rod, (f) Disturbance speaker, (g) Anechoic Chamber, (h) Optics bench, (i) Enclosure, (j) Laser beam

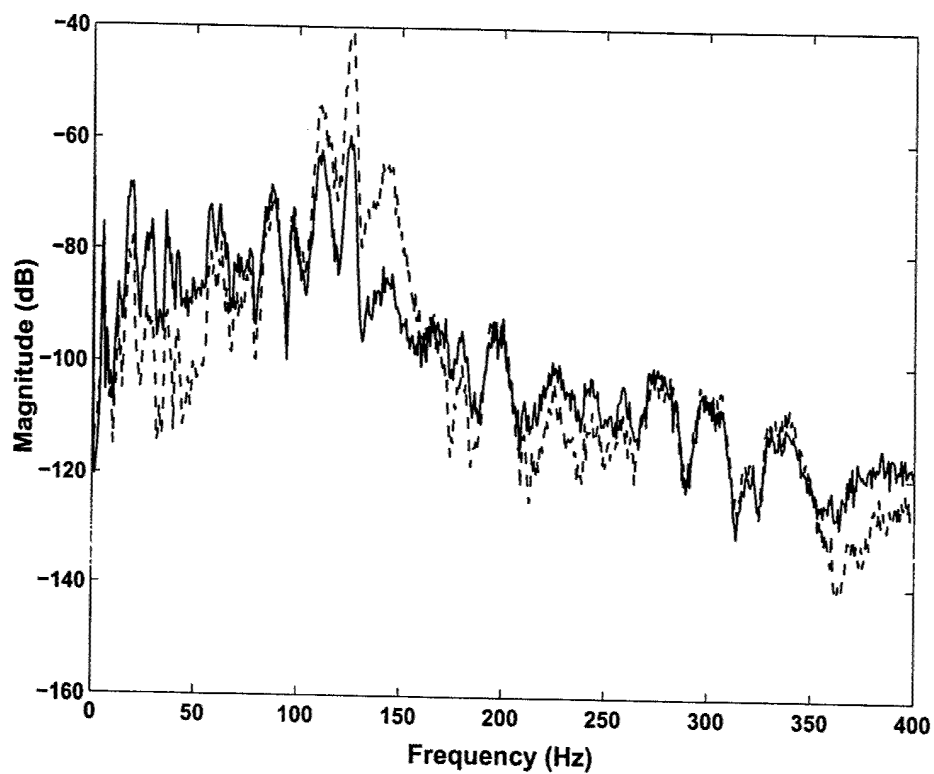


Figure 15. Comparison of computed open-loop (dashed line) and closed-loop (solid line) auto-spectrum estimation of the vertical position with 1 disturbance source ($t_s = 600Hz$).

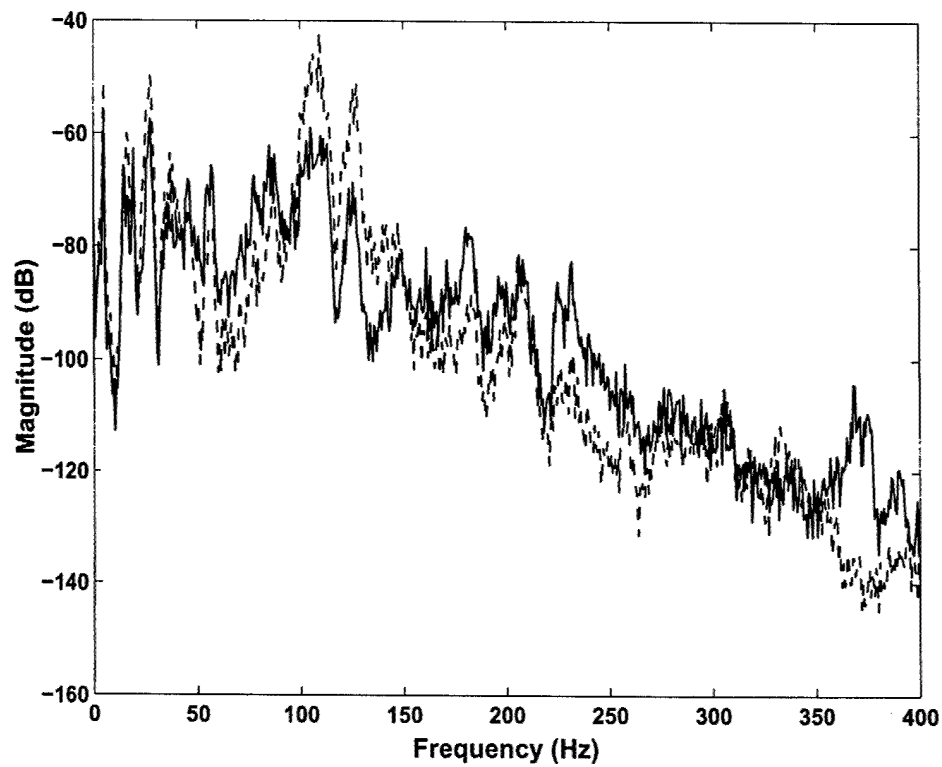


Figure 16. Comparison of computed open-loop (dashed line) and closed-loop (solid line) auto-spectrum estimation of the vertical position with 3 disturbance sources ($t_s = 600Hz$).

Noise reduction in a launch vehicle fairing using actively tuned loudspeakers^{a)}

Jonathan D. Kemp

Acentech, Inc., Cambridge, Massachusetts 02138-1118

Robert L. Clark

Department of Mechanical Engineering and Materials Science, Duke University, Durham, North Carolina 27708-0300

(Received 17 April 2001; revised 19 November 2002; accepted 8 January 2003)

Loudspeakers tuned as optimal acoustic absorbers can significantly reduce damaging, low frequency, reverberant noise in a full-scale launch vehicle fairing. Irregular geometry, changing payloads, and the compliant nature of the fairing hinder effective implementation of a passively tuned loudspeaker. A method of tuning the loudspeaker dynamics in real time is required to meet the application requirements. Through system identification, the dynamics of the enclosure can be identified and used to tune the dynamics of the loudspeaker for reduction of targeted, high intensity, low-frequency modes that dominate the acoustic response in the fairing. A loudspeaker model with desired dynamics serves as the reference model in a control law designed to tune the dynamics of a non-ideal loudspeaker to act as an optimal tuned absorber. Experimental results indicate that a tuned loudspeaker placed in the nose cone of the fairing significantly reduces acoustic energy and verifies results calculated from the simulation. © 2003 Acoustical Society of America.

[DOI: 10.1121/1.1558371]

PACS numbers: 43.50.Ki [MRS]

I. INTRODUCTION

The high-intensity, low frequency acoustic excitation that occurs in a rocket fairing at launch can induce structural-acoustic vibrations that damage the payload. As engineers endeavor to create larger, lightweight, cost-effective fairings, acoustic excitation becomes a more critical factor in payload launch survivability. Previous research in this area has investigated both active and passive methods for acoustic attenuation,¹⁻³ in addition to vibration control of the fairing itself.^{4,5} At low frequencies, lightly damped modes dominate the interior acoustic response of the fairing, and the ineffectiveness of passive methods such as acoustic blankets, fiberglass, or acoustic foam impels consideration of active and hybrid control methods. This study presents the experimental results of an actively controlled, optimally tuned acoustic absorber implemented in a full-scale fairing testbed.

Previous work has shown that dissipative control can be achieved in acoustic enclosures using a collocated pressure sensor and a constant volume-velocity source.^{6,7} Extension of this principle yielded significant attenuation of low frequency acoustic modes in a launch vehicle fairing by utilizing arrays of sensors and actuators working cooperatively to achieve global control. The transducer arrays were spatially weighted in order to selectively couple to low-frequency modes, which reduced the order of the controller and yielded significant modal control with minimal control spillover.⁸ Global peak reductions (8–10 dB) of targeted acoustic modes required an extensive array of control sources, condi-

tioning and amplification measures, microphones, control hardware, and wiring. Further review of these requirements has prompted investigation of less equipment intensive, “hybrid” active/passive controllers.

Previous research involving hybrid systems for sound absorption demonstrated the effectiveness of surface impedance control in rectangular enclosures^{9,10} and impedance tubes¹¹ with low modal density. Both loudspeaker diaphragms and panels with tuned dynamics demonstrated attenuation through active impedance changes at enclosure boundaries, but none demonstrated acoustic absorption from within the enclosure. More relevant to this work, the authors joined an effort to develop a passive vibroacoustic attenuator based on a hybrid of a proof-mass actuator (PMA) and a shunted loudspeaker.¹² That study highlighted the possibility of combining a tuned mass damper for structural damping and a tuned diaphragm for acoustic damping. The attenuator was dynamically modeled and placed within a fully coupled structural-acoustic finite element model of the fairing. Results predicted a broadband noise reduction of 3 dB, but difficulties in the experimental development and application of such an attenuator left room for improvement.

As an extension of the hybrid principle, this work applies tuned mass damping theory to sound absorption applications in a flexible, irregular cavity that encloses changing payloads and demonstrates significant, three-dimensional modal complexity. This study proposes to attenuate low frequency modes in a launch vehicle fairing with loudspeakers tuned as optimal acoustic absorbers. The absorbers promote efficiency of the control system while demonstrating control results comparable to previous active studies. As a primary advantage, the significant logistical issues of typical active systems have been eliminated. The control law discussed herein actively tunes a loudspeaker to passively reduce the

^{a)}Portions of this work were presented in “Noise reduction in a launch vehicle fairing using actively tuned loudspeakers,” Proceedings of Joint 140th Meeting of the Acoustical Society of America and NOISE-CON 2000, Newport Beach, CA, 2000.

targeted mode(s), removing typical acoustic spillover in the control bandwidth, and allowing global attenuation with a single actuator. A parametric optimization scheme selects an optimal tuned absorber model which is compared to an identified model of the non-ideal loudspeaker in the fairing; the difference between them is minimized by a model reference control law, based on H_2 design. Loudspeaker tuning requires only low-order control in a limited bandwidth. These achievements increase the performance and stability of the controller, while reducing control energy and hardware by more than 90%.

Preliminary investigation of actively tuned acoustic absorber design facilitates application of that technology for noise control in acoustic enclosures, and more specifically, in an experimental, full-scale, composite launch vehicle fairing model at Duke University. In support of continuing efforts to improve payload survivability, the research sought definitive control results to promote further study of the effectiveness and efficiency of adaptive acoustic control within the fairing volume.

II. THEORY

A. Fairing acoustics

A rocket fairing is essentially a flexible-walled structure surrounding an acoustic enclosure that protects the payload during launch. Fairings have typically been constructed of metal, such as aluminum, but composites have been used more recently. Although composites offer many advantages, they are less massive and therefore allow increased transmission of exterior disturbances. Vibration of the fairing excites acoustic resonances within the enclosure, which detrimentally couple to the payload. Data from previous satellite launches indicate that the overall acoustic levels inside the fairing during launch can exceed 140 dB. At low frequencies (10 to 200 Hz), the levels reach approximately 120 to 130 dB.¹³

The fairing considered in this work is based on the Orbital Sub-orbital Program Space Launch Vehicle (OSPSLV) minotaur. The shroud is 5.3 meters long with a maximum diameter of approximately 1.3 meters. Therefore, the low-frequency modes are longitudinal rather than radial. The fairing is excited by a number of disturbances, including aerodynamic buffeting during flight,¹⁴ structural vibrations induced by the rocket motors, and pyrotechnic shocks during stage separations. These sources act in addition to the explosive noise produced by the motors themselves.

The most harmful vibration occurs in the first 30–45 seconds after ignition, as both acoustic transmission and aerodynamic buffeting decrease with decreasing atmospheric pressure and density. While on the launch pad, the earth acts as an acoustic baffle, reflecting enormous waves of energy at the payload. As the vehicle lifts away from earth, increased speed causes significant aerodynamically induced noise. When the payload exhibits a structural resonance near the acoustic resonances of the fairing, the acoustic loading can result in appreciable damage to the payload. The Department of Defense reports that at least 40% of first-day satellite failures result from vibration damage incurred at launch.¹⁵ Flat

surfaces of solar panels and light-weight structures such as thin films, membranes, and precision optics are particularly susceptible to damage from the low frequency excitation. The presence of multiple, random, low-frequency disturbance sources precludes passive and feedforward control, compelling the use of an innovative feedback control scheme.

B. Tuned acoustic absorbers

The concept of loudspeakers tuned as optimal acoustic absorbers grew from the familiar use of tuned mass-spring systems for vibration absorption in structures. Here, active tuning controls enclosed acoustics. Departing from previous acoustic approaches which attempted to change the enclosure boundary, this work develops the ability of production loudspeakers to act in reverse, or as self-contained tunable absorbers. Essentially, a loudspeaker is actively tuned to respond passively as though it were an ideal absorber for a targeted modal frequency.

Realization of the ideal absorber begins with development of a theoretical model that couples the response of the fairing enclosure to a disturbance source and a typical loudspeaker. An optimization scheme then selects an ideal absorber for reduction of global acoustic energy at a targeted modal frequency. A model reference control law can then minimize the response difference between the ideal model and the actual loudspeaker, forcing that loudspeaker to act as an ideal absorber.

III. MODELING, DESIGN, AND OPTIMIZATION

The combined behavior of the fairing disturbances is unpredictable, but the modal acoustic response in the enclosure due to the vibration of the fairing structure can be easily modeled. A rigid walled cylinder model of equal dimension provides a strong prediction of the magnitude, phase, and frequency of the lowest modal frequencies, and is constructed here for the purposes of absorber design and optimization. The development follows Morse and Ingard¹⁶ and Cheng and Nicolas.¹⁷ Application of the appropriate boundary conditions allows solution of the homogeneous wave equation in a cylinder of length L with a Hankel function of order m :

$$p(r, \theta, z, t) = \sum_{m=0}^{\infty} \sum_{n=1}^{\infty} \sum_{\mu=1}^{\infty} A_{mn\mu} \sin\left(m\theta + \gamma \frac{\pi}{2}\right) \times J_m(k_r r) \cos\left(\frac{\mu\pi}{L} z\right) e^{i(\omega t - k_\theta \theta - k_z z)}, \quad (1)$$

where p represents the pressure in the fluid, c is the local speed of sound, and r , z , and θ are the cylindrical coordinates within the cavity. Here, m , n , and μ , and γ are the azimuthal, radial, longitudinal, and symmetric (rotational) modal indices, respectively. Here, k_θ is the azimuthal wave number and k_z is the longitudinal wave number. The radial wave number k_r is the n th root of the derivative of the Bessel function of the first kind evaluated at the cavity wall.

The model includes a vibrating rectangular panel, curved and placed at the enclosure wall to simulate the trans-

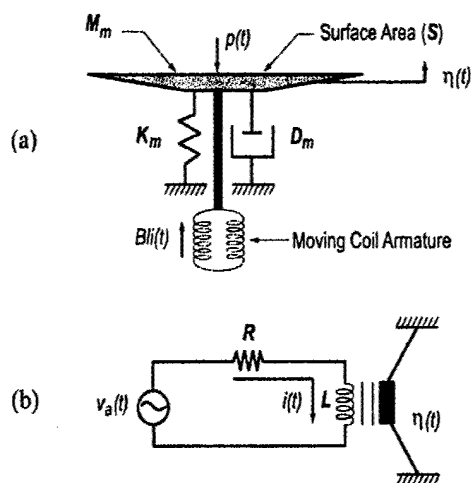


FIG. 1. (a) Mechanical schematic of loudspeaker system. (b) Electrical schematic of loudspeaker system [after Clark *et al.* (Ref. 20)].

mission path in the actual fairing. Following fluid-structure coupling techniques, the modal interaction model by Fahy,¹⁸ and recent work by Henry and Clark,¹⁹ the model results. From the inhomogeneous wave equation for the pressure in the cavity, the equations of motion for the enclosure as disturbed by the curved panel can be written as

$$\Lambda_{n_p} \ddot{v}_{n_p}(t) + \Lambda_{n_p} \omega_{n_p}^2 v_{n_p}(t) = -\rho_0 c^2 S_0 \sum_{k=1}^K C_{n_p k} \ddot{w}_k(t), \quad (2)$$

where ρ_0 is the density of the fluid in the cavity, and $v_{n_p}(t)$ is a generalized modal coordinate. The panel undergoing out-of-plane displacement, w , is modeled as a distributed volume velocity source just inside the enclosure boundary. The modal volume, Λ_{n_p} , is represented by the integral of spatial mode shape functions, and the subscripts m , n , and μ have been replaced in by the generalized modal index n_p . The coupling coefficient $C_{n_p k}$ is the surface integral of the product of the mode shape functions of the panel and the enclosure.

A. Tuned absorber coupling

Modeling and design of the tunable acoustic absorber requires coupling the equations of motion for a typical loudspeaker to the acoustics of the enclosure model developed above. The passive interaction of the tuned loudspeaker with the fairing acoustics forms the tunable boundary condition for control application. In preliminary tests, the nose cone seemed ideal for installation of the tuned absorber: the primary active control targets are the modes of lowest frequency, so the absorber should interact with longitudinal, not radial or azimuthal, wave forms. These wavelengths are most easily targeted spatially by observation and control at the end caps of the fairing. Applied damping at the boundary condition responsible for longitudinal modal response will reduce acoustic energy at the modal frequency, thereby reducing overall acoustic energy propagation within. Additionally, placement of the tuned absorber in the nose cone minimizes the control system impact on available payload volume.

A model of a loudspeaker, radiating in its piston mode, was therefore incorporated in one end cap of the enclosure. The electromechanical coupling and structural acoustic coupling are described by assimilating the typical loudspeaker equations of motion²⁰ with the enclosure model above. Figure 1(a) provides a schematic representation of the mechanical system, and the respective equation of motion can be written as

$$M_m \ddot{w}(t) + D_m \dot{w}(t) + K_m w(t) = Bl i(t) - S_0 p(t), \quad (3)$$

where M_m , D_m , and K_m are the mechanical mass, damping, and stiffness of the speaker, and $w(t)$ represents the displacement of the speaker coil. The force input has two components: electromotive force is the product of the field strength of the inductor B , the conductor length l , and the current $i(t)$; and the pressure input is the product of the surface area of the loudspeaker diaphragm, S_0 , and the acoustic pressure, $p(t)$. This pressure input, or radiation resistance, is the most crucial coupling term for this application. Figure 1(b) provides a schematic representation of the electrical system, governed by the following equation:

$$L \frac{di(t)}{dt} + R i(t) = v_a(t) - Bl \dot{w}(t). \quad (4)$$

Note that the voice coil (Bl) couples the electrical and mechanical systems in the speaker. These equations of motion can now be coupled through diaphragm displacement w and acoustic pressure p to the acoustic model of the enclosure for full system modeling and optimal design.

B. Optimization

A constrained optimization scheme determines the optimal mechanical and electrical parameters of the loudspeaker for acoustic energy absorption at a targeted mode in the enclosure. Within reasonable constraints, the routine could select candidate speakers by arbitrary variation of each significant property of the loudspeaker system: B , l , R , M_m , K_m , D_m , and S_0 . However, to enhance the feasibility of actual loudspeaker construction and tuning, the parameter field was narrowed to those available for physical tuning: the resistance R of the circuit, and the apparent spring stiffness, K_m , of the mechanical system. The cost functional was calculated as the H_2 norm of the targeted modal acoustic output v_n of the coupled loudspeaker/enclosure system. The routine utilized a constrained optimization function provided in the optimization toolbox for MATLAB. The function, *fmincon.m*, follows a sequential quadratic programming method in which a quadratic programming subproblem with linearized constraints is solved at each iteration as the routine searches for the minimum of the given cost functional. A positive definite quasi-Newton estimate of the Hessian of the Lagrangian function is updated at each iteration to provide the direction and magnitude of the next iteration. This estimate is calculated with the BFGS (Broyden, Fletcher, Goldfarb, and Shanno) formula which enhances the efficiency of the scheme.²¹

To assure the accuracy of the optimization results, several sets of initial conditions were passed to the routine for

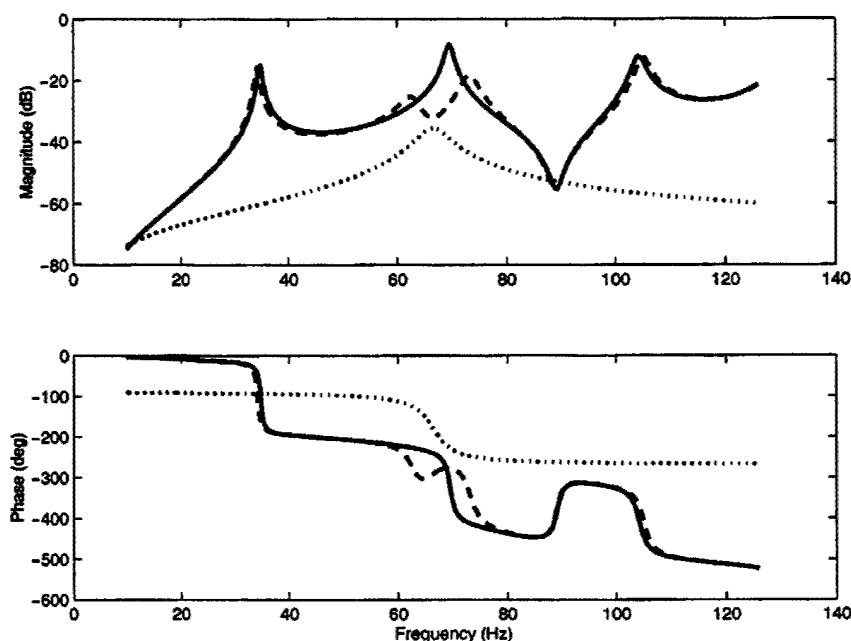


FIG. 2. Frequency response of enclosure without (—) and with (---) reduction due to coupled tuned absorber (···).

each targeted mode. The routine repeatedly selected similar models within one hundred iterations. The dynamic response of a typical optimal absorber demonstrates increased response at a frequency slightly above or below the targeted modal frequency. This observation confirmed initial hypotheses about the parallels between optimal acoustic absorbers and tuned vibration control devices. Figure 2 displays the predicted acoustic response of an optimal loudspeaker coupled to the acoustic enclosure developed above. Note the significant reduction in response at the second mode. This pressure response, taken in the acoustic far field of the tuned loudspeaker, demonstrates significant global reduction from a single tuned actuator. This ideal actuator serves as the reference model in a control scheme designed to tune the actual loudspeaker to act as the ideal absorber.

IV. EXPERIMENTAL IMPLEMENTATION

Development of the tuned absorber continues with application of model reference control to the loudspeaker in the fairing. Based upon work by Ogata,²² the development of a model reference plant involves evaluation of a performance

metric calculated as the response difference between the actual system and the model reference system, given identical inputs.

An approach based on the eigensystem realization algorithm^{23,24} identifies low-order, discrete, state-space realizations of the untuned speaker for comparison with the optimal loudspeaker model developed above. A common source then disturbs both the realized system and the optimal model through the respective voltage inputs, ensuring that the controller affects the loudspeaker regardless of acoustic pressure input. The characteristics of the disturbance and its coupling to the fairing are irrelevant to the controller, broadening the scope of possible application. The outputs of the two systems are compared and the difference between them serves as the performance variable in the control law.

The augmented system^{25,26} was then assembled and modeled using Simulink,²⁷ and H_2 control laws were computed using MATLAB. Filters designed to shape the controller are added for stability but increase the order (number of states) of the augmented plant and the resulting control law. The controller, now of unnecessarily large order, is reduced

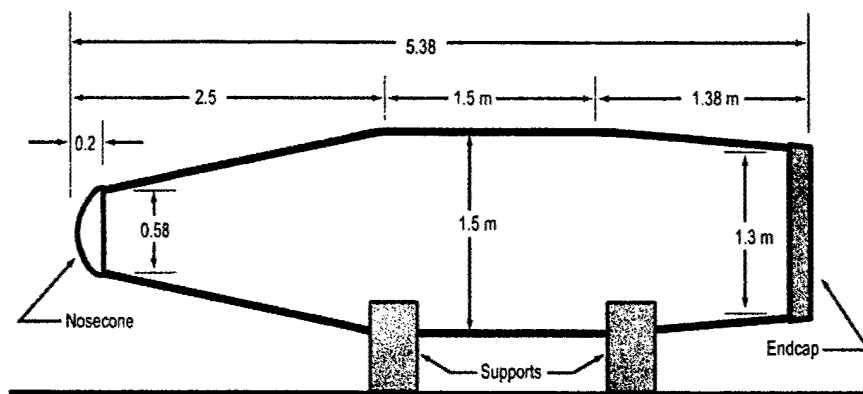


FIG. 3. Illustration of fairing testbed.

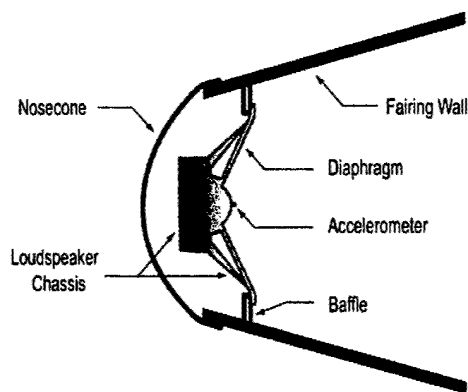


FIG. 4. Schematic of absorber system mounted in nose cone.

through model reduction techniques, such as balanced residualization or truncation.^{26,28} After computation, a Tustin routine transforms the reduced-order control law into the discrete domain and the control law is downloaded to a digital signal processor (DSP) for implementation.

Comparison of the open-loop and closed-loop frequency response functions from a disturbance input (band-limited random noise) to an array of performance microphones yields a controller performance metric. Averaging these frequency response measurements provides representative open-loop and closed-loop frequency responses and facilitates evaluation of the overall effects of the controller as a function of frequency. From this evaluation, the occurrence of spillover, the degree of coupling to the target modes, and the average amount of local and global attenuation is observed.

A. Fairing testbed

Experiments are conducted on a full scale composite fairing model containing the loudspeaker/absorber, the accelerometer sensor, the acoustic disturbance source, and sixteen arbitrarily positioned performance microphones. The fairing (shown schematically in Fig. 3) is approximately 5.3 meters in length, 1.3 meters in diameter (maximum), and tapered at both ends. A plywood end cap is attached to the base of the fairing and sealed appropriately. A hemispherical aluminum end cap completes the nose cone and seals the acoustic

chamber behind the loudspeaker, as shown in Fig. 4. The loudspeaker and baffle are rigidly attached to the nose cone. The loudspeaker is a manufactured 18 inch subwoofer, occupying roughly 60% of the area of the nose cone baffle.

The accelerometer is fixed at the diaphragm center for maximum signal and focus on the piston mode of the speaker. A small conditioning device located within the fairing amplifies the accelerometer signal. A disturbance loudspeaker in the corner of the fairing near the base end cap excites the interior cavity modes. The performance microphones were distributed throughout the interior at arbitrary positions to measure the overall controller effects. All cabling was connected through a panel at the base of the fairing. The controller, spectrum analyzers, power amplifiers, microphone conditioners, and other required hardware were housed external to the fairing. A block diagram of the setup is presented in Fig. 5.

V. RESULTS

A. Tuned absorber

The experiment begins with an investigation of the coupling effects between the loudspeaker and the fairing acoustics. Figure 6 supports the predicted effects of this coupling. The frequency response of the loudspeaker is measured both in open air and after installation in the fairing nose cone baffle. Both were measured as frequency response functions between a band-limited random disturbance applied to the voltage input of the loudspeaker and the voltage signal from the accelerometer mounted on the loudspeaker diaphragm. Note the strong modal response when the loudspeaker is coupled to the fairing acoustics. The modes apparent here are coupled mechanoacoustic modes of the loudspeaker and fairing, not merely a reflection of the fairing acoustics. This coupling is crucial to the success of the tuned absorber, as discussed in Sec. III, and verifies conjecture about this pressure input to the dynamic system modeled herein.

Modeling of the loudspeaker dynamics for the purpose of control is accomplished through system identification techniques. Following identification, the control law is applied to tune the loudspeaker as an optimal absorber. The controller effectively changes the dynamic response of the loudspeaker, as shown in Fig. 7. The loudspeaker response is

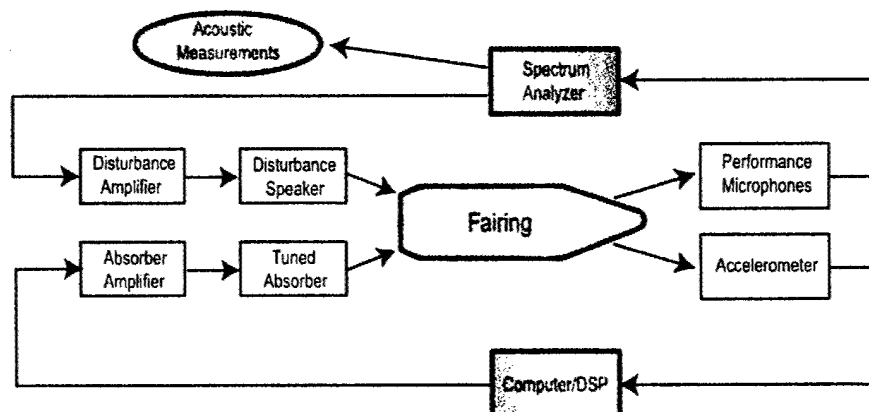


FIG. 5. Schematic of experimental setup.

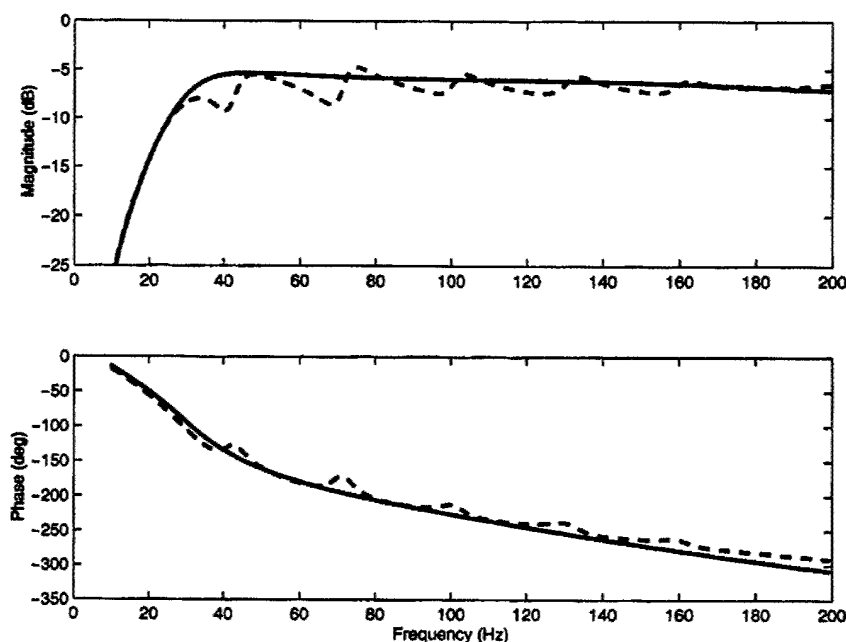


FIG. 6. Acoustic coupling demonstrated by loudspeaker responses measured from voltage input to accelerometer in open air (—) and after mounting in nose cone baffle (---).

measured by the accelerometer relative to an acoustic disturbance applied to the fairing volume. Note the significant peak introduced at the targeted frequency of 65 Hz. Figure 7 details the effects of the controller when the disturbance is purely acoustic; the modes of the fairing are apparent. The controller does not retard response of the loudspeaker at the non-targeted first acoustic mode, so the response of the speaker at that frequency remains unchanged.

Model reference control demonstrates authority over the dynamics of an actual loudspeaker. By design, the control law can tune the loudspeaker to absorb at any frequency, though some frequencies are more conducive to tuning than others. The efficiency of the controller and the magnitude of resulting effects are dependent on the dynamics of the speaker, as expected. If the desired tuning frequency is proximal to a coupled mode of the loudspeaker and fairing, then the controller is more successful, as the effort required to

move a system pole is significantly less than that required to introduce a new pole. Additionally, the modal targeting introduced by the noise filters in the control law prevents placement of control effort out of the most efficient bandwidth. An inherently efficient controller results from this combination of control strategies.

B. Acoustic control in the fairing

Demonstration of a stable tuned loudspeaker allows implementation in the fairing volume. Key to the stability and minimal energy consumption of the controller is the separation of the controller from the acoustics of the fairing. The control law seeks only to tune the mechanics of the loudspeaker, not to actively control the fairing acoustics. This separation precludes the development of typical acoustic instabilities found in most active acoustic control systems,

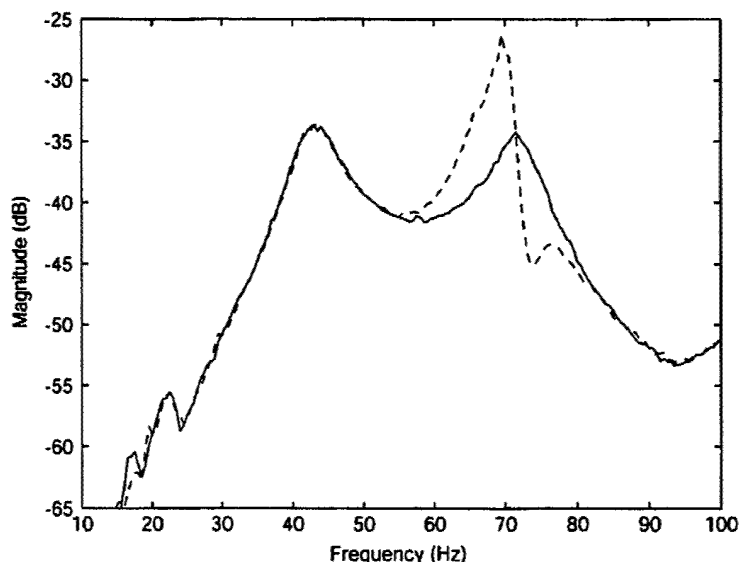


FIG. 7. Loudspeaker acceleration response measured from acoustic disturbance to accelerometer without (—) and with active tuning (---).

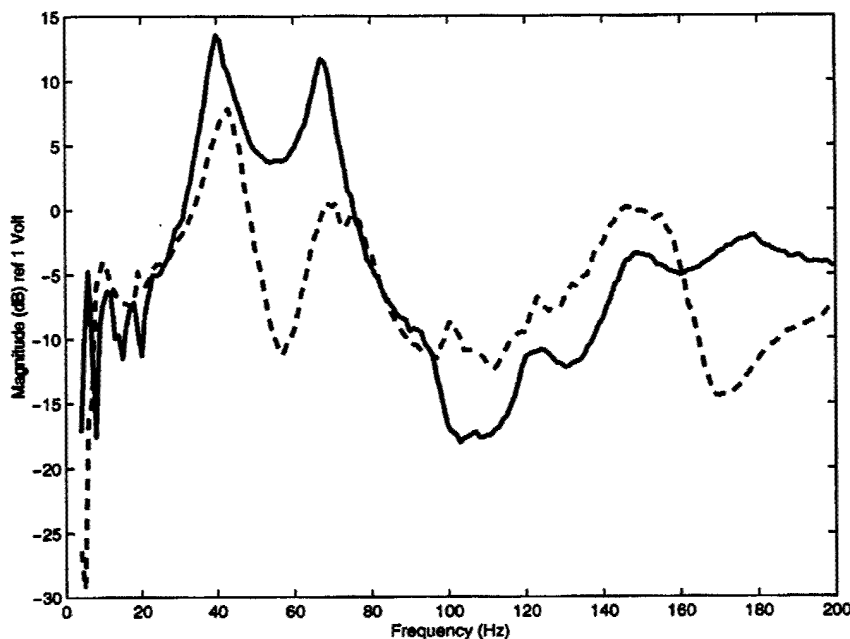


FIG. 8. Local acoustic pressure response measured from acoustic disturbance to a single microphone (No. 3) without (—) and with active tuned absorber (---) targeting second acoustic mode (69 Hz).

allowing significant control signal gain without fear of unstable acoustic feedback. In other words, the controller actively tunes the loudspeaker to act as a passive acoustic absorber, as discussed in the preceding sections.

Optimization efforts revealed significant control capability at the second mode of the fairing, 69 Hz. Proximity to an actual coupled modal frequency of the loudspeaker and fairing promotes effective control of loudspeaker dynamics. Candidate absorber models with natural frequencies slightly above or below the targeted 69 Hz were chosen by the optimization routine. The best results, both predicted and actual, utilized an absorber tuned to 80 Hz. The optimal tuning frequency is roughly 15% above the targeted modal frequency, a result typical of tuned mass absorber design. Figure 8 displays the local pressure response for this control configura-

tion, measured at a microphone located in the cross-sectional center of the fairing, approximately 0.8 meters from the tuned diaphragm. The 12 dB reduction at the second mode (69 Hz) is apparent; the resonant peak is split and of greatly reduced magnitude. This microphone represents the response of the fairing in the acoustic near field of the tuned loudspeaker.

An evaluation of global performance in the fairing yields the acoustic response shown in Fig. 9. This response was measured as the simple average of the pressures recorded at 16 arbitrary positions within the fairing. Significant global peak reduction (4 dB) is apparent; control is achieved.

Note that the global reduction is less significant than the local control shown in Fig. 8, as expected. To investigate the performance at individual microphones throughout the space,

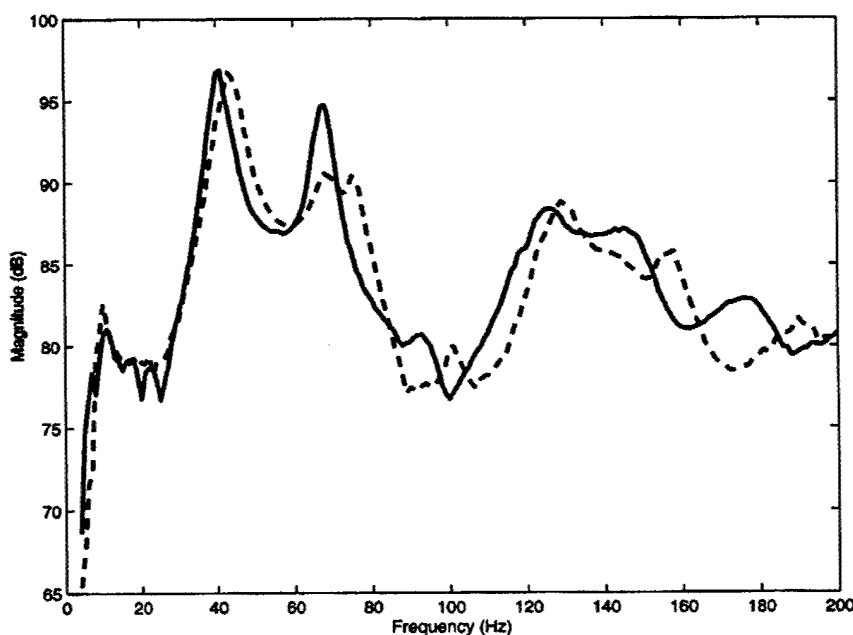


FIG. 9. Global acoustic pressure response, as averaged from acoustic disturbance to 16 microphones, without (—) and with active tuned absorber (---) targeting second acoustic mode (69 Hz).

TABLE I. 69 Hz mode peak pressure reductions achieved with an actively tuned loudspeaker, calculated from measurements of frequency responses between acoustic disturbance and each microphone.

Microphone ID	Peak reduction (69 Hz)
1	7 dB
2	8 dB
3	12 dB
4	8 dB
5	0 dB
6	1 dB
7	0 dB
8	6 dB
9	6 dB
10	5 dB
11	12 dB
12	4 dB
13	-3 dB
14	3 dB
15	5 dB
16	5 dB

Table I details the second mode (69 Hz) peak reduction measured at each location. The microphone locations are numbered consecutively from forward to aft. The local frequency response plotted in Fig. 8 corresponds to microphone number 3, as the first two positions were closer to the loudspeaker but not in the center of the fairing. Note that attenuation is achieved at 13 of the 16 microphone locations, the exceptions being two microphones where no attenuation was noted and a 3 dB increase measured at microphone number 13. However, the overall RMS pressure level in the 200 Hz bandwidth was still reduced by 0.61 dB at microphone No. 13. Additionally, two separate locations, one in the acoustic near field (No. 3) and one in the far field (No. 11) measured peak reductions of 12 dB. The previous active system requiring 16 actuators did not achieve any peak reduction greater than 12 dB.⁸

A promising observation throughout the tests is the voltage necessary to achieve this level of control. A frequency spectrum of the control voltage is provided in Fig. 10. This controller, by design as merely an enabling device for pas-

sive absorption, required 0.216 Volts RMS (1.180 V peak) for the duration of the testing. These levels are at least an order of magnitude less than the voltage required per actuator by active systems achieving similar levels of control with multiple actuators.⁸ Power requirements are also appropriately reduced. Each of the above results demonstrates the effectiveness of a low-order model-reference controller used to tune a loudspeaker to act as an optimal tuned acoustic absorber in a full-scale payload fairing.

VI. CONCLUSION

Preliminary results presented here demonstrate the effectiveness of a tuned loudspeaker acting as a self-contained optimal acoustic absorber in a launch vehicle fairing. Application of structural tuned mass absorber theory to the realm of acoustics has allowed efficient acoustic reduction with active technology but without the logistical cost of previous active and passive control apparatus.

Following development of a theoretical model of the enclosure and of a typical loudspeaker, an optimization scheme selects the dynamic properties of an ideal absorber for a chosen acoustic mode of the enclosure. This optimal absorber then serves as the reference model in a control law designed to actively tune an off-the-shelf loudspeaker to act as an optimal tuned absorber. Placement of this tuned loudspeaker in the nose cone of a full-scale launch vehicle fairing allows experimental verification of the tuned absorber concept. A tuned loudspeaker acting passively in the fairing enclosure absorbs significant acoustic energy at targeted modal frequencies.

The feasibility of a launchable application remains the quest of this technological development. The advantages here are simple: the actively tuned absorber minimizes controller impact on payload weight and volume. The system requires only one actuator per acoustic mode to be controlled, rather than the array used for active studies. With each actuator goes an accompanying amplifier, microphone, and signal conditioner. Further, control signal voltage and actuator power requirements are orders of magnitude less

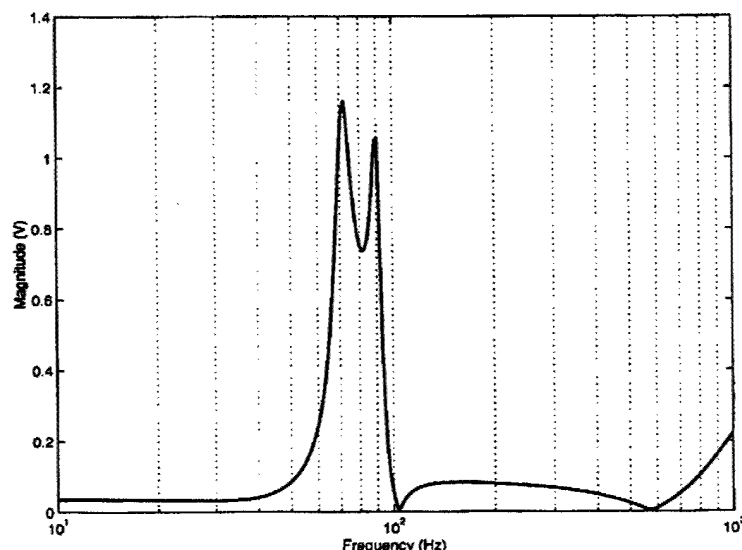


FIG. 10. Frequency spectrum of the model reference control signal voltage for the actively tuned loudspeaker.

than active counterparts, relieving battery weight. This hybrid controller accomplishes efficient, lightweight noise attenuation in a frequency range where both active and passive control have significant logistical and performance problems.

Future work will address challenges that arise in the application of any controller to a launchable enclosure. Acoustic response of the fairing, and therefore optimization and modal targeting parameters, will change with payload and atmospheric conditions, so the tuned system must be able to react accordingly. The tuned absorber system offers feasible solutions. Because the tuning parameters are based solely on a targeted frequency, they could be updated without continuous system identification. In fact, these tracking adjustments could be incorporated in the control law. Additionally, further studies should include the use of multiple tuned loudspeakers targeting single and multiple frequencies in the enclosure. Development of these concepts holds promise for future investigations, as the actively tuned loudspeaker has demonstrated acoustic control in a full-scale fairing.

ACKNOWLEDGMENTS

The authors would like to gratefully acknowledge the partial support for this research provided under the AFOSR Presidential Early Career Award for Scientists and Engineers, Grant No. F49620-98-1-0383, monitored by Major Brian Sanders and Dr. Dan Segalman. We would also like to express our gratitude to the Air Force Research Laboratory for providing the rocket fairing model used in these experiments.

¹L. Bradford and J. Manning, "Attenuation of Cassini spacecraft acoustic environment," *Sound Vib.* **30**, 303–337 (1996).

²K. Weissman, M. E. McNellis, and W. D. Pordan, "Implementation of acoustic blankets in energy analysis methods with application to the atlas payload fairing," *J. IES* **34**, 32–39 (1994).

³C. Niezrecki and H. Cudney, "Preliminary review of active control technology applied to the fairing acoustic problem," Proceedings of the AIAA Adaptive Structures Forum, Salt Lake City, UT, 1996, pp. 101–108.

⁴D. Leo and E. Anderson, "Vibroacoustic modeling of a launch vehicle payload fairing for active acoustic control," AIAA 39th Annual SDM Conference, Long Beach, CA, 1998, AIAA-98-2086.

⁵F. Shen and D. Pope, "Design and development of composite fairing structures for space launch vehicles," SAE Technical Paper 901836, Aerospace Technology Conference and Exposition, Long Beach, CA, October 1990.

⁶S. A. Lane and R. L. Clark, "Dissipative feedback control of a reverberant enclosure using a constant volume velocity source," *J. Vibr. Acoust.* **120**, 987–993 (1998).

⁷S. A. Lane and R. L. Clark, "Improving loudspeaker performance for active noise control applications," *J. Audio Eng. Soc.* **46**, 508–519 (1998).

⁸S. A. Lane, J. D. Kemp, R. L. Clark, and S. Griffin, "Feasibility analysis for active acoustic control of a rocket fairing using spatially weighted transducer arrays," *J. Spacecr. Rockets* **38**, 112–119 (2001).

⁹M. Furstoss, D. Thenail, and M. A. Galland, "Surface impedance control for sound absorption," *J. Sound Vib.* **203**, 219–236 (1997).

¹⁰O. Lacour, M. A. Galland, and D. Thenail, "Preliminary experiments on noise reduction in cavities using active impedance changes," *J. Sound Vib.* **230**, 69–99 (2000).

¹¹J. P. Smith, B. D. Johnson, and R. A. Burdisso, "A broadband passive-active sound absorption system," *J. Acoust. Soc. Am.* **106**, 2646–2652 (1999).

¹²S. F. Griffin, J. Gussy, S. A. Lane, J. D. Kemp, and R. L. Clark, "Innovative passive mechanisms for control of sound in a launch vehicle fairing," Proceedings of the 41st Structures, Structural Dynamics, and Materials Conference, Atlanta, GA, 2000.

¹³*Multi-Service Launch System Payload Planners Guide* (Martin Marietta Technologies, Inc., Denver, CO, 1994). Prepared for the USAF Space and Missile Command/CUBM.

¹⁴K. Dotson, R. L. Baker, and B. H. Sako, "Launch vehicle buffeting with aeroelastic coupling effects," *J. Fluids Struct.* **14**, 1145–1171 (2000).

¹⁵Calming bad vibes in launch vehicles, Ballistic Missile Defense Organization Update Newsletter, Summer 1999.

¹⁶P. M. Morse and H. Feshbach, *Methods of Theoretical Physics* (McGraw-Hill, New York, 1953).

¹⁷L. Cheng and J. Nicolas, "Radiation of sound into a cylindrical enclosure from a point-driven end plate with general boundary conditions," *J. Acoust. Soc. Am.* **91**, 1504 (1992).

¹⁸F. Fahy, *Sound and Structural Vibration* (Academic, London, 1985).

¹⁹J. K. Henry and Robert L. Clark, "Noise transmission from a curved panel into a cylindrical enclosure: Analysis of structural-acoustic coupling," *J. Acoust. Soc. Am.* **109**, 1456–1463.

²⁰R. L. Clark, K. D. Frampton, and D. G. Cole, "Phase compensation for feedback control of enclosed sound fields," *J. Sound Vib.* **195**, 710–718 (1996).

²¹T. Coleman, M. A. Branch, and A. Grace, *Optimization Toolbox User's Guide* (The Mathworks, Inc., Natick, MA, 1999), pp. 2-1–2-44. Third printing Revised for Version 2(R11).

²²K. Ogata, *Modern Control Engineering* (Prentice-Hall, Upper Saddle River, NJ, 1997), pp. 912–915.

²³J. Juang, *Applied System Identification* (Prentice-Hall, Englewood Cliffs, NJ, 1994).

²⁴J. Juang and R. S. Pappa, "An eigensystem realization algorithm for modal parameter identification and model reduction," *J. Guid. Control* **8**, 620–627 (1985).

²⁵R. L. Clark, G. P. Gibbs, and W. R. Saunders, *Adaptive Structures, Dynamics and Control* (Wiley, New York, 1998).

²⁶S. Skogestad and I. Postlewaite, *Multivariable Feedback Control* (Wiley, Chichester, England, 1996).

²⁷*Simulink, Dynamic Simulation for Matlab* (The Mathworks, Inc., Natick, MA, 1999). Revised for Version 2(R11).

²⁸*Robust Control Toolbox User's Guide* (The Mathworks, Inc., Natick, MA, 1999). Revised for Version 2(R11).

Design of an Aeroelastic Delta Wing Model for Active Flutter Control

John A. Rule*

Active Control eXperts, Inc., Cambridge, Massachusetts 02142

and

Robert E. Richard† and Robert L. Clark‡

Duke University, Durham, North Carolina 27708

Ongoing research into the active control of aeroelastic structures has resulted in a new model for the control of delta wing flutter. An analytical and numerical formulation for both the aerodynamic forcing and structural response of the wing was developed. The order of the aerodynamic model was reduced through balanced model reduction, yielding an accurate, low-order representation of the three-dimensional flowfield around the delta wing. This fully coupled aero/structural model was used to investigate the optimal placement of piezoelectric sensors and actuators to design an adaptive structure that emphasized control of the flutter mode. Previous work has shown that such control schemes can delay the onset of flutter to increased dynamic pressure. This work extends the practical use of reduced-order aerodynamic modeling to the realm of real-time control system design, while simultaneously applying recently developed techniques for open-loop design and selection of sensors and actuators. Results indicate that a single sensor/actuator pair can be designed to significantly extend the flutter boundary.

Nomenclature

A, B	= aerodynamic influence matrices
A_p	= piezoelectric patch area
AR	= wing aspect ratio
C_p	= piezoelectric capacitance
c	= wing chord
D	= wing displacement modeshape
d_{31}	= piezoelectric strain constant
E_p	= piezoelectric modulus
F	= aerodynamic force coefficient
G, \dots	= aerodynamic Gramian controllability/observability matrices
h	= wing thickness
h_p	= piezoelectric patch thickness
K	= structural stiffness matrix
K_p	= piezoelectric stiffness matrix
M	= structural mass matrix
M_p	= piezoelectric stiffness matrix
q	= piezoelectric charge
R	= generalized structural force
r	= generalized structural coordinate
s	= wing span
T	= balancing transformation matrix
TR	= wing taper ratio (tip chord/root chord)
U_∞	= freestream velocity
u	= normalized beam coordinate, chordwise
v	= normalized beam coordinate, spanwise
v_p	= piezoelectric applied voltage
w	= normal wash on wing
x	= wing physical coordinate, chordwise
y	= wing physical coordinate, spanwise
Γ	= vortex circulation
γ	= balanced aerodynamic coordinates
ϕ	= assumed spatial modeshape function

ϵ_1^S	= piezoelectric dielectric constant
θ	= electromechanical coupling matrix
κ	= spanwise spatial wave number
ν_p	= piezoelectric Poisson ratio
σ	= chordwise spatial wave number
τ	= dimensionless aerodynamic time
ψ	= spanwise assumed mode
ψ	= chordwise assumed mode

Introduction

A COMBINATION of efforts is underway to create a computational and experimental model for the study of aeroelastic control. As each layer of complexity is added to the model, which must accurately capture the structural mechanics of a delta wing, the aerodynamic loads on that structure, the electromechanical behavior of surface-mounted piezoelectric sensors and actuators, and the implementation of a real-time adaptive control algorithm, real-time design constraints demand that each component of the model be reduced to its essential physics. To this end, work has progressed to achieve a low-order model that embodies the behavior of the true physical system for initial adaptive structure design.

The present research effort began with a focus on aerodynamic model reduction.¹ A summary of this issue can be stated as follows: The choice to spatially discretize the governing equations of fluid flow, whether linearized or full potential, Euler or Navier–Stokes, yields a remarkably inefficient representation of the flow from a computational standpoint. The number of degrees of freedom, or states, used to model the flow in this manner far exceeds the optimal number of well-chosen, spatially continuous, distributed states that might otherwise be used to represent the flow. Recent model reduction techniques focus on finding, or at least approaching, these optimal states.^{2–6}

The first attempts to construct reduced-order aerodynamic models were based on standard eigenanalysis techniques.^{2,3} Under the assumption that the discretized numerical model could be expressed as a generalized eigenvalue problem, the eigenmodes of the fluid were found. Model reduction was achieved by retaining only lightly damped modes, neglecting the rest. Unfortunately, accurate solutions required substantial numbers of modes to be retained, limiting the amount of reduction that could be achieved. More recent developments have focused on the use of proper orthogonal decomposition^{7,8} or balanced realization^{5,6,9–11} instead. Both techniques have at their heart a singular value decomposition that finds

Received 12 November 1999; revision received 17 January 2001; accepted for publication 20 January 2001. Copyright © 2001 by the authors. Published by the American Institute of Aeronautics and Astronautics, Inc., with permission.

*Senior R&D Engineer, 215 First Street. Member AIAA.

Research Assistant, Department of Mechanical Engineering and Materials Science.

Professor, Department of Mechanical Engineering and Materials Science. Member AIAA.

the strongest path through the aerodynamic system between system inputs, typically wing or control surface motion, and system outputs, such as aerodynamic loads. The present analysis makes use of balanced realization to reduce the size of a three-dimensional, incompressible vortex lattice model from 1000 states down to roughly the number of structural states, in this study 50, used to model the delta wing.

A simple Ritz method is employed for the structural model of the delta wing, following the work of Andersen.¹² Sets of beam displacement functions are assumed in the chordwise (free-free) and spanwise (clamped-free) directions of a rectangular plate, with products of these functions giving the assumed displacement at any point on the wing. This plate is then mapped into a triangular domain. Mass and stiffness matrix integrals are performed in a rectangular computational domain and converted to the triangular physical domain through an appropriate coordinate transformation. An additional transformation is employed to convert from the assumed structural modes to an approximation of the natural modes of the system, using standard eigenanalysis techniques. The formulation is sufficiently general that it can model plates of arbitrary constant taper, from rectangular all of the way down to triangular, and arbitrary aspect ratio. The present work deals only with the case of a right-triangular delta wing.

The computational aeroelastic model outlined was used to perform control system design studies, with the goal of delaying the onset of wing flutter¹³⁻¹⁵ to a higher flow velocity. The linear theory flutter boundary was identified, and piezoelectric sensors and actuators were placed on the wing based on an open-loop spatial optimization design procedure.¹⁶⁻²⁰ Under this procedure, many candidate sensors and actuators, of varying size, shape, and orientation, were placed on the wing. With piezomass and stiffness effects neglected, electromechanical coupling matrices were computed for all of the piezos.²¹ An appropriate performance metric was chosen for flutter control, resulting in a sensor and actuator displaying maximum coupling to selected modes in the bandwidth of interest, with a penalty applied to out-of-bandwidth coupling.¹⁹

A controller was designed for operation at a flow velocity slightly below the linear flutter boundary. Closed-loop performance was then assessed based on the predicted increase in flutter velocity. The candidate sensor/actuator pair and controller discussed in this paper resulted in a 20% increase in predicted flutter velocity.

Theoretical Development

The fully coupled aeroelastic model with embedded piezoelectric sensors and actuators is developed hereafter as a series of state-space models. First, a simple structural model of the wing is developed based on the Ritz method (see Ref. 12). The structural model includes a brief review of the correct modeling of the electromechanical coupling between the piezoelectric sensors and actuators and the wing. Next, the unsteady aerodynamic equations governing the three-dimensional flow about the model delta wing are derived. Aerodynamic model reduction is discussed as a way to create an accurate, low-order representation of the flow. Finally, an outline is

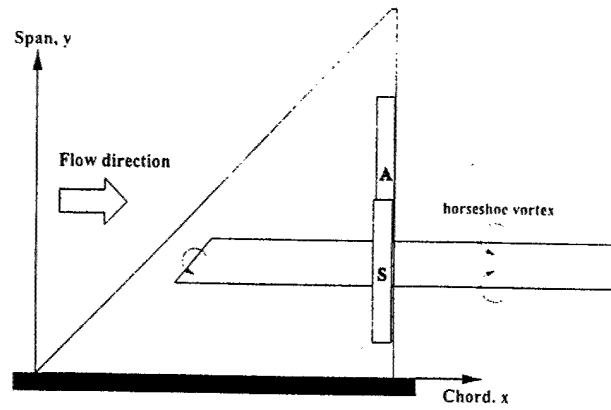


Fig. 1 Delta wing geometry with aerodynamic grid and sensor *S* and actuator *A* piezoelectric transducers.

With standard aerodynamic nomenclature, wing taper ratio is defined as the ratio of the wing tip chord over the root chord, and aspect ratio is defined in terms of root chord, span, and taper ratio as

$$AR \equiv \frac{\text{span}^2}{\text{wing area}} = \frac{2}{1 + TR} \left(\frac{s}{c} \right) \quad (1)$$

To facilitate the use of clamped-free and free-free beam functions later on, any wing fitting the preceding description can be mapped to a unit square domain, referred to here as normalized beam coordinates. The transformations of Eq. (2) map any point on the wing from physical coordinates to normalized beam coordinates.

$$u = \frac{x/c - 2(1 - TR)y/s}{1 - 2(1 - TR)y/s}, \quad v = \frac{2y}{s} \quad (2)$$

and a corresponding pair of inverse transformations maps them back.

$$x/c = u + (1 - TR)(1 - u)v, \quad y/s = v/2 \quad (3)$$

For this study, a delta wing with 45-deg leading-edge sweep is considered, as shown in Fig. 1. This corresponds to a taper ratio of zero and an aspect ratio of four.

In accordance with the Ritz method, the total transverse displacement at any point on the wing can be expressed as a time-dependent weighted sum of assumed spatial mode shape functions.

$$D(x, y, t) = \sum_{n=1}^N \delta_n(x, y) r_n(t) \quad (4)$$

These spatial shape functions are in turn products of assumed beam modes in the chordwise and spanwise directions:

$$\delta_n(x, y) = \psi_{i(n)}[u(x, y)] \times \phi_{j(n)}[v(x, y)] \quad (5)$$

where $\psi_i(u)$ are the one-dimensional free-free beam modes in the chordwise direction of the plate.

$$\psi_i(u) = \begin{cases} 1 & i = 1 \\ \sqrt{3}(1 - 2u) & i = 2 \\ [\cos(\sigma_i u) + \cosh(\sigma_i u)] - \left[\frac{\cos(\sigma_i) - \cosh(\sigma_i)}{\sin(\sigma_i) - \sinh(\sigma_i)} \right] [\sin(\sigma_i u) + \sinh(\sigma_i u)] & i \geq 3 \end{cases} \quad (6)$$

given of the open-loop design procedure used to select spatially optimal sensor and actuator locations for flutter control.

Delta Wing Structural Model

The delta wing model under consideration is assumed to behave as a thin plate of uniform mass and stiffness. The following general formulation allows for the treatment of a whole family of rectilinear wings of arbitrary constant taper ratio and aspect ratio through the use of a transformation to normalized beam mode coordinates, defined hereafter.

and $\phi_j(v)$ are the one-dimensional clamped-free beam modes in the spanwise direction.

$$\phi_j(v) = -[\cos(\kappa_j v) - \cosh(\kappa_j v)] - \left[\frac{\sin(\kappa_j) - \sinh(\kappa_j)}{\cos(\kappa_j) + \cosh(\kappa_j)} \right] \times [\sin(\kappa_j v) - \sinh(\kappa_j v)] \quad j \geq 1 \quad (7)$$

These functions are orthonormal over the range $0 < u, v < 1$ and have associated wave numbers given in Table 1.

Table 1 Approximate spatial wave numbers for free-free and clamped-free beam modes

i	σ_i	j	κ_j
3	4.7300407	1	1.8751041
4	7.8532046	2	4.6940911
5	10.995608	3	7.8547574
≥ 6	$(\pi/2)(2i+1)$	≥ 4	$(\pi/2)(2j-1)$

With a standard application of Lagrange's equations (see Ref. 22) using the assumed mode shapes of Eqs. (5-7), a system of linear equations governing the motion of the wing results,

$$M\ddot{r} + Kr = R \quad (8)$$

The integrals that define the mass and stiffness matrices are most easily evaluated in normalized beam coordinates. In these coordinates, the domain of integration is square, with limits from zero to one in both directions.

Piezoelectric patches are added to the structural model of Eq. (8) following a method first suggested by Hagood, et al. in Ref. 21. Considerable simplification of the necessary mathematics exists for the case of rectangular surface-mounted patches with an electric field applied normal to the surface.²² For this case, an electromechanical coupling matrix results for each patch,

$$\Theta = \frac{d_{31} E_p}{1 - \nu_p} \left(\frac{h + h_p}{2c^2} \right) \int_{x_1}^{x_2} \int_{y_1}^{y_2} \left[\frac{\partial^2 \delta_n(x, y)}{\partial^2 x} + \frac{\partial^2 \delta_n(x, y)}{\partial^2 y} \right] dx dy \quad (9)$$

Each piezoelectric patch will contribute additional mass and stiffness to the structure as well. Under the assumption that the electric field across each piezo takes the form of an applied voltage, the new structural system, with piezoelectric actuators is

$$(M + M_p)\ddot{r} + (K + K_p)r = R + \Theta v_p \quad (10)$$

If these same piezoelectric patches are used as sensors, the measured charge is given by

$$q = \Theta^T r + C_p v_p \quad (11)$$

where the piezoelectric capacitance is defined for each patch in terms of patch area, thickness, and dielectric constant as $C_p = \epsilon_1^S A_p / h_p$.

A complete state-space structural model of the delta wing, with piezoelectric voltages and generalized modal forces as inputs and piezoelectric charges, modal position, and modal velocity as outputs, is given by

$$\begin{Bmatrix} \dot{r} \\ \ddot{r} \\ q \\ r \\ \dot{r} \end{Bmatrix} = \begin{bmatrix} 0 & I & 0 & 0 \\ -\hat{M}^{-1}\hat{K} & 0 & -\hat{M}^{-1}\Theta & -\hat{M}^{-1} \\ \Theta^T & 0 & C_p & 0 \\ I & 0 & 0 & 0 \\ 0 & I & 0 & 0 \end{bmatrix} \begin{Bmatrix} r \\ \dot{r} \\ v_p \\ R \end{Bmatrix} \quad (12)$$

This structural model has been validated against the classical results of Ref. 23 for a variety of rectangular, tapered, and triangular plates, including the delta wing configuration under consideration here.

Baseline Aerodynamic Model

The aerodynamic method used for discussion purposes here is the unsteady, incompressible vortex lattice method developed by Hall in Ref. 2. The details of that formulation will not be repeated here due to length considerations, but it will be assumed that the appropriate discrete-time aerodynamic influence matrices have been constructed as a starting point. Refer back to Fig. 1, which shows the aerodynamic grid laid on top of the delta wing plate. The wing is assumed to be symmetric about the midspan, $y = 0$, and this symmetry is accounted for in the aerodynamic influence matrices discussed hereafter.

In general, the strengths of the vortices modeling the flow about the wing at time $n+1$ are related to the vortex strengths at time n

and the normal wash on the wing at the mid-time step $n + \frac{1}{2}$ by a pair of aerodynamic influence matrices as follows:

$$A\{\Gamma/U_\infty c\}^{n+1} + B\{\Gamma/U_\infty c\}^n + \{w/U_\infty\}^{n+\frac{1}{2}} = 0 \quad (13)$$

For simplicity, restrict the system input, which in this case is the normal wash on the wing, to be a function of wing assumed modal displacement and velocity only,

$$\left\{ \frac{w}{U_\infty} \right\}^{n+\frac{1}{2}} \equiv W \begin{Bmatrix} r/c \\ \dot{r}/U_\infty \end{Bmatrix} \quad (14)$$

Vortex lattice methods typically require a discrete-time formulation, as can be seen in Eq. (13). This is partly due to restrictions on vortex spacing, which must be uniform in the chordwise direction, fixing the wake convection time step to the grid spacing. Rather than accepting these limitations, it is convenient to convert to a continuous time model via a series expansion,

$$\begin{aligned} \Gamma^n &= \Gamma^{n+\frac{1}{2}} + \left(-\frac{\Delta\tau}{2} \right) \frac{d\Gamma^{n+\frac{1}{2}}}{d\tau} + \dots \\ \Gamma^{n+1} &= \Gamma^{n+\frac{1}{2}} + \left(-\frac{\Delta\tau}{2} \right) \frac{d\Gamma^{n+\frac{1}{2}}}{d\tau} + \dots \end{aligned} \quad (15)$$

where $\tau \equiv U_\infty t/c$ is the standard dimensionless aerodynamic timescale. The constant $\Delta\tau$ is set by the aerodynamic grid resolution. After substitution of Eq. (15) into Eq. (13) and some manipulation, the following system results:

$$\begin{aligned} \frac{d}{d\tau} \left\{ \frac{\Gamma}{U_\infty c} \right\} &= -\frac{2}{\Delta\tau} [A - B]^{-1} [A + B] \left\{ \frac{\Gamma}{U_\infty c} \right\} \\ &\quad - \frac{2}{\Delta\tau} [A - B]^{-1} W \begin{Bmatrix} r/c \\ \dot{r}/U_\infty \end{Bmatrix} \\ &\equiv A' \left\{ \frac{\Gamma}{U_\infty c} \right\} + B' \begin{Bmatrix} r/c \\ \dot{r}/U_\infty \end{Bmatrix} \end{aligned} \quad (16)$$

Note that the time index, $n + \frac{1}{2}$, is no longer necessary and has been dropped.

The generalized aerodynamic forces are calculated by integrating the product of the surface pressure on the wing times each assumed mode shape over the wing surface,

$$R_n = \iint \Delta p(x, y) \delta_n(x, y) dx dy \quad (17)$$

where pressure is calculated from the vortex strengths using the linearized Bernoulli equation,

$$\frac{\Delta p(x, y)}{\rho_\infty} = \frac{\partial \Gamma}{\partial t} + U_\infty \frac{\partial \Gamma}{\partial x} \quad (18)$$

After some standard manipulations,²⁴ the generalized forces on the wing can be written as a vector of aerodynamic coefficients

$$\hat{R} \equiv \frac{R}{1/2 \rho_\infty U_\infty^2 S} = F_1 \left\{ \frac{\Gamma}{U_\infty c} \right\} + F_2 \frac{d}{d\tau} \left\{ \frac{\Gamma}{U_\infty c} \right\} \quad (19)$$

There is now sufficient information to create an aerodynamic state-space model,

$$\left\{ \frac{(d/d\tau)(\Gamma/U_\infty c)}{\hat{R}} \right\} = \begin{bmatrix} A' & B' \\ F_1 + F_2 A' & F_2 B' \end{bmatrix} \begin{Bmatrix} \Gamma/U_\infty c \\ r/c \\ \dot{r}/U_\infty \end{Bmatrix} \quad (20)$$

There are several important points to note here. First, all of the quantities in the aerodynamic state-space model are nondimensional, as is traditional in aerodynamic analyses. As a consequence, manipulations of the model, such as the model reduction technique that is about to be discussed, are independent of flow velocity U_∞ and need only be performed once for a given

wing geometric configuration. Care must be taken when coupling this model to the structural model of the preceding section, which was constructed with dimensional force inputs and dimensional position and velocity outputs. Also, the structural and aerodynamic timescales differ between Eq. (12) and Eq. (20), by the constant factor U_∞/c .

Reduced-Order Aerodynamic Model

For a typical calculation using the model of the preceding section, one might choose to represent the aerodynamics about the wing with a vortex lattice consisting of 8 chordwise by 10 spanwise vortices, and track 4 chords of wake of the same lattice density. This translates to a 400-state model for the aerodynamics alone, without accounting for the states due to the structural model or controller. Note that this is a very low grid density. Flutter calculations would typically require only the first few dozen natural structural modes, or on the order of 50 additional states. The dynamic compensator used for control would be expected to have even fewer states because only a single mode destabilizes the aeroelastic system. For design purposes, the size of the aerodynamic state-space model is unacceptable and provides the necessary motivation to consider balanced model reduction.

Aerodynamic systems provide an ideal opportunity for the application of balanced model reduction^{5,6} because it is frequently the case that a large number of states must be used to transmit information from a small number of inputs (system geometry, surface position, and velocity), to a small number of outputs (net lift, generalized forces on each structural mode), which is exactly the case

here. From a systems point of view, the details of the flow are unimportant; the aerodynamics are simply providing a transmission path from wing geometry to forces. Creating a balanced realization of this system requires the application of a similarity transformation such that the resulting system controllability and observability gramians (see Ref. 25) are equal and diagonal.¹⁰ Such a system is said to be internally balanced.

Under the assumption that a transformation matrix exists such that

$$\begin{aligned} G'_c &= T G_c T^T \\ G'_o &= T^{-T} G_o T^{-1} \end{aligned} \quad G'_c = G'_o = \text{diag}(\lambda) \quad (21)$$

the balanced aerodynamic state-space model now takes the form

$$\left\{ \frac{(d/d\tau)\{\gamma/U_\infty c\}}{\hat{R}} \right\} = \begin{bmatrix} \tilde{A} & \tilde{B} \\ \tilde{C} & F_2 B' \end{bmatrix} \begin{Bmatrix} \gamma/U_\infty c \\ r/c \\ \dot{r}/U_\infty \end{Bmatrix} \quad (22)$$

where

$$\begin{aligned} \gamma &= T \Gamma, & \tilde{A} &= T A' T^{-1}, & \tilde{B} &= T B' \\ \tilde{C} &= [F_1 + F_2 A'] T^{-1} \end{aligned} \quad (23)$$

The primary benefit of the system in this form is that the diagonal elements of the balanced gramian matrix, defined in Eq. (21), now provide an indication of the relative importance of a particular state to the system input/output path. Large values of λ indicate states that are both highly controllable and highly observable, whereas smaller values signify states that are neither very controllable nor observable. In the present context, the first few states provide the strongest transmission path through the aerodynamics from the structural inputs of delta wing position and velocity to the generalized forces acting on the wing. Algorithms are available, for example, `balreal()` in MATLAB[®],²⁶ for finding the transformation matrix T . This is computationally expensive, but must be done only once during the design process.

Control System Design

An earlier section detailed the method for incorporating piezoelectric sensors and actuators into the structural model for control. The choice of placement of those sensors and actuators and the design of an appropriate compensator for aeroelastic flutter control are the topics of this section. To begin, consider the block diagram of the coupled aeroelastic system, presented in Fig. 2. The system has been cast here in two-port form.²² Note that the aerodynamics simply act as a flow-speed-dependent feedback loop to the structural system.

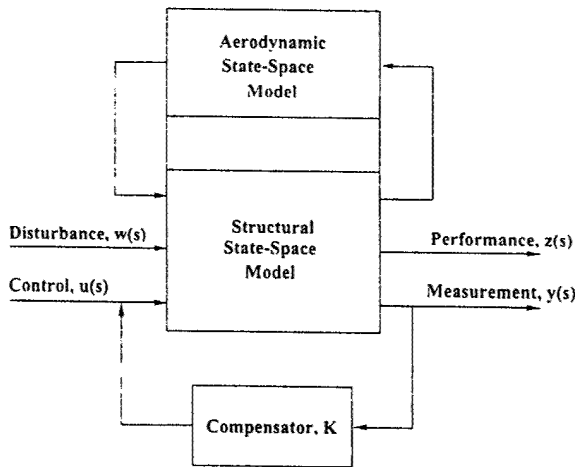


Fig. 2 Block diagram of coupled aeroelastic model cast in two-port form for controller design.

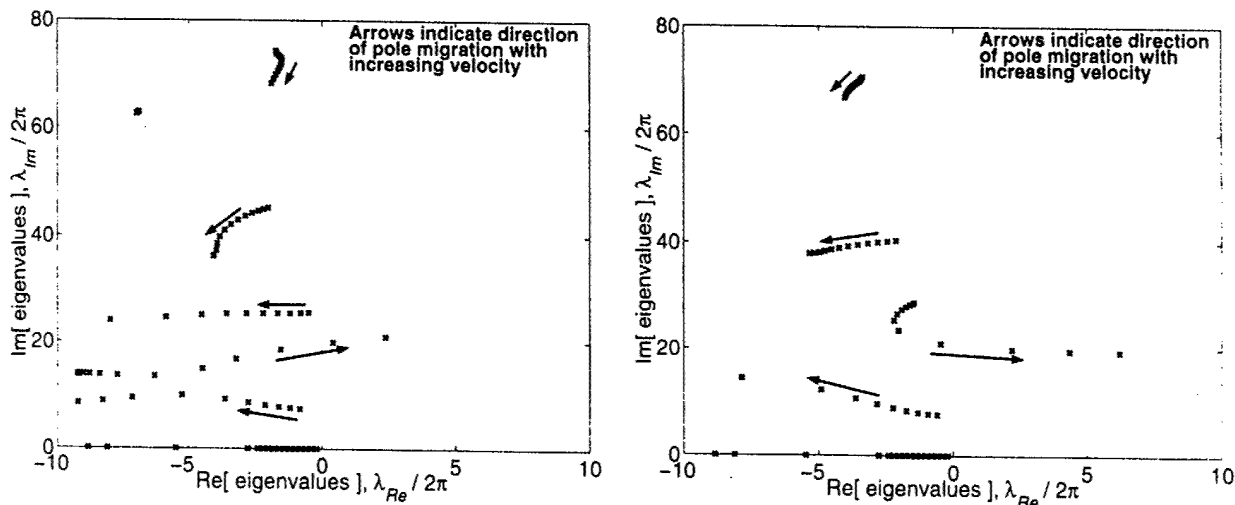


Fig. 3 Open-loop (left) and closed-loop (right) poles at 5-m/s increments from 5 to 60 m/s.

A representative model delta wing (see Table 2 for physical parameters) was determined to have a linear flutter speed of 45 m/s, with the instability occurring in the second aeroelastic mode (see Fig. 3 for open- and closed-loop poles over a range of flow velocities.) A disturbance input was constructed to excite the first 15 modes of the structure at just below this operating condition. The performance metric was chosen to be a weighted combination of the first 15 modal velocities. With the open-loop spatial optimization technique of Smith and Clark,²⁰ an assortment of 726 candidate sensors and actuators were distributed over the surface of the wing, and the electromechanical coupling matrix for each was computed. All of the candidate patches were assumed to be 0.2-mm-thick single sheet lead zirconate titanate (PZT) from Piezo Systems, Inc. The trial patch set consisted of patches of the following discrete sizes: 1×6 ,

1.5×4 , 2×3 , 3×2 , 4×1.5 , and 6×1 in. Note that all patches have an area of six in.² and that the repeating of the dimensions reflects the two possible orientations of each patch relative to the wing chord. The candidates were overlapped by an automatic placement algorithm to provide complete coverage of the wing, resulting in approximately equal numbers of each size.

With an algorithm first employed by Lim¹ and Gawronski,¹⁶ the approximate Hankel singular values (HSVs) were estimated from a discrete time representation of the open-loop ($K = 0$), coupled aeroelastic system. The HSVs can be used to determine the open-loop controllability and observability gramians and provide an effective measure of the sensor or actuator's ability to couple to particular modes of the system. The goal, of course, is to find a sensor/actuator pair that strongly couples to a select few modes within the bandwidth of interest (here, below 200 Hz) and exhibits limited coupling to out-of-bandwidth modes, providing a natural rolloff of the control loop with frequency. The advantage of the Lim and Gawronski method is that it does not require a full singular value decomposition of the system, which could be computationally expensive, but instead relies on the assumption of lightly damped complex modes in the system to estimate the HSVs. Again, following Smith and Clark,²⁰ a modal selection vector was chosen to emphasize coupling to the first four structural modes. The optimal sensor to actuator pair was selected from $(726 \times 726)/2 = 263,538$ unique possible combinations in just a few seconds on a desktop personal computer.

A simplified system matrix in modal coordinates is provided in Fig. 4 for illustration purposes. Note that the system has been divided into three zones: in bandwidth, out of bandwidth, and real poles. The method of Lim and Gawronski¹⁶ is only valid for lightly damped, complex poles. Thus, the real poles, which in this case correspond to the heavily damped aerodynamic states, are truncated prior to performing the HSV estimates. The performance metric rewards coupling to modes that are in bandwidth and penalizes coupling to modes that are out of bandwidth. The resulting spatially optimal sensor/actuator pair are shown in Fig. 1.

The final step in model construction was compensator design. H_2 -synthesis was used to design a controller at a single flow condition just below the flutter velocity. With reference to the two-port block diagram of Fig. 2, the disturbance and performance metrics that were used for actuator selection were used for controller design. The control input was the single spatially optimal actuator, and the measurement was the corresponding optimal sensor. In addition, both process noise and sensor noise were included as additional disturbance inputs, as is typical of linear quadratic Gaussian design,^{27,28} and the performance path was augmented by a control effort penalty. The cost function was constructed from the square of the two-norm between the performance (error) z and the

Table 2 Physical parameters of model delta wing

Parameter	Value
Chord	0.381 m (15 in.)
Semispans	0.381 m
Thickness	0.794×10^{-3} m
Density	3.36×10^3 Kg/m ³
Young's modulus	71.0×10^9 N/m ²

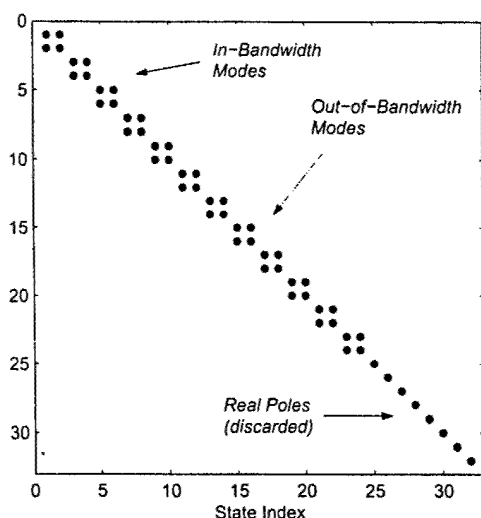


Fig. 4 System matrix demonstrating classification of in-bandwidth and out-of-bandwidth modes and real poles.

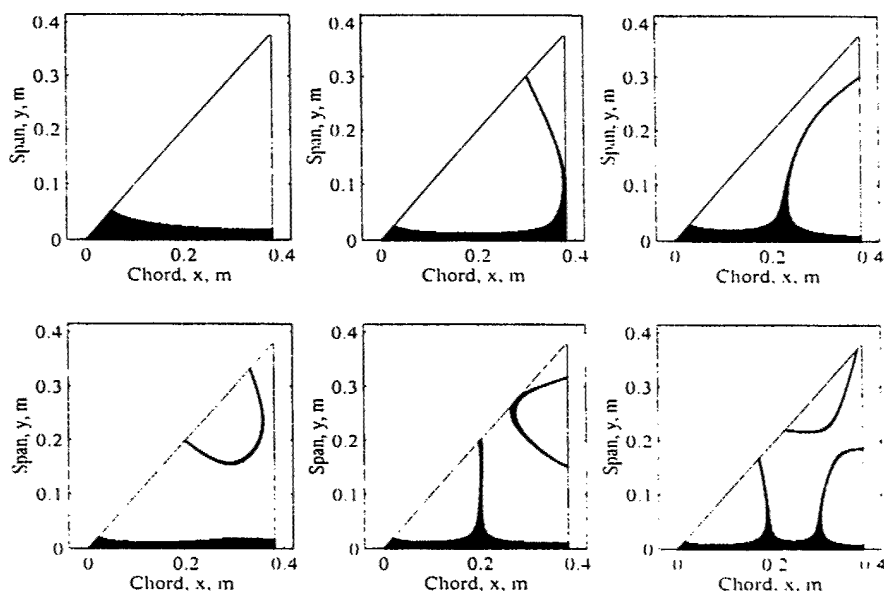


Fig. 5 Nodal lines of first six natural vibrational modes of a right triangular plate (clamped along x axis).

disturbance w . The cost function can be expressed mathematically as follows:

$$J = \lim_{t \rightarrow \infty} E[z^T(t)z(t)] = \|T_{zw}\|_2^2 \quad (24)$$

where T_{zw} is the closed-loop transfer function between z and w . The design process resulted in a 25-state compensator. This compensator was then used over a range of flow velocities to evaluate closed-loop system performance.

Results and Discussion

Extensive work was done to validate both the structural and aerodynamic models independently, before coupling them together. The work of Leissa²³ regarding the vibration of plates, including a right-triangular wing, was used to check the accuracy of the assumed modes plate model given by Eq (12). Both natural frequencies and computed natural mode shapes compared favorably between the computational model and the experimentally tabulated results on page 219 of Ref. 23. The first six modes are shown in Fig. 5 for comparison. The authors have found it helpful to refer to these nodal line plots when assessing sensor and actuator placement schemes on the wing structure.

The aerodynamic model reduction technique was checked for accuracy by running several classical unsteady aerodynamics problems with both the full- and reduced-order models. Rule et al. demonstrated in Ref. 6 that the balanced aerodynamic states in a two-dimensional flow can be related to analytical potential flow solutions. Work is ongoing to address this issue with regard to the

delta wing. For the problem at hand, the important question is the amount of model reduction that is achieved using the balanced realization technique. The values of the internally balanced gramian matrix for the aerodynamic system, defined in Eq. (21), are plotted in Fig. 6. Recall that these values provide a measure of the importance of the corresponding state to the input/output path of interest. Furthermore, the cumulative sum of a subset of gramian values can be used to determine the fractional contribution of that subset to the controllability (or observability) of the full model. This provides a convenient criterion for retaining or neglecting states. A conservative cutoff criterion requiring the reduced model to retain 99.9% of the controllability of the full model was employed in this study. This resulted in a reduced-order aerodynamic model of only 40 states, as indicated in Fig. 6. This is exactly 10% of the original 400 states, with only a 0.1% loss of accuracy.

Next, characterization of the open-loop aeroelastic system was carried out before starting the controller design process. With the test configuration of Table 2, the system eigenvalues were examined over a range of flow velocities from 5 to 60 m/s. A root locus of these values is plotted in Fig. 3. In Fig. 3, the modes that are predominantly structural appear as densely packed lines that originate at each of the first five natural frequencies of the wing (7.6, 29, 41, 71, and 96 Hz). The aerodynamics have the effect of causing pole migration, modifying both the frequency and damping ratio of each mode. The system goes unstable when the pole associated with the second structural mode crosses into the right half-plane at approximately 45 m/s. The remaining sparsely distributed poles in Fig. 3 are primarily associated with the aerodynamics; they move radially away from the origin, exhibiting a linear variation in frequency with velocity, as shown in Ref. 1.

After the selection of the spatially optimal sensor/actuator pair based on modal coupling near the flutter boundary, a compensator was designed to stabilize the system. The success of this controller design was evaluated by comparing the open- and closed-loop frequency response in the disturbance-to-performance path at the design point, as shown in Fig. 7. In Fig. 7, the open-loop resonant peak clearly dominates the system response, whereas in the closed-loop system, the instability has been eliminated. The off-design performance of the controller was satisfying as well; the system remained stable, though with little performance, at low velocity. Above the design point, the closed-loop system is stable up to a velocity of 54 m/s, which represents a 20% increase in the flutter boundary.

Conclusions

A model was developed to investigate the aeroelastic behavior and active control of a family of thin rectilinear wings of arbitrary aspect ratio and taper ratio. Performance of this model has been detailed here for the case of a right-triangular delta wing. The

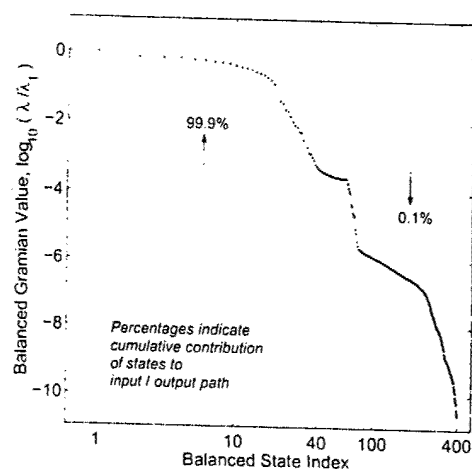


Fig. 6 Controllability/observability Gramian resulting from aerodynamic system balancing.

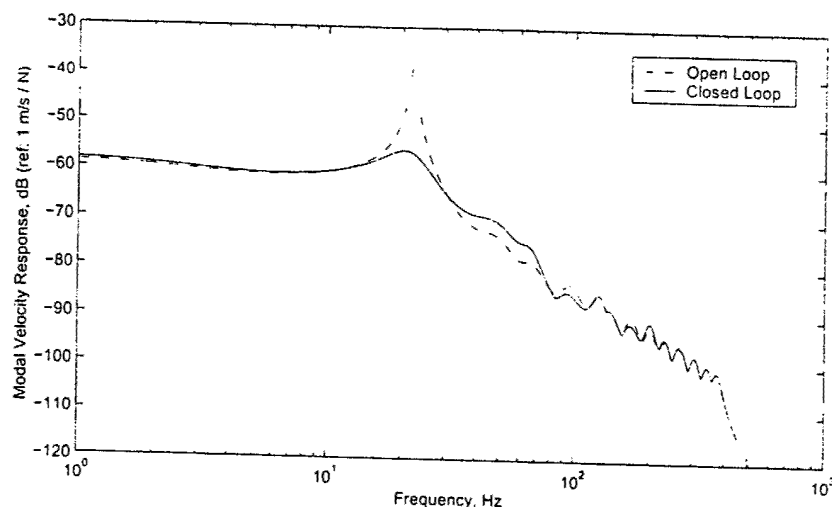


Fig. 7 Maximum singular values in the disturbance (modal forcing) to performance (modal velocity) path of the open- and closed-loop systems at the nominal design condition.

fully coupled model incorporated the use of balanced realization for aerodynamic model reduction, resulting in an accurate, computationally efficient model only 10% the size of the baseline aerodynamic model. A new spatial optimization technique was employed for sensor and actuator placement, resulting in a 20% increase in the flutter boundary of the system. The model provides a fast, accurate way to investigate various adaptive structural wing designs for control. Results from this study serve to demonstrate that adaptive structures can be designed to facilitate control. Furthermore, through design, performance can be directed at specific structural modes, simplifying the resulting system.

Acknowledgments

This research was supported by the Air Force Office of Scientific Research under Grants F49620-98-1-0383 and F49620-96-1-0385, with Brian Sanders serving as Technical Monitor. The authors would like to thank Earl H. Dowell for many helpful discussions regarding aeroelastic behavior and Kenneth C. Hall for his insight on reduced-order aerodynamic modeling.

References

- ¹Dowell, E. H., Hall, K. C., and Romanowski, M. C., "Eigenmode Analysis in Unsteady Aerodynamics: Reduced Order Models," *Applied Mechanics Review*, Vol. 50, No. 6, 1997, pp. 371-386.
- ²Hall, K. C., "Eigenanalysis of Unsteady Flows About Airfoils, Cascades, and Wings," *AIAA Journal*, Vol. 32, No. 12, 1994, pp. 2426-2432.
- ³Dowell, E. H., "Eigenmode Analysis in Unsteady Aerodynamics: Reduced-Order Models," *AIAA Journal*, Vol. 34, No. 8, 1996, pp. 1578-1583.
- ⁴Romanowski, M. C., and Dowell, E. H., "Reduced-Order Euler Equations for Unsteady Aerodynamic Flows: Numerical Techniques," *AIAA Paper 96-0528*, Jan. 1996.
- ⁵Baker, M., "Model Reduction of Large, Sparse, Discrete Time Systems with Application to Unsteady Aerodynamics (Finite Element, Lyapunov Equations)," Ph.D. Dissertation, Univ. of California, Los Angeles, CA, May 1996.
- ⁶Rule, J. A., Cox, D. E., and Clark, R. L., "Aerodynamic Model Reduction Through Balanced Realization," *AIAA Journal* (to be published).
- ⁷Florea, R., Hall, K. C., and Cizmas, P. G. A., "Reduced-Order Modeling of Unsteady Viscous Flows in a Compressor Cascade," *AIAA Journal*, Vol. 36, No. 6, 1998, pp. 1039-1048.
- ⁸Romanowski, M. C., "Reduced-Order Unsteady Aerodynamic and Aeroelastic Models Using Karhunen-Loève Eigenmodes," *AIAA Paper 96-3981*, Sept. 1996.
- ⁹Baker, M. L., Mingori, D. L., and Goggin, P. J., "Approximate Subspace Iteration for Constructing Internally Balanced Reduced-Order Models of Unsteady Aerodynamic Systems," *Proceedings of the 37th AIAA/ASME/ASCE/ASC Structures, Structural Dynamics, and Materials Conference*, AIAA, Reston, VA, 1996, pp. 1070-1085.
- ¹⁰Moore, B. C., "Principal Component Analysis in Linear Systems: Controllability, Observability, and Model Reduction," *IEEE Transactions on Automatic Control*, Vol. AC-26, No. 1, 1981, pp. 17-32.
- ¹¹Laub, A. J., Heath, M. T., Paige, C. C., and Ward, R. C., "Computation of System Balancing Transformations and Other Applications of Simultaneous Diagonalization Algorithms," *IEEE Transactions on Automatic Control*, Vol. AC-32, No. 1, 1987, pp. 115-122.
- ¹²Andersen, B. W., "Vibration of Triangular Cantilever Plates by the Ritz Method," *Journal of Applied Mechanics*, Dec. 1954, pp. 365-370.
- ¹³Theodoresen, T., "General Theory of Aerodynamic Instability and the Mechanism of Flutter," NACA TR 496, 1935.
- ¹⁴Bisplinghoff, R. L., Ashley, H., and Halfman, R. L., *Aeroelasticity*, Addison Wesley Longman, Reading, MA, 1955, pp. 527-626.
- ¹⁵Dowell, E. H., *A Modern Course in Aeroelasticity*, Kluwer Academic, Dordrecht, The Netherlands, 1989, Chap. 2.
- ¹⁶Lim, K. B., and Gawronski, W., "Hankel Singular Values of Flexible Structures in Discrete Time," *Journal of Guidance, Control, and Dynamics*, Vol. 19, No. 6, 1996, pp. 1370-1377.
- ¹⁷Gawronski, W., and Lim, K. B., "Balanced Actuator and Sensor Placement for Flexible Structures," *International Journal of Control*, Vol. 65, No. 1, 1996, pp. 131-145.
- ¹⁸Lim, K. B., "Disturbance Rejection Approach to Actuator and Sensor Placement," *Journal of Guidance, Control, and Dynamics*, Vol. 20, No. 1, 1997, pp. 202-204.
- ¹⁹Clark, R. L., and Cox, D. E., "Band-Limited Actuator and Sensor Selection for Disturbance Rejection," *Journal of Guidance, Control, and Dynamics*, Vol. 22, No. 5, 1999, pp. 740-743.
- ²⁰Smith, G. C., and Clark, R. L., "Adaptive Structure Design Through Optimal Spatial Compensation," *Proceedings of Active-99, Noise Control Foundation*, Poughkeepsie, NY, 1999, pp. 1013-1024.
- ²¹Hagood, N. W., Chung, W. H., and von Flotow, A., "Modelling of Piezoelectric Actuator Dynamics for Active Structural Control," *Proceedings of the 31st AIAA/ASME/ASCE/AHS Structures, Structural Dynamics, and Materials Conference*, AIAA, Washington, DC, 1990, pp. 2242-2256.
- ²²Clark, R. L., Saunders, W. R., and Gibbs, G. P., *Adaptive Structures*, Wiley, New York, 1998, pp. 27-30.
- ²³Leissa, A. W., *Vibration of Plates*, Acoustical Society of America, Sewickley, PA, 1993, pp. 195-200.
- ²⁴Katz, J., and Plotkin, A., *Low Speed Aerodynamics, From Wing Theory to Panel Methods*, McGraw-Hill Series in Aeronautical and Aerospace Engineering, McGraw-Hill, New York, 1991, pp. 421-435.
- ²⁵Skogestad, S., and Postlewaite, I., *Multivariable Feedback Control*, Wiley, Chichester, England, U.K., 1996, pp. 122-126.
- ²⁶*MATLAB Control System Toolbox User's Guide*, Vol. 4, MathWorks, Inc., Natick, MA, 1998, pp. 11-16-11-18.
- ²⁷Hong, J., and Bernstein, D. S., "Bode Integral Constraints, Collocation, and Spillover in Active Noise and Vibration Control," *IEEE Transactions on Control System Technology*, Vol. 6, 1998, pp. 111-120.
- ²⁸Doyle, J. C., Glover, K., Khargonekar, P. P., and Francis, B. A., "State-Space Solutions to Standard H_2 and H_∞ Control Problems," *IEEE Transactions on Automatic Control*, Vol. 34, No. 8, 1989, pp. 831-847.

Adaptive structures: Compensators by design

Robert L. Clark^{a)}

(Received 2000 April 03; revised 2000 August 30; accepted 2000 September 10)

In the design of adaptive structures, actuator and sensor selection are critical to closed-loop stability and performance. In theory, for feedback control, all one requires is that the system is detectable and reachable from the chosen array of transducers. Loop shaping is typically accomplished through the design of a dynamic compensator based upon trade-offs between desired performance and stability. A crude method of loop-shaping through actuator/sensor selection is provided herein. A fast, simple, open-loop method of choosing actuators and sensors that couple to structural modes contributing to the performance path while concurrently penalizing coupling to modes not in this path is provided. Examples of adaptive structures designed for vibration, structural acoustic, and aeroelastic control are presented. © 2001 Institute of Noise Control Engineering.

Primary subject classification: 38.3; Secondary subject classification: 38.2

1. INTRODUCTION

In the initial design of adaptive structures, one seeks to capture 95% of the physics while using 5% of the modeling requirements when possible. As such, reduced-order modeling techniques for rapidly considering multiple design options are extremely important. In recent years, methods of developing reduced-order models based upon principal components or singular values have emerged.^{1,2} Control system engineers have used these techniques to reduce the order of models used in the design of compensators and to further reduce the order of the compensators directly. Application of model reduction has recently been extended to include aerodynamic models,³⁻⁸ making it possible to cast the fully coupled aeroelastic system in a compact, low-order, state-variable form.⁹⁻¹¹ In the design of adaptive structures, such reduced order models greatly facilitate the integration and design of transducers required for active control.

To design/select transducers in the development of adaptive structures, one typically identifies a specific performance metric. This metric may involve vibration control, structural acoustic control, aeroelastic control, etc. However, the performance metric contains the application physics to be emphasized in the design.¹² Lim recently proposed a methodology for selecting actuator and sensor placement for disturbance rejection based upon the Hankel singular values of lightly damped structures.¹³ Compared to previous methodologies which emphasized the use of iterative, nonlinear optimization techniques in structural acoustic control,¹⁴⁻¹⁸ the approach outlined by Lim is computationally efficient.¹³ For lightly damped structures, the Hankel singular values can be estimated from the modal properties of the discrete time system models. Thus, the participation of each structural mode in the control path (actuator to sensor) can be weighted by the participation of this mode on the performance path (disturbance to performance). While this method is efficient and computationally direct (i.e., no iteration), it does lack a robustness metric.

Typically, in feedback control, performance is constrained to a finite bandwidth, owing to practical limitations imposed by sample-rate, through-put, and order of the compensator which can be accurately realized. Once transducers are configured on or within a structure, experimental system identification is utilized to provide a dynamic model of the system for controller design. Model fidelity is of primary concern with respect to robust stability, and unmodeled dynamics, particularly dynamics outside of the bandwidth of interest consistently pose difficulties and limit the level of performance which can be achieved given the need for robust stability. Low-pass filters are frequently employed to provide roll-off at high frequency, but such filters also introduce phase-lag which can affect stability and performance. To address this issue, Clark and Cox developed a design methodology for penalizing the selection of transducers that couple to modes beyond the bandwidth of interest while simultaneously emphasizing the selection of transducers that couple effectively to the defined performance path.¹⁹ In so doing, a crude method of loop shaping by actuator/sensor design was formulated. The technique was applied to a structural acoustic control problem and was demonstrated experimentally.²⁰

Smith and Clark further developed the technique to penalize coupling to modes in the bandwidth that were not important to stability or performance in addition to penalizing coupling to the out of bandwidth modes.²¹ The design approach has been applied to vibration and aeroelastic control.^{21,22} Within this manuscript, a tutorial overview of the design approach is provided. Several adaptive structure designs are then considered, including structures aimed at vibration control, structural acoustic control, and aeroelastic control. The results provided serve to demonstrate the power of this computationally fast, efficient, open-loop design procedure for achieving crude loop-shaping through actuator/sensor design/selection.

2. DESIGN

Before considering adaptive structure designs based upon a variety of application physics, an overview of the design

^{a)} Department of Mechanical Engineering and Material Science, Duke University, Durham, NC 27708 U.S.A.; E-mail: rclark@egr.duke.edu

metric is provided. A formal design procedure is then discussed for preliminary development of adaptive structures.

A. Overview of design metric

The design metric for optimum spatial compensation is developed from the work presented by Smith and Clark,²¹ Clark and Cox,¹⁹ and Lim,¹³ Lim and Gawronski,²³ and Gawronski and Lim.²⁴ This method is based upon estimating the Hankel singular values (HSVs) from a discrete time presentation of the system. The HSVs can be used to determine the open-loop controllability and observability Gramians and provide an effective measure of the sensor or actuator's ability to couple to a particular mode of the system. As such, one can utilize this measure of coupling to determine the actuators and sensors best suited for control.

As detailed by Smith and Clark,²¹ the problem must first be cast into the proper form. Figure 1 shows a block diagram of the generalized plant. The transfer matrix $G(s)$ in Fig. 1 represents the dynamics of the adaptive structure in the absence of control. Four transfer matrices can be identified through this standard generalized plant format. The upper transfer matrix, G_{zw} , represents the path from the disturbance inputs to the performance outputs. The application physics of interest are defined in this path. The lower transfer matrix, G_{yu} , defines the path from the control inputs to the sensor outputs, and is determined by the selection of transducer type, size, and placement. The remaining two transfer matrices, G_{yw} and G_{zu} , define the influence of the disturbance on the measured output and the influence of the control input on the performance. For most practical control system realizations involving disturbance rejection, the designer cannot measure the performance directly and cannot locate control actuators at the location of the disturbance. If it is possible to set $u = w$ and $y = z$, a servo-control problem results. However, since this case is the exception and not the rule, we attempt to design the adaptive structure such that the frequency response or modal coupling found in the control path is similar to that found in the performance path.

In refs. 23 and 24, the authors utilized an estimate of the HSVs to determine actuators and sensors which maximized the controllability and observability of the system through the control path, G_{yu} . However, Lim later refined the work to emphasize the selection of transducers which couple to modes present in the disturbance path, G_{zw} .¹³ The performance metric is defined as follows:

$$J_{qp} \equiv \sum_{i=1}^{N_m} \frac{\gamma_{y_p u_i}^4}{\bar{\gamma}_{y_{ui}}^4} \gamma_{z w_i}^4 \quad (1)$$

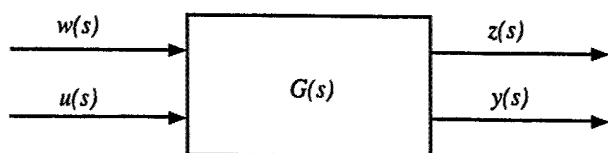


Fig. 1—Block diagram of generalized plant.

where $\gamma_{y_p u_i}^4$ is the square of the i -th HSV associated with the p -th sensor and q -th actuator, $\bar{\gamma}_{y_{ui}}^4$ is the square of the i -th HSV associated with all possible sensors and actuators, $\gamma_{z w_i}^4$ is the square of the i -th HSV associated with all possible disturbance inputs and performance outputs, and N_m is the number of modes included in the performance metric. J_{qp} takes on its maximum value when a single actuator/sensor pair provide the highest degree of modal coupling found in the performance path.

Clark and Cox modified the selection method to further penalize coupling to modes outside of the bandwidth of interest.¹⁹ This penalty served to produce "roll-off" through spatial compensation, reducing the sensitivity to unmodeled dynamics beyond the bandwidth of interest. The performance metric can be represented as follows:

$$\hat{J}_{qp} \equiv \left[\sum_{i=1}^{n_n} \frac{\gamma_{y_p u_i}^4}{\bar{\gamma}_{y_{ui}}^4} \gamma_{z w_i}^4 \right] + \left[\sum_{i=n_n+1}^N \frac{\gamma_{y_p u_i}^4}{\bar{\gamma}_{y_{ui}}^4} \gamma_{z w_i}^4 \right]^{-1} \quad (2)$$

where n_n defines the number of modes in the bandwidth of interest, emphasizing performance. The $|\cdot|$ indicates that the individual metrics have been normalized before summing. \hat{J}_{qp} takes on its maximum value when a single actuator/sensor pair provide the highest degree of coupling found in the performance path and the lowest degree of coupling to out-of-bandwidth modes.

Smith and Clark continued the advancement of spatial compensator design for robustness by providing a means of de-emphasizing modes considered unimportant over the bandwidth desired for control.²¹ Targeting in-bandwidth modes important for closed-loop control further reduces the order of the system model required in the design and the order of the resulting compensator. The metric is written as follows:

$$\tilde{J}_{qp} \equiv \left(\sum_{i=1}^{N_m} \Lambda_i \frac{\gamma_{y_p u_i}^4}{\bar{\gamma}_{y_{ui}}^4} \gamma_{z w_i}^4 \right) \times \left(\sum_{i=1}^{N_m} (\sim \Lambda_i) \left(\frac{\gamma_{y_p u_i}^4}{\bar{\gamma}_{y_{ui}}^4} \gamma_{z w_i}^4 \right) \right)^{-1} \quad (3)$$

where Λ is a binary vector of length N_m . Modes to be controlled have an element value of 1 in Λ and the \sim operator is the one's complement or binary NOT. The selection of modes considered important or unimportant is predetermined by the control system designer and serves to reflect the performance goals for the adaptive structure.

B. Design procedure

The design procedure is summarized in the flowchart presented in Fig. 2. The first objective is to develop a basic model of the structure. Upon developing a model of the structure, the designer must then choose an array of "target" actuators and sensors. Unlike nonlinear programming approaches whereby one iterates toward a final design, in the approach outlined herein, one chooses an arbitrarily large set of target actuators and sensors. Because all of the performance metrics are computed based upon an estimate of the HSVs, one can choose thousands of target locations. It is important in the initial design phase to ignore the added mass and stiffness associated with the transducer array, otherwise, the structure used in the early design phase would be grossly

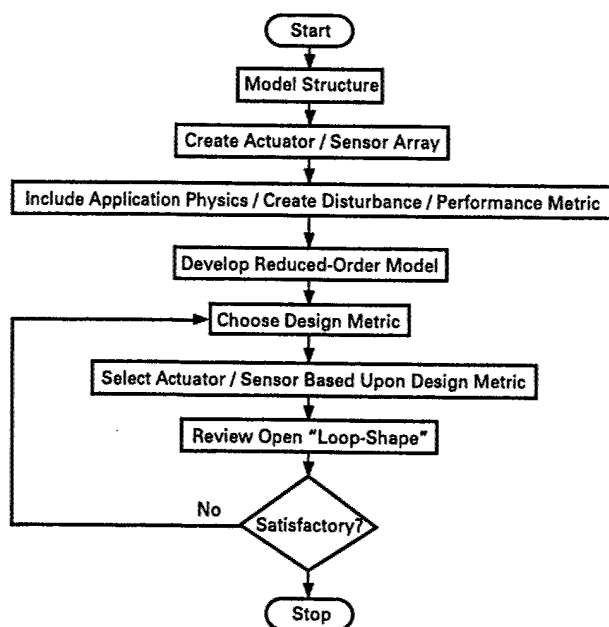


Fig. 2—Flow chart of design procedure.

inaccurate. Thus, only the modal participation coefficients associated with the sensors and actuators are used in the design model. The application physics appropriate for the model must then be selected to develop a model of the performance metric. Knowledge of the disturbance path, primary modes affected, and desired performance must be used in this phase. For example, if the objective is structural acoustic control, one would choose the radiated sound power as the performance metric.^{19,20} At this state of the design, the performance path and control path have been identified. Thus all inputs and outputs important in the design of the adaptive structure are present. As such, model reduction can be used to render the lowest order model for all identified inputs and outputs that captures the essential physics necessary for the design. The appropriate design metric can then be selected as indicated by Eqs. (1), (2), or (3). The design engineer has liberty in the choice of in-bandwidth and out-of-bandwidth modes as well as the relative importance of each mode in the design. Once the design metric is chosen, the estimate of the HSVs from the discrete-time model can be used to determine the best actuators and sensors. At this point, the designer should review the open-loop frequency response of the chosen actuator(s) and sensor(s) to determine if sufficient coupling and roll-off is achieved. If satisfactory, the preliminary design phase is complete. If not, the designer can modify the design metric and proceed as before. Once a satisfactory design is achieved, a refined model of the adaptive structure, including mass and stiffness effects of transducers can be developed to further evaluate the design.

3. ADAPTIVE STRUCTURE DESIGN EXAMPLES

Three design examples are provided within this section. The first example is based upon structural acoustic control,

comparing two designs based upon the metrics of Eqs. (1) and (2). The remaining two examples emphasize the use of the metric defined in Eq. (3) and address vibration control and aeroelastic control.

A. Structural acoustic example

A detailed analysis of the results presented here are provided in refs. 19 and 20. The objective of the work was to compare the design resulting from the metric of Eq. (1) to that resulting from the metric of Eq. (2). The design example was based upon a plate with simply supported boundary conditions, and the chosen performance metric was based upon the radiation of sound into a half space. An efficient method of producing a performance metric based upon sound power radiation into a half space is provided in ref. 25. A schematic diagram of the plate is presented in Fig. 3. As illustrated by the + symbols, there were seven target locations for actuators or sensors, allowing collocation as an option. Due to reciprocity, some of the conditions were redundant, and due to symmetry, only one quadrant of the plate was considered. Piezoelectric transducers were selected and the relative dimensions of the transducers are indicated in Fig. 3.

Upon applying the design metrics outlined in Eqs. (1) and (2), two different solutions resulted. The objective was to control the sound radiation below 1200 Hz (based upon the dimensions of the plate chosen), a bandwidth containing the (1,1), (3,1), (1,3), and (3,3) modes of the structure. For the structure studied, there are 10 modes within the design bandwidth, and a 30 mode model was used to capture the structural dynamics within and beyond the desired bandwidth for control, yielding a 60 state model of the structural system. The radiation filters used in the performance metric resulted in an additional 9 states to represent the structural acoustic coupling. Applying the metric of Eq. (1), which emphasizes performance, a collocated actuator and sensor placed in the center of the plate (transducer position 3 of Fig. 3)

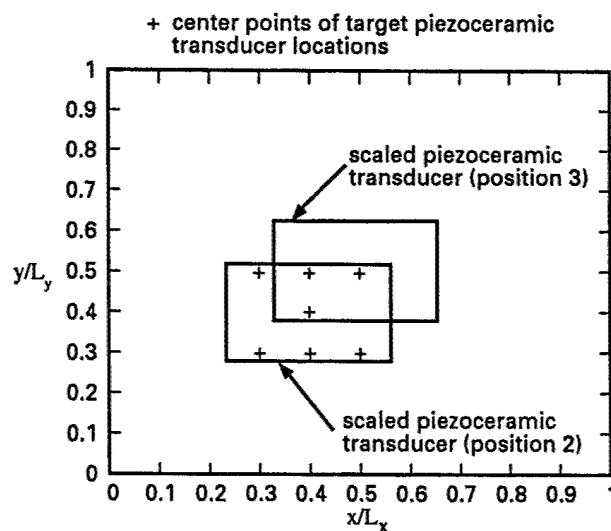


Fig. 3—Schematic diagram of plate with piezoceramic transducers.

demonstrated maximum modal coupling with the chosen performance path. However, upon applying the metric of Eq. (2), a non-collocated transducer pair resulted. This transducer pair is also illustrated in Fig. 3 and is represented by transducers at positions 2 and 3. Due to reciprocity, one can use either transducer as the sensor or actuator. Upon comparing the frequency response characteristics of these two design options, illustrated in Fig. 4, the difference resulting from the imposed "roll-off" of the metric based upon Eq. (2) is obvious. As illustrated, both transducer options result in dominant coupling to the desired modes within the identified bandwidth of control; however, the frequency response of the transducer pair chosen as a result of Eq. (2) yields no coupling to the structural modes included in the model above 1200 Hz (i.e., beyond the (3,3) mode). Due to the dimensions of the transducers, coupling to higher-order modes not included in the model will be minimized as well since the dimensions far exceed the trace structural wavelength at these frequencies. Additionally, both designs are non-minimum phase over the bandwidth of interest as indicated by the variation in the phase.

B. Structural vibration example

To provide an alternative application, we consider the design of an adaptive structure for vibration control, and the metric of Eq. (3) is applied. The design objective was to select a single piezoceramic actuator and sensor capable of coupling to the first four odd modes of a plate having pinned boundary conditions. Over 500,000 design options for actuators and sensors were considered. The candidate set included transducers ranging in x and y dimensions between 50 mm and 150 mm. Based upon the metric of Eq. (3) and the chosen emphasis placed upon the first four odd structural modes, the actuator and sensor pair illustrated in Fig. 5 was selected. For comparison, a nominal location for a collocated transducer pair was also chosen from a previous study which included the transducer pair in an array used for structural acoustic control.²⁶ The actuator and sensor dimensions are scaled to that of the plate in Fig. 5. As illustrated by the magnitude of the frequency response presented in Fig. 5, the

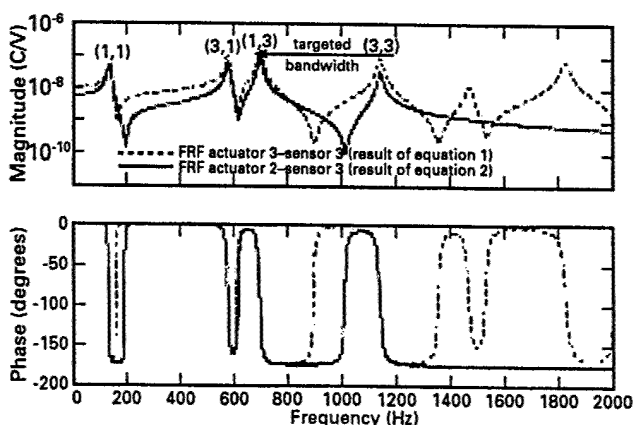


Fig. 4—Bode plots for the two transducer pair options resulting from design metrics of Eqs. (1) and (2).

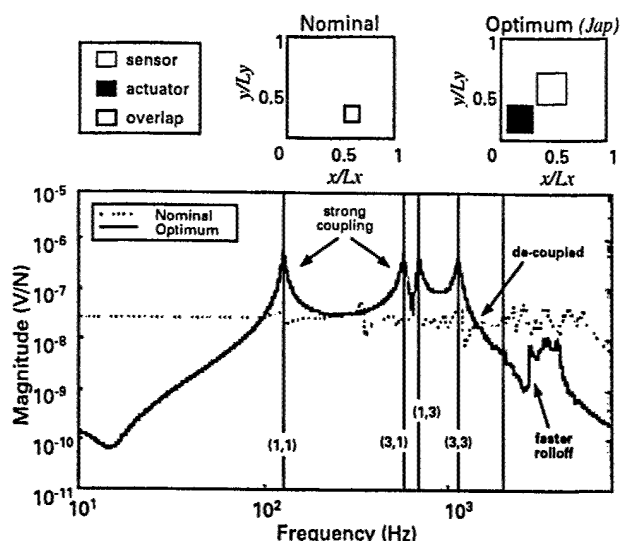


Fig. 5—Schematic diagram of plate with piezoceramic transducers and magnitude of frequency response functions comparing the nominal transducer pair to the optimal transducer pair for a plate with pinned boundary conditions.

optimum transducer pair resulting from the candidate set provides dominant coupling to the (1,1), (3,1), and (3,3) structural modes. The coupling to structural modes beyond that of the (3,3) mode is relatively insignificant, nearly 2 orders of magnitude less than that for the desired modes. Further, the coupling to other modes within the bandwidth of interest is also minimized (i.e., the coupling to the (2,1), (1,2), and (2,2) modes is insignificant). The contrast in design is emphasized upon comparing the magnitudes of the frequency response for the optimal and nominal transducer pairs. This comparison serves to emphasize the level of tailoring which can be accomplished with respect to the open-loop frequency response through adaptive structure design approaches. The resulting transducer pair chosen provides selective coupling to the desired modes and minimizes coupling to all other modes. Thus, the order of the analytical or experimental model required to describe the dynamics of the adaptive structure through the actuator and sensor path is greatly reduced. The natural "roll-off" at high frequency serves to reduce the ill effects of unmodeled dynamics outside of the desired bandwidth for control.

C. Aeroelastic example

Rule et al., utilized the design metric of Eq. (3) to determine the best target locations for an actuator and sensor used to suppress flutter in a delta wing model.¹¹ As detailed by the authors, a fully coupled aeroelastic model of the system is developed, including the dynamics of the transducers. Based upon prior work in the development of reduced-order aerodynamic models,³⁻⁸ it is now possible to cast the fully coupled aeroelastic system model in a compact, low-order, state-variable form.⁹⁻¹¹ The fully coupled model can be further reduced, emphasizing the dynamics important through the chosen inputs and outputs used in the control system design.

The objective of the current design example is aimed at the selection of a transducer pair which can be used to extend the open-loop flutter boundary of the delta wing model illustrated in Fig. 6. For the example provide, the flutter speed is designed to occur at 54 m/s (open-loop), and the interaction between the third structural mode and the fluid is responsible for the aeroelastic instability. Based upon this observation, a disturbance was created to drive each of the first five structural modes of the aeroelastic system, and the chosen performance metric was based upon reducing the structural response of the first five modes.

Over 455 possible piezoceramic transducer options were considered in the design, and an actuator/sensor pair capable of coupling to the first four structural modes was sought. While it was recognized that some coupling would occur with higher order modes, the objective was to impose spatial "roll-off" after the fourth mode. The resulting actuator/sensor pair selected based upon the design metric of Eq. (3) and the stated design parameters is illustrated in Fig. 6. In addition to illustrating the optimal transducer pair, "contours of goodness" are also depicted. The contours were generated by identifying regions on the surface of the structure where candidate transducer pairs resulted in the highest levels of the performance index of Eq. (3). Obviously the optimal transducer pair falls within the region. The frequency response corresponding to this transducer pair at a flow speed near the flutter boundary is depicted in Fig. 7. The dominant peak in the magnitude of the response corresponds to the resonance of the third structural mode. As indicated, the response of structural modes beyond 100 Hz is greatly diminished. This natural "roll-off" greatly facilitates the compensator design and allows for more aggressive designs in the presence of unmodeled dynamics at higher frequencies.

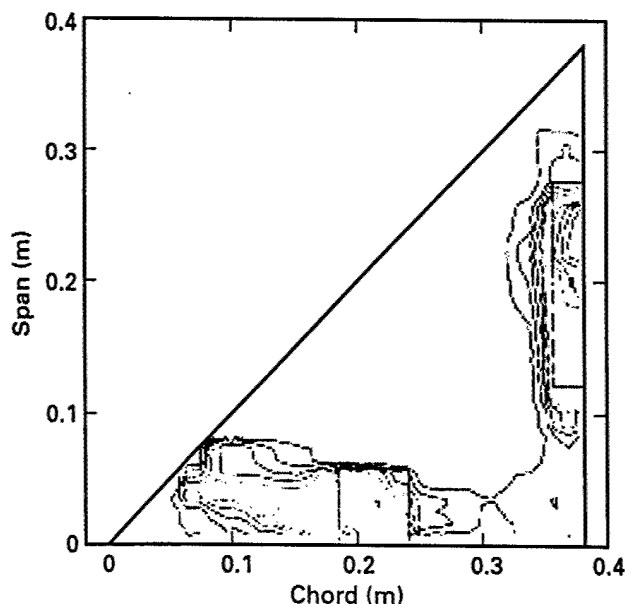


Fig. 6-Schematic diagram of delta wing with piezoceramic transducers.

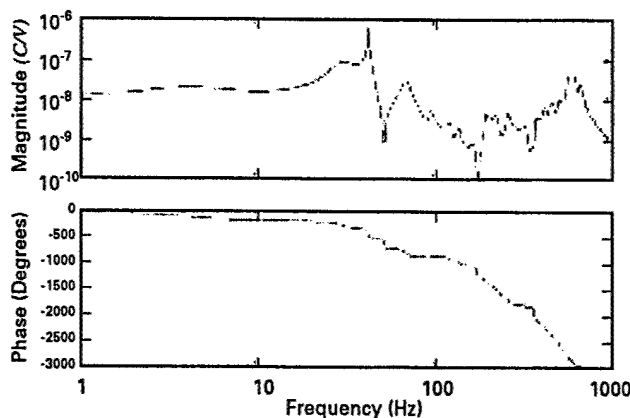


Fig. 7-Bode plots for the two transducer pair options resulting from design metric of Eq. (3) for the aeroelastic model.

4. CONCLUSIONS

Reduced order models of dynamic systems greatly facilitate the initial design of adaptive structures, providing an efficient means of considering multiple design options. An open-loop design procedure for selecting transducer locations based upon a computationally efficient estimate of the system Hankel singular values was reviewed. The technique provides a crude method of "loop-shaping" through spatial compensation in the design of adaptive structures. The selection/design approach was applied to a structural acoustic example, a structural vibration example, and an aeroelastic example. In all cases, actuator/sensor pairs were identified which coupled effectively to modes present in the performance path and coupled poorly to out-of-bandwidth modes. Roll-off provided through transducer design/selection serves to reduce the sensitivity of the control system design to unmodeled dynamics. The application of such design procedures is important in the design of adaptive structures at the early development stage.

5. ACKNOWLEDGMENT

This work was supported by AFOSR, contract monitor Major Brian Sanders, under grant F49620-98-1-0383.

6. REFERENCES

1. B. C. Moore, "Principal component analysis in linear systems: Controllability, observability, and model reduction," *IEEE Trans. Automatic Control* AC-26(1), 17-32 (1981).
2. A. J. Laub, M. T. Heath, C. C. Paige, and R. C. Ward, "Computation of system balancing transformations and other applications of simultaneous diagonalization algorithms," *IEEE Trans. Automatic Control* AC-32(1), 115-122 (1987).
3. E. H. Dowell, K. C. Hall, and M. C. Romanowski, "Eigenmode analysis in unsteady aerodynamics: Reduced order models," *Appl. Mech. Rev.* 50(6), 371-386 (1997).
4. K. C. Hall, "Eigenanalysis of unsteady flows about airfoils, cascades, and wings," *AIAA J.* 32(12), 2426-2432 (1994).
5. E. H. Dowell, "Eigenmode analysis in unsteady aerodynamics: Reduced order models," *AIAA J.* 34(8), 1578-1583 (1996).

- ⁶ M. C. Romanowski and E. H. Dowell, "Reduced order Euler equations for unsteady aerodynamic flows: Numerical techniques," Presented at AIAA Aerospace Sciences meeting, AIAA Paper 96-0528 (1996).
- ⁷ R. Florea, K. C. Hall, and P. G. A. Cizmas, "Reduced-order modeling of unsteady viscous flows in a compressor cascade," AIAA J. 36(6), 1039-1048 (1998).
- ⁸ M. C. Romanowski, "Reduced order unsteady aerodynamic and aeroelastic models using Karhunen-Loève eigenmodes," Presented at AIAA Symposium on Multidisciplinary Analysis and Optimization, AIAA Paper 96-3981 (1996).
- ⁹ M. Baker, Model reduction of large, sparse, discrete time systems with application to unsteady aerodynamics (finite element, Lyapunov equations), Ph.D. thesis, University of California, Los Angeles, 1996.
- ¹⁰ M. L. Baker, D. L. Mingori, and P. J. Goggin, "Approximate subspace iteration for constructing internally balanced reduced order models of unsteady aerodynamic systems," Proc. 37th AIAA/ASME/ASCE/ASC Structures, Structural Dynamics, and Materials Conference, AIAA Paper 96-1441-CP (1996), pp. 1070-1085.
- ¹¹ J. A. Rule, D. E. Cox, and R. L. Clark, "Aerodynamic model reduction through balanced realization," to appear in AIAA J. (2000).
- ¹² R. L. Clark, W. R. Saunders, and G. P. Gibbs, *Adaptive Structures* (John Wiley and Sons, Inc., New York, 1998), Chap. 9.
- ¹³ K. B. Lim, "Disturbance rejection approach to actuator and sensor placement," AIAA J. Guidance, Control and Dyn. 20(1), 202-204 (1997).
- ¹⁴ B. T. Wang, R. A. Burdisso, and C. R. Fuller, "Optimal placement of piezoelectric actuators for active control of sound radiation from elastic plates," *Proc. NOISE-CON91*, edited by Daniel A. Quinlan and Maharelli G. Prasad (Noise Control Foundation, Poughkeepsie, NY, 1991), pp. 267-274.
- ¹⁵ R. L. Clark and C. R. Fuller, "Optimal placement of piezoelectric actuators and polyvinylidene fluoride error sensors in active structural acoustic control approaches," J. Acoust. Soc. Am. 92(3), 1521-1533 (1992).
- ¹⁶ C. E. Ruckman and C. R. Fuller, "Optimizing actuator locations in active noise control systems using subset selection," J. Sound Vib. 186(3), 395-406 (1995).
- ¹⁷ G. C. Smith, R. L. Clark, and K. D. Frampton, "Optimal transducer placement for active control of sound transmission through aeroelastic plates," J. Intell. Mat. Sys. Struc. bf 9, 975-987 (1999).
- ¹⁸ G. C. Smith, R. L. Clark, and K. D. Frampton, "The effect of convected fluid loading on the optimal transducer placement for active control of sound transmission through an aeroelastic plate," AIAA Paper 98-1981 (1998).
- ¹⁹ R. L. Clark and D. E. Cox, "Band-limited actuator and sensor selection for disturbance rejection," AIAA J. Guidance, Control and Dyn. 22(5), 740-743 (1999).
- ²⁰ R. L. Clark and D. E. Cox, "Experimental demonstration of a band-limited actuator/sensor selection strategy for structural acoustic control," J. Acoust. Soc. Am. 106(6), 3407-3414 (1999).
- ²¹ G. C. Smith and R. L. Clark, "Frequency shaping with spatial compensators," *Proc. ACTIVE 99*, edited by Scott Douglas (Noise Control Foundation, Poughkeepsie, New York, 1999).
- ²² J. A. Rule, R. E. Richard, and R. L. Clark, "Active control of delta wing flutter through optimal placement of piezoelectric sensors and actuators," *Proc. ACTIVE 99*, edited by Scott Douglas (Noise Control Foundation, Poughkeepsie, New York, 1999).
- ²³ K. B. Lim and W. Gawronski, "Hankel singular values of flexible structures in discrete time," AIAA J. Guidance, Control and Dyn. 19(6), 1370-1377 (1996).
- ²⁴ W. Gawronski and K. B. Lim, "Balanced actuator and sensor placement for flexible structures," Intl. J. Control 65(1), 131-145 (1996).
- ²⁵ G. P. Gibbs, R. L. Clark, D. E. Cox, and J. S. Vipperman, "Radiation modal expansion: Application to active structural acoustic control," J. Acoust. Soc. Am. 107(1), 332-339 (1999).
- ²⁶ J. S. Vipperman and R. L. Clark, "Implications of using collocated strain-based transducers for active structural acoustic control," J. Acoust. Soc. Am. 106(3), 1392-1400 (1999).

Genetic Spatial Optimization of Active Elements on an Aeroelastic Delta Wing

Robert E. Richard
Research Assistant

John A. Rule*

Robert L. Clark
Professor

Department of Mechanical Engineering and
Material Science
Duke University,
Durham, NC 27708-0302

This work outlines a cohesive approach for the design and implementation of a genetically optimized, active aeroelastic delta wing. Emphasis was placed on computational efficiency of model development and efficient means for optimizing sensor and actuator geometries. Reduced-order models of potential-flow aerodynamics were developed to facilitate analysis and design of the aeroelastic system in the early design phase. Using these methods, models capturing "95% of the physics with 8% of the modeling effort" can be realized to evaluate various active and passive design considerations. The aeroelastic delta wing model was employed in determining the most effective locations and sizes for transducers required to provide flutter control. The basic design presented is based upon an analytical model of the structure. A comparison of optimization strategies led to the use of a genetic algorithm to determine the optimal transducer locations, sizes, and orientations required to provide effective flutter control based upon an open-loop performance metric. The genetic algorithm and performance metric essentially provided loop shaping through the adaptive structure design. An experimental model was then developed based upon the optimal transducer designs. Wind tunnel tests were performed to demonstrate closed-loop performance for flutter control. Results from this study indicate that a single sensor/actuator pair can be designed to extend the flutter boundary and selectively couple to only those modes required to control the response.
[DOI: 10.1115/1.1389458]

Introduction

Advancing research into methods for controlling flutter in an aeroelastic delta wing has yielded considerable progress. A primary focus of this work has been to develop and implement open-loop design techniques to determine optimal geometric parameters of piezoelectric sensors and actuators with respect to feedback control. This investigation involved the use of a previously developed computational model of a thin plate delta wing in an aerodynamic field [1]. Consistent with this model, piezoelectric sensors and actuators were integrated into the structure. The dramatic reduction in size of the aerodynamic model through the use of balanced realization made for a computationally efficient representation of the aeroelastic system that captured the great majority of the significant dynamics. An improvement on previously developed methods allowed for arbitrary size, shape, placement, and orientation of the piezo patches in the design.

A genetic algorithm based on a previously developed technique was implemented to determine the optimal parameters for a sensor/actuator patch pair [2]. The ranking of a particular patch pair combination was accomplished through the application of a design metric based upon a computationally efficient estimate of the Hankel Singular Values (HSV's) developed from previous work [3-5]. Modifications were made to these techniques that improved their ability to rapidly and consistently converge on an optimal solution. The control authority of the optimal actuator-sensor pair in implementing a feedback control algorithm on the structure was predicted to considerably raise the flutter boundary of the wing.

An experimental model of the active delta wing structure was mounted in a low speed wind tunnel to verify the predicted re-

sponse of the wing. The results of these tests demonstrated the structure's predicted capability of delaying the onset of flutter by a consistent amount.

Overall, this work verified the validity of the computationally efficient aeroelastic modeling methods described, as well as showing the benefits of using a genetic algorithm over exhaustive search approaches in optimizing the results of HSV based ranking methods. Both the genetic and direct optimization schemes led to similar actuators (small and centrally located along the root chord). However, the genetic approach suggested a leading edge sensor while the direct method led to a small root chord sensor with increased higher frequency coupling. The simulation predicted that these optimally placed active elements would be capable of reducing structural response of the targeted mode by approximately 22 dB while avoiding undesirable spillover effects. The wind tunnel tests, showing a 16 dB reduction, were reasonably consistent with this prediction and proved the methods to be mutually supportive. Additionally, the agreement of the predicted and observed flutter boundaries served to validate the approach (31.5 m/s, and 35 m/s respectively for the given parameters). Both the simulation and the experimental model showed control capable of increasing the flutter boundary to approximately 38 m/s.

Model Development

The focus of this work was to investigate the effectiveness of optimizing patch parameters for a sensor-actuator pair and to develop an experimental demonstration of the design. The steps involved consisted of:

- (1) Developing an aeroelastic model in which to incorporate electro-mechanically coupled piezoelectric patches
- (2) Devising a scheme to rank the effectiveness of different sensor-actuator pairs with respect to desired mode coupling.
- (3) Implementing an optimization routine that would consistently converge on a solution, balancing opposing metrics.

*Corresponding R&D Engineer, ACX, Inc.

Contributed by the Technical Committee on Vibration and Sound for publication in the JOURNAL OF VIBRATION AND ACOUSTICS. Manuscript received Sept. 2000; revised May 2001. Associate Editor: L. A. Bergman.

- (4) Performing wind tunnel tests to verify the simulation results.

These model development steps are described in relative detail in this section.

Delta Wing Aeroelastic Model. The simulated aeroelastic model was consistent with that developed in [6]. It was constructed from two main components: a structural model incorporating piezoelectric patches and a reduced-order aerodynamic model. The structural model was coupled to the aerodynamic model, through feedback, to simulate the aeroelastic structure. The structural "modal" inputs and outputs became increasingly coupled with increasing flow speed due to the effects of the aerodynamic feedback and were thus not modal with respect to the aeroelastic model. Figure 1 shows this construction along with the sensor and actuator paths.

The structural model was built using the Ritz method [7] to develop the mass and stiffness matrices associated with the thin plate delta wing model. A coordinate transformation mapped the model from rectangular to trapezoidal coordinates. This transformation allowed for a variable taper ratio (root chord/tip chord) enabling construction of wings varying from rectangular to nearly triangular. For the purpose of this investigation, the taper ratio was set to be approximately zero (0.01) along with proportions representing a 45 deg delta wing. The model was developed to have outputs of (25) modal positions and modal velocities and inputs of (25) modal forces. Once constructed, proportional modal damping (δ) was added to the system. Additionally, piezoelectric sensors and actuators were added to provide control inputs and outputs. The overall equation governing this construction, as outlined in [8], is expressed in Eq. (1), where $r(t)$ and $R(t)$ are the generalized displacements and forces respectively, θ the piezo electro-mechanical coupling matrix, M and K the mass and stiffness influence matrices, and $V_p(t)$ the piezo input voltages. For the purpose of patch optimization, the mass and stiffness effects of the piezo elements (M_p , K_p) were assumed to be insignificant.

$$(M + M_p)\ddot{r}(t) + \delta\dot{r}(t) + (K + K_p)r(t) = R(t) + \theta V_p(t) \quad (1)$$

The aerodynamic model was constructed from a vortex lattice method as in [6]. The model was non-dimensional with respect to flow speed rendering recalculation of the model for various flow speeds unnecessary. This technique, along with model truncation through the use of balanced realization, made the model modular and of a workable size. The model reduction involved the truncation of a 600-state model to a 50-state model based on the Hankel singular values of the transformed states [9]. The reduction retained approximately 95 percent of the physics while reducing its size by 92 percent. This enabled efficient use of the patch placement optimization scheme that was to be implemented in the adaptive structure design.

One of the functions of the fully coupled aeroelastic model was to predict the flutter characteristics of the wing in an aerodynamic flow field. For the parameters in this case, as laid out in Table 1, it

Table 1 Properties of the simulated delta wing model

Geometry	90° delta, clamped @ root
Proportions	15" × 15" (.381 m)
Material	Acrylic
Thickness	0.062" (1.58 × 10 ⁻³ m)
Elastic Modulus	4.200 × 10 ⁹ N/m ²
Poisson Ratio	0.45
Density	1.009 × 10 ³ kg/m ³

was predicted that the second mode would advance from a 26 Hz oscillation (in vacuo) to an 18 Hz oscillation occurring at 31.5 m/s as illustrated in Fig. 2.

Piezo Structure Modeling. A new development in the piezo structures modeling technique involved the use of a piezo element grid in which small, contiguous, nonoverlapping piezo patches covering the entire surface area of the wing model were coupled to the structural model. In this case, an element grid containing 2mm square elements was employed. Equation (2) shows the associated electro-mechanical patch coupling equation as derived in [8,10].

$$\Theta = \left(\frac{C^2}{S} \right) \left(\frac{d_{31} E_p}{(1 - \nu^2)} \right) \left(\frac{h_s^2 + 2h_s h_p + 4}{4} \right) \left\{ \int_{\hat{x}_1}^{\hat{x}_2} \int_{\hat{y}_1}^{\hat{y}_2} \left[\frac{\partial^2 \theta_j(\hat{x}, \hat{y})}{\partial \hat{x}^2} + \frac{\partial^2 \theta_j(\hat{x}, \hat{y})}{\partial \hat{y}^2} \right] d\hat{x} d\hat{y} \right\} \quad (2)$$

Due to the minute element areas relative to the structural mode shapes, the coupling effects of these elements could be calculated using single point evaluation of the integral without significant loss of accuracy. Because of the linearity associated with the electro-mechanical coupling and capacitance effects, the trial patches could be constructed by summing the effects of the piezo elements contained within the patch's prescribed geometric boundaries. This method for calculating the coupling coefficients of a particular patch proved to be much more computationally efficient, and at least as accurate as previously utilized numerical integration schemes [11]. This efficiency was due, in part, to the fact that the coupling effects of the element grid only needed to be calculated once, enabling the construction of any number of patches from those elements. Due to the relative computational ease of this approach, rapid construction of actuators and sensors on the wing of arbitrary size, shape, placement, and orientation

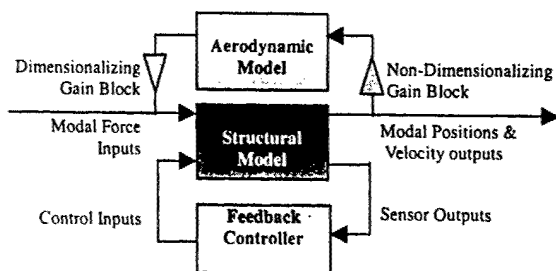


Fig. 1 Block diagram of aeroelastic system

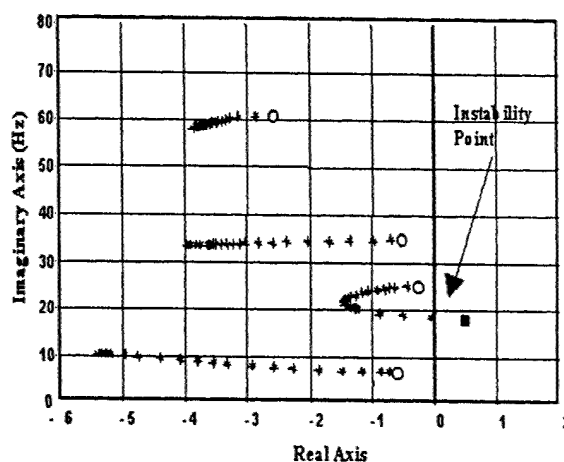


Fig. 2 Migration of the open-loop aeroelastic poles with flow speed. Instability was predicted where the second mode moved into the right half plane corresponding to 31.5 m/s at 18 Hz.

(with marginal errors due to area) was possible. In this application, shape was not a variable parameter but the building scheme would allow for it. In addition, this approach simplified the modeling of patch effects by requiring no error checking to determine if a prescribed patch was entirely on the wing. Since the elements were all on the wing, their summed effects could only involve effects on the wing.

Spatial Optimization of Piezo Patches

Once a simulation model had been constructed, the next step was to develop a means for determining geometric parameters of a sensor-actuator pair coupled to the structure. An optimal pair would couple effectively to structural modes of interest while exhibiting poor coupling to modes where control spillover would be likely to occur due to model uncertainty typical at higher frequencies. With these sorts of coupling characteristics and the associated increased gain margins, the system would be capable of using higher controller voltages while avoiding closed-loop instability. This would enable the active structure to achieve a greater level of control on the modes of interest. The optimization required a means to rank patch pairs as well as a way to converge on an optimal solution based on these rankings. The pairs were ranked through a previously developed process involving the application of Hankel Singular Value (HSV) approximations [3]. The final optimization was accomplished using a genetic algorithm.

Determination of Pair Ranking. The rank of a particular sensor-actuator pair was determined through a method based on a procedure first employed by Lim [3,4] and extended by Clark et al. [5] and Smith [2]. In this method, HSV's of the open-loop controllability and observability Gramians were estimated from a state-space representation of the aeroelastic system. These approximations were shown to be valid estimates for lightly damped modes, the modes of interest in this case. These HSV estimates were applied to Eqs. (3) and (4) giving raw measures of a patch pair's desirable (J_{pert}) and undesirable (J_{robust}) coupling with respect to modes included in the binary selection vectors (Λ_{pert} , Λ_{robust}). In these equations, the indices (p, q) corresponded to a particular sensor-actuator combination while (n) tracked modal indices. The γ^4 's were the squared HSV estimates specific to a sensor-actuator path ($\gamma_{\Lambda_{pert},n}^4$), the overall performance path ($\gamma_{\Lambda_{robust},n}^4$), and the system of all sensor-actuator combinations under consideration ($\gamma_{\Lambda,n}^4$), normalization purposes.

$$J_{pert}^{p,q} = \sum_{n=1}^{\Lambda_m} \Lambda_{pert} \frac{\gamma_{\Lambda_{pert},n}^4}{\gamma_{\Lambda,n}^4} \gamma_{\Lambda_{robust},n}^4 \quad (3)$$

$$J_{robust}^{p,q} = \sum_{n=1}^{\Lambda_m} \Lambda_{robust} \frac{\gamma_{\Lambda_{robust},n}^4}{\gamma_{\Lambda,n}^4} \gamma_{\Lambda_{pert},n}^4 \quad (4)$$

In previous implementations [5,2], these raw scores were then divided (J_{pert}/J_{robust}) or scaled versions were summed ($J_{pert} + \alpha J_{robust}$). A modification was made to the technique that made the scheme considerably less sensitive to minute changes in patch parameters as well as more prone to giving compromise solutions. It was discovered that if one of the metrics had a significantly larger range of values than the other, that metric would dominate the results and no compromise solutions would result. This problem arose due to the inherently competing nature of the dual metric (i.e., large patches tended to score high values of J_{pert} , while small patches did the same with J_{robust}). In addition, the scores for each of the two metrics varied exponentially causing dramatic variations in the scores of patch pairs of very similar construction. To correct this, J_{pert} and J_{robust} vectors were post-processed (see Eqs. (5) and (6)), such that each varied linearly from zero to one. The metrics were then multiplied as in Eq. (7). This post-processing modification effectively addressed both issues and yielded a stable and consistently compromising metric.

$$\bar{J}_{pert,n} = \left[1 - \frac{\min(\log(J_{pert}))}{\log(J_{pert})_n} \right] / \left[1 - \frac{\min(\log(J_{pert}))}{\max(\log(J_{pert}))} \right] \quad (5)$$

$$\bar{J}_{robust,n} = \left[1 - \left[1 - \frac{\min(\log(J_{robust}))}{\log(J_{robust})_n} \right] / \left[1 - \frac{\min(\log(J_{robust}))}{\max(\log(J_{robust}))} \right] \right] \quad (6)$$

$$\bar{J}_n = [\bar{J}_{pert,n} * \bar{J}_{robust,n}] \quad (7)$$

Genetic Optimization of Patches. The optimization procedure was based on one developed by Smith [2]. This work followed previous work outlined in [12,13,14]. The algorithm was designed to converge on an optimal solution through a series of iterations of prioritized mating based on the beneficial ranking of the pairs.

The initial population was generated by randomly constructing 400 rectangular patches of varying center locations, heights, widths, and angular orientations. Each of the five parameters necessary to describe a patch were normalized and converted to 16 bit binary vectors. Pairing of the sensor and actuator patches was done arbitrarily and these pairs constituted the individual elements of the population. The pair description vectors were then combined to form a 16×10 binary matrix as shown in Fig. 3, with five of the columns corresponding to actuator parameters and five corresponding to the accompanying sensors. The initial population was then ranked using the previously described HSV ranking scheme. The succeeding generations were built by mating and mutating pairs from the previous generation with the chance of a pair being selected for mating proportional to its score. This allowed for reproduction of low scoring traits but made the likelihood low. This gave the process a means of breaking out of local maxima. Mating was accomplished by the Matlab routine: *mate.m*, which uses a binary crossover strategy. In order to keep the population size constant, each pair chosen for reproduction was mated twice with partners chosen randomly from the selected mating pool. The crossover operation took the first n elements of the binary vector from one of the parents (randomly chosen) and the remaining $16-n$ from the other. The crossover point (n) was randomly determined with each mating. The mutation operation flipped elements of the offspring binary vector a defined percentage of the time (5 percent in this case). This arrangement restricted the patches to a rectangular shape and thus limited the number of parameters needed to describe an individual pair for computational efficiency. The patch modeling method itself imposed no such limitations on actuator and sensor shape.

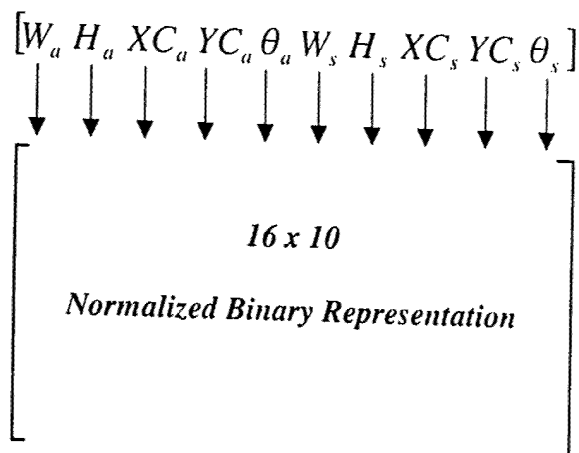


Fig. 3 Conversion of the ten parameter patch-pair description vector to normalized binary form

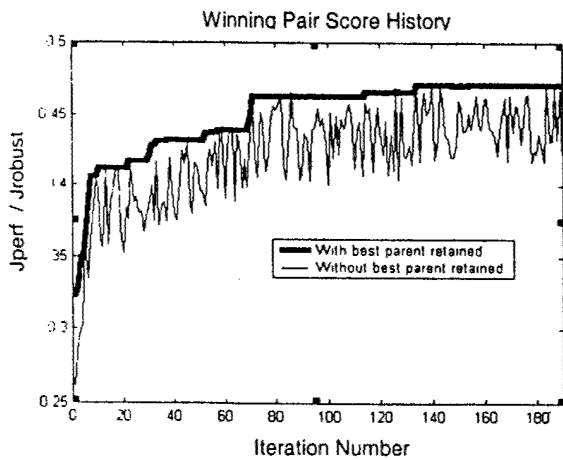


Fig. 4 Plot shows contrast in goal convergence between routine with best parent retained and discarded

After numerous trials involving 200 pairs each, the algorithm was ineffective at converging on a stable solution. To remedy this, an adjustment was made to the method involving the retention of the highest scoring pair for the next iteration. This adjustment forced the winner of each successive iteration to be at least as good as the previous one. This effectively increased the routine's ability to converge as shown in Fig. 4.

Overall, this strategy forced convergence much more rapidly than the random pair generation in the direct method. This technique consistently yielded similar results regardless of the parameters of the original population. The 200 iteration run, shown in

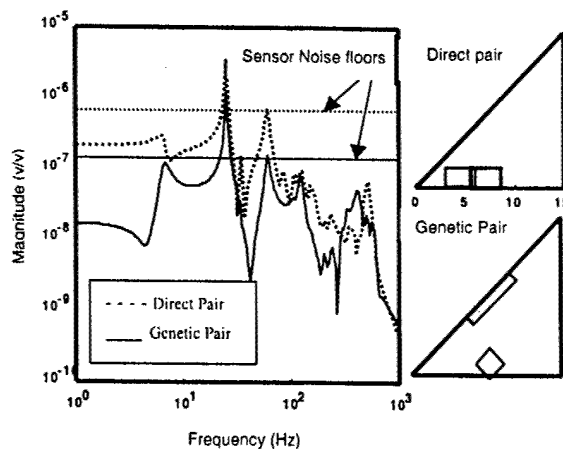


Fig. 6 Comparison between pairs determined by alternate optimization methods

Fig. 4, was exceptionally long for the illustrative purposes; most runs converged within 40 iterations involving 200 pairs as compared to 10^6 combinations in previously employed direct, exhaustive methods [6].

The resulting best pairs from numerous runs can be seen in Fig. 5 along with their associated response plots. The similarities between the conclusions of independent runs with random starting points, as well as the desirable response curve shapes showing significant second mode coupling and high frequency roll off, inspired confidence in the validity of the approach. In addition to showing patch geometries, contours were generated on the wing plots showing the areas of greatest patch building activity throughout all iterations. The fact that the contours lined up so well with the winning patches further validated that the routine was consistently converging on a stable answer. In all cases, the root patches were actuators and the leading edge patches were sensors. For a purely structural model, sensor-actuator reciprocity would have applied to sensor and actuator locations but that was not the case in this situation due to the aerodynamic loading.

Figure 6 shows the best genetically chosen pair compared to the best pair chosen by previously used exhaustive approach. The two frequency responses show that the genetically chosen pair exhibited similar coupling to the second mode with considerably more high frequency roll-off.

Closed-Loop Predictions

By integrating the patch pair configuration, determined from averaging the four trials into the aeroelastic model, an adaptive structure model was generated for the controller design. The actuator patch was $2'' \times 2''$, (0.0503m) at 45 deg with center location at $X=8''$, $Y=1.2''$ (0.198m, 0.0305m). The sensor was $1'' \times 6''$ (0.0254m, 0.152m) rotated 45 deg at $X=8''$, $Y=7.3''$ (0.283m, 0.185m). These center locations are noted with respect to the origin at the leading edge root of the wing. The augmented two-port system consisted of a disturbance, sensor noise and control inputs along with a performance, control effort, and sensor signal outputs as shown in Fig. 7. The actuator patch was used for the disturbance and control actuator signals, a point velocity measurement at the center of the leading edge was the performance output, and the sensor patch was the control sensor. A routine for calculating an H_2 minimizing controller was applied to this system generating an optimal controller for reduction of the established performance measures [15]. The controller design was adjusted by varying the control effort penalty (increasing controller voltage sent to the actuator) as well as the level of sensor noise (effectively adjusting the noise floor for the sensor signal). The superior coupling of the sensor-actuator path to the mode of interest, along with the high

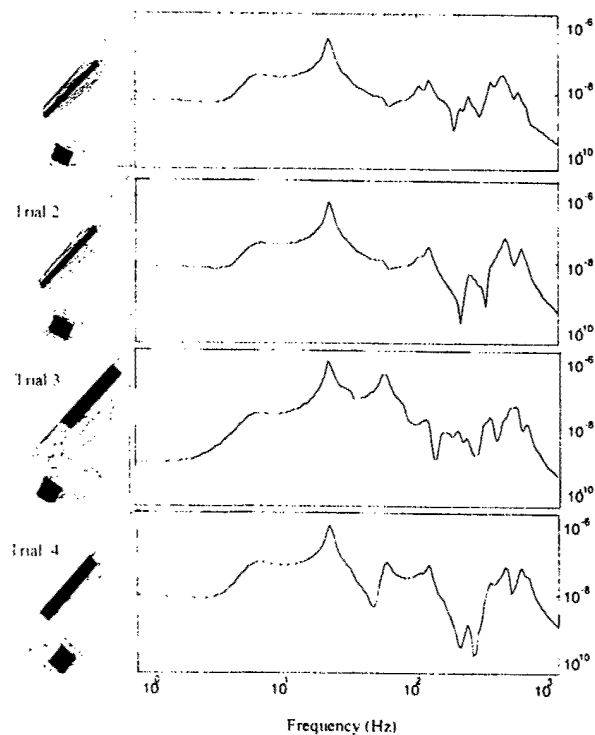


Fig. 5 Results comparison of four independent optimization runs showing patch placement and associated response plots. The contours around the patches indicate areas of high likelihood for patch construction. The vertical axes correspond to magnitudes of (v/v).

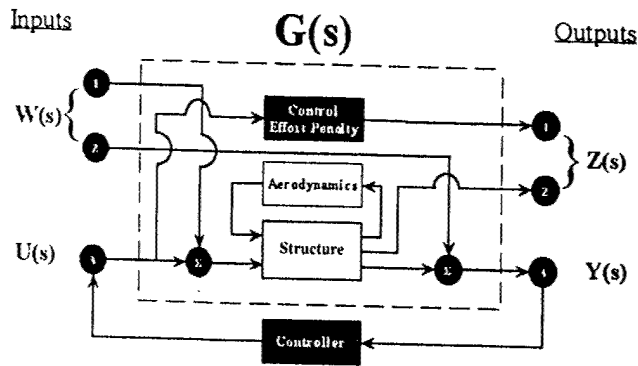


Fig. 7 Block diagram of two-port for controller design

frequency roll off, allowed for the noise floor to be set such that the controller worked on an error signal within a narrow bandwidth around the targeted mode. This method of selectively targeting a frequency range enabled the controller to provide significantly higher loop gains in that range while avoiding spillover at

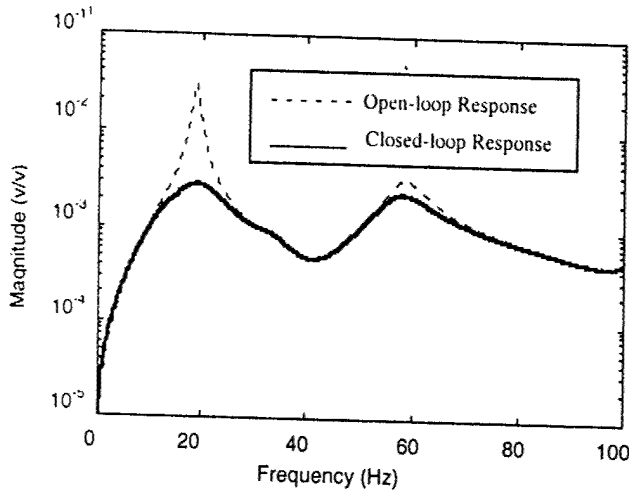


Fig. 8 Predicted open and closed-loop response of the wing in pre-flutter flow (31 m/s) with the selected patch pair

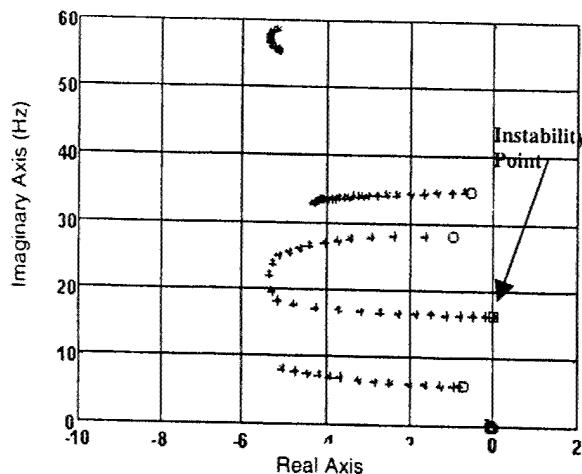


Fig. 9 Closed-loop aeroelastic pole migrations (parameterized by flow velocity), showing a 17 Hz instability at 38.3 m/s.

higher frequencies. Greater control authority was thus achieved without causing instability at higher frequencies. This was the primary goal of the spatial optimization.

A plot comparing the predicted open-loop response with the controlled closed-loop response just below the flutter speed (31 m/s) is shown in Fig. 8. The controller was predicted to reduce the second mode response by 35 dB. Figure 9 shows the closed-loop aeroelastic root migration as compared to the open-loop plot in Fig. 2. The predicted flutter boundary was raised in the closed-loop system by 20 percent to 38.3 m/s at 17 Hz.

Experimental Verification

The experimental wing model was constructed according to the specifications listed in Table 1. The mounted actuator was constructed from 0.028" (7.1×10^{-4} m) PZT material with silver electrode layers while the sensor was made from 0.003" (7.6×10^{-5} m) PVDF material (including electrode layer thickness). The structural response of the wing with mounted active elements proved to be indistinguishable from that of a bare wing. This fact served to justify the strategy of ignoring the mass and stiffness effects in the simulation model.

Wind tunnel testing of the nonactive wing demonstrated a flutter boundary of 35 m/s @ 19 Hz showing less than 10 percent variation from the predicted response. The flutter boundary was considered to be the point at which clear harmonics appeared in the measured frequency response; this point is generally thought to be above the actual flutter boundary. This observation was made by Tang and Dowell in [16] in addition to showing that structural nonlinearities can lead to limit cycle oscillations (LCO's), as was observed in this experimental model. For the purpose of this work, the analysis and design were restricted to linear models. However, the working thesis here was that the LCO could be eliminated and the onset of flutter delayed by designing a compensator based on a pre-flutter linear model of the system. This proved to be a valid assumption as indicated by the experimental results.

A system identification routine was developed to construct a model of the physical system for the purpose of controller design. As in the simulated model, the actuator and disturbance signals were summed and sent to the actuator patch. An Ometron VPI 4000 scanning laser vibrometer measuring the velocity of a central point on the leading edge of the wing was used to track the performance. Measured voltages across the PVDF sensor electrodes acted as sensor signals. A controller was then designed and implemented on the wing employing the same design approach used for the simulation. The controlled, closed-loop response of

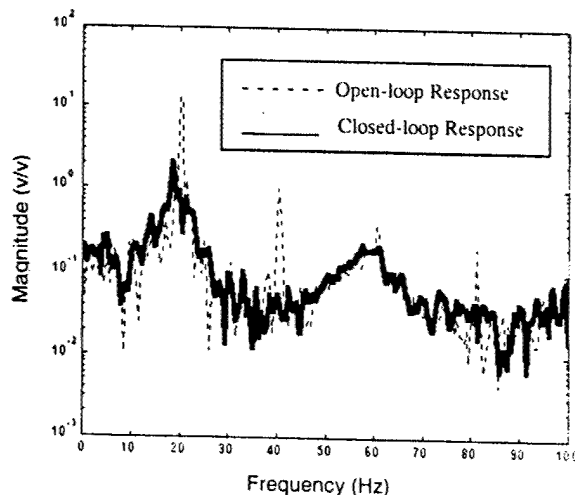


Fig. 10 Open-loop vs. closed-loop response of wing at 38 m/s with clearly visible harmonics in the uncontrolled case

the wing showed a significant increase in the damping of the second mode near flutter. Though somewhat less dramatic than what was predicted by the simulation (due to voltage limitations of the actuator patch), the increased damping raised the flutter boundary by approximately 10 percent to 38.3 m/s. Figure 10 shows the measured frequency response plot of the controlled wing versus the uncontrolled wing in flutter at 38 m/s. The lack of harmonics in the closed-loop response, in addition to the 16 dB reduction in magnitude of the second mode, showed significant control effect.

Conclusions

The analytical model of an aeroelastic delta wing developed herein proved to be an accurate representation of the tested physical model. The dramatic model reduction techniques employed retained the great majority of the significant response characteristics while reducing the model size by over 90 percent. Design of optimal sensor and actuator parameters was accomplished efficiently through the combined use of element based piezo modeling and a genetic algorithm. The optimization design parameters based on Hankel Singular Value estimates associated with the input-output paths of each sensor-actuator pair proved to be useful design metric. This approach proved to be an accurate and computationally efficient means of determining a pair's modal coupling characteristics. The genetic algorithm was shown to consistently converge on similar solutions regardless of the starting set. Use of the design in experimental testing showed the active structure to substantially increase the damping of the flutter mode above the uncontrolled flutter velocity. This active damping was responsible for an increase in the flutter boundary of approximately 10 percent. Future work will focus on methods to allow for random (nonrectangular) patches to be considered in the optimization routine as well as efficiency improvements to the design metric, incorporation of structural nonlinear effects to illustrate LCO's, and the development of increased modularity of the optimization procedure allowing for a broader range of application.

Acknowledgments

This research was supported by the AFOSR under grant number F49620-98-1-0383. The authors would like to thank Dr. Earl

Dowell for his helpful discussions regarding aeroelastic behavior as well as Dr. Deman Tang for his invaluable assistance with the experimental setup.

References

- [1] Rule, J. A., Richard, R. E., and Clark, R. L., 2000, "Experimental Investigation of Delta Wing Flutter Control," *AIAA J.*
- [2] Smith, G. C., 2000, "Design Methodologies for Optimum Spatial Compensation of Adaptive Structures," Ph.D. Dissertation, Duke University, Durham, NC.
- [3] Lim, K. B., and Gawronski, W., 1996, "Hankel Singular Values of Flexible Structures in Discrete Time," *J. Guid. Control Dyn.*, **19**(6), pp. 131–145.
- [4] Lim, K. B., 1997, "Disturbance Rejection Approach to Actuator and Sensor Placement," *J. Guid. Control Dyn.*, **20**(1), pp. 202–204.
- [5] Clark, R. L., and Cox, D. E., 1999, "Band-Limited Actuator and Sensor Selection for Disturbance Rejection: Application to Structural Acoustic Control," *J. Guid. Control Dyn.*, **22**(5), pp. 740–743.
- [6] Rule, J. A., Richard, R. E., and Clark, R. L., 2000, "Design of an Aeroelastic Wing Model for Active Flutter Control," *J. Guid. Control Dyn.*
- [7] Andersen, B. W., 1954, "Vibration of Triangular Cantilever Plates by Ritz Method," *ASME J. Appl. Mech.*, pp. 356–370.
- [8] Clark, R. L., Saunders, W. R., and Gibbs, G. P., 1998, *Adaptive Structures*, John Wiley and Sons, Inc., New York, N.Y.
- [9] Rule, J. A., Cox, D. E., and Clark, R. L., 2000, "Aerodynamic Model Reduction Through Balanced Realization," *AIAA Journal*.
- [10] Hagood, N. W., Chung, W. H., and Von Flotow, A., 1990, "Modeling of Piezoelectric Actuator Dynamics for Active Structural Control," *Proceedings of the 31st AIAA/ASME/ASCE/AHS Structures, Structural Dynamics and Materials Conference*, April 2–4, pp. 2242–2256, AIAA-90-1087-CP.
- [11] Press, W. H., Flannery, B. P., Teukolski, S. A., and Vetterling, W. T., 1988, *Numerical Recipes in C: The Art of Scientific Computing*, pp. 111–141, Cambridge University Press, New York, NY.
- [12] Goldberg D. E., 1989, *Genetic Algorithms in Search, Optimization, and Machine Learning*, Addison-Wesley, Reading, MA.
- [13] Baek, K. H., and Elliot, S. J., 1995, "Natural Algorithms for Choosing Source Locations in Active Control Systems," *J. Sound Vib.*, **186**, pp. 245–267.
- [14] Rao, S. S., Pan, T. S., and Venkayya, V. B., 1999, "Optimal Placement of Actuators in Actively Controlled Structures Using Genetic Algorithms," *AIAA J.*, **37**(10), pp. 1180–1186.
- [15] Skogestad, S., and Postlethwaite, I., 1996, *Multivariable Feedback Control: Analysis and Design*, pp. 349–396, John Wiley & Sons, West Sussex, England.
- [16] Tang, D., Henry, J. K., and Dowell, E. H., 1999, "Limit Cycle Oscillations of Delta Wing Models in Low Subsonic Flow," *AIAA J.*, **37**(11).

Active Acoustic Control of a Rocket Fairing Using Spatially Weighted Transducer Arrays

Steven A. Lane*

Jackson and Tull Engineering, Albuquerque, New Mexico 87106

Jonathan D. Kemp†

Duke University, Durham, North Carolina 27708

Steven Griffin‡

U.S. Air Force Research Laboratory, Kirtland Air Force Base, New Mexico 87117

and

Robert L. Clark§

Duke University, Durham, North Carolina 27708

A preliminary study, including experimental results for a novel active acoustic control approach to reduce the low-frequency modal response in a rocket fairing, is presented. The control method uses spatially weighted transducer arrays with H_2 feedback control laws to attenuate globally the targeted acoustic modes. The nature of the fairing acoustic problem is described, the theory of the control approach is discussed, and important feasibility issues regarding the actual implementation of the control method are presented. Several controllers were implemented on a full-scale composite model of a small rocket fairing. The results demonstrate that the controller was able to reduce the response of the low-frequency modes by 6–12 dB with very little spillover. In addition, a spatially averaged reduction of the acoustic response of the fairing interior in excess of 3 dB over the 20–200-Hz bandwidth was demonstrated. The feasibility studies indicate that limitations on actuator power and volumetric displacement under actual launch conditions are not necessarily prohibitive, but may be satisfied with continued development of actuator technology and placement optimization.

Nomenclature

A_c, B_c, C_c, D_c	= state-space representation of a dynamic control law
A'_c, B'_c, C'_c, D'_c	= state-space representation of the control law augmented with spatial weighting vectors or matrices
$G_{act}(j\omega)$	= frequency response of the actuator transfer function relating the applied control signal to the actuator output signals
$G_{mic}(j\omega)$	= frequency response of the microphone transfer function relating the measured pressure to the output signal, V/Pa
$G(s)$	= Laplace transform of the system transfer matrix
$H(j\omega)$	= frequency response of the control law, V/V
I_{rms}	= root mean square of the current acting on an actuator at a frequency, A
$i_s(j\omega)$	= current signal applied to the actuators, A
P_{av}	= average power delivered to an actuator at a frequency, W
$p(j\omega)$	= microphone pressure measurement, Pa
$\hat{p}(j\omega)$	= scaled pressure signal, Pa
P_{ref}	= reference pressure, 20 μ Pa
R	= resistance of the series resistor contained in the constant volume-velocity actuators, Ω
u	= vector of control inputs
u_m	= denotes the m th system input

$\hat{u}(s)$	= spatially weighted system input
V_{rms}	= root-mean-square voltage acting on an actuator at a frequency, V
$v_a(j\omega)$	= control signal applied to an actuator, V
$v_r(j\omega)$	= voltage measured across the series resistor of an actuator circuit, V
$v_s(j\omega)$	= voltage applied to a speaker in the control experiments, V
W_u	= spatial weighting matrix for actuators
W_y	= spatial weighting matrix for sensors
w_u	= spatial weighting vector applied to actuators
w_y	= spatial weighting vector applied to sensors
$x(j\omega), \dot{x}(j\omega)$	= diaphragm displacement, m, and velocity, m/s, respectively
y	= vector of system outputs
$\hat{y}(s)$	= spatially weighted system output
α	= constant scaling factor for microphone signals
θ	= power factor of an actuator (speaker)
ω_{max}	= maximum frequency of measured data, rad/s
ω_{min}	= minimum frequency of measured data, rad/s

Superscript

T	= transpose operator
-----	----------------------

Introduction

THE high-level, low-frequency acoustic excitation that occurs at launch can induce structural-acoustic vibrations that cause payload damage. As engineers endeavor to create larger, lightweight fairings, that is, launch vehicles, acoustic excitation becomes a more critical factor in payload launch survivability. Research in acoustic attenuation within the fairing has investigated the use of both active control and passive treatments, in addition to controlling the vibration of the fairing itself.^{1–5} At low frequencies, lightly damped modes dominate the interior acoustic response of the fairing. The ineffectiveness of passive treatments, such as acoustic blankets, fiberglass, and acoustic foam, at low frequencies impels consideration of active control methods.

Received 11 May 2000; revision received 15 September 2000; accepted for publication 30 September 2000. Copyright © 2000 by the American Institute of Aeronautics and Astronautics, Inc. All rights reserved.

*Research Scientist, Space and Aeronautics Technology Division, 1900 Randolph Road, SE, Ste. H. Member AIAA.

†Graduate Research Assistant, Department of Mechanical Engineering and Material Science, Box 90302. Member AIAA.

‡Basic Research Manager, Spacecraft Component Technologies Branch, 3550 Aberdeen Avenue, Kirtland. Member AIAA.

§Professor, Department of Mechanical Engineering and Material Science, Box 90300. Member AIAA.

Previous work has shown that dissipative control can be achieved in one-dimensional acoustic enclosures by using a collocated pressure sensor and a constant volume-velocity source.^{6,7} This approach was extended to control low-frequency modes in an aircraft fuselage by utilizing arrays of spatially weighted sensors and actuators. The transducer arrays were spatially weighted to selectively couple with low-frequency modes, which has the advantage of reducing the order of the control law. Significant damping of the low-frequency modes was achieved without producing significant spillover.⁸ Here, this control approach is extended to the fairing problem.

The present work proposes to attenuate the response of low-frequency acoustic modes in a launch vehicle fairing by using an active feedback controller in conjunction with an array of nearly collocated microphones and moving-coil actuators (speakers). Collocation reduces the phase lag between the sensors and actuators and, packaged as a single unit, limits the spatial impact of the system on the payload volume of the fairing. Spatially weighting the array of sensors (microphones) allows measurements taken by each individual sensor to be used collectively, forming a more accurate measurement of the acoustic dynamics of the enclosure. The weighting process emphasizes the coupling with the target mode or modes to be controlled and reduces the coupling with nontarget modes. Likewise, collective implementation of the actuator array enables greater control authority over the low-frequency acoustic modes. Spatial weighting results in a simplified system identification process and control law design. Because only low-frequency modes are targeted by the controller, control can be achieved with relatively low-order control laws, that is, less than 20 states. By the incorporation of low-order dynamic control laws with nearly collocated pressure sensors and volume-velocity actuators, significant controller rolloff is achieved both above and below the control bandwidth, which increases the performance and stability of the controller.

This report presents the results of a preliminary investigation of this control approach applied to a full-scale composite model of a small fairing at Duke University. Primarily, this investigation sought to determine the effectiveness of the control approach in reducing the response of the low-frequency acoustic modes of the fairing. Additionally, this work investigated the feasibility of using the control approach in an actual launch vehicle, where the overall acoustic levels exceed 140 dB over the bandwidth of 10 Hz–10 kHz.

The following discourse first focuses on the fairing acoustics, the spatial-weighting concept and its application, and the method for designing and implementing control laws. Then a discussion is presented that addresses the primary concerns regarding feasibility and the methods used here to investigate these concerns. Next, the experimental testbed, hardware, facilities, and procedure are described. Results from several controllers are presented to provide an indication of controller performance and to illustrate important controller design issues. Finally, conclusions based on this preliminary effort are given.

Theory

Fairing Acoustics

A rocket fairing is essentially a flexible, thin-walled structure that protects the payload during launch. Fairings are typically constructed of metal, such as aluminum, but more recently composites have been used. Although composites offer many advantages, they are less massive and, therefore, allow increased transmission of exterior disturbances. Acoustic waves within the fairing interact detrimentally with the payload. Typically, the overall acoustic levels inside small fairings during launch can exceed 140 dB. At low frequencies (10–200 Hz), the levels reach approximately 120–130 dB.

The length of the fairing considered in this work was 5.3 m, and the maximum diameter was approximately 1.3 m. For this geometry, the low-frequency acoustic modes are longitudinal. A model of a rigid-walled cylinder of similar dimensions provides a reasonable prediction of the lowest acoustic natural frequencies of the fairing. If the longitudinal mode-shapes can be approximated as cosine functions, the first three acoustic natural frequencies occur at approximately 32, 65, and 97 Hz, with the corresponding wavelengths being 10.6, 5.3, and 3.5 m (Ref. 9). Though a very rough approximation, it is apparent that at such long wavelengths passive damping treatments such as acoustic blankets and liners are impractical.

Because of the low amount of damping provided by the fairing, the low-frequency acoustic modes are lightly damped, further exacerbating the problem. If the payload exhibited a structural resonance near an acoustic resonance, the acoustic loading could cause damage to the payload. Flat surfaces of solar panels and lightweight structures such as thin films and membranes would be especially susceptible to damage from low-frequency excitation.

The acoustic modes of the fairing are excited by a number of disturbance sources, including aerodynamic buffeting during flight, structural vibrations induced by the rocket motors, and pyrotechnic shocks during stage separations. These sources act in addition to the explosive noise produced by the motors themselves. The presence of multiple, random disturbance sources precluded adaptive feed-forward control and compelled the use of active feedback control in the present investigation.

Spatial Weighting

Previous research has demonstrated the advantages of employing spatially weighted, discrete transducer arrays to emphasize coupling with target modes.^{8,10–14} Applications have typically involved structural systems where the sensors and actuators were spatially weighted to couple with particular modes of the structure. Sensor and actuator weights were related to the mode shape of the structure and the relative positions of the sensors and actuators. To illustrate spatial weighting for a one-dimensional acoustic application, consider the rigid-walled, simply supported cylinder presented in Fig. 1a, with sensors mounted along the length as indicated. The corresponding first acoustic mode for this hypothetical system is presented in Fig. 1b. The appropriate spatial weight for each of the actuators shown corresponds to the modal amplitude evaluated at the sensor position. Notice that the spatial-weighting values for the first three sensors are positive, whereas the last three are negative. The change of sign indicates that the last three sensors are 180 deg out of phase with the first three. The fourth sensor is located near the node of the mode shape; therefore, its corresponding spatial weight would be near zero.

For complex structures and enclosures such as the fairing, the spatial-weighting vector or matrix must be determined from experimental measurements. The method presented herein estimates the appropriate spatial-weighting vector from frequency-response measurements. Because the sensors and actuators in the experiments were collocated with respect to the acoustic wavelength, the spatial weight for each actuator was approximated as the weight determined for the corresponding sensor. This approximation is sufficient for control of low-frequency modes in a lightly damped enclosure.

Consider an enclosure with an array of pressure sensors (microphones) positioned arbitrarily throughout. A loudspeaker is positioned arbitrarily in the enclosure to provide a stochastic noise input. The frequency responses between the noise input and the sensor microphones reveal the degree of coupling between each sensor and the acoustic modes of the enclosure.⁸ At a particular modal frequency, the weight for a given sensor can be defined as the real part of the complex frequency response of the sensor at the modal frequency. Weights are calculated for each sensor in this fashion from the respective frequency-response measurements. The weights collectively form a vector of weighting values for the sensor array and,

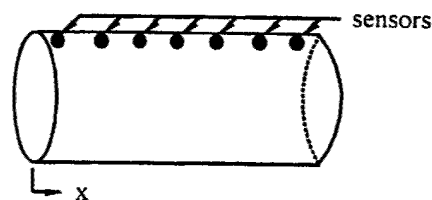


Fig. 1a Simply supported cylinder.

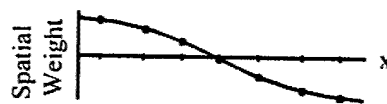


Fig. 1b Fundamental acoustic mode shape

hence, for the actuator array. The weighting vector is normalized to unity for convenience.

Consider a system with M inputs u and P outputs y , represented by the transfer matrix $G(s)$. The spatial-weighting vector used to emphasize a single target mode is denoted as w_y for the sensors and w_u for the actuators, where

$$w_y = w_u^T \quad (1)$$

Application of the weighting vectors w_u and w_y to the system inputs and outputs, respectively, reduces the system to a single input $\hat{u}(s)$ and a single output $\hat{y}(s)$. The output is expressed as a linear combination of the sensor measurements,

$$\hat{y}(s) = w_y y \quad (2)$$

Because the sensor outputs can be expressed as

$$y = G(s)u \quad (3)$$

substituting Eq. (3) into Eq. (2) yields

$$\hat{y}(s) = w_y G(s)u \quad (4)$$

Because the inputs to the plant are given as

$$u_m = w_{u_m} \hat{u}, \quad m = 1, 2, \dots, M \quad (5)$$

the output can be expressed as

$$\hat{y}(s) = \sum_{p=1}^P w_{y_p} \sum_{m=1}^M G_{p,m}(s) w_{u_m} \hat{u}(s) \quad (6)$$

which yields

$$\frac{\hat{y}(s)}{\hat{u}(s)} = \sum_{p=1}^P \sum_{m=1}^M w_{y_p} G_{p,m}(s) w_{u_m} \quad (7)$$

Therefore, the resulting single-input/single-output system is expressed as

$$\hat{y}(s)/\hat{u}(s) = w_y G(s) w_u \quad (8)$$

For a system where Q modes are to be selected for control, the order (i.e., the number of inputs and outputs, as opposed to the number of states) of the system is expanded from a single-input/single-output system to one having an input and output corresponding to each targeted mode. In this case, the weighting vectors are replaced by the matrices W_u and W_y ($M \times Q$ and $Q \times P$, respectively) with rows and columns corresponding to the spatial-weighting vector for each target mode.

To achieve global dissipation of acoustic energy in the fairing, a measurement or linear combination of states differing from that of the sensors must be included, otherwise control effects may only be local, that is, limited to servocontrol. In this investigation, this measurement, referred to as the performance signal, was generated by using a second array of microphones distributed arbitrarily throughout the interior of the fairing. Measurements from these performance microphones were not measured by the controller, but were only used as a performance metric in the design of the control law. Spatial-weighting vectors were measured and applied to the performance microphones to emphasize the same modes targeted by the controller.

Control Design

Dynamic controllers can be shaped to emphasize control over a specific bandwidth and to produce rolloff above the control bandwidth. Therefore, dynamic controllers can provide better performance and increased stability in comparison to static gain controllers. The control laws used in the present work were computed to minimize the two norm H_2 of the transfer matrix between the performance variables and the exogenous inputs.^{12,15} Criteria for control law design included disturbance rejection at low frequen-

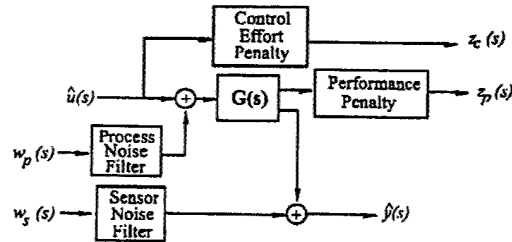


Fig. 2 Block diagram of the augmented plant used in H_2 control law synthesis.

cies while maintaining low sensitivity to noise and modeling errors at higher frequencies.

In the subsequent experiments, models of the open-loop system were computed by using an approach based on the eigensystem realization algorithm.¹⁶ This method of system identification yielded low-order, discrete state-space models that were used in control law synthesis. Frequency-dependent weighting filters were added to the open-loop system model to form the augmented plant presented in Fig. 2. The inputs to the augmented plant included the control signal $\hat{u}(s)$, the process noise input that represents exogenous inputs and disturbances $w_p(s)$, and the sensor noise input $w_s(s)$. The outputs of the augmented plant included the control effort penalty $z_c(s)$, the spatially weighted performance microphone measurements $z_p(s)$, and the sensed variable $\hat{y}(s)$, which represents the spatially weighted sensor microphone measurements.

For system modeling, the disturbance loudspeaker and the acoustic paths from the disturbance to the performance microphones were not measured or included. This exclusion prevented the controller from attempting to impedance load the disturbance. Instead, the controller should yield attenuation regardless of the source or the location of the disturbance. For modeling purposes, the process noise input was summed into the control input (see Fig. 2). Therefore, the plant (fairing acoustics) shaped the effects of the process noise as recommended.¹² To generate a well-posed control problem, a low-pass filter was added to the process noise input to eliminate feedthrough terms. The cutoff frequency of the low-pass filter was set to 10 kHz, well above the bandwidth of interest.

The augmented system was assembled and modeled using Simulink,¹⁷ and H_2 control laws were computed using MATLAB.¹⁸ Filters used to shape the controller increased the order (number of states) of the augmented plant and of the resulting control law. This resulted in a control law of much larger order than necessary. Model reduction techniques, such as balanced residualization or truncation,^{15,19} were applied to reduce the order of the controller without significantly affecting the dynamics of the controller or the closed-loop system.

After computation, the reduced-order control law was transformed into the discrete domain using a Tustin transformation, the spatial-weighting vectors were applied, and the control law was downloaded to a digital signal processor (DSP) for implementation. A control law given as $\{A_c, B_c, C_c, D_c\}$ can be expanded for $M = P$ collocated sensors and actuators such that

$$A'_c = A_c, \quad C'_c = w_u C_c, \quad B'_c = B_c w_y, \quad D'_c = w_u D_c w_y \quad (9)$$

For a multimode ($Q > 1$) controller, the weighting vectors are replaced by the corresponding weighting matrices.

Controller performance was determined by comparing the open-loop and closed-loop frequency-response functions from a disturbance input (band-limited random noise) to the performance microphone array and the sensor microphone array. Averaging these frequency-response measurements provided representative open-loop and closed-loop frequency responses and facilitated evaluation of the overall effects of the controller as a function of frequency. From this evaluation, the occurrence of spillover, the degree of coupling to the target modes, and the average amount of attenuation at the sensors and globally at the performance microphones can be observed.

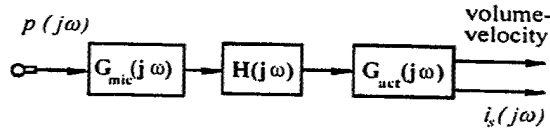


Fig. 3 Path from sensor to actuator.

Feasibility Issues

An active control system must meet many criteria to be practical in a launch vehicle. The additional weight and expense of the control system is of primary concern. Another important consideration is the performance-to-weight ratio, which indicates how much attenuation is provided for a given weight of the control system. In some situations, it might be determined that simply adding an equivalent amount of mass to the structure would provide the same attenuation levels without the additional complexity.

In this investigation, issues such as actuator power requirements, actuator diaphragm displacement, and signal clipping were considered. Although the controller would only operate for the several minutes between launch and orbit, it is important to determine the amount of power required by the controller (specifically the actuators) to determine feasibility from a power-supply/battery standpoint. Another important issue involves the response of the actuator to the control input. A control signal for high-level disturbances could command a response beyond reasonable actuator abilities, such as an extreme volumetric displacement. By the measurement of the response of the actuators and the transfer function from the sensor inputs to the actuators, the power and diaphragm displacement were extrapolated from the experimental data to higher sound pressure levels. Although the relatively low sound pressure levels used in these preliminary experiments (90 dB) deemed clipping an unimportant issue, clipping would be a critical consideration in an actual implementation where the acoustic disturbance is orders of magnitude larger.

The path from the sensor input to the actuator output is presented in Fig. 3. The pressure response measured at each sensor, $p(j\omega)$, for a band-limited random disturbance was used as a rough approximation of the pressure response that would be experienced in the fairing at launch. The microphone response was integrated over the bandwidth to compute the total rms pressure at the microphone. The total rms pressure was then converted to sound pressure level [SPL(dB)], which is given by

$$\text{SPL(dB)} = 20 \log_{10} \left(\frac{\sqrt{\sum_{i=\omega_{\min}}^{\omega_{\max}} |p(j\omega_i)|^2}}{P_{\text{ref}}} \right) \quad (10)$$

By scaling the sound pressure level [SPL(dB)] spectrum measured at lower disturbance levels, the pressure spectrum corresponding to the total rms pressure for any desired level can be predicted, that is,

$$\hat{\text{SPL(dB)}} = 20 \log_{10} \left(\frac{\sqrt{\sum_i \alpha^2 |p(j\omega_i)|^2}}{P_{\text{ref}}} \right) \quad (11)$$

where α is a constant scaling factor for each microphone and is determined by

$$\alpha = \frac{P_{\text{ref}} 10^{\hat{\text{SPL}}/20}}{\sqrt{\sum_i |p(j\omega_i)|^2}} \quad (12)$$

where $\hat{\text{SPL}}$ is the desired SPL. This scaling yields a rough prediction of the pressure measurement $\hat{p}(j\omega)$ that would occur for an actual launch,

$$\hat{p}(j\omega) = \alpha p(j\omega) \quad (13)$$

Each microphone transduced the pressure inside the fairing to an equivalent output voltage that was defined by the microphone sensitivity. This signal was then filtered and amplified by the microphone conditioning hardware. Thus, the gain of the microphone conditioning circuitry and the microphone sensitivity, collectively referred to

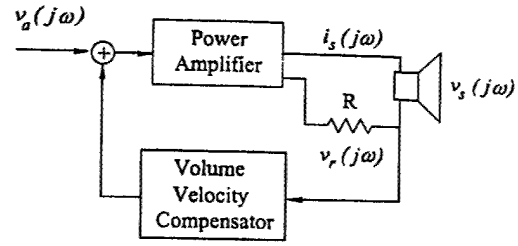


Fig. 4 Schematic of the actuator setup.

as $G_{\text{mic}}(j\omega)$, were necessary for calculating the interior SPLs from the output signals of the microphone conditioning hardware.

For feedback controller implementation, the voltage signals from the sensor microphones and the conditioning hardware were sampled by the DSP and filtered by the discrete control law to compute the control signals. The control law, which is referred to as $H(j\omega)$, was characterized by measuring the frequency response across the input and output channels of the DSP. This measurement verified that the dynamics of the downloaded controller corresponded to the designed control law and revealed any effects from antialiasing and reconstruction filters of the DSP.

The output voltages from the DSP as applied to the actuators, denoted as $v_a(j\omega)$, were predicted by using the controller transfer matrix $H(j\omega)$, the transfer functions across the microphones $G_{\text{mic}}(j\omega)$, and the estimated pressure signals acting on the microphones $\hat{p}(j\omega)$,

$$v_a(j\omega) = H(j\omega)G_{\text{mic}}(j\omega)\hat{p}(j\omega) \quad (14)$$

From this prediction, the controller voltages were estimated as a function of fairing interior sound level for a given controller.

As shown in Fig. 4, the actuator hardware included a power amplifier, a moving-coil speaker, a series resistor for sensing the current, and a constant volume-velocity compensator. In the subsequent experiments, 14-cm-diam loudspeakers mounted in small enclosures were used as control actuators. Each loudspeaker system was compensated by using a feedback loop around the actuator to cause the loudspeaker to approximate constant volume-velocity behavior over the control bandwidth.⁷ This feedback loop reduced the effects of the loudspeaker dynamics on the closed-loop system and simplified control law design.

The diaphragm velocity $\dot{x}(j\omega)$ and displacement $x(j\omega)$ were measured as a function of voltage applied to the actuator $v_a(j\omega)$ using a laser vibrometer. The frequency response of the actuator displacement to applied voltage was used to extrapolate the actuator displacement corresponding to higher SPLs. This calculation assumes linearity and ignores possible peak-to-peak voltage limits of the DSP. Although free-air measurements give a good estimate of the velocity and displacement response, they do not account for the coupling between the actuator and the acoustic system. In the coupled system, the acoustic modes of the fairing affect the actuator response. However, these effects are small and were neglected in the present study.

For a voltage applied to an actuator, the average power delivered to the speaker can be computed as²⁰

$$P_{\text{av}} = V_{\text{rms}} I_{\text{rms}} \cos \theta \quad (15)$$

The power spectrum of the voltage applied to a speaker can be calculated by using the frequency-response function $v_s(j\omega)/v_a(j\omega)$:

$$|v_s(j\omega)|^2 = \left| \frac{v_s(j\omega)}{v_a(j\omega)} \right|^2 |v_a(j\omega)|^2 \quad (16)$$

where $v_s(j\omega)$ is the voltage acting on the speaker as shown in Fig. 4. The power spectrum of the current $i_s(j\omega)$ is readily available by dividing the frequency response of the series resistor voltage signal to the applied voltage by the series resistor resistance, which yields

$$|i_s(j\omega)|^2 = \left| \frac{v_r(j\omega)}{R v_a(j\omega)} \right|^2 |v_a(j\omega)|^2 \quad (17)$$

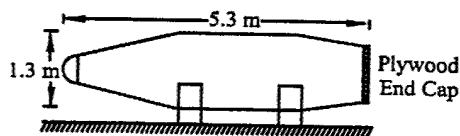


Fig. 5 Illustration of the fairing testbed.

The power delivered to a speaker as a function of frequency for an applied voltage $v_a(j\omega)$ is computed from

$$P_{av}(j\omega) = \sqrt{|v_s(j\omega)|^2} \sqrt{|i_s(j\omega)|^2} \cos \theta(j\omega) \quad (18)$$

This can be summed over the bandwidth to yield an overall actuator (OA) power requirement, computed as

$$P_{OA} = \sqrt{\sum_{i=\omega_{min}}^{\omega_{max}} P_{av}^2(j\omega_i)} \quad (19)$$

Experimental Equipment and Testbed

Experiments were conducted on a full-scale composite fairing model using 16 constant volume-velocity actuators with 16 collocated sensor microphones and 16 performance microphones. The fairing (shown in Fig. 5) was approximately 5.3 m in length, 1.3 m in diameter (maximum), and tapered at both ends. An aluminum end cap was fixed to the nose, and a plywood end cap was attached to the base. Each sensor/actuator pair was rigidly attached to the composite structure. The sensor/actuator pairs were evenly distributed along the length and circumference of the fairing interior to yield unbiased spatial sampling. For these experiments, off-the-shelf loudspeakers that were rated at 100 W with a maximum linear excursion of 4.5 mm were used as actuators. A disturbance loudspeaker was placed in the corner of the fairing near the base end cap and was used to excite the interior cavity modes. The performance microphones were distributed throughout the interior at arbitrary positions to measure the overall controller effects. All cabling was connected through a panel at the base of the fairing. The controller, spectrum analyzers, power amplifiers, microphone conditioners, and other required hardware were housed outside of the fairing. A block diagram of the setup is presented in Fig. 6.

Both the sensor and performance microphones were calibrated, ICP devices that, according to the manufacturer's specifications, were accurate to within ± 1 dB over the bandwidth of 20–7000 Hz and were linear within 3% up to 128 dB. Stated temperature effects were less than ± 0.5 dB over the range of -20 – 65°C . The microphone conditioning hardware provided 12-bit accuracy and 72-dB channel isolation and had a low-frequency response of $\pm 5\%$ at 0.5 Hz and a high-frequency response of $\pm 5\%$ at 100 kHz. Because the control bandwidth in these experiments was roughly 20–200 Hz, the uncertainty of the conditioning hardware was conservatively assumed to be 3%. The accuracy of the laser vibrometer used to characterize the actuators was specified by the manufacturer to be within 3% over its bandwidth.

Multichannel Rane amplifiers were used to drive the actuators. Each amplifier channel was ac coupled and was capable of approximately 100 W. Amplifier specifications included a 103-dB signal-to-noise ratio, and -60 -dB cross-talk. The frequency response was measured to be flat (0 dB) from 20 Hz to over 10 kHz. A Siglab spectrum analyzer system was used to generate disturbance signals and to measure open- and closed-loop frequency responses. The analyzer used a 20-bit analog-to-digital converter and an 18-bit digital-to-analog converter. The manufacturer's specifications indicated an absolute accuracy of 0.0025% of full-range, 90-dB alias protection and greater than 90-dB dynamic range. The DSP used for implementing the control law was a 32-bit TMS320C40 processor that used 16-bit converters.

The greatest source of experimental uncertainty originated from the microphones, microphone conditioning hardware, and the vibrometer measurements. The resulting uncertainty of the micro-

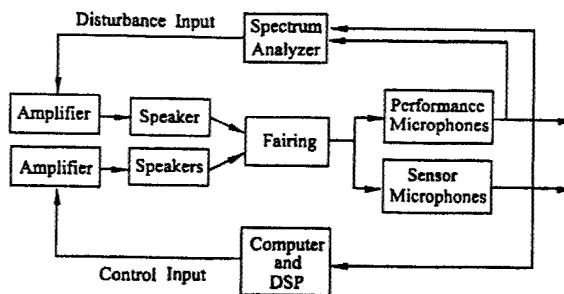


Fig. 6 Schematic of the experimental setup.

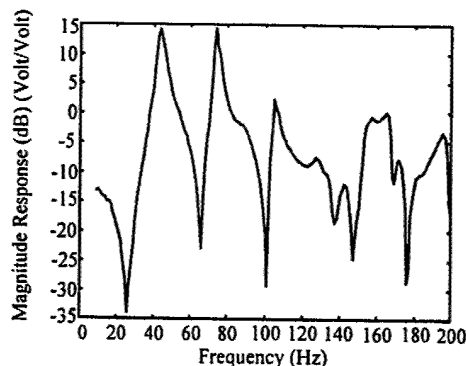


Fig. 7 Representative response at a sensor microphone (± 0.51 -dB uncertainty).

phones and the microphone conditioning hardware was assumed to be the product of the uncertainties, which yielded approximately 6.1%, that is, 1.03×1.03 . This is equivalent to an experimental error range of approximately ± 0.51 dB over the control bandwidth. For the vibrometer measurements, the experimental error range was only ± 0.26 dB across the bandwidth.

Results

Sensors

The response measured at a representative sensor microphone for band-limited (200-Hz) random noise acting on the disturbance loudspeaker is shown in Fig. 7. The response clearly indicates the lightly damped modal nature of the fairing interior. From this frequency-response function, the resulting interior SPL for a unit-magnitude voltage (rms) applied to the disturbance loudspeaker can be determined. Including the microphone sensitivity of 20.61 mV/Pa and the conditioning hardware gain of 50, the voltage response in Fig. 7 can be converted to pascal per volt, where

$$\frac{\text{pressure (Pa)}}{\text{disturbance (V)}} = \left(\frac{1 \text{ Pa}}{20.61 \text{ mV}} \right) \left(\frac{1000 \text{ mV}}{\text{V}} \right) \left(\frac{1 \text{ V}}{50} \right) \times \left(\frac{\text{microphone voltage output}}{\text{disturbance voltage input}} \right)$$

For a band-limited random noise disturbance input of 1 V rms, the resulting rms pressure response at this microphone would be approximately 117 dB (relative to a reference pressure of $20 \mu\text{Pa}$). To scale this pressure spectrum such that the rms pressure level was 120 dB, the scaling factor α , determined from Eq. (12), would be approximately 1.275.

Actuators

The diaphragm velocity response as measured with a laser vibrometer relative to a 1-V rms band-limited random noise input $v_a(j\omega)$ for a typical actuator is presented in Fig. 8. Figure 8 shows the open-loop velocity response and the closed-loop response with the constant volume-velocity compensator. The diaphragm velocity of the compensated actuator was nearly constant at roughly 18 mm/s/V

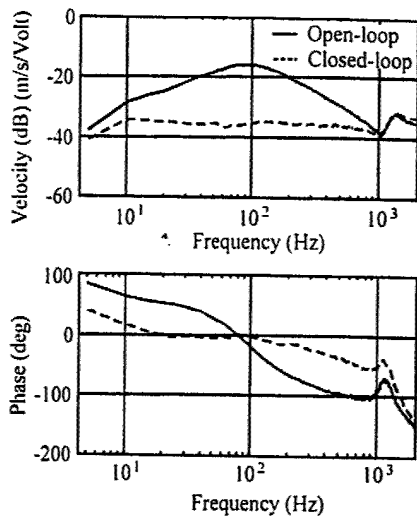


Fig. 8 Measured velocity response of the actuator diaphragm (± 0.26 -dB uncertainty).

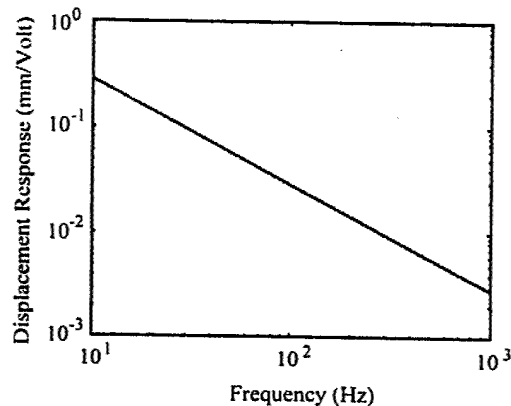


Fig. 9 Computed displacement response of the actuator diaphragm ($\pm 3\%$ uncertainty).

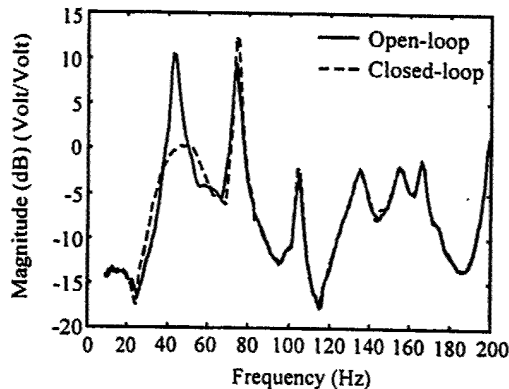


Fig. 10 Average sensor microphone response for the first-mode controller (± 0.51 -dB uncertainty).

from 10 to 900 Hz. The phase lag resulting from the actuator dynamics was significantly reduced over this bandwidth. After integration, the assumed constant velocity response of 18 mm/s/V yielded the diaphragm displacement approximation presented in Fig. 9.

Single-Mode Controllers

Initially, experiments were performed to attenuate the response of a single acoustic mode of the fairing. Figures 10 and 11 show the results of a controller designed for the fundamental mode at 47 Hz. Figure 10 presents the averaged open-loop and closed-loop frequency-response functions measured at the sensor microphones relative to the disturbance input. Figure 11 presents the averaged

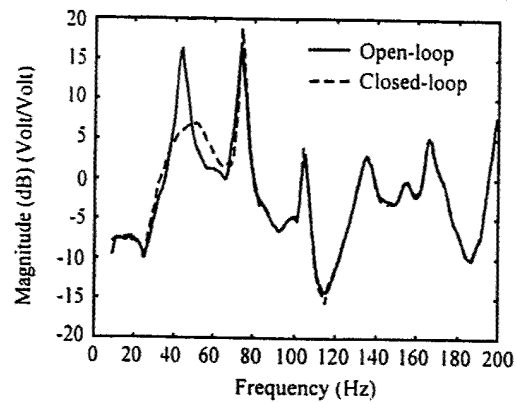


Fig. 11 Average performance microphone response for the first-mode controller (± 0.51 -dB uncertainty).

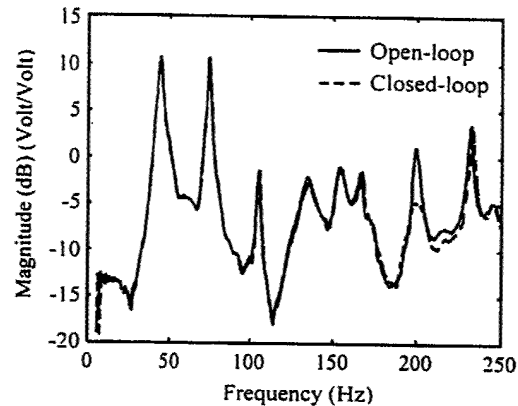


Fig. 12 Average sensor microphone response for the seventh-mode controller (± 0.51 -dB uncertainty).

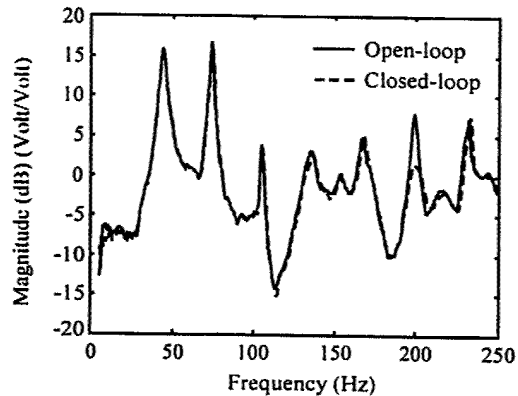


Fig. 13 Average performance microphone response for the seventh-mode controller (± 0.51 -dB uncertainty).

open-loop and closed-loop frequency-response functions measured at the performance microphones. Note that Figs. 10 and 11 present the microphone output voltages, which indicate the reduction in the interior SPL achieved by the controller. These results demonstrate that the controller successfully reduced the response of the target mode, both at the sensor microphones and at the performance microphones. This controller was designed to be aggressive, yielding 10 dB of reduction of the target mode at the sensors and performance microphones, respectively, but also creating spillover at the second mode. Computing the open-loop and closed-loop rms pressure reductions indicated that only 0.88 and 0.85 dB of attenuation was achieved at the sensor and performance microphones, respectively, over the 200-Hz bandwidth.

The next experiments investigate the ability of the controller to control higher frequency modes of the fairing. Figures 12 and 13 present the results for a controller designed to target the seventh

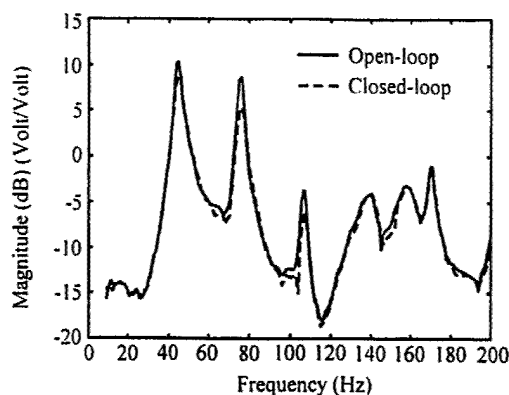


Fig. 14 Average sensor response for the three-mode controller (nonaggressive) (± 0.51 -dB uncertainty).

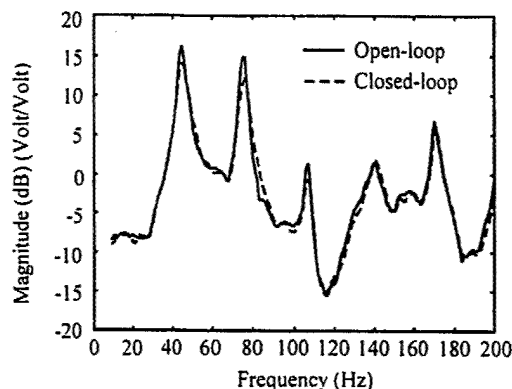


Fig. 15 Average performance microphone response for the three-mode controller (nonaggressive) (± 0.51 -dB uncertainty).

acoustic mode of the fairing at 200 Hz. This controller was less aggressive than the preceding one (i.e., more control effort penalty, see Fig. 2), and yet the response of the target mode was reduced by 6 dB at both the sensor and performance microphone locations. The data indicate that this controller produced very little spillover. In spite of the significant attenuation measured at the single target mode, the overall rms reductions were only 0.17 and 0.32 dB over the 250-Hz bandwidth at the sensor and performance microphones, respectively. However, in both cases, the spatially weighted controller successfully coupled with the target mode and achieved significant attenuation.

Three-Mode Controllers

The next experiments demonstrate the ability of the controller to attenuate multiple acoustic modes. Controllers were designed to attenuate the first, second, and third acoustic modes at 47, 75, and 107 Hz, respectively. The first controller was designed by using a relatively large control effort penalty, which yielded only slight attenuation at each mode, as shown in Figs. 14 and 15. The controller reduced the response of the target modes with negligible spillover. Over the 200-Hz bandwidth, the rms reduction was computed to be 1.19 dB at the sensor microphones and 1.13 dB at the performance microphones.

In the final experiments, a more aggressive controller was implemented, and the results are presented in Figs. 16 and 17. The first and second modes were reduced by approximately 12 dB and the third by 5 dB at the sensor microphones and the performance microphones. The controller had very little effect on the nontarget modes, which is desirable from a stability standpoint. This controller achieved an overall reduction in the rms response at the sensor microphones of 3.46 and 3.30 dB at the performance microphones. This reduction is very significant and is highlighted by measurement of the reduction at arbitrary points throughout the fairing. The first two modes were well controlled, and little more improvement could be achieved at these frequencies. As with the preceding controller, there was very little spillover produced. These results illustrate the importance of

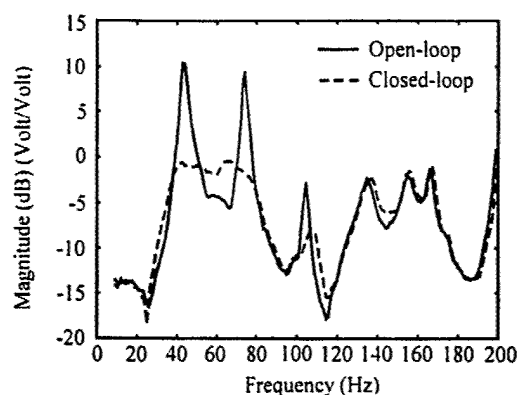


Fig. 16 Average sensor response for the three-mode controller (aggressive) (± 0.51 -dB uncertainty).

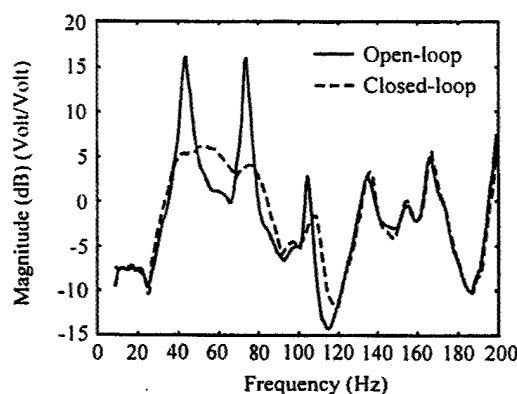


Fig. 17 Average performance microphone response for the three-mode controller (aggressive) (± 0.51 -dB uncertainty).

achieving an optimal balance of control effort penalty and performance penalty in controller design. These results also demonstrate that the control approach can attenuate multiple modes and achieve significant levels of reduction across the control bandwidth.

Computation of Diaphragm Excursion and Power Requirements

Because the final three-mode controller provided attenuation levels that would be necessary to justify implementing the controller in an actual launch vehicle, the measurements taken from this controller were used to investigate power requirements and actuator diaphragm displacement. The voltage applied to the actuators for various SPLs can be computed by measuring the open-loop pressure responses $p_i(j\omega)$ for the 16 sensor microphones, measuring the controller frequency-response functions $H(j\omega)$ and measuring $G_{mic}(j\omega)$ and $G_{act}(j\omega)$. From these measurements, the rms diaphragm displacement and power can be determined as discussed earlier. Results of the displacement and power calculations are presented in Tables 1 and 2, respectively, for the 200-Hz bandwidth.

Table 1 indicates that, for this controller, the diaphragm displacement was less than 2 mm for disturbance levels up to 120 dB. This displacement is within the linear excursion range of the off-the-shelf actuators used in this investigation. At 130 dB, some actuator displacements exceeded the nominal linear excursion limits, and at 140 dB, the predicted excursions were on the order of centimeters. Note that there were considerable discrepancies between the displacements of the various actuators, which indicates that some actuators were not used effectively. Also note that the rms displacement increased roughly an order of magnitude for every 20-dB increase in the SPL (which corresponds to an order of magnitude increase in sound pressure). Because these predictions were based on both microphone measurements, which have an uncertainty of approximately 6.1%, and vibrometer measurements, which have an uncertainty of approximately 3%, the overall uncertainty of these estimates is approximately 9%.

Table 2 shows the power delivered to the speakers that was estimated using Eqs. (18) and (19). Based on the uncertainty of the

Table 1 Predicted rms displacement (millimeters) of speaker diaphragms as a function of SPL (9% uncertainty)

Actuator	SPL, dB				
	100	110	120	130	140
1	0.042	0.132	0.418	1.322	4.181
2	0.056	0.178	0.563	1.779	5.625
3	0.049	0.156	0.494	1.563	4.942
4	0.051	0.160	0.505	1.596	5.047
5	0.049	0.156	0.494	1.562	4.939
6	0.043	0.137	0.432	1.367	4.322
7	0.042	0.132	0.416	1.316	4.162
8	0.045	0.141	0.445	1.407	4.450
9	0.049	0.154	0.488	1.542	4.875
10	0.064	0.201	0.637	2.013	6.366
11	0.064	0.203	0.640	2.025	6.404
12	0.099	0.312	0.987	3.120	9.866
13	0.095	0.300	0.948	2.999	9.483
14	0.076	0.241	0.761	2.407	7.612
15	0.073	0.231	0.730	2.307	7.295
16	0.052	0.163	0.515	1.629	5.150

Table 2 Predicted power (watts) applied to speakers as a function of SPL (27% uncertainty)

Actuator	SPL, dB				
	100	110	120	130	140
1	0.019	0.19	1.9	19	192
2	0.088	0.88	8.8	88	880
3	0.001	0.01	0.1	1	9
4	0.001	0.01	0.1	1	9
5	0.042	0.42	4.2	42	417
6	0.016	0.16	1.6	16	159
7	0.008	0.08	0.8	8	82
8	0.001	0.00	0.0	0	5
9	0.000	0.00	0.0	0	2
10	0.004	0.04	0.4	4	39
11	0.001	0.01	0.1	1	12
12	0.031	0.31	3.1	31	311
13	0.014	0.14	1.4	14	140
14	0.015	0.15	1.5	15	146
15	0.010	0.10	1.0	10	97
16	0.003	0.03	0.3	3	33

microphone measurements, 6.1%, and allowing for uncertainty in frequency response measurements of 0.1%, this yields a total uncertainty in the estimated power requirements of approximately 27%. The values given in Table 2 indicate that the power levels were within the allowable range up to 130 dB. At 140 dB, there were several actuators above the nominal rating. The data indicate that the power requirements increased two orders of magnitude for every 20-dB increase in the SPL. Again, there were considerable variations of the power requirements for each speaker, most notably between speakers 2 and 9.

Conclusions

The preliminary set of experiments presented herein demonstrated that active acoustic control with spatially weighted transducer arrays has the potential to significantly reduce the low-frequency modal response of a launch vehicle fairing. Over 3 dB of reduction was measured throughout the fairing interior over the 20–200-Hz bandwidth. The results demonstrated that the proposed control method successfully coupled with and controlled the target mode(s), attenuating the individual target modes by as much as 12 dB without producing significant spillover.

Feasibility issues for practical implementation of the control system were presented and discussed. For an aggressive three-mode controller, data measured at disturbance levels near 90 dB were extrapolated to predict rms diaphragm displacement and power requirements corresponding to higher SPLs. The data indicated that the required power levels on some speakers exceeded 100 W above

130 dB. However, the diaphragm displacement was less than a few millimeters below 130 dB. The displacement and power requirements are not unrealistic at low frequency, where levels are approximately 130 dB, and may be achieved with better designed actuators and optimization of the number and placement of the actuators.

Acknowledgments

The authors would like to gratefully acknowledge the partial support for this research provided under the Air Force Office of Scientific Research Presidential Early Career Award for Scientists and Engineers, Grant F49620-98-1-0383, monitored by Brian Sanders and Daniel Segalman. We would also like to express our gratitude to the U.S. Air Force Research Laboratory for providing the rocket fairing model used in these experiments.

References

1. Leo, D. J., and Anderson, E. H., "Vibroacoustic Modeling of a Launch Vehicle Payload Fairing for Active Acoustic Control," AIAA Paper 98-2086, April 1998.
2. Shen, F., and Pope, D., "Design and Development of Composite Fairing Structures for Space Launch Vehicles," Society of Automotive Engineers, TP 901836, Oct. 1990.
3. Bradford, L., and Manning, J., "Attenuation of Cassini Spacecraft Acoustic Environment," *Sound and Vibration*, Vol. 30, No. 10, 1996, pp. 30–37.
4. Weissman, K., McNelis, M. E., and Pordan, W. D., "Implementation of Acoustic Blankets in Energy Analysis Methods with Application to the Atlas Payload Fairing," *Journal of the Institute of Environmental Sciences*, Vol. 37, No. 4, 1994, pp. 32–39.
5. Niezrecki, C., and Cudney, H. H., "Preliminary Review of Active Control Technology Applied to the Fairing Acoustic Problem," *Proceedings of the AIAA/ASME/AHS Adaptive Structures Forum*, AIAA, Reston, VA, 1996, pp. 101–108; also AIAA Paper 96-1275, 1996.
6. Lane, S. A., and Clark, R. L., "Dissipative Feedback Control of a Reverberant Enclosure Using a Constant Volume Velocity Source," *Journal of Vibration and Acoustics*, Vol. 120, No. 4, 1998, pp. 987–993.
7. Lane, S. A., and Clark, R. L., "Improving Loudspeaker Performance for Active Noise Control Applications," *Journal of the Audio Engineering Society*, Vol. 46, No. 6, 1998, pp. 508–519.
8. Lane, S. A., "Active Noise Control in Acoustic Enclosures Using a Constant Volume Velocity Source," Ph.D. Dissertation, Dept. of Mechanical Engineering and Material Science, Duke Univ., Durham, NC, March 1999.
9. Shirahtati, U. S., and Crocker, M. J., "Standing Waves," *Encyclopedia of Acoustics*, Vol. 1, edited by M. J. Crocker, Wiley, New York, 1997, pp. 81–89, Chap. 7.
10. Burke, S., and Hubbard, J., "Spatial Filtering Concepts in Distributed Parameter Control," *Journal of Dynamic Systems, Measurement and Control*, Vol. 112, No. 4, 1990, pp. 565–573.
11. Burke, S., Hubbard, J., and Meyer, J., "Distributed Transducers and Colocation," *Mechanical Systems and Signal Processing*, Vol. 7, No. 4, 1993, pp. 349–361.
12. Clark, R. L., Saunders, W. R., and Gibbs, G. P., *Adaptive Structures, Dynamics and Control*, 1st ed., Wiley, New York, 1998, pp. 212–219, 310–312, and 340–354.
13. Fuller, C., Elliott, S., and Nelson, P., *Active Control of Vibration*, 1st ed., Academic Press, New York, 1996, pp. 141–143.
14. Morgan, D. R., "An Adaptive Modal-Based Active Control System," *Journal of the Acoustical Society of America*, Vol. 89, No. 1, 1991, pp. 248–256.
15. Skogestad, S., and Postlethwaite, I., *Multivariable Feedback Control*, 1st ed., Wiley, New York, 1996, pp. 349–369, 452, 453.
16. Juang, J., *Applied System Identification*, 1st ed., Prentice-Hall, Englewood Cliffs, NJ, 1994, pp. 133–139.
17. *Simulink, Dynamic Simulation for Matlab*, Ver. 3.0, Release 11, MathWorks, Natick, MA, Sept. 1998.
18. *Matlab, The Language of Technical Computing*, Ver. 5.3, Release 11, MathWorks, Natick, MA, Jan. 1999.
19. *μ-Analysis and Synthesis Toolbox*, Ver. 3.0.4, Release 11, MathWorks, Natick, MA, April 1998.
20. Balabanian, N., and Bickart, T. A., "Power and Energy," *The Electrical Engineering Handbook*, 1st edition, edited by R. C. Dorf, CRC Press, Boca Raton, FL, 1993, Sec. 3.4, pp. 81–87.

Frequency-Shaping with Spatial Compensators

G. CLARK SMITH* AND ROBERT L. CLARK

Department of Mechanical Engineering and Materials Science, Duke University, Durham, NC 27708-0302

ABSTRACT: Practical realizations of adaptive structures should be designed and implemented to maximize performance, robustness and efficiency. A method of frequency-shaping the compensation of an adaptive structure is developed for increased performance, system robustness and efficiency. Robustness is defined as reduced coupling to out-of-bandwidth modes, where model fidelity frequently suffers, and to in-bandwidth modes that are considered not important for control. This method utilizes an open-loop metric of system coupling, through Hankel singular values of the controllability and observability Gramians, to determine the optimum transducer placements and sizes. The design metric is maximized with genetic algorithms. This optimum design process is computationally efficient. Results demonstrate that optimizing the design metric with genetic algorithms yields better performance and efficiency when compared to previous optimization methods and forms a basic method of "loop-shaping" by spatial design.

INTRODUCTION

IN a feedback control system, the actuator input signals are created by modifying the temporal response of the sensor signals with a controller. The optimum controller, or temporal compensator, is usually realized by frequency-shaping the system open- and closed-loop transfer functions [1]. Previous work in adaptive structures has also shown that optimum compensator design may be augmented by considering the design of the spatial compensator of the control system [1]. Spatial compensation is defined as the influence of the type, placement, size, and shape of the transducers on the open-loop response and, as a result, the closed-loop temporal compensator design. When combined, the temporal and spatial compensators form the complete control system for the adaptive structure.

The objective of this work is to continue the development of open-loop design techniques for frequency-shaping with spatial compensators, thereby providing greater levels of system performance, efficiency and robustness. The design technique introduced is based upon the open-loop metric developed by Smith and Clark [2]. The genetic algorithms optimization routine is then introduced as the method of determining the transducer placements and sizes. This design technique is applied to vibration control of a simply supported plate with one piezoelectric sensor and actuator. Results are compared to the optimum result from previous work. These results demonstrate that the design technique presented is more effective at meeting the prescribed objectives.

THEORY

The discussion of frequency-shaping through optimum spatial compensation begins with a description of the test structure. For this work, an analytical model of a simply-supported plate is developed; the simplicity of a plate structure allows one to focus on the influence of the design process versus characteristics of the structural dynamics. The development of the open-loop design metric is then presented, and is based upon Hankel singular values (HSVs) as a measure of both performance and robustness. The design metric is presented in two-port or two-input, two-output (TITO) form, allowing for application to any general control system architecture. Genetic algorithms are developed as the method to determine the optimum transducer placements and sizes, where the optimum solution maximizes the open-loop design metric. Finally, the \mathcal{H}_2 control design process is used to design the temporal compensator, i.e., controller, for the adaptive structure, and a summary of this technique is given.

Plate Model

The simply-supported plate test structure is modeled using the assumed-modes method [1]. In this approach, the plate transverse displacement is represented by a finite series of in vacuo eigenfunctions of the form

$$z(x, y, t) = \sum_{n=1}^{N_m} \Psi_n(x, y) q_n(t) \quad (1)$$

where N_m is the number of modes included in the model and $q_n(t)$ are the plate generalized coordinates. For a simply-supported plate, the assumed modes are

*Author to whom correspondence should be addressed.

$$\Psi_n(x, y) = \frac{2}{\sqrt{m_s'' L_x L_y}} \sin\left(\frac{n_x \pi x}{L_x}\right) \sin\left(\frac{n_y \pi y}{L_y}\right) \quad (2)$$

where m_s'' is the mass per unit area of the plate, the terms L_x and L_y are the plate width and height, respectively, and (n_x, n_y) is the indice pair for mode n .

Substituting Equations (1) and (2) into the partial differential equation describing a plate leads to a set of ordinary differential equations of the form:

$$M_n[\ddot{q}_n(t) + \omega_n^2 q_n(t)] = Q_n^d(t) + Q_n^a(t) \quad (3)$$

where $n = 1, 2, \dots, N_m$, M_n is the modal mass, ω_n is the natural frequency, $Q_n^d(t)$ is the generalized force associated with the disturbance(s) and $Q_n^a(t)$ is the generalized force associated with the control actuator(s).

To bound the plate response on resonance, a proportional damping term can be included in the model by adding the term $2\zeta_n \omega_n \dot{q}_n(t)$ to the left-hand side of Equation (3). For this work, the localized mass, stiffness and damping of the distributed piezoelectric control transducers are assumed negligible during the open-loop design process, but are included, using the approaches presented by Hagood et al. [5], for performance, robustness, and efficiency analysis.

A diagram of the simply-supported plate structure is shown in Figure 1. Two rectangular, distributed transducers are applied to the plate: an actuator is applied at placement (x_a, y_a) and a sensor is applied at placement (x_s, y_s) . A SISO pair is investigated in this work since the optimum design should reflect the minimum number of inputs and outputs required to meet the objectives of the adaptive structure control problem. The transducer placements and sizes shown in Figure 1 are arbitrary; the optimum transducer placements and sizes are to be selected by maximizing the open-loop design metric.

Figure 1 does not detail a specific disturbance source. For

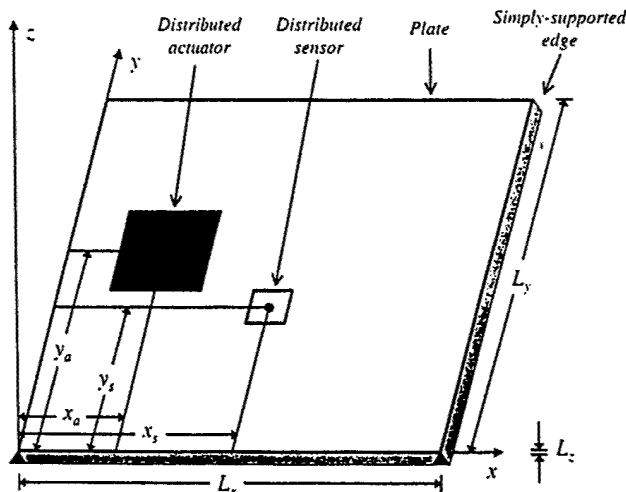


Figure 1. Diagram of simply-supported plate (arbitrary transducer placements and sizes).

adaptive structure design problems, it is advantageous to assume that the structure is excited by a generalized disturbance if the location of the disturbance is unknown a-priori. This disturbance source is presented by Smith and Clark [6] and assumes that each structural mode is excited by an independent, uncorrelated signal with unity power spectrum, i.e., $S_{mm}(\omega) = 1$. This form of structural excitation omits the spatial filtering effects that would occur if a specific disturbance type and path were assumed. Thus, the optimal design results are applicable to a wide variety of disturbance scenarios since each of the structural modes are excited uniformly. Obviously, if the disturbance type and path is known a-priori, this information should be used for design instead.

Design Metric

The design metric for frequency-shaping with spatial compensators is developed from the work presented by Smith and Clark [2], Clark and Cox [3], Lim [4], and Lim and Gawronski [7]. These methods determine control transducer placements and sizes using Hankel singular values of the open-loop controllability and observability Gramians.

The first step in developing any compensator design metric is to cast the control problem into proper form. Figure 2 shows a block diagram of the two-port or two-input, two-output (TITO) closed-loop system. The system $T(s)$ is composed of the generalized plant, $P(s)$, with controller, $K(s)$. The transfer matrix $P(s)$ in Figure 2 represents the dynamics of the adaptive structure and transducer coupling, and is written in equation form as

$$\begin{bmatrix} z(s) \\ y(s) \end{bmatrix} = \begin{bmatrix} P_{zw}(s) & P_{zu}(s) \\ P_{yw}(s) & P_{yu}(s) \end{bmatrix} \begin{bmatrix} w(s) \\ u(s) \end{bmatrix} \quad (4)$$

As shown by Figure 2 and Equation (4), $P(s)$ is partitioned according to the input-output variables, and four sub-matrices are identified. The upper-left transfer matrix, P_{zw} , represents the path from the input disturbance signals to the measured performance. The lower-right transfer matrix, P_{yu} , is the path from the input actuator signal to the response of the sensor, and is determined by the selection of trans-

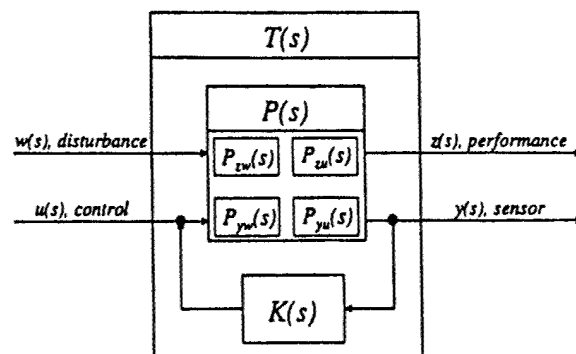


Figure 2. Block diagram of generalized plant with feedback controller.

ducer type, placement, size, and/or shape. The cross transfer matrices P_{zu} and P_{yw} show that the design of the control transducers also affects system performance and that the disturbance signals affect the measured outputs, respectively.

Each transfer matrix is formed from the states of the system and the respective input-output characteristics. When optimized, the design of the spatial compensators alters the coupling characteristics of the system for increased performance and robustness.

The Hankel singular values (HSVs) from the input actuator signal to the sensor output are written as

$$\Gamma_{yu}^2 = \text{diag}(\gamma_{yu1}^2, \dots, \gamma_{yum}^2, \dots, \gamma_{yuN_m}^2) \quad (5)$$

The HSVs defined by Equation (5) provide a measure of the degree of coupling between each of the N_m modes associated with the transducer path of the control problem. Physically, HSVs measure the amount of energy that can be stored into the system by the actuators and the amount of energy that can be retrieved in the output of the sensors [8]. These two parts form the measure of the complete coupling between the actuators and sensors.

A spatial compensator design metric based entirely upon evaluating Equation (5) was presented by Lim and Gawronski [7]. In this case, the HSVs defined by Equation (5) were computed from a predetermined set of candidate transducer locations and the optimum location is that which provided the greatest HSV measurement. The conclusion being that selecting transducer locations with the largest degree of coupling increases control system efficiency and, thus, performance.

Lim [4] recognized that the purpose of the control problem defined in Figure 2 is to reduce/control the measure of performance, $z(s)$, and that Equation (5) could be weighted by a measure of the system performance to provide for spatial compensator designs that are efficient at coupling the modes with the greatest effect on the measured performance.

Again using HSVs, a measure of the degree of coupling of each mode associated with the performance-disturbance path, P_{zw} , is

$$\Gamma_{zw}^2 = \text{diag}(\gamma_{zw1}^2, \dots, \gamma_{zwm}^2, \dots, \gamma_{zwN_m}^2) \quad (6)$$

and the design metric defined by Lim [4] is written as

$$J_{qp} \equiv \sum_{i=1}^{N_m} \frac{\gamma_{yp^{uq}i}^4}{\bar{\gamma}_{yui}^4} \gamma_{zwi}^4 \quad (7)$$

where J_{qp} is the metric for the p -th candidate sensor and q -th candidate actuator. The value $\bar{\gamma}_{yui}^4$ is the squared HSVs of the system where all possible actuators and sensors are considered; it is used to normalize the HSV calculations. As shown in Reference [4], Equation (7) is a computationally efficient means of determining transducer designs that increase system performance.

Based upon Equation (7), Clark and Cox [3] developed a design metric which also provided for system robustness. This metric emphasizes coupling to modes within the bandwidth of control, but de-emphasizes coupling to modes outside the performance bandwidth.

Clark and Cox [3] distinguished between the number of in-bandwidth modes, n_{in} , and the number of out-of-bandwidth modes, $n_{out} = N_m - n_{in}$, by forming the design metric as

$$\hat{J}_{qp} \equiv \bar{J}_{qp}^{in} + \bar{J}_{qp}^{out} \quad (8)$$

The cost for the in-bandwidth modes, \bar{J}_{qp}^{in} is defined as Equation (7) over the first n_{in} modes and normalized with respect to its maximum entry. The cost for the out-of-bandwidth modes is defined to emphasize poor coupling and is written as

$$J_{qp}^{out} = \left(\sum_{i=n_{in}+1}^{N_m} \frac{\gamma_{yp^{uq}i}^4}{\bar{\gamma}_{yui}^4} \gamma_{zwi}^4 \right)^{-1} \quad (9)$$

where \bar{J}_{qp}^{out} is defined as Equation (9) divided by its maximum entry over the entire candidate set.

As shown by Clark and Cox [3], design with Equation (8) resulted in an adaptive structure that efficiently coupled to modes at low frequencies and rolled-off naturally at high frequencies. This method provided a type of "loop-shaping" by spatial design and increased the robustness of the adaptive structure by balancing in-bandwidth performance and out-of-bandwidth stability.

Smith and Clark [2] continued the advancement of spatial compensator design for robustness by extending the design metric presented in Reference [3]. Beyond considering roll-off, the metric developed in Reference [2] selected modes for control and de-emphasized modes not considered important, both in-bandwidth and out-of-bandwidth. As such, model order can be reduced which, as discussed below, leads to lower order controllers.

The coupling measure for this metric is written over all modes as

$$J_{qp}^c = \sum_{i=1}^{N_m} \Lambda_i \left(\frac{\gamma_{yp^{uq}i}^4}{\bar{\gamma}_{yui}^4} \gamma_{zwi}^4 \right) \quad (10)$$

where Λ is a binary vector of length N_m . Modes to be controlled have an element value of 1 in Λ . The de-coupling metric over all modes is then written as

$$J_{qp}^m = \left(\sum_{i=1}^{N_m} (\sim \Lambda)_i \frac{\gamma_{yp^{uq}i}^4}{\bar{\gamma}_{yui}^4} \gamma_{zwi}^4 \right)^{-1} \quad (11)$$

where the \sim operator is the one's complement or binary NOT.

Based upon the given adaptive structure design problem, the control system designer predetermines modes which are considered important or unimportant for control. The design metric developed by Smuth and Clark [2] for mode selection is written as

$$\tilde{J}_{qp} \equiv \overline{(J_{qp}^c J_{qp}^m)} \quad (12)$$

Again, the overbar indicates that the metric is normalized by its maximum value.

Equation (12) multiplies the coupling and de-coupling measures, whereas the measures in Equation (8) are summed. As shown by Smith and Clark [9], a design metric based upon summation of normalized measures may not provide a balance between the goals of controlling selected structural modes and not controlling others. This is because the summed metric may be dominated by one of the two normalized terms, a result of widely varying coupling gain levels from varying transducer sizes. For example, in the common case of controlling low order structural modes and not controlling higher order modes, the optimum spatial compensator design from a summed metric may be one of two extremes: a large transducer with good coupling to all modes for performance or a small transducer with poor coupling to all modes for de-coupling. This phenomena is demonstrated and discussed in Reference [9]. The previous work by Clark and Cox [3] considered a fixed transducer size and, thus, the optimum results were not affected by variation in coupling gain level.

The goal of the adaptive structure design problem is to maximize the open-loop design metric through the proper design of the control transducers. The simplest method to achieve this result is to select a number of candidate transducer designs and evaluate the metric for every combination.

This "candidate set" approach is feasible as an optimization strategy because of the computational efficiency of evaluating the Hankel singular values. The candidate set method is utilized in all of the development work on the open-loop design metric [2-4,7] and is, to a degree, requisite to this approach. Specifically, each design metric includes the normalizing term $\bar{\gamma}_{mi}^4$, which is the square of the i -th HSV of the system when all possible actuators and sensors are considered. As discussed by Lim [4], the normalizing term is included to make all modes equally important.

The candidate set must be of sufficient richness to ensure that the HSVs are normalized properly, and to achieve the desired optimum results. Computational and memory constraints limit the formation of a single, large candidate set which includes every conceivable transducer design. However, there are a number of approaches to forming a candidate set of sufficient richness.

The candidate set method is well suited for applications where the designer has experience and insight into the dynamics of the structure. Using this knowledge, the designer forms a candidate set which represents the known solution

space. Clark and Cox [3] demonstrated this approach, where transducers of large size were only considered based upon prior experience in controlling the structure [10].

Two other common approaches to forming the candidate set involve incrementing or stepping the transducer characteristics and arbitrarily varying the transducer characteristics. For example, transducer placements and sizes can be stepped across the structural surface in a fixed, discrete manner. This method is an effective technique to ensure that transducers within a given design range are considered. Arbitrarily selecting transducer characteristics is similar to the random search techniques for solving nonlinear programming problems. If a sufficiently large number of transducers is considered, the design metric should be optimized.

The candidate set method is limited by the need to create a transducer set that is both computationally reasonable and has sufficient richness. This motivates the development of the genetic algorithms method, which approximates the transducer characteristics as continuous variables and has been shown as efficient at solving complex optimization problems [11].

Genetic Algorithms

Genetic algorithms have found wide application in the area of aerospace and structural design [12]. They have also been previously utilized to optimize transducer placements for active control applications [13-15]. Genetic algorithms are a stochastic search method based upon the heuristic application of the principles of evolution and heredity: they maintain a population of potential solutions, have a search process related to the fitness of individuals, and use genetics based update operators. A canonical discussion of genetic algorithms is well covered by Michalewicz [11]. Modifications to the traditional algorithm, required to handle needed constraints on transducer placements and sizes, are presented here.

When optimizing both placements and sizes, transducers must be placed within the structural boundary and transducers with reasonable sizes are desired. The technique developed to handle these constraints is based upon application of special repair algorithms to "correct" infeasible individuals. In the genetic algorithms vernacular, such corrections are referred to as forced mutations [11]. They are applied immediately after the binary genetic code has been decoded to a real number, and before the design metric of the new solution is evaluated.

Four design variables are required to characterize the placement and size of a single distributed transducer. In this work, the minimum and maximum x - and y -locations (x_{min} , x_{max} , y_{min} , y_{max}) of the transducer form these design variables, and the first forced mutation step is to ensure that the decoded design variables are in the proper min-max order. The next step is to ensure that the x - and y -dimensions of the patch are within a given minimum and maximum range. Undersized patch dimensions are expanded to L_{min}^p and oversized

patch dimensions are contracted to L_{max}^p . This work assumes that both contraction and expansion operations preserve transducer center placement. The final step in the forced mutation process is to ensure that the transducer is placed within the structural boundaries.

As discussed by Michalewicz [11], forced mutations may lead to computationally intensive runs and a lack of fitness convergence. The genetic algorithms method, including the forced mutations, is explored in this work to maximize the design metric.

\mathcal{H}_2 Control

The \mathcal{H}_2 controller design process involves the minimization of the \mathcal{H}_2 norm of closed-loop transfer matrix, $T_{zw}(s)$, by the specification of a proper $K(s)$. \mathcal{H}_2 controller designs are dynamic, i.e., can vary as a function of frequency. This offers increased closed-loop performance and design flexibility over static (constant-gain) controller designs [6]. Further, \mathcal{H}_2 controller designs have a reduced sensitivity to signal uncertainty when compared to other dynamic control techniques [16], e.g., LQG control.

The \mathcal{H}_2 controller design problem is solved using the state-space solutions presented by Doyle et al. [17]. This process involves solving two Riccati equations by Schur decomposition and realizes a full dynamic controller, $K(s)$. The solution is stable, proper and, hence, realizable. Dimension of the controller $K(s)$ is equal to that of the observed and controlled plant model, $P(s)$. Therefore, reducing the order of the adaptive structure model, through optimum spatial compensation, leads directly to lower controller order.

PHYSICAL SYSTEM

The geometry of the physical plate structure is shown in Figure 1. The plate dimensions and material properties are given in Table 1. The thickness and properties of the distributed piezoelectric transducers are given in Table 2. Throughout this work, the values given in the tables are assumed fixed.

The mass and stiffness effects of the distributed piezoelectric transducers are minimized by specifying a patch thick-

Table 2. Properties of distributed piezoelectric transducers.

Property	Value
Material	G-1195 PZT
Thickness, L_z^p	0.0002 m
Density, ρ_p	7650 kg/m ³
Young's modulus in E_{11} , E_p	4.9×10^{10} N/m ²
Poisson's ratio, ν_p	0.30
Strain coefficient, d_{31}	-166×10^{-12} m/V

ness that is significantly less than the plate thickness. Again, these effects are only included in the model used to design the controller and analyze the results.

The analytical plate model is calculated over the first sixty plate modes ($N_m = 60$), and are thus accurate to approximately 3000 Hz. However, the design bandwidth for the results is selected as 10–2000 Hz.

For comparison with the results from the genetic algorithms method, the optimum result from a given set of candidate transducers is obtained. To form the complete candidate set, the x - and y -dimensions of distributed transducers are varied from 0.0508 m (2 inches) to 0.1524 m (6 inches), in steps of 0.0254 m (1 inch). The center placement of each candidate transducer is then varied across the plate, from edge-to-edge, in steps of $0.1 L_x$ and $0.1 L_y$. This produces 3,027 potential transducers, of which $N_c = 1,523$ lie completely within the plate boundaries and are kept in the candidate set. The variable N_c is the number of transducers in a given candidate set. In this development, all transducers are assumed rectangular and aligned with the coordinates of the plate.

Both the sensor and actuator are given the same candidate set. Thus, there are over 2.3×10^6 possible transducer combinations (N_c^2) that are being considered as solutions to the design problem. Due to plate symmetry and reciprocity, there is redundancy in the transducer combinations. Considering both redundancy and actuator-sensor reciprocity reduces the actual number of transducer combinations considered to $[N_c \times (N_c + 1)]/4$. Thus, for the candidate set given above there are 580,263 individual transducer combinations considered.

To further demonstrate the benefit of the optimum spatial compensator design techniques developed, a pair of 0.0508 m (2 inch) square transducers, colocated, with center placement at (0.2742, 0.0894) m, is selected as a nominal design case. This transducer design was utilized in previous studies on control of simply-supported plate structures [10].

RESULTS AND DISCUSSION

The adaptive structure control problem investigated in this work is to reduce, with a single sensor and actuator transducer pair, the vibration response of the (1,1), (1,3), (3,1) and (3,3) modes of a simplysupported plate. These four modes contribute to the plate's most efficient acoustic radiators [1].

Table 1. Properties of plate structure.

Property	Value
Material	Aluminum
Width, L_x	0.4572 m
Height, L_y	0.4064 m
Thickness, L_z	0.0048 m
Density, ρ_s	2700 kg/m ³
Young's modulus, E_s	7.1×10^{10} N/m ²
Poisson's ratio, ν_s	0.33
Damping ratio, ζ_s	0.02

Table 3. Plate modes, index, natural frequencies, and selection vector.

Mode Number, n	Index (n_x, n_y)	w_n (Hz)	Λ_n
1	(1,1)	127	1
2	(2,1)	296	0
3	(1,2)	340	0
4	(2,2)	509	0
5	(3,1)	576	1
6	(1,3)	695	1
7	(3,2)	789	0
8	(2,3)	864	0
9	(4,1)	969	0
10	(3,3)	1144	1

To add robustness with respect to unmodeled dynamics and limit controller order, it is also desirable to minimize coupling to all the other plate modes. This is a relatively challenging design goal, and the optimum transducer sizes and placements are not immediately obvious.

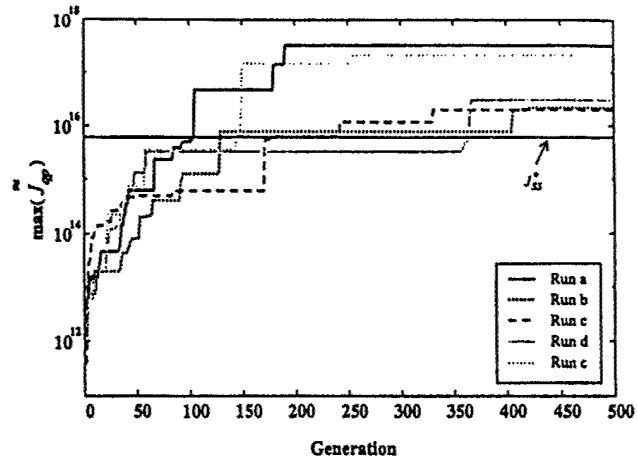
The first ten natural frequencies of the plate are given in Table 3. The selection vector for this control problem is shown as the last column. The four modes which are selected as important for control have a Λ value of 1. Other modes have a Λ value of 0, which denotes that they are not important for control and the optimum design should, ideally, not couple to them. To ensure high frequency roll-off, all modes above the (3,3) have a selection value of 0, i.e., $\Lambda_{11 \dots N_m} = 0$.

The parameters for the genetic algorithm runs are given in Table 4. Since the genetic algorithm method is stochastic, five runs are performed. At completion, each run will have considered 15,000 transducer combinations. Finally, the design variables for each run are initialized with an arbitrary vector of zeros and ones.

The optimum design results determined by the N_{run} runs of the genetic algorithm method are given below, and labeled J_{GG}^* . These results are compared to the nominal design and the optimum results from the candidate set method, which are labeled J_{SS}^* . The coupling between actuator input and sensor output for each of the three design cases is then discussed. The loop-gain of each system is given, and discussed in terms of both the control objectives and system robustness. Frequency shaping through optimum spatial compensator design is demonstrated. To ensure that comparison of

Table 4. Parameters for genetic algorithm method determining placements and sizes.

Parameter	Value
Number of runs, N_{run}	5
Number of bits, N_{bits}	16
Population size, N_{pop}	30
Max. number of generations, N_{gen}	500
Mutation probability, p_m	0.0333
Crossover probability, p_c	1
Min. patch size, L_{min}^p	0.0508 m
Max. patch size, L_{max}^p	0.1524 m

**Figure 3. Design metric convergence for each run of genetic algorithms method determining placements and sizes.**

the results is appropriate, the broadband control energy level for each design case is normalized by adjusting the control effort weighting during \mathcal{H}_2 controller synthesis [16]. Finally, the closed-loop performance is presented and discussed.

Optimum Designs

The design metric convergence for each of the N_{run} runs of the genetic algorithms method is given in Figure 3. Each run reached the maximum number of generations and shows convergence. The forced mutations are not impeding fitness convergence for the given design problem. Test runs were conducted for 2000 generations, with no greater design metric values achieved. The maximum design metric for each run is given in Table 5. The line labeled J_{SS}^* in Figure 3 is the maximum design metric value determined by the candidate set method, which is detailed below. In all cases, the genetic algorithms method achieved a greater design metric value than the candidate set method.

The transducer placements and sizes for each genetic algorithms run are shown in Figure 4. The best results for each run are different from each other, with only run (b) and run (e) showing a slight similarity in placement. These results demonstrate that there are multiple extreme in the design space, and further motivates the use of genetic algorithms as an optimization routine. Due to maximum design metric value, run (a) is selected as the optimum design. J_{GG}^* .

Table 5. Maximum design metric for each run of genetic algorithms method determining placements and sizes.

Run	$\max(\bar{J}_{ap})$
a, J_{GG}^*	3.2659×10^{17}
b	2.1641×10^{16}
c	1.9787×10^{16}
d	2.9720×10^{16}
e	2.1087×10^{17}

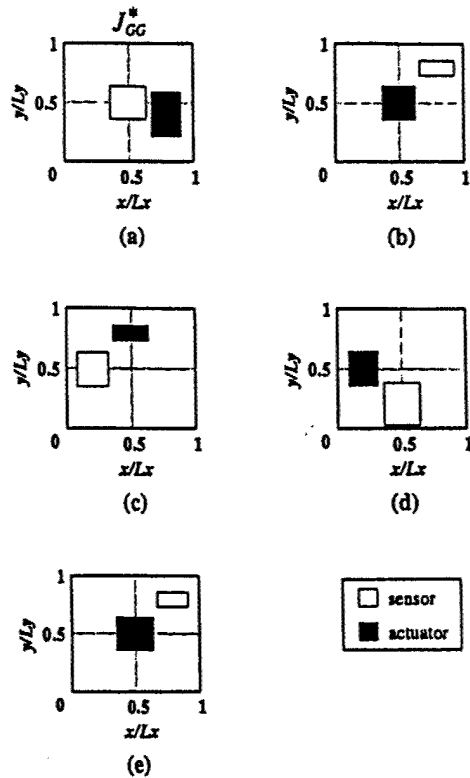


Figure 4. Transducers for the best design of each run of genetic algorithms method determining placements and sizes.

The transducer placements and sizes for the nominal and J_{SS}^* designs are given in Figure 5 and Table 6. (For completeness, the transducer placements and sizes for the J_{GG}^* design are also given in Table 6.) The optimum designs, as selected by both the candidate set and genetic algorithms optimization methods, have relatively large apertures. It has been previously demonstrated by Viperman and Clark [10] that large spatial apertures serve as spatial wavenumber filters and provide greater control over the low-bandwidth modes. These modes have been targeted for control in this work by

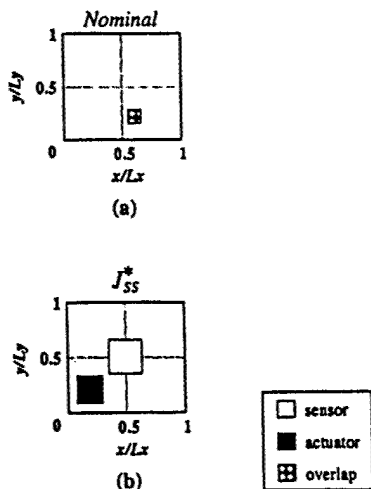


Figure 5. Sensor and actuator size and placement for nominal and J_{SS}^* design cases (normalized dimensions).

Table 6. Transducer placements and sizes, in meters, for the nominal, J_{SS}^* and J_{GG}^* designs.

Transducer	Center	Width	Height
Nominal			
actuator	(0.2743, 0.0894)	0.0508	0.0508
sensor	(0.2743, 0.0894)	0.0508	0.0508
J_{SS}^*			
actuator	(0.0914, 0.0813)	0.1016	0.1016
sensor	(0.2286, 0.2032)	0.1270	0.1270
J_{GG}^*			
actuator	(0.3656, 0.1630)	0.1026	0.1521
sensor	(0.2287, 0.2037)	0.1299	0.1130

the selection vector. Thus, the large spatial apertures are expected. Also, both the candidate set method and genetic algorithm method determine similar optimum sensor placement and size. However, the actuator placement and size are different.

The design metrics for the nominal and J_{SS}^* designs are given in Table 7. The candidate set method increases the design metric value more than five orders-of-magnitude from the nominal design. Comparison to run (a) in Table 5, shows that the genetic algorithms method further increases the design metric value by two orders-of-magnitude.

Comparison of Actuator-to-Sensor Coupling

Figure 6 shows the magnitude of the frequency response of the actuator-to-sensor transfer function, T_{ys} , for each design case. The input signal to each actuator is the prescribed voltage and the sensor output is the piezoelectric charge, which is proportional to plate strain.

The actuator-to-sensor transfer function for the nominal design is immediately recognizable. Due to its colocated positioning and small aperture, the curve is an alternating set of zeros and poles, and relatively constant in magnitude with frequency [1]. Constant gain with frequency greatly limits the low-frequency performance and high-frequency stability of adaptive structures designed with small transducers. The optimum designs show a T_{ys} curve with relatively large modal peaks on the four selected modes. There is considerably less relative coupling to the non-selected modes than with the nominal design.

The optimum spatial compensator design metric adds ro-

Table 7. Design metric value for the nominal and J_{SS}^* design cases.

Design	$\max(\bar{J}_{qp})$
Nominal	3.0368×10^{10}
J_{SS}^*	6.1606×10^{15}

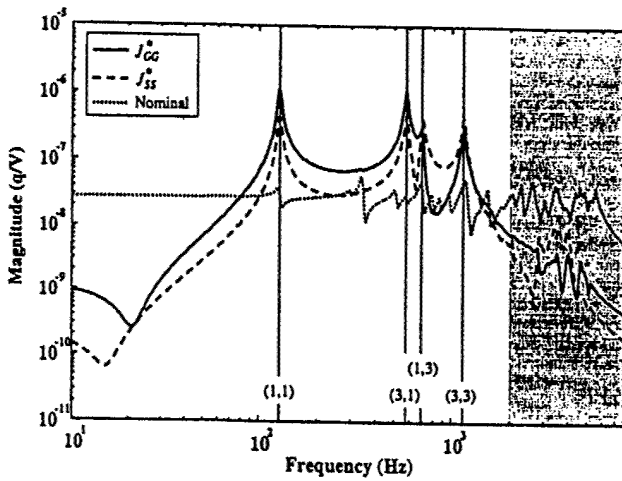


Figure 6. Actuator-to-sensor transfer function for each design case.

busness to the adaptive structure by choosing transducer placements and sizes that frequency-shape the P_{yu} transfer function. In Figure 6, the J_{SS}^* and J_{GG}^* designs show both high-frequency roll-off and de-coupling to modes not considered important for control, i.e., excluded from the selection vector, Λ .

Figure 6 shows that the J_{GG}^* design achieves the greatest coupling to the (1,1) and (3,1) modes. Both optimum designs provide similar high-frequency roll-off. However, the J_{SS}^* design provides greater coupling to the (1,3) and (3,3) modes. The increase in design metric for the J_{GG}^* design is achieved by increasing coupling to the lowest two modes and de-coupling between the (1,3) and (3,3) modes.

The choice of transducer placements and sizes influences the actuator-to-sensor coupling of the adaptive structure. Through the cross transfer matrices, P_{zu} and P_{yu} , spatial compensator design also affects the controller design and, thus, system loop gain and performance. Results and analysis of this influence are presented next.

Comparison of Loop Gain

One method to analyze the robustness of an adaptive structure design is through the loop gain [1]. Loop gain is defined as the open-loop transfer matrix PK , where the input is the control input and the output is that of the compensator. It is desirable to have high loop gain at low frequencies, where the disturbance signal dominates the sensor response and the

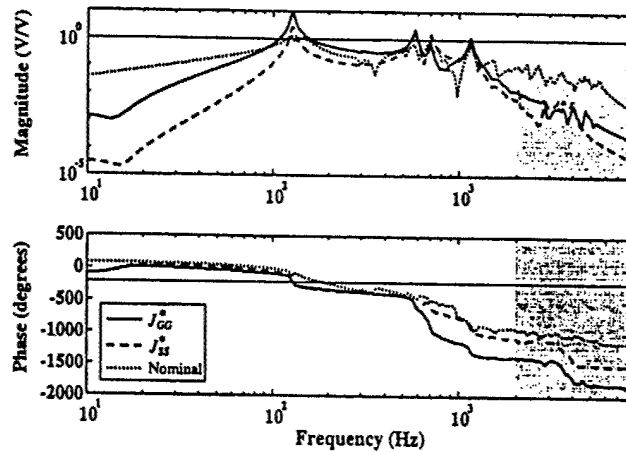


Figure 7. Loop gain for each design case.

plant is well modeled. However, at high frequencies the noise signals dominate the sensor response and the plant has unmodeled dynamics. Therefore, the loop gain should be small at high-frequency to avoid stability issues. The exact transition point depends on the design problem. For this example, the point is set at 2000 Hz.

Both the loop gain and performance curves involve the design of a proper H_2 controller. The sensor noise gain and control effort weighting for the nominal, J_{SS}^* , and J_{GG}^* designs are given in Table 8. To ensure proper comparison of the results, the control signal energy was normalized. Specifically, the value of R_c is adjusted such that all the control signal energy of all designs is within ± 0.005 V/N of 149.198 V/N. The gain values given in the bottom row of Table 8 are utilized to compare compensator efficiency, and are discussed below.

The loop gain results for the J_{GG}^* design are compared to the J_{SS}^* and nominal designs in Figure 7. The design obtained by the genetic algorithm method shows a greater peak at the (1,1) mode than the J_{SS}^* design, with similar high frequency roll-off. The J_{GG}^* design has a smaller loop gain at the (1,3) mode, as expected from the coupling curves in Figure 6. The loop gain results demonstrate that the genetic al-

Table 8. Sensor noise gain, control effort weighting, and resulting control signal energy for nominal, J_{SS}^* , and J_{GG}^* designs.

Design	V_s	R_c	$\ T_{uw}\ _2$ (V/N)
Nominal	2.3×10^{-3}	4.0×10^{-4}	149.198
J_{SS}^*	7.5×10^{-3}	4.301×10^{-4}	149.193
J_{GG}^*	6.2×10^{-3}	3.839×10^{-5}	149.198
J_{GG}^*	6.2×10^{-3}	1.01×10^{-3}	69.156

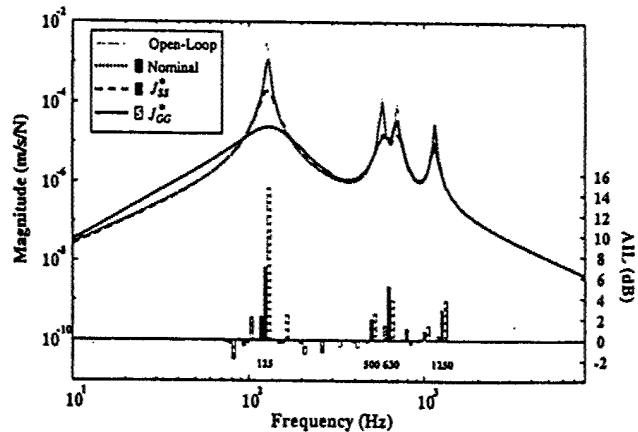


Figure 8. Vibration control performance and active insertion loss for each design case.

Table 9. AIL, in selected 1/3-Octave bands, for nominal, J_{SS}^* , and J_{GG}^* designs with equal control signal energy.

Design	AIL (dB)			
	1/3-Octave			
	125 Hz	500 Hz	630 Hz	1250 Hz
Nominal	2.1	0.3	1.4	0.4
J_{SS}^*	6.9	1.9	5.1	2.9
J_{GG}^*	14.6	2.5	3.8	3.8

gorithm method is capable of shaping transfer functions by optimizing transducer placements and sizes. These results also allude to greater mode 1 performance than obtained from the nominal and candidate set designs.

Comparison of Performance

The vibration control performance for each design case is given in Figure 8. The top, solid line is the open-loop response of the system; here the control transducers are attached (with nominal size and placement), but not activated. The three lower curves show the vibration performance where each closed-loop system design has been activated. The vibration performance curves are the square-root of the sum of the square of the singular values of T_{zw} over the frequency range of interest. The units of performance are structural velocity per unit of input force.

The active insertion loss (AIL) in 1/3-Octave bands of each design is also given in Figure 8. Active insertion loss is defined as the reduction of performance by the activation of the control system [18]. It is characterized as $AIL \equiv 20 \log_{10} (\|P_{zw}\|_2 / \|T_{zw}\|_2)$. The term $\|T_{zw}\|_2$ is the \mathcal{H}_2 norm of the closed-loop disturbance-to-performance transfer matrix over 1/3-Octave frequency bands and $\|P_{zw}\|_2$ is the \mathcal{H}_2 norm of the open-loop performance transfer matrix [T_{zw} where $K(s) = 0$] over the same bands. The units of AIL are decibels and positive values correspond to a reduction in plate response. The AIL ordinate is shown on the right of the

Table 10. AIL, in selected 1/3-Octave bands, for J_{GG}^* design with similar mode 1 performance as J_{SS}^* .

Design	AIL (dB)			
	1/3-Octave			
	125 Hz	500 Hz	630 Hz	1250 Hz
J_{SS}^*	6.9	1.9	5.1	2.9
J_{GG}^*	6.9	0.8	3.0	2.9

figure and the 1/3-Octave band center frequencies of selected bands are shown directly below the bands.

The performance results given in Figure 8 demonstrate that the nominal design is ineffective at controlling the plate response of the (3,1) and (3,3) modes. The J_{SS}^* and J_{GG}^* designs are controlling these modes and are also much more effective at controlling the (1,1) and (1,3) modes, as expected from the larger loop gain peaks of Figure 7. AIL results for the 1/3-Octave bands that include a selected mode are detailed in Table 9. These results show that the optimum designs provide much greater control of the plate vibration. Control of all selected modes is more than tripled between the nominal and J_{SS}^* spatial compensator designs, while both controllers are using the same amount of signal energy. Compared to the other designs, the J_{GG}^* design shows greater control of the plate's first mode and similar control of the other three selected modes. Control of the 1/3-Octave band at 125 Hz has more than doubled to 14.6 dB between the genetic algorithm and candidate set methods. The J_{GG}^* design also shows greater control of the 1/3-Octave bands at 500 and 1250 Hz, but slightly less control at 630 Hz. By determining the placements and sizes of the control transducers with the genetic algorithm optimization method, the performance of the adaptive structure has been greatly increased.

An interesting case to consider is normalizing performance and comparing control signal energy requirements for different transducer designs. The bottom row of Table 8 gives the control effort weighting and resulting control signal energy for the J_{GG}^* design with equal mode 1 performance as the J_{SS}^* design. Figure 9 shows the performance and AIL for these designs. The AIL in selected 1/3-Octave bands is given in Table 10. For similar performance levels, the voltage requirement is halved by utilizing the J_{GG}^* design.

CONCLUSIONS

For practical realizations, adaptive structures should be designed to include performance, robustness and efficiency metrics for control. A method of frequency-shaping the spatial compensation of an adaptive structure has been developed for both maximum performance, system robustness and efficiency. Robustness is defined as reduced coupling to all modes not considered important for control. This design process unites the computationally efficient design metric de-

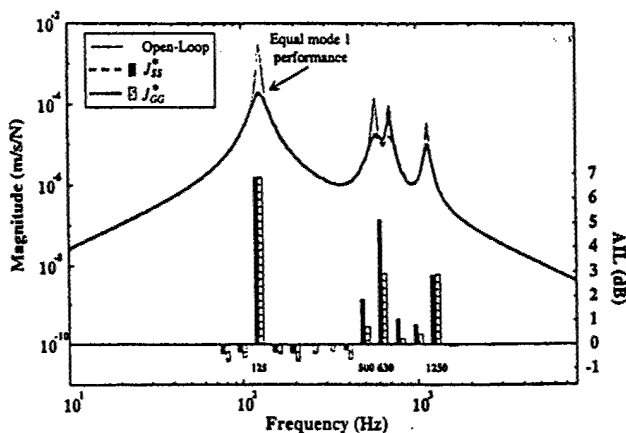


Figure 9. Vibration control performance (equal mode 1 performance) and active insertion loss for J_{SS}^* and J_{GG}^* designs.

veloped by Smith and Clark [2] with the genetic algorithms optimization method.

The genetic algorithms method determines transducer placements and sizes that maximize the \tilde{J}_{qp} design metric, and has distinct advantages over the previously considered candidate set method. Genetic algorithms approximate the design variables as continuous functions, allowing precise placement and sizing of transducers for maximum design metric value.

Comparison of the optimum designs for the genetic algorithms and candidate set methods shows similar loop shaping abilities with the two methods, but greater performance and efficiency with designs from the genetic algorithms method. The genetic algorithms method is effective at determining optimum transducer placements and sizes for adaptive structure design problems. These results further demonstrate the basic ability to frequency-shape the adaptive structure through optimum spatial compensator design.

REFERENCES

1. Clark, R. L., G. P. Gibbs, and W. R. Saunders, *Adaptive Structures, Dynamics and Control*, John Wiley and Sons, 1998.
2. Smith, G. C. and R. L. Clark, "A crude method of loop-shaping adaptive structures through optimum spatial compensator design," submitted for publication in *Journal of Sound and Vibration*, 1999.
3. Clark, R. L. and D. E. Cox, "Band-limited actuator and sensor selection for disturbance rejection," accepted for publication in *AIAA Journal of Guidance, Control and Dynamics*, 22(5):740-743, 1999.
4. Lim, K. B., "Disturbance rejection approach to actuator and sensor placement," *AIAA Journal of Guidance, Control and Dynamics*, 20(1):202-204, 1997.
5. Hagood, N. W., W. H. Chung, and A. von Flotow, "Modelling of piezoelectric actuator dynamics for active structural control," AIAA Paper 90-1087-CP, 1990.
6. Smith, G. C. and R. L. Clark, "Tradeoffs in design complexity—Temporal versus spatial compensation," *Journal of Sound and Vibration*, 228(5):1182-1194, 1999.
7. Lim, K. B. and W. Gawronski, "Hank singular values of flexible structures in discrete time," *AIAA Journal of Guidance, Control and Dynamics*, 19(6):1370-1377, 1996.
8. Boyd, S. and C. Baratt, *Linear Controller Design: Limits of Performance*, Prentice-Hall, Inc., 1991.
9. Smith, G. C. and R. L. Clark, "Adaptive structure design through optimum spatial compensation," *Proceedings of Active 99: The 1999 International Symposium on Active Control of Sound and Vibration*, Fort Lauderdale, FL, December 1999.
10. Viperman, J. S. and R. L. Clark, "Implications of using colocated strain-based transducers for active structural acoustic control," *Journal of Acoustical Society of America*, 106(3):1392-1399, 1999.
11. Michalewicz, Z. *Genetic Algorithms + Data Structures = Evolution Programs*, Springer-Verlag, 1992.
12. Ahmed, Q., K. Krishnakumar and J. Neidhoefer, "Applications of Evolutionary Algorithms to Aerospace Problems—A Survey," *Computational Methods in Applied Sciences '96*, 236-242, John Wiley & Sons, 1996.
13. Onoda, J. and Y. Hanawa, "Actuator Placement Optimization by Genetic and Simulated Annealing Algorithms," *AIAA Journal*, 31(6):1167-1169, 1992.
14. Kim, S. J. and K. Y. Song, "Active Control of Sound Fields from Plates in Flow by Piezoelectric Sensor/Actuator," *AIAA Journal*, 37(10):1180-1186, 1999.
15. Gaudenzi, P., E. Fantini, V. K. Koumoussis, and C. J. Gantes, "Genetic Optimizations for the Active Control of a Beam by Means of PZT Actuators," *Journal of Intelligent Material Systems and Structures*, 9:291-300, 1998.
16. Skogestad, S. and I. Postlewaite, *Multivariable Feedback Control: Analysis and Design*, John Wiley & Sons, 1996.
17. Doyle, W. C., K. Glover, P. P. Khargonekar, and B. A. Francis, "State-space solutions to standard H_2 and H_∞ control problems," *IEEE Transactions on Automatic Control* AC-34(8): 831-847, 1989.
18. Smith, G. C. and R. L. Clark, "Active insertion loss (AIL)," submitted to *Noise Control Engineering Journal*, 1999.

Experimental demonstration of a band-limited actuator/sensor selection strategy for structural acoustic control

Robert L. Clark

Department of Mechanical Engineering and Materials Science, Duke University, Durham, North Carolina 27708-0300

David E. Cox

NASA Langley Research Center, Hampton, Virginia 23681

(Received 25 November 1998; accepted for publication 14 September 1999)

A band-limited method of selecting actuators and sensors for structural acoustic control is reviewed, and experimental results are presented to demonstrate the approach. The selection methodology is based upon the decomposition of the Hankel singular values of a system model in terms of individual sensor and actuator configurations for lightly damped structures. The technique selects sensor and actuator combinations which couple well to structural modes that radiate efficiently. However, it rejects sensor and actuator combinations which couple well to modes that are inefficient acoustic radiators or are outside of the desired bandwidth of control. Selecting transducer combinations which filter modes outside of the desired bandwidth serves to minimize the potential for spillover and instability associated with unmodeled or poorly modeled dynamics. The approach is computationally efficient since it is based upon open-loop dynamics and does not require iterative nonlinear optimization. © 1999 Acoustical Society of America. [S0001-4966(99)06812-5]

PACS numbers: 43.40.Vn [PJR]

INTRODUCTION

Various approaches for optimizing the location of actuators and sensors for structural acoustic control have been proposed in the past (Snyder and Hansen, 1990; Wang *et al.*, 1991; Clark and Fuller, 1991, 1992a; Heck and Naghshineh, 1994; Ruckman and Fuller, 1995). The ultimate goal of such studies has been aimed at a reduction in the complexity associated with the compensator in favor of wave number filtering through the distributed actuator and/or sensor (Fuller and Burdisso, 1991; Clark and Fuller, 1992b; Clark *et al.*, 1993; Snyder *et al.*, 1993; Gu *et al.*, 1994; Fuller *et al.*, 1996; Johnson and Elliott, 1995; Maillard and Fuller, 1998; Charette *et al.*, 1998). However, for many of these studies, the emphasis was placed upon adaptive feedforward control. For such control, the focus can be limited to spatial apertures which couple well to the performance path over the bandwidth of interest. Additionally, spillover into modes outside of the bandwidth of interest is of little concern since control effort is extended only over the bandwidth of the reference signal. However, for feedback control, a necessity for structural acoustic systems driven by exogenous inputs such as turbulent boundary layer noise, spillover is a primary concern (Thomas and Nelson, 1995; Clark and Frampton, 1997, 1998; Frampton and Clark, 1997).

Lim (1997) recently proposed a methodology for selecting actuator and sensor placement for disturbance rejection based upon the Hankel singular values of lightly damped structures. Compared to previous methodologies which emphasized the use of iterative, nonlinear optimization techniques (Wang *et al.*, 1991; Clark and Fuller, 1992a; Ruckman and Fuller, 1995; Smith and Clark, 1998; Smith *et al.*, 1998), the approach outlined by Lim (1997) is computationally efficient. For lightly damped structures, the Hankel sin-

gular values can be estimated from the modal properties of the discrete time system models. Thus, the participation of each structural mode in the control path (actuator to sensor) can be weighted by the participation of this mode on the disturbance to performance path. While this method is efficient and computationally direct (i.e., no iteration), it does lack a robustness metric.

For experimental implementation of feedback control, we often seek to design a controller for a reduced-order model of the system. Due to practical constraints imposed by finite bandwidths of digital signal processors, an accurate model of the structure is obtained over a limited bandwidth, and the compensator is designed to 'roll-off' at frequencies outside of the bandwidth of interest. However, this roll-off and the application of low-pass filters to attenuate the coupling of higher-order modes complicates the design, leading to stability issues which limit closed-loop performance. In a recent study by Clark and Cox (1998), a methodology for band-limited actuator/sensor selection for disturbance rejection was proposed, extending the work of Lim (1997).

In this method, actuator/sensor pairs are selected based upon a combined metric which provides a tradeoff between the coupling to structural modes related to performance within the bandwidth of interest, and the *lack of coupling* to structural modes outside of the identified bandwidth of interest. An analytical example for structural acoustic control was provided by Clark and Cox (1998), and the complementary experimental demonstration is the subject of this work.

A brief review of the actuator/sensor selection methodology is provided in the subsequent section. Upon outlining the selection methodology, the experimental system is described including the optimal piezoceramic actuator and sensor for structural acoustic control of a panel radiating into a half-space. H_2 design methodologies were applied (Clark

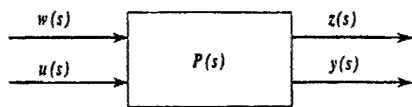


FIG. 1. Block diagram of generalized plant.

et al., 1998), and the experimental results are compared to the predicted results. The experimental results demonstrate that the band-limited transducer selection methodology for disturbance rejection provides the structural acoustic control system engineer with a powerful and simple technique for selecting transducers from analytical or experimental models of systems.

I. BAND-LIMITED TRANSDUCER SELECTION FOR DISTURBANCE REJECTION

In structural acoustic control we seek to reduce sound radiation from a structure (Fuller, 1988). Under such constraints, previous research has demonstrated that only some of the structural modes are efficient acoustic radiators within the low-frequency bandwidth targeted for such application (Wallace, 1972a, b; Lomas and Hayek, 1977). As such we typically modify models of structures to incorporate radiation filters which provide, as a performance output, a measure of sound power radiated (Baumann *et al.*, 1991; Cunnefare, 1991; Gibbs *et al.*, 1998). Such filters, when augmented to a structural model, yield what is frequently termed a generalized plant in control terminology, $P(s)$. A block diagram of the generalized plant is presented in Fig. 1. As illustrated, the plant is subjected to disturbance inputs, $w(s)$, and control inputs, $u(s)$. The outputs of the generalized plant are the performance variables, $z(s)$, and the sensed or measured variables, $y(s)$. The corresponding input-output equations can be expressed as follows (Clark *et al.*, 1998):

$$\begin{bmatrix} z(s) \\ y(s) \end{bmatrix} = \begin{bmatrix} P_{zw}(s) & P_{zu}(s) \\ P_{yw}(s) & P_{yu}(s) \end{bmatrix} \begin{bmatrix} w(s) \\ u(s) \end{bmatrix}. \quad (1)$$

The performance path is defined by the transfer matrix existing between the exogenous input disturbances and the performance outputs, $P_{zw}(s)$. The control path is defined by the transfer matrix existing between the control inputs and the measured or sensed outputs, $P_{yu}(s)$. In structural acoustic control, the performance path is defined between the disturbances which serve to excite the structure and the radiation filters used to estimate the sound power radiated.

Lim (1997) proposed a method of determining the optimal subset of actuators and sensors for control based upon a weighted measure of the modal participation of each sensor/actuator combination. To determine the transducer pairs best suited for control, the Hankel singular values of the system through the performance path and the control path were determined. Lim and Gawronski (1996) noted that the Hankel singular values of a discrete time model of a lightly damped structure can be efficiently computed from a diagonalized form of the state space model of the system, denoted by the quadruple (A, B, C, D) . As noted by Lim and Gawronski (1996), a similarity transform can be constructed such that the transformed system matrix is block diagonal:

$$\tilde{A} = \begin{pmatrix} \tilde{A}_1 & 0 & \dots & 0 \\ 0 & \tilde{A}_2 & & \\ \vdots & & \ddots & \\ 0 & \dots & & \tilde{A}_n \end{pmatrix}, \quad (2)$$

where

$$\tilde{A}_i = \begin{bmatrix} \text{Re}(z_i) & -\text{Im}(z_i) \\ \text{Im}(z_i) & \text{Re}(z_i) \end{bmatrix} \quad (3)$$

and

$$z_i = \exp(\delta_i + j\psi_i)T \quad (4)$$

is the i th discrete eigenvalue of A with corresponding eigenvector, v_i . (Note that $\delta_i \pm j\psi_i$ are the eigenvalues of the corresponding continuous time system.) The similarity transform is defined by the transformation matrix,

$$V = [r_1, \dots, r_n], \quad (5)$$

where $r_i = [\text{Re}(v_i) - \text{Im}(v_i)]$. The resulting transformation produces states whose eigenvectors approximately correspond to principal directions. The corresponding transformations of the B , C , and D matrices are defined as follows:

$$\tilde{B} = V^{-1}B, \quad (6)$$

$$\tilde{C} = CV, \quad (7)$$

$$\tilde{D} = D. \quad (8)$$

Owing to the diagonal dominance of the discrete controllability and observability grammian for lightly damped structures, the square of the i th Hankel singular value (HSV) can be approximated as follows (Lim and Gawronski, 1996):

$$\gamma_i^4 \approx \frac{\text{tr}[\tilde{B}\tilde{B}^T]_{ii} \text{tr}[\tilde{C}^T\tilde{C}]_{ii}}{(4\delta_i T)^2}. \quad (9)$$

Note that $\delta_i \leftrightarrow \zeta_i \omega_i$, where ζ_i is the damping ratio of the i th mode and ω_i is the natural frequency of the i th mode. Thus, the i th HSV is directly related to the time scale, $1/(\zeta_i \omega_i)$, of the i th, lightly damped, structural mode. As detailed by Lim and Gawronski (1996), the approximation is accurate up to frequencies near 90% of the Nyquist frequency.

Defining the HSVs through the disturbance path as

$$\Gamma_{zw}^2 = \text{diag}(\gamma_{zw_1}^2, \dots, \gamma_{zw_n}^2), \quad (10)$$

and the HSVs through the control path as

$$\Gamma_{yu}^2 = \text{diag}(\gamma_{yu_1}^2, \dots, \gamma_{yu_n}^2), \quad (11)$$

one obtains a measure of the level of participation of each structural mode or state in the performance path, $P_{zw}(s)$, and control path, $P_{yu}(s)$, respectively. One can compute the HSVs defined in Eq. (11) for every possible input-output path (i.e., every possible combination of an array of transducers targeted for control). Additionally, one can compute the HSVs for the general vector of inputs and outputs (i.e., using all possible actuators and sensors) as a baseline:

$$\Gamma_{yu}^2 = (\bar{\gamma}_{yu_1}^2, \dots, \bar{\gamma}_{yu_n}^2). \quad (12)$$

From Eqs. (10)–(12), Lim (1997) defined the following performance metric for sensor/actuator selection:

$$J_{qp} = \sum_{i=1}^n \frac{\gamma_{y_{q^u p_i}}^4}{\bar{\gamma}_{y_{u_i}}^4} \gamma_{z_{w_i}}^4, \quad (13)$$

where J_{qp} is the performance metric associated with the q th sensor and p th actuator, and n is the number of complex conjugate pole pairs (i.e., modes) of the system. The performance metric defined by Eq. (13) thus provides a measure of the relative modal participation of each sensor/actuator combination over the relative modal participation of all possible sensor/actuator combinations weighted by the modal participation through the performance path. Obviously, if a mode (state) does not exist in the performance path, it is weighted by zero. The metric outlined by Lim (1997) thus offers a convenient and computationally efficient means of determining a subset of actuators and sensors which couple well to modes present in the performance path.

However, for feedback control applications, practical constraints impose limitations on bandwidth, and as such there are always modes outside of the bandwidth of interest which present problems with respect to the trade-off between stability and performance. We often seek to limit the participation of out-of-bandwidth modes by implementing low-pass filters or by forcing the compensator to “roll-off” at some predetermined frequency through loop-shaping techniques. However, such practices can serve to complicate the compensator design. Additionally, we often seek to design compensators based upon reduced-order models of the system, reducing the order of the resulting compensator for practical implementation. All of these practical design issues serve to introduce sensitivity to structural modes present outside of the bandwidth identified for control. Ideally, we would seek a set of sensor/actuator pairs which naturally filter the contribution of out-of-bandwidth modes while at the same time couple well to those modes which dominate the disturbance path.

As was demonstrated by Clark and Cox (1998), a performance metric can be developed which emphasizes band-limited coupling to structural modes important in the disturbance path and de-emphasizes coupling to structural modes outside of the identified bandwidth. To develop this metric, Clark and Cox (1998) distinguished between the number of in-bandwidth modes, n_{in} , and the number of out-of-bandwidth modes, $n_{out} = n - n_{in}$, used in their performance metric. For the in-bandwidth modes, the selection metric is identical to that presented by Lim (1997):

$$J_{qp}^{in} = \sum_{i=1}^{n_{in}} \left(\frac{\gamma_{y_{q^u p_i}}^4}{\bar{\gamma}_{y_{u_i}}^4} \right) \gamma_{z_{w_i}}^4. \quad (14)$$

However, to enhance stability, we prefer to limit the coupling through the control path, P_{yu} , to the out-of-bandwidth modes. As such, a metric is defined by weighting the normalized HSVs for the control path with themselves and taking the reciprocal of the result to emphasize poor coupling:

$$J_{qp}^{out} = \left(\sum_{i=n_{in}+1}^n \left(\frac{\gamma_{y_{q^u p_i}}^4}{\bar{\gamma}_{y_{u_i}}^4} \right) \gamma_{y_{q^u p_i}}^4 \right)^{-1}. \quad (15)$$

If each metric of Eqs. (14) and (15) are normalized with respect to their maximum entry, and the normalized metrics are defined by \bar{J}_{qp}^{in} and \bar{J}_{qp}^{out} , respectively, the sum of the two normalized metrics results in a selection methodology which provides a trade-off between in-bandwidth performance and out-of-bandwidth stability:

$$\hat{J}_{qp} = \bar{J}_{qp}^{in} + \bar{J}_{qp}^{out}. \quad (16)$$

Selection is based upon those sensor/actuator pairs that couple well to modes present in the disturbance path over the desired bandwidth of control and those that couple poorly to modes present in the control path outside of the desired bandwidth of control.

II. REVIEW OF STRUCTURAL ACOUSTIC MODEL

The emphasis of the work presented herein is placed upon the experimental demonstration of the band-limited sensor/actuator selection methodology for disturbance rejection. A test structure was machined from steel, measuring $18 \times 16 \times 0.1875$ in.³ thick. The boundaries were constructed to approximate that of a simply supported plate, and piezoceramic transducers measuring $6 \times 4 \times 0.0075$ in.³ thick were available for experimental implementation. These relatively large piezoceramic patches were not sized for control authority, rather they were selected based upon the results of a prior study which demonstrated that large aperture transducers serve as spatial wave number filters and provide greater control over the low-bandwidth modes required for structural acoustic control (Vipperman and Clark, 1999).

In a previous study by Clark and Cox (1998), the performance metrics defined in Eqs. (13) and (16) were used to select a single sensor/actuator pair devoted to controlling the sound power radiated from the panel, assuming that it radiates into a half-space. The objective was to determine the optimal transducer pair from a predetermined array of possible transducers for control of sound power radiated below approximately 1 kHz. To accomplish this task, radiation modal expansion (Gibbs *et al.*, 1998) was used to generate filters modeling the rms sound power radiated. For the bandwidth identified, only the first radiation mode was used. The first radiation mode captures the radiation of volumetric modes at low frequency. Essentially, sound radiation from the (1,1), (1,3), (3,1), and (3,3) modes is targeted.

For the chosen test structure, an analytic model was developed in an earlier study (Clark and Cox, 1998) using an assumed modes approach with simply supported boundary conditions and proportional damping. This model was suitable for the actuator/sensor optimization process, however, it neglected filter dynamics and nonideal boundary conditions present in the experimental setup. Therefore, for control design and evaluation an experimentally identified model was used, as described in the next section.

In the analytic model there are ten structural modes within the bandwidth of interest. A total of seven target locations were identified resulting in 49 possible sensor/

TABLE I. Center-points of piezoceramic transducers in nondimensional plate coordinates.

Transducer	x coordinate	y coordinate
1	0.3	0.3
2	0.4	0.4
3	0.5	0.5
4	0.3	0.5
5	0.4	0.5
6	0.5	0.3
7	0.4	0.3

actuator combinations including colocated options. Due to the use of piezoelectrics patches as both the sensor and actuator transducer many of these combinations are redundant. For example, using sensor-2 and actuator-3 is equivalent to using sensor-3 and actuator-2. This reciprocity is apparent in the results. The target center-point locations for each transducer in nondimensional plate coordinates are presented in Table I. Additionally, the center-points are indicated by asterisks on the schematic diagram of the plate illustrated in Fig. 2. Also shown in Fig. 2 are the resulting optimal locations for a single sensor/actuator pair based upon the selection metric defined by Clark and Cox (1998) of Eq. (16).

Upon applying the metric developed by Lim (1997), Eq. (13), the optimal sensor/actuator combination selected was a colocated transducer centered on the plate (sensor 3/actuator 3). Due to the efficient coupling of modes with odd indices, this location was anticipated for low-frequency (<1 kHz) structural acoustic control. However, the sensor/actuator pair (sensor 3/actuator 2) resulting from the metric defined by Clark and Cox (1998), Eq. (16), was nonintuitive. It was assumed *a priori* that a single patch centered on the plate would couple well to efficient radiators at low frequency and adequately filter modes at higher frequency due to the dimension of the transducer and its relative symmetry in location. To reconcile the two transducer pair options, the frequency response of each was plotted. As illustrated in Fig. 4, it is obvious why sensor 3/actuator 2 resulted as the optimal transducer pair based upon the metric of Eq. (16): the response to out-of-bandwidth modes (>1 kHz) is significantly less through this sensor/actuator pair than it is through the colocated transducer pair centered on the plate. However,

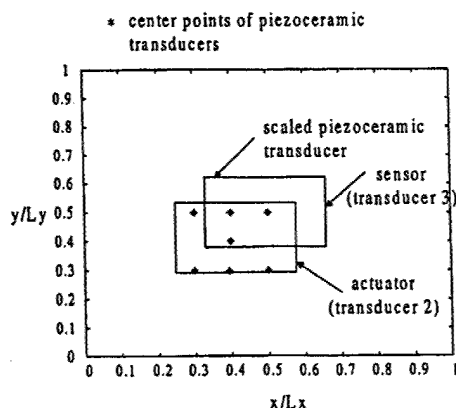


FIG. 2. Schematic diagram of test panel showing center-points of transducer options and optimal sensor/actuator location.

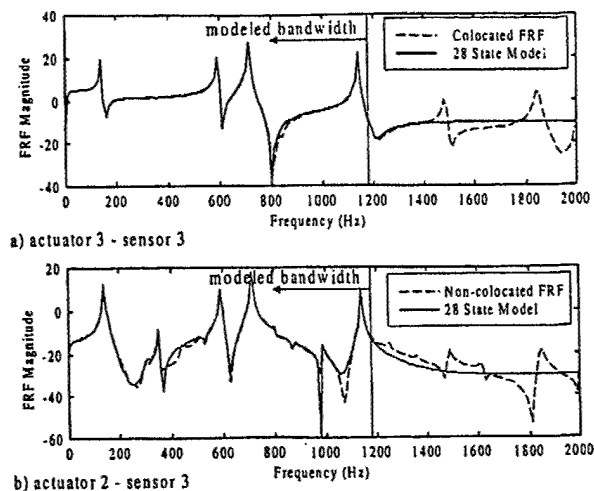


FIG. 3. Comparison of measured frequency response function and that predicted with model obtained through experimental system identification for both transducer pair options.

there is very little difference in the in-bandwidth (<1 kHz) response.

To test the sensor/actuator selections, two transducers were bonded to the test plate as illustrated in the schematic diagram of Fig. 2. Transducers were bonded to opposite sides of the plate due to the required overlap in the optimal locations from the metric of Eq. (16). The transducer centered on the structure was operated as an adaptive sensori-actuator (Vipperman and Clark, 1999) to achieve the colocated transducer pair selected by the metric of Eq. (13). An adaptive sensoriactuator is defined as a transducer used simultaneously for sensing and actuation and capable of continuously rejecting the electrical contribution of the output associated with the feedthrough from the applied electrical input. Specific details of implementation for piezoceramic transducers are outlined in the prior work of Vipperman and Clark (1999).

III. SYSTEM IDENTIFICATION AND CONTROL SYSTEM DESIGN

Prior to designing the control system, the experimental test structure was identified using the time-domain eigenvalue realization algorithm (ERA) (Juang and Pappa, 1985). Each transducer illustrated in Fig. 2 was operated as a sensoriactuator, and the multi-input, multi-output (2I2O) system was identified. A plot of the frequency responses, both measured and from the identified model, of the piezoceramic transducer centered on the plate (transducer 3 of Fig. 2) and operated as a sensoriactuator are presented in Fig. 3(a). As illustrated, the dynamic response of the system is accurately captured with a 28-state model over the bandwidth presented. In Fig. 3(b), the frequency responses of the measured and identified model of the structure using transducer 3 as a sensor and transducer 2 as an actuator are presented. Again, the measured frequency response and that resulting from the identified model correlate well below approximately 1200 Hz.

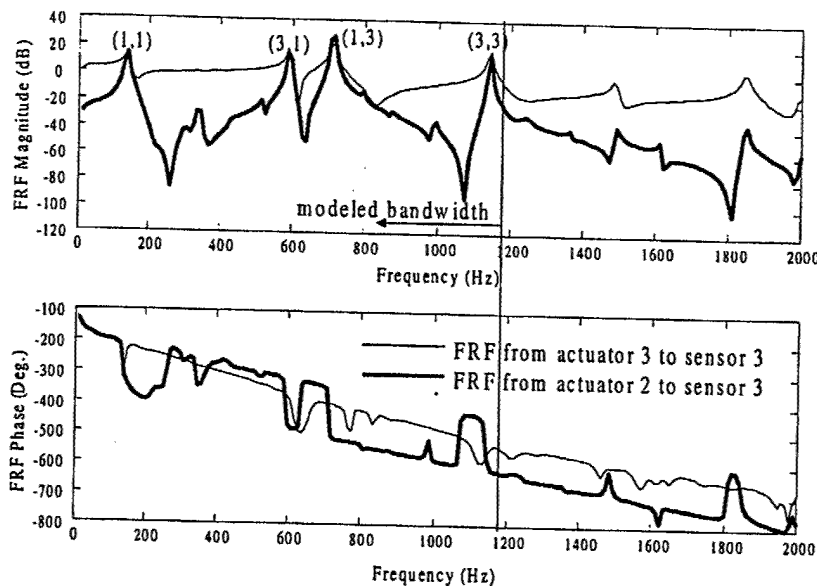


FIG. 4. Comparison of measured frequency response functions for each transducer pair, emphasizing roll-off resulting from spatial filtering through sensor 3-actuator 2..

The bode plots of the two transducer pair options are presented in Fig. 4. As illustrated, both the colocated transducer pair (sensor 3-actuator 3) and the non-colocated transducer pair (sensor 3-actuator 2) couple well to structural modes below 1 kHz. However, above 1 kHz, the non-colocated transducer pair (sensor 3-actuator 2) provides "roll-off" due to spatial filtering, which serves to reduce the effects of structural modes on the closed-loop response outside of the identified bandwidth for control. If a low-pass filter was introduced to achieve this same reduction in magnitude, an additional phase-lag would result. However, due to the spatial filtering provided by the distributed, non-colocated transducers, the reduction in magnitude is achieved at frequencies greater than 1200 Hz with no additional phase-lag. This crude "spatial loop-shaping" provides the control system designer with an added benefit since the in-bandwidth compensator can be designed for more aggressive control without increasing the loop-gain outside of the desired bandwidth for control.

For the experimental results presented, a two-pole Ithaco high-pass filter with a corner frequency of 10 Hz and a four-pole Ithaco low-pass filter with a corner frequency of 2 kHz were used to filter the sensor signals. The data was collected with a TMS320C40 digital signal processor using a 16-input-8-output analog to digital (A/D) and digital to analog (D/A) board. The same boards were used in the implementation of the compensator, at a sample rate of 5 kHz. A four-pole smoothing filter was implemented on the outputs of the D/A at a frequency of 2 kHz. Krohn-Hite model 7600 power amplifiers were used to drive the piezoceramic transducers. A custom designed circuit implemented the adaptive sensor/actuator to operate the center transducer simultaneously as a sensor and an actuator (Vipperman and Clark, 1999).

To develop a model of the radiation filters, the radiation modal expansion (RME) technique was applied (Gibbs *et al.*, 1998), and the plate was subdivided into 20 rectangular elements of equal surface area. The response between each actuator and the acceleration measured at the center-point of

each elemental area was obtained and included as part of the identified model. Through RME, a weighted sum of the velocity measured at each coordinate is developed for each radiation filter used. Thus, if four radiation filters are used, then the 20 velocity measurements can be reduced to four signals whose weighted sum is dependent upon the "shape" (applied through the weighted sum) of the radiation mode. This greatly simplifies the time required for system identification and provides a measure of the radiated sound power over the bandwidth of interest.

A loudspeaker was used to generate the disturbance, and it was placed on center with the plate at a 45-degree angle of incidence and 18 in. from the plate. The input was band-limited noise up to 2 kHz. A comparison of the sound power radiated to that predicted using a single radiation filter is presented in Fig. 5. Recording the frequency response between the disturbance and all 20 accelerometer positions and storing the data provides a mechanism for estimating the radiated power. The power computed from the discretized approximation of the Rayleigh integral is computed and la-

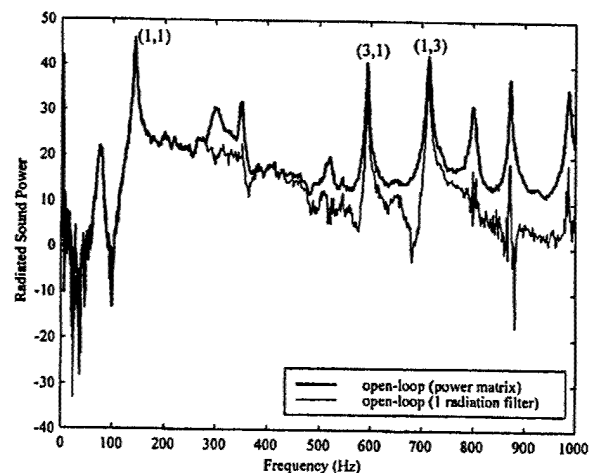


FIG. 5. Comparison of predicted sound power radiated using the power matrix and the first radiation mode.

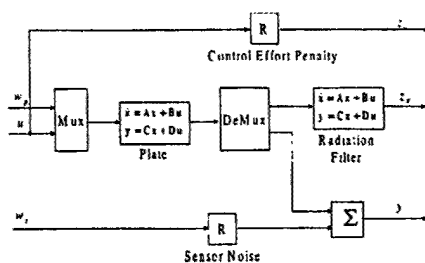


FIG. 6. Block diagram of control system design plant.

beled "power matrix" in Fig. 5. This measure serves as the reference (i.e., best that can be computed using all radiation filters). As illustrated, below 800 Hz, a performance measure based solely upon a single radiation filter is sufficient for designing compensators for dynamic control. While adding additional higher-order radiation filters leads to a better estimate of the radiated power at higher frequency, the single radiation filter, which requires only a single-state filter, sufficiently characterizes the desired performance of the volumetric radiators. Note also that peaks corresponding to resonances of the (1,2), (2,1), and (2,2) structural modes are notably absent from the measured estimate of sound power, owing to their poor radiation efficiency.

From these dynamic models, compensators were designed based upon H_2 -synthesis (Clark *et al.*, 1998). A block diagram of the model used for compensator design is presented in Fig. 6. As illustrated, radiation filters were applied to the output of the experimental model of the plate. A 28-state, reduced-order model of the plate was developed including a one-state model for the radiation filter. Performance variables were selected from z_u , a signal representing control effort penalty, and z_r , a signal representing the radiated power. Measured outputs, y , consisted of transducer 3 as a sensor for both control cases examined. However, control inputs, u , were selected from either transducer 3 for selection metric of Eq. (13) or transducer 2 for selection metric of Eq. (16). The process noise, w_p , was constructed by driving the modeled dynamics through transducer 3 and transducer 2 with independent, spectrally white inputs, and the sensor noise, w_s , was constructed with a spectrally white input applied to the sensors. A comparison of the measured output, y , for a given process noise and sensor noise are plotted for the identified model of the structure in Fig. 7. Since the same sensor was used in each control system design case, the process noise and sensor noise weightings were held at consistent levels in the design process.

IV. RESULTS

Applying H_2 -synthesis, a compensator was designed for each single-input, single-output (SISO) transducer pair selected by the two alternative performance metrics. The loop-gains for each are presented in Fig. 8. In calculating the loop-gain a full order evaluation model of the system was used, which contained the effects of structural modes outside of the desired bandwidth for control. As illustrated, the transducer pair (sensor 3-actuator 3) selected by the performance metric defined in Eq. (13) results in loop-gains near unity at a frequency of approximately 1838 Hz. Given that the dy-

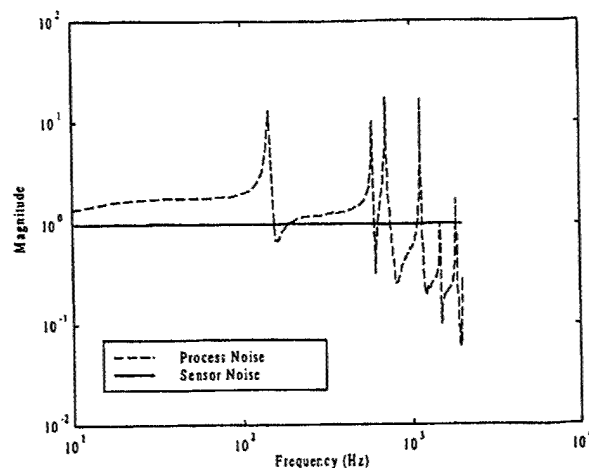


FIG. 7. Sensor output due to process and sensor noise inputs, as used for both control system designs.

namics of the system are ignored at this frequency in the design model, one would expect possible stability problems. However, for the transducer pair (sensor 3-actuator 2) selected by the performance metric defined in Eq. (16), the loop-gain is much less than unity at higher frequencies due to the inherent "roll-off" resulting from the spatial filtering. The in-bandwidth loop-gain (<1 kHz) is roughly the same at all of the resonance frequencies desired in the performance path as illustrated in Fig. 8.

The predicted performance based upon the full-order, experimentally identified dynamics of the system are presented in Fig. 9. The sound power radiated by the (1,1) mode (142 Hz), (3,1) mode (593 Hz), and (1,3) mode (712 Hz) are all attenuated significantly for both transducer pair options. However, at approximately 1838 Hz, an increase in acoustic response is predicted for the colocated transducer pair (sensor 3-actuator 3). In fact, the predicted closed-loop response was on the border of instability, consistent with expectation based upon the loop-gains of Fig. 8. The predicted instability for the experimental system was also consistent with that

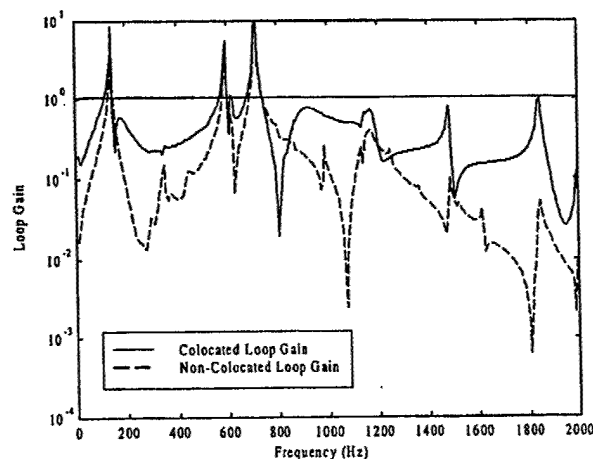


FIG. 8. Predicted loop-gain for alternative transducer pairs given the same design parameters (control effort penalty of 1.5×10^{-5} and sensor noise of 1).

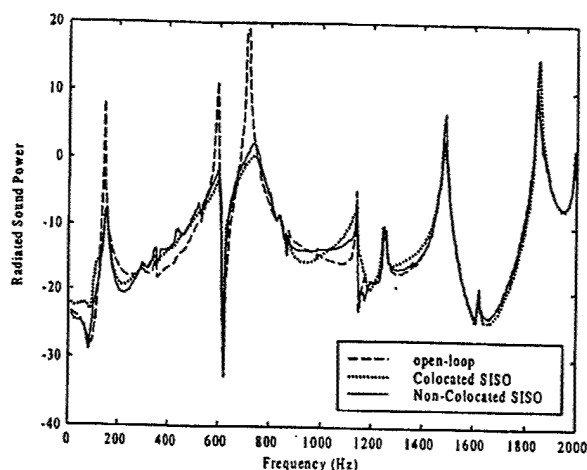


FIG. 9. Predicted closed-loop performance for SISO transducer pair alternatives given a disturbance introduced through the two piezoceramic transducers and a performance measure based upon the first radiation mode.

predicted for the analytical model considered previously by Clark and Cox (1998).

Upon implementing the two compensators on the experimental test-rig, the closed-loop response presented in Fig. 10 was obtained. The frequency responses between the disturbance applied through the loudspeaker and the acceleration measured at the 20 discrete points on the structure required to estimate the sound power radiated were obtained. Applying the full radiation matrix to these measured frequency response functions provides a means of estimating the total sound power radiated. Notice that the performance of the two SISO controllers is nearly identical below 1000 Hz as illustrated in Fig. 10. Also note that the only structural modes controlled are those present in the performance path associated with the first radiation mode. The acoustic power at structural resonances greater than 800 Hz are not modeled and are thus ignored in the dynamic compensator. Including more radiation modes would serve to enhance performance at higher frequencies.

However, upon considering the frequency responses above 1000 Hz (presented in Fig. 11), one observes that the

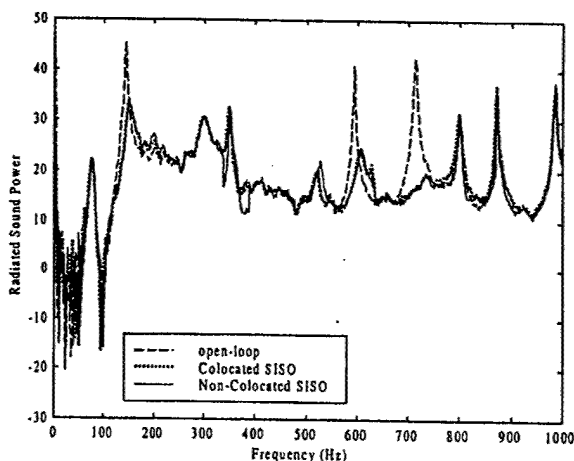


FIG. 10. Measured estimate of open- and closed-loop sound power radiated over the bandwidth targeted for control.

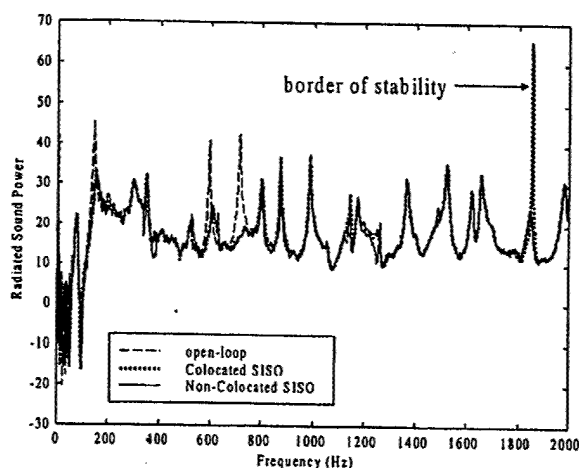


FIG. 11. Measured estimate of open- and closed-loop sound power radiated up to 2 kHz.

controller implemented with the colocated transducer pair (sensor 3–actuator 3) results in significant spillover at approximately 1838 Hz, as was predicted. In fact, the controller for this SISO transducer pair is on the border of instability for the given design parameters (a control effort penalty of $1.5e-5$ and a sensor noise of 1). Thus, through appropriate transducer selection, one can obtain the same level of performance within a prescribed bandwidth while minimizing the effects of spillover outside of the identified bandwidth, as demonstrated by the closed-loop response of the non-colocated transducer pair (sensor 3–actuator 2).

V. CONCLUSIONS

A band-limited method of selecting actuators and sensors for structural acoustic control is reviewed, and experimental results are presented to demonstrate the approach. By applying a selection metric which emphasizes in-bandwidth coupling to structural modes present in the performance path and de-emphasizes out-of-bandwidth coupling to structural modes in the control path, a crude method of “spatial loop-shaping” is developed. The results presented show that this technique can be used to define transducer locations which reduce the effect of spillover in feedback controllers. The technique serves to solidify methods applied in structural acoustic control and adaptive structures in a synergistic design philosophy which incorporates the selection of the transducers as part of the integrated control system design process.

ACKNOWLEDGMENTS

The authors would like to gratefully acknowledge the support of the Structural Acoustics Branch of the NASA Langley Research Center under Grant No. NCC-1-250, Dr. Richard Silcox, Contract Monitor, and the AFOSR PECASE under Grant No. F49620-98-1-0383, Major Brian Sanders, Contract Monitor.

Baumann, W. T., Saunders, W. R., and Robertshaw, H. H. (1991). “Active suppression of acoustic radiation from impulsively excited structures,” *J. Acoust. Soc. Am.* **90**, 3202–3208.

- Charette, F., Berry, A., and Guigou, C. (1998). "Active control of sound radiation from a plate using a polyvinylidene fluoride volume displacement sensor," *J. Acoust. Soc. Am.* **103**, 1493-1503.
- Clark, R. L., and Cox, D. E. (1998). "Band-Limited Actuator and Sensor Selection of Disturbance Rejection: Application to Structural Acoustic Control," submitted to *AIAA Journal of Guidance, Control, and Dynamics*.
- Clark, R. L., and Frampton, K. D. (1997). "Aeroelastic structural acoustic coupling: Implications on the control of turbulent boundary layer noise transmission," *J. Acoust. Soc. Am.* **102**, 1639-1647.
- Clark, R. L., and Frampton, K. D. (1999). "Aeroelastic structural acoustic control," *J. Acoust. Soc. Am.* **105**, 743-754.
- Clark, R. L., and Fuller, C. R. (1991). "Control of sound radiation with adaptive structures," *J. Intell. Mater. Syst. Struct.* **2**, 431-452.
- Clark, R. L., and Fuller, C. R. (1992a). "Optimal placement of piezoelectric actuators and polyvinylidene fluoride error sensors in active structural acoustic control approaches," *J. Acoust. Soc. Am.* **92**, 1521-1533.
- Clark, R. L., and Fuller, C. R. (1992b). "Modal sensing of efficient acoustic radiators with PVDF distributed sensors in active structural acoustic approaches," *J. Acoust. Soc. Am.* **91**, 3321-3329.
- Clark, R. L., Saunders, W. R., and Gibbs, G. P. (1998). *Adaptive Structures: Dynamics and Control* (Wiley, New York).
- Clark, R. L., Burdisso, R. A., and Fuller, C. R. (1993). "Design approaches for shaping polyvinylidene fluoride sensors in active structural acoustic control (ASAC)," *J. Intell. Mater. Syst. Struct.* **4**, 354-365.
- Cunneffare, K. A. (1991). "The minimum multimodal radiation efficiency of baffled finite beams," *J. Acoust. Soc. Am.* **90**, 2521-2529.
- Frampton, K. D., and Clark, R. L. (1997). "Control of sound transmission through a convected fluid loaded plate with piezoelectric sensor/actuators," *J. Intell. Mater. Syst. Struct.* **8**(8), 686-696.
- Fuller, C. R. (1998). "Analysis of Active Control of Sound Radiation from Elastic Plates by Force Inputs," in *Proceedings of Inter-Noise '88*, Avignon, Vol. 2, pp. 1061-1064.
- Fuller, C. R., and Burdisso, R. A. (1991). "A wave number domain approach to active control of structure-borne sound," *J. Sound Vib.* **148**, 355-360.
- Fuller, C. R., Elliott, S. J., and Nelson, P. A. (1996). *Active Control of Vibration* (Academic, London).
- Gibbs, G. P., Clark, R. L., Cox, D. E., and Vipperman, J. S. (1999). "Radiation modal expansion: Application to active structural acoustic control," *J. Acoust. Soc. Am.* (to be published).
- Gu, Y., Clark, R. L., Fuller, C. R., and Zander, A. C. (1994). "Experiments on active control of plate vibration using piezoelectric actuators and polyvinylidene fluoride PVDF modal sensors," *Trans. ASME, J. Vib. Acoust.* **116**, 303-308.
- Heck, L. P., and Naghshineh, K. (1994). "Large-Scale, Broadband Actuator Selection for Active Noise Control," in *Proceedings of Noise-Con 94*, pp. 291-296.
- Johnson, M. E., and Elliott, S. J. (1995). "Active control of sound radiation using volume velocity cancellation," *J. Acoust. Soc. Am.* **98**, 2174-2186.
- Juang, J.-N., and Pappa, R. S. (1985). "An eigensystem realization algorithm for modal parameter identification and model reduction," *J. Guid. Control. Dyn.* **8**(5), 620-627.
- Lim, K. B., and Gawronski, W. (1996). "Hankel singular values of flexible structures in discrete time," *J. Guid. Control. Dyn.* **19**(6), 1370-1377.
- Lim, K. B. (1997). "Disturbance rejection approach to actuator and sensor placement," *J. Guid. Control. Dyn.* **20**(1), 202-204.
- Lomas, N. S., and Hayek, S. I. (1977). "Vibration and acoustic radiation of elastically supported rectangular plates," *J. Sound Vib.* **52**(1), 1-25.
- Maillard, J. P., and Fuller, C. R. (1998). "Comparison of two structural sensing approaches for active structural acoustic control," *J. Acoust. Soc. Am.* **103**, 396-400.
- Ruckman, C. E., and Fuller, C. R. (1995). "Optimizing actuator locations in active noise control systems using subset selection," *J. Sound Vib.* **186**(3), 395-406.
- Smith, G. C., and Clark, R. L. (1999). "Optimal Transducer Placement for Output Feedback Control of Broadband Structural Acoustic Radiation," *Journal of Intelligent Material Systems and Structures* (to be published).
- Smith, G. C., Clark, R. L., and Frampton, K. D. (1998). "The Effect of Convected Fluid Loading on the Optimal Transducer Placement for Active Control of Sound Transmission Through an Aeroelastic Plate," *AIAA Paper 98-1981*.
- Snyder, S. D., and Hansen, C. H. (1990). "Using multiple regression to optimize active noise control system design," *J. Sound Vib.* **148**(3), 537-542.
- Snyder, S. D., Hansen, C. H., and Tanaka, N. (1993). "Shaped vibration sensors for feedforward control of structural radiation," in *Proceedings of the Second Conference on Recent Advances in Active Control of Sound and Vibration*, 28-30 April 1993, Blacksburg, VA.
- Thomas, D. R., and Nelson, P. A. (1995). "Feedback control of sound radiation from a plate excited by a turbulent boundary layer," *J. Acoust. Soc. Am.* **98**, 2651-2662.
- Vipperman, J. S., and Clark, R. L. (1999). "Implications of using colocated strain-based transducers for active structural acoustic control," *J. Acoust. Soc. Am.* **106**, 1392-1399.
- Wallace, C. E. (1972a). "Radiation resistance of a baffled beam," *J. Acoust. Soc. Am.* **51**, 936-945.
- Wallace, C. E. (1972b). "Radiation resistance of a rectangular panel," *J. Acoust. Soc. Am.* **51**, 946-952.
- Wang, B. T., Burdisso, R. A., and Fuller, C. R. (1991). "Optimal Placement of Piezoelectric Actuators for Active Control of Sound Radiation from Elastic Plates," in *Noise-Con*, pp. 267-274.

¹¹Yang, H., and Saif, M., "Robust Observation and Fault Diagnosis in a Class of Time-Delay Control Systems," *Proceedings of American Control Conference*, Vol. 5, Inst. of Electrical and Electronics Engineers, New York, 1997, pp. 478-482.

¹²Guan, Y., and Saif, M., "A Novel Approach to the Design of Unknown Input Observers," *IEEE Transactions on Automated Control*, Vol. 36, No. 5, 1991, pp. 632-635.

¹³Zoran, G., and Qureshi, M. T. J., *Lyapunov Matrix Equation in System Stability and Control*, Academic, San Diego, 1995, pp. 42-44.

¹⁴Douglas, R. K., and Speyer, J. L., "Robust Fault Detection Filter Design," *Journal of Guidance, Control, and Dynamics*, Vol. 19, No. 1, 1996, pp. 214-218.

¹⁵Chung, W. H., and Speyer, J. L., "A Game Theoretic Fault Detection Filter," *IEEE Transactions on Automated Control*, Vol. 43, No. 2, 1998, pp. 143-161.

Band-Limited Actuator and Sensor Selection for Disturbance Rejection

Robert L. Clark*

Duke University, Durham, North Carolina 27708-0300

and

David E. Cox†

NASA Langley Research Center,
Hampton, Virginia 23681-0001

Introduction

A METHOD of selecting actuator and sensor locations from a predetermined set of candidate locations based on the Hankel singular values of the controllability and observability Gramian of flexible structures was outlined previously.¹⁻⁴ Within the original formulation, the actuator/sensor selection methodology was based entirely on the Hankel singular values of the control path (P_{yu}) for some finite set of modes and some predetermined set of actuators and sensors.^{1,2} Later revisions to this method have included a weighting of the Hankel singular values of the control path (P_{yu}) by that of the Hankel singular values of the performance path (P_{zw}) (Refs. 3 and 4). In the most recent application, the disturbance rejection approach to actuator/sensor selection was applied to the piezoceramic aeroelastic response tailoring investigation wind-tunnel model at the NASA Langley Research Center.⁴ The results of that study demonstrated a significant advantage to the application of the disturbance rejection approach.

The methodology outlined herein serves as an extension to the disturbance rejection approach with an added metric aimed at robustness with respect to out-of-bandwidth response. Although the method proposed by Lim³ determines the actuators and sensors that couple best to modes present in the disturbance path, there is no penalty associated with coupling to higher-order modes that are out of the desired bandwidth for control. All practical realizations of control systems are implemented over some finite bandwidth, and for digital realizations, bandwidth limitations are typically imposed by the computational speed of the digital signal processor and the number of modes within the desired bandwidth. Accurate models of the dynamics within the desired bandwidth for control are required; however, model fidelity typically suffers beyond the

identified bandwidth. This is particularly true for distributed parameter systems that have infinite dimensional theoretical models. As a result, compensators that incorporate a roll-off are desired and low-pass filters are frequently used in practice to attenuate the response at higher frequency. The response of out-of-bandwidth modes can lead to spillover and stability issues, particularly in the presence of "aggressive" controllers. However, the best method of attenuating the response out of the desired bandwidth is to have poor observability and/or controllability of such modes as an intrinsic property of the open-loop plant. The proposed approach thus serves to simplify robust controller design in the mitigation of spillover.

To this end, an additional metric is introduced for the selection of actuators and sensors for disturbance rejection. Within the bandwidth of desired performance, a metric consistent with that outlined by Lim³ is computed to determine the actuators and sensors that couple best for disturbance rejection. However, out of the desired bandwidth, a metric is introduced that penalizes the coupling of actuators and sensors to out-of-bandwidth modes. A combination of the two metrics leads to a tradeoff between performance and robustness to spillover effects in the actuator/sensor selection methodology.

The methodology proposed is outlined in the subsequent section. Following the introduction of the new metric, an analytical example based on a structural acoustic control problem is presented. Conclusions are drawn from the results.

Band-Limited Placement Metric for Disturbance Rejection

The problem of interest is the control of a standard two-port system, as shown in Fig. 1. The upper transfer function $P_{zw}(s)$ represents the path from disturbances $w(s)$ to a measure of the closed-loop system performance $z(s)$. This path is determined by the definition of the active control problem, with tradeoffs that reflect available resources, e.g., control energy, or robustness requirements. The lower transfer function $P_{yu}(s)$ represents the path from the control inputs $u(s)$ to the measured outputs $y(s)$ and is a function of the choice and placement of actuators and sensors, respectively, for the control system. Although usually taken as a given for control design, often there is freedom determining sensor and actuator locations, yielding a design decision that impacts the closed-loop performance. Good placement for control design can be determined from the influence of transducers on the open-loop system's controllability and observability, measured in terms of the Hankel singular values.

As noted by Lim,³ the Hankel singular values (HSVs) from the disturbance to performance outputs illustrated in Fig. 1 are denoted as

$$\Gamma_{zw}^2 = \text{diag}(\gamma_{zw1}^2, \dots, \gamma_{zwn}^2) \quad (1)$$

where Γ_{zw}^2 is a diagonal matrix of the n HSVs of the system. The HSVs provide a measure of the degree of coupling of each of the n modes associated with the performance path of the plant $P_{zw}(s)$. The HSV for each of the p th actuators and q th sensors of the control path can be defined as

$$\Gamma_{yqup}^2 = \text{diag}(\gamma_{yqup1}^2, \dots, \gamma_{yqupn}^2) \quad (2)$$

A baseline reference of HSVs for all p actuators and q sensors is defined as

$$\bar{\Gamma}_{yu}^2 = \text{diag}(\bar{\gamma}_{yu1}^2, \dots, \bar{\gamma}_{yun}^2) \quad (3)$$

The placement metric for disturbance rejection, as outlined by Lim,³ can be expressed as follows for the q th sensor and p th actuator:

$$J_{qp} = \sum_{i=1}^n \left(\frac{\gamma_{yqup i}^4}{\bar{\gamma}_{yu i}^4} \right) \gamma_{zw i}^4 \quad (4)$$

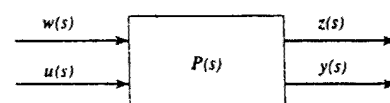


Fig. 1 Block diagram of the two-port design model.

Received 13 November 1998; revision received 29 March 1999; accepted for publication 30 March 1999. Copyright © 1999 by Robert L. Clark and David E. Cox. Published by the American Institute of Aeronautics and Astronautics, Inc., with permission.

*Associate Professor, Department of Mechanical Engineering and Materials Science, Box 90300, Member AIAA.

†Research Scientist, Flight Dynamics and Control Division, Building 1268A, Room 1156.

This metric positively weights all coupling to the dynamic modes of the system. If we further distinguish between in-bandwidth modes n_{in} and out-of-bandwidth modes $n_{out} = n - n_{in}$, the placement metric for disturbance rejection can be expressed as follows:

$$J_{qp_{in}} = \sum_{i=1}^{n_{in}} \left(\frac{\gamma_{yq_{ui}}^4}{\bar{\gamma}_{yui}^4} \right) \gamma_{zui}^4 \quad (5)$$

For added robustness, we prefer to limit the coupling through the control path P_{yu} to the out-of-bandwidth modes. As such, a metric is defined by weighting the normalized HSVs for the control path with themselves and taking the reciprocal of the result to emphasize poor coupling:

$$J_{qp_{out}} = \left[\sum_{i=n_{in}+1}^n \left(\frac{\gamma_{yq_{ui}}^4}{\bar{\gamma}_{yui}^4} \right) \gamma_{yq_{ui}}^4 \right]^{-1} \quad (6)$$

Combining the metric associated with in-bandwidth disturbance rejection by the metric associated with out-of-bandwidth robustness, the following metric for actuator/sensor selection results:

$$\bar{J}_{qp} = \bar{J}_{qp_{in}} + \bar{J}_{qp_{out}} \quad (7)$$

where the overbar serves to indicate that the in-bandwidth and out-of-bandwidth metrics have been normalized relative to their maximum entry, and \bar{J}_{qp} is the band-limited metric. Thus, a tradeoff exists in the selection of the actuators and sensors based on those that couple well to modes present in the disturbance path over the desired bandwidth of control and those that couple poorly to modes present in the control path outside of the desired bandwidth of control. Therefore, the optimal sensor/actuator pairings should not only couple strongly at low frequencies, but also roll-off naturally at high frequencies.

Description of a Structural Acoustic Model

In preparation for the design of an experimental test rig for structural acoustic control, the actuator/sensor design methodology was applied to an approximate model of a system to determine the best target locations for the transducers. The test rig was constructed from aluminum, measuring $18 \times 16 \times 0.1875$ in. thick. The boundaries were constructed to approximate that of a simply supported plate, and piezoceramic transducers measuring $6 \times 4 \times 0.0075$ in. thick were available for experimental implementation. The larger piezoceramic patches were selected based on the results of a prior study that demonstrated that large aperture transducers serve as spatial wave number filters and provide greater control over the low-bandwidth modes required for structural acoustic control.⁵

The model of the piezostucture was developed from an assumed modes approach as outlined by Clark et al.⁶ Seven target locations for piezoceramic sensors and actuators were studied. As single-input/single-output control was desired for the experiment the best two transducers were sought from the possible set of 49. For simplicity, the mass and stiffness contributions of the transducers were omitted from the analytical model. A schematic diagram of target locations is depicted in Fig. 2. The center coordinates of each patch are indicated by an asterisk on the nondimensional schematic of the plate. Additionally, the nondimensional coordinates are provided in Table 1. Only one quadrant of the plate was explored for actuator/sensor placement. The magnitudes of simply supported modal shapes are symmetric about the vertical and horizontal axis and thus

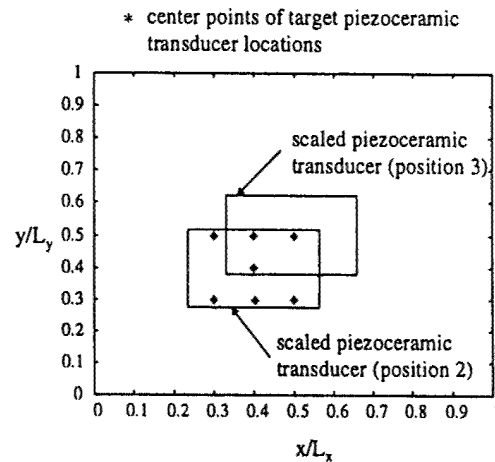


Fig. 2 Schematic of the plate identifying center points of piezoceramic transducers.

coupling strength, which the placement metric measures, are equivalent in the four quadrants. Given that the objective was to reduce the sound power radiated, intuition suggested that a patch centered on the structure and operated as a collocated transducer pair would produce the best result (modes with even indices are inefficient acoustic radiators). Alternative candidate transducer positions were also included along the diagonal of the nondimensional plate as well as on nodal lines of modes with even indices in x and y .

Performance of the closed-loop system is defined in terms of the total power radiated into the far-field. For the purpose of estimating the sound power radiated, the plate was subdivided into 20 rectangular elements having equal surface area. The velocity at the center point of each elemental area was modeled to provide inputs to radiation filters. Assuming that the plate is coupled to a half-space with rigid boundaries, the sound power radiated can be obtained by applying the Rayleigh integral to compute the far-field sound pressure levels in terms of the surface velocity of the vibrating, flexible panel. As detailed by Gibbs et al.,⁷ radiation modal expansion can be applied to generate a filter that estimates the sound power radiated in terms of a finite set of discrete velocity outputs. For the purpose of this study, the first radiation mode was used to define the performance path between a generalized force applied uniformly to each mode of the structure and the sound power radiated. The first radiation mode results from a series expansion over all of the structural modes that radiate volumetrically. In developing the radiation filter, a state variable model of the system was constructed. (For greater details on the construction of the piezostucture model and the radiation filter, refer to Ref. 6.)

The model included 60 states for the structural system and 9 states for the radiation filters. A bandwidth of interest was defined below 1200 Hz; thus the first 20 structural states were included in the in-bandwidth computation of the performance metric and the remaining 40 structural states were included in the out-of-bandwidth computation of the performance metric.

Comparison of Actuator/Sensor Selection Strategies

To form a basis of comparison, the proposed strategy for band-limited actuator/sensor selection was compared to the selection strategy outlined in Ref. 4. Limiting the selection to the metric defined in Eq. (4), one obtains the result presented in Fig. 3, which shows the relative merit of all 49 possible SISO transducer paths. As illustrated there is symmetry in the selection because, due to reciprocity, either transducer of a given pair can be used as an actuator or a sensor and result in the same frequency response. For the case presented, the optimal transducer pair is actuator 3 and sensor 3, which corresponds to a single piezoceramic transducer positioned in the center of the plate and operated as a collocated pair. The result of this actuator/sensor selection is consistent with physical intuition because modes with even indices are inefficient acoustic radiators when the structural wave number exceeds the acoustic wave number.

The result obtained with the band-limited actuator/sensor selection strategy for disturbance rejection is distinctly different. Using

Table 1 Center points of piezoceramic transducers in nondimensional plate coordinates

Transducer	x coordinate	y coordinate
1	0.3	0.3
2	0.4	0.4
3	0.5	0.5
4	0.3	0.5
5	0.4	0.5
6	0.5	0.3
7	0.4	0.3

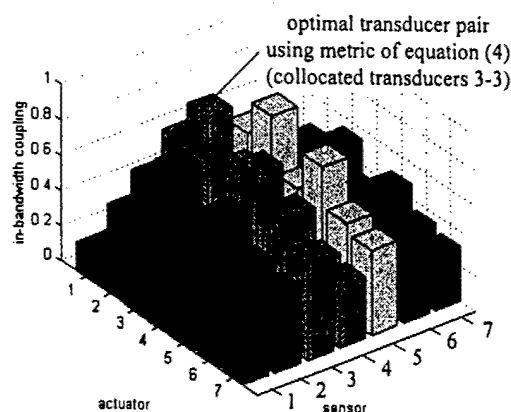


Fig. 3 Barchart of actuator/sensor selection for disturbance rejection outlined in Eq. (4) (Ref. 3).

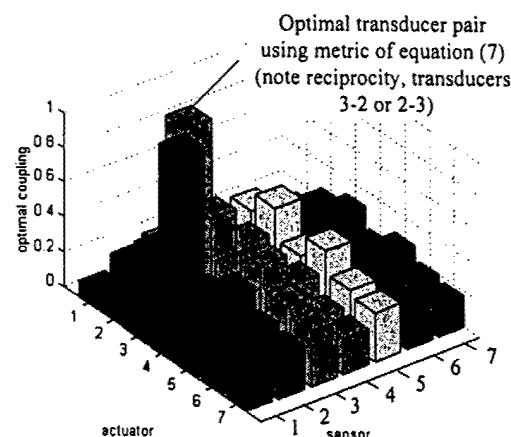


Fig. 4 Barchart of band-limited actuator/sensor selection for disturbance rejection outlined in Eq. (7).

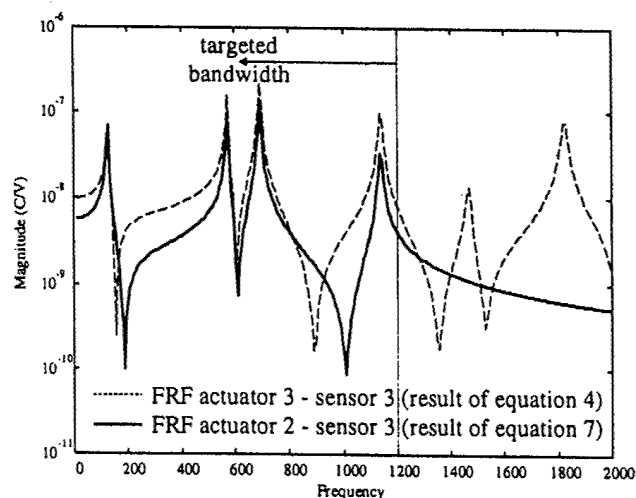


Fig. 5 Magnitude of frequency responses associated with the transducer pairs selected based on Eqs. (4) and (7).

this metric, as outlined in Eq. (7), one obtains the result presented in Fig. 4. For the case studied, the band-limited selection strategy suggests the use of transducer 3 and transducer 2. Again, because of reciprocity one can select either as an actuator or a sensor. This result was nonintuitive, and a schematic diagram of the pair, showing relative position on the structure, is presented in Fig. 2.

Upon comparing the frequency response between the transducer pair resulting from the application of the metric in Eq. (4) and that resulting from the band-limited metric outlined in Eq. (7), one observes that the in-bandwidth (< 1200 Hz) response associated with

actuator 3 and sensor 3 is slightly greater than that of actuator 2 and sensor 3, as illustrated in Fig. 5. Also note that neither transducer pairs observe or control the (1, 2) or (2, 1) modes of the structure, noted by the absence of resonances corresponding to these modes. As noted in the previous section, the (1, 2), (2, 1), and (2, 2) modes are inefficient acoustic radiators at low frequency and thus are absent from the chosen performance path. Comparing the out-of-bandwidth response of the two transducer options in Fig. 5, one observes that the actuator/sensor pair selected including the band-limited metric results in significantly less response out of the bandwidth of interest (> 1200 Hz). Thus, the response of modes outside of the desired bandwidth of operation, which typically lead to stability issues, are suppressed.

Closed-Loop Results

To demonstrate the effect of actuator/sensor selection on closed-loop response, compensators were designed for the best transducers using both metrics, and the resulting closed-loop performance was compared. The analytical plant model had 60 structural states that represented plate dynamics up to about 5000 Hz. The compensators, however, were designed on a reduced-order model that contained only 20 structural states. This reduced-order model is representative of the type of model that would result from experimental system identification.

Linear quadratic Gaussian (LQG) compensators were designed under the model structure of Fig. 1 with control effort penalty of $R = 5 \times 10^{-5}$ (1/V), sensor noise of $V = 1.5 \times 10^{-8}$ (C), and unity process noise and performance weight. The sensor noise was selected to be comparable to the effect of process noise at the frequency where the controller should begin to roll off. Because the piezoceramic element centered on the plate was used as a sensor in both cases, this sensor noise was consistent for both designs. A comparison of the measured output because of unit norm process noise and unit norm sensor noise is shown in Fig. 6.

The control effort penalty was decreased until the closed-loop system, based on the full-order model, was at the border of instability for the collocated actuator/sensor selected by the metric defined in Eq. (4). Applying the same control effort penalty, sensor noise, and process noise, however, for the transducer pair selected from the metric of Eq. (7) resulted in a stable closed-loop response.

The closed-loop responses for each transducer pair are presented in Fig. 7. The response below 1200 Hz is essentially the same for each of the resulting transducer pairs. However, above 1200 Hz, the actuator 3/sensor 3 pair chosen based on the performance metric defined in Eq. (4) results in an unstable response at approximately 1838 Hz. However, the actuator 2/sensor 3 pair chosen based on the band-limited metric defined in Eq. (7) is stable and does not show the effect of spillover at high frequencies.

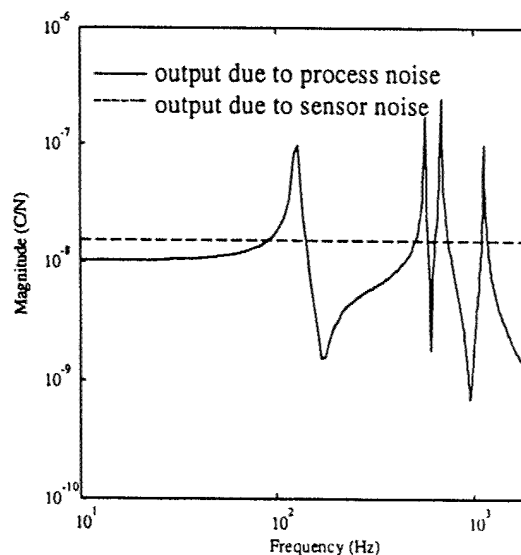


Fig. 6 Magnitude of process noise and sensor noise used in the LQG design.

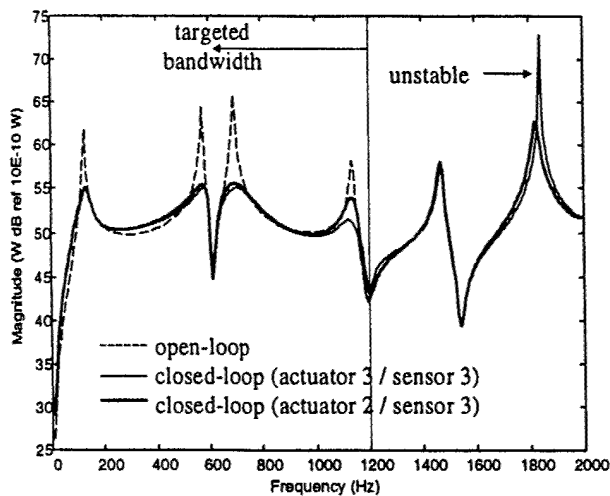


Fig. 7 Magnitude of the closed-loop response for the two alternative transducer pairs selected.

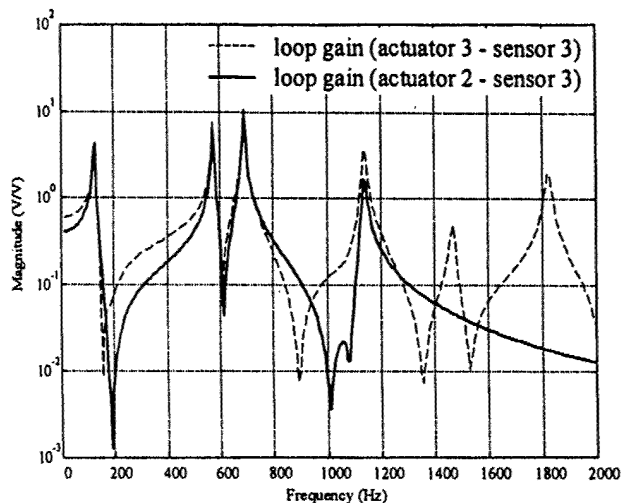


Fig. 8 Loop-gains for actuator 3/sensor 3 [Eq. (4)] and actuator 2/sensor 3 [Eq. (7)].

These results can be anticipated by looking at the loop-gain for each system, presented in Fig. 8. As illustrated, below 1200 Hz, the loop-gains are roughly the same; however, above 1200 Hz, the loop-gain through the collocated transducer pair (actuator 3/sensor 3) is much higher because of significant contribution from out-of-bandwidth modes, exceeding unity at approximately 1838 Hz, resulting in the unstable frequency shown in Fig. 8. The loop-gain associated with the noncollocated transducer pair (actuator 2/sensor 3) above 1200 Hz is much less than unity, explaining the reduced spillover seen in its closed-loop response. This is a result of the spatial filtering in the open-loop plant, achieved by the

transducer placement associated with the band-limited metric of Eq. (7). The natural roll-off in frequency response resulting from the metric imposed by the band-limited disturbance rejection actuator selection metric of Eq. (7) resulted in small loop-gains out of the desired bandwidth identified for structural acoustic control, leading to a stable compensator based on a reduced-order model of the system.

Conclusions

A band-limited actuator/sensor selection methodology for disturbance rejection was outlined. Unlike prior methods, which emphasized disturbance rejection in selecting transducers that couple best to modes present in the performance path, the proposed methodology serves to further impose a penalty on the selection of transducer pairs that couple well to modes beyond the identified bandwidth of interest, creating a natural roll-off in the frequency response from the selected spatial apertures of the transducers. Adding the band-limited metric of Eq. (6) to the disturbance rejection metric of Eq. (4) provides the control system engineer with a very powerful method of selecting transducers for feedback control including both disturbance rejection and robustness to model uncertainty outside of the identified bandwidth of interest. For the structural acoustic example provided, a single transducer pair was selected from a possible choice of 49 transducer pairs for reducing the sound power radiated. Although both the disturbance rejection selection method of Eq. (4) and the band-limited disturbance rejection method of Eq. (7) resulted in transducer pairs with very similar performance over the identified bandwidth (<1200 Hz), the band-limited disturbance rejection selection method further resulted in a transducer pair that coupled poorly to structural modes outside of the identified bandwidth of interest. This selection methodology provides the control system engineer with a crude means of introducing loop-shaping concepts in the open-loop plant through the actuator/sensor selection.

References

- Gawronski, W., and Lim, K. B., "Balanced Actuator and Sensor Placement for Flexible Structures," *International Journal of Control*, Vol. 65, No. 1, 1996, pp. 131-145.
- Lim, K. B., and Gawronski, W., "Hankel Singular Values of Flexible Structures in Discrete Time," *Journal of Guidance, Control, and Dynamics*, Vol. 19, No. 6, 1996, pp. 1370-1377.
- Lim, K. B., "Disturbance Rejection Approach to Actuator and Sensor Placement," *Journal of Guidance, Control, and Dynamics*, Vol. 20, No. 1, 1997, pp. 202-204.
- Lim, K. B., Lake, R. C., and Heeg, J., "Effective Selection of Piezoceramic Actuators for an Experimental Flexible Wing," *Journal of Guidance, Control, and Dynamics*, Vol. 21, No. 5, 1998, pp. 704-709.
- Vipperman, J. S., and Clark, R. L., "Implications of Using Collocated Strain-Based Transducers for Active Structural Acoustic Control," *Journal of the Acoustical Society of America* (to be published).
- Clark, R. L., Saunders, W. R., and Gibbs, G. P., *Adaptive Structures. Dynamics and Control*, Wiley, New York, 1998, pp. 376-393.
- Gibbs, G. P., Clark, R. L., Cox, D. E., and Viperman, J. S., "Radiation Modal Expansion: Application to Active Structural Acoustic Control," *Journal of the Acoustical Society of America* (submitted for publication).